Cooling strategies for the atomization of glass-forming alloys

Vom Fachbereich Produktionstechnik

der

UNIVERSITÄT BREMEN

zur Erlangung des Grades

Doktor-Ingenieur

genehmigte

Dissertation

von

Nevaf Ciftci, M.Sc.

Gutachter:

Prof. Dr.-Ing. habil. Lutz Mädler (Universität Bremen)
Prof. Dr.-Ing. habil. Dr. h.c. Jürgen Eckert (Montanuniversität Leoben/Österreich)

Tag der mündlichen Prüfung: 26.05.2020

Zusammenfassung

Metallische Gläser bzw. massive metallische Gläser (bulk metallic glasses, BMG) sind relativ neue Werkstoffe, die aufgrund ihrer regellosen atomaren (amorphen) Anordnung gegenüber kristallinen Werkstoffen hohe Festigkeiten, Härten, elastische Dehnungen sowie gute Korrosionseigenschaften und besondere weichmagnetische Eigenschaften aufweisen. Außerdem zeichnen sie sich durch eine einmalige Prozessierbarkeit aus, da sie sich in einem bestimmten Temperaturfenster — ähnlich wie Kunststoffe — plastisch verformen lassen. Trotz ihrer relativ geringen plastischen Bruchdehnung werden sie häufig als Strukturwerkstoffe in Erwägung gezogen und haben bereits erste kristalline Werkstoffe in industriellen Anwendungen (Transformatoren, Spulen, Induktoren, Federn, Gehäuse, Skalpelle, Sportartikel etc.) ersetzt.

Die Herstellbarkeit von amorphen Produkten ist abhängig von der Legierungszusammensetzung und den Abkühlbedingungen. Die Legierung muss schnell abgekühlt werden, damit sich die Atome nicht zu einer Kristallstruktur ordnen können. Die Schmelze erstarrt bei der Glasübergangstemperatur kristallin, wenn die Abkühlrate nicht ausreichend ist. Die erforderlichen Abkühlraten führen dazu, dass die erzielbaren Bauteilabmessungen auf kleine Dimensionen beschränkt sind. Diese geometrischen Restriktionen können durch einen zweistufigen Prozess aus Pulververdüsung und anschließender Pulververdichtung überwunden werden. Zerstäubungstechniken sind vielversprechende Techniken, da die Schmelzetropfen durch das große Oberflächen-Volumen-Verhältnis in den amorphen Zustand überführt werden können. Bei der Pulververdüsung werden typischerweise Abkühlraten von 10^2 bis 10^5 $\mathrm{K\,s^{-1}}$ erreicht.

Das Ziel der Dissertation war die Erweiterung der Abkühlstrategien bei der Zerstäubung glasbildender Schmelzen. Der Fokus lag auf der Verdüsung von Legierungen mit Einschmelzmaterialien, die zu moderaten Preisen erhältlich sind. Diese Glasbilder können aufgrund des geringeren Reinheitsgrades (commercial purity, CP) im Vergleich zu Materialien mit Laborreinheit (high purity, HP) nur durch höhere Abkühlraten amorph verdüst werden. Hierbei war es notwendig, den Wärmeübergangskoeffizienten zu erhöhen. Dies setzte eine gezielte Abstimmung hinsichtlich der Prozessgrößen voraus, sodass neben Legierungen mit geringen Reinheitsgraden auch größere Schmelzetropfen amorph verdüst werden konnten. Durch den Einsatz verschiedener Abkühlstrategien sollten neue Prozessfenster eröffnet werden, die bei der konventionellen Pulververdüsung nicht erreicht werden. Die entwickelten Abkühlstrategien wurden erstmalig auf glasbildende Legierungen übertragen: (i) Variation der Überhitzungstemperatur, (ii) Heißgaszerstäubung, (iii) Sprühkegelkühlung sowie (iv) Flüssigabschreckung. Diese Abkühlstrategien hatten zusätzlich das Ziel, heterogene Keimbildung zu minimieren und kleinere Partikel zu erzeugen, da die Abkühlrate der Schmelzetropfen während der Erstarrungsphase im Wesentlichen von der Partikelgrösse und dem GMR (Massenstromverhältnis aus Gas zu Metallschmelze) abhängig ist.

Die höchsten Abkühlraten wurden für flüssig-abgeschreckte Partikel erreicht. Die $\{(Fe_{0.6}Co_{0.4})_{0.75}B_{0.2}Si_{0.05}\}_{96}Nb_4$ bzw. $Fe_{76}B_{10}Si_9P_5$ Pulver konnten dabei vollständig amorph erzeugt werden (< 200 µm), wohingegen FeCoBSiNb Partikel bei der konventionellen Pulververdüsung nur bis zu 63 µm amorph waren. Selbst die kleinsten FeBSiP Partikel (< 25 µm) waren bei der konventionellen Pulververdüsung nur teilamorph. Ferner zeigte sich, dass induzierter Wasserstoff (10^2 - 10^4 ppm) beim Abschrecken mit Wasser die Glasbildungseigenschaften und die Sättigungsmagnetisierung der Pulver verbesserte. Eine weitere Fragestellung im Rahmen der Arbeit war, inwieweit die flüssig-abgeschreckten Partikel weiterverarbeitet werden können, da ein starker Oxidfilm um die Partikel vermutet wurde. Mittels Spark Plasma Sintering konnten unabhängig von den verwendeten Abkühlstrategien amorphe Ringe mit einer relativen Dichte $> 98\%$ erzeugt werden. Die Ringe zeigten dabei eine nahezu unveränderte Sättigungsmagnetisierung, wobei die Koerzitivfeldstärke leicht anstieg bzw. die Permeabilität stark abnahm. Durch den Einsatz der Flüssigabschreckung konnten diese Legierungen mit CP erstmalig in feste Probekörper gepresst werden und bieten dabei durch ihre guten magnetischen Eigenschaften (unabhängig von der Reinheit) ein hohes Potential für industrielle Anwendungen.

Die zweithöchsten Abkühlraten wurden für die Abkühlstrategie Sprühkegelkühlen beobachtet. Die FeCoBSiNb bzw. FeBSiP Partikel waren bis zu 125 µm bzw. 45 µm vollständig amorph. Eine erhöhte Überhitzungstemperatur führte trotz der Annahme, dass Nukleationskeime in der Schmelze aufgelöst bzw. verringert werden nicht zu einer signifikanten Erhöhung des amorphen Anteils. Es zeigte sich jedoch, dass höhere Überhitzungstemperaturen die Partikelformfaktoren vebesserten. Höhere Formfaktoren führen dabei zu einer höheren Pulverfließfähigkeit. Es wurden neben den beiden Fe-Legierungen zwei weitere Legierungen betrachtet: $Zr_{59.3}Cu_{28.8}Al_{10.4}Nb_{1.5}$ und $Cu_{47}Ti_{33}Zr_{11}Ni_6Si_1Sn_2$. Die ZrCuAlNb Legierung wies unabhängig von der Überhitzungstemperatur eine hohe Anzahl an nicht-sphärischen Partikeln auf. Dieses Verhalten war konträr zu den anderen Legierungen und kann auf unterschiedliche Viskositäten zurückgeführt werden. Eine hohe Schmelzeviskosität beeinflusst maßgeblich die Tropfenverformung.

Erhöhte Zerstäubergastemperaturen führten zu einer geringeren Gasdichte und damit zu einer höheren Gas- bzw. Relativgeschwindigkeit, wobei der Temperaturgradient zwischen Schmelzetropfen und Gas abnahm. Dieser gegenseitige Effekt führte zu einer Kompensation, sodass der amorphe Anteil unverändert blieb bzw. leicht abnahm. Neue semi-empirische Korrelationen zur Bestimmung der Abkühlraten bestätigten dabei die experimentellen Beobachtungen. Die Heißgaszerstäubung ist jedoch eine vielversprechende Methode zur industriellen Großproduktion von amorphen Metallpulvern. Am Beispiel der FeCoBSiNb Legierung wurde gezeigt, dass durch die verringerte Gasdichte des Zerstäubergases signifikant kleinere Partikel erzeugt wurden und der Gasverbrauch um bis zu 50% gesenkt werden konnte. Ferner konnte die amorphe Pulverausbringung um ca. 20% erhöht werden. Jedoch verschlechterten sich die Partikelformfaktoren zu geringeren Werten.

Summary

Metallic glasses or bulk metallic glasses are a new class of materials. These amorphous metals have a disordered structure, resulting in outstanding properties when compared to crystalline materials such as high hardness, strength, elasticity, good wear and corrosion resistance, and superior soft magnetic properties. Similar to thermoplastics, they are easily deformable due to a highly viscous state between the glass transition temperature and the crystallization temperature. Despite their low plasticity and tendency for catastrophic failure through instantaneous shear band propagation, they are often considered as structural materials and have already been implemented in industrial applications (transformers, coils, inductors, springs, micro gears, cases, scalpels, sporting goods etc.).

The properties of metallic glasses depend on alloy composition and cooling conditions during solidification. The liquid must be cooled rapidly to avoid crystallization, forcing the melt to retain its liquid atomic structure. The required cooling rates to obtain an amorphous solid are limited by time-dependent heat conduction, restricting product dimensions. Geometric limitations can be overcome by powder synthesis and consolidation to introduce metallic glasses to the commercial market. Gas atomization is a promising technique in the commercial production of metallic glasses, as amorphous particles can be produced due to the high surface-to-volume ratio through conduction and radiation. The cooling rate in molten gas atomization typically ranges from 10^2 to 10^5 $\mathrm{K\,s^{-1}}$.

The aim of this PhD thesis was the development of novel cooling strategies for the atomization of glass-forming alloys to increase cooling rates during droplet solidification. The focus was on the atomization of soft ferromagnetic glass-forming alloys with commercial purity. These alloys are difficult to atomize into an amorphous state due to cooling rate limitations and their low glass-forming ability. For this purpose, it was necessary to increase the heat transfer coefficient. This resulted in higher cooling rates, allowing for the atomization of soft ferromagnetic glass-forming alloys with commercial purity and larger particle sizes that normally tend to crystallize during droplet solidification. With the development of novel cooling strategies, new process windows have been made available that are typically inaccessible in conventional gas atomization. Therefore, four cooling strategies were developed for the atomization of glass-forming alloys: (i) increasing the melt superheat temperature, (ii) hot gas atomization, (iii) spray cone cooling, and (iv) liquid quenching. The developed cooling strategies were used to decrease potent nucleation sites in the melt as well as to produce smaller particles, as the cooling rate strongly depends on droplet size and gas-to-melt mass flow ratio.

The highest cooling rates were achieved for liquid quenched particles, as the $\{(Fe_{0.6}Co_{0.4})_{0.75}B_{0.2}Si_{0.05}\}_{96}Nb_4$ and $Fe_{76}B_{10}Si_9P_5$ powders were fully amorphous for the entire particle size range (< 200 µm). Conventionally atomized FeCoB-

SiNb particles were only fully amorphous up to 63 μm and FeBSiP particles were partially-crystalline even for the smallest particle size class (< 25 μm). Hydrogen inducement during water quenching (10^2 - 10^4 ppm) had a positive effect on the glass-forming ability and saturation magnetization. Since it was expected that an oxide film would be formed during liquid water quenching, the powder consolidation ability was also investigated. Amorphous rings with a relative density > 98% were produced via Spark Plasma Sintering, regardless of the cooling strategies used. The saturation magnetization of the sintered rings remained nearly constant, while the coercivity slightly increased and the permeability distinctly decreased. Liquid quenching resulted in an increased amorphous fraction and improved powder properties as well as consolidation feasibility, making liquid quenching an influential opportunity for the commercialization of these alloys with commercial purity feedstock.

The second highest cooling rates were achieved for spray cone cooling. The FeCoBSiNb and FeBSiP particles were amorphous up to 125 μm and 45 μm, respectively. An increased melt superheat temperature resulted in a slightly higher amorphous fraction. It was assumed that a high melt superheat temperature reduced or destroyed any potential nucleation sites in the melt.

An increased melt superheat temperature ranging from 250 to 450 K significantly increased particle shape factors such as sphericity and aspect ratio. For the particle shape study, a $Zr_{59.3}Cu_{28.8}Al_{10.4}Nb_{1.5}$ and a $Cu_{47}Ti_{33}Zr_{11}Ni_6Si_1Sn_2$ (at%) alloy were also selected. The ZrCuAlNb glass-forming alloy showed a significantly higher amount of non-spherical particles and had a rougher surface, while the three other glass-forming alloys exhibited smooth surfaces and a nearly spherical particle morphology. This is due to the higher viscosity as the droplet break-up and formation process depends on viscosity.

The FeCoBSiNb glass-forming alloy was used to demonstrate the effect of hot gas atomization on cooling rates. A higher gas velocity was introduced by a decreased gas density (through elevated gas temperatures), leading to a higher relative velocity, while the temperature gradient between the melt droplet and surrounding gas was reduced. The relative velocity and the temperature gradient compensated for each other and resulted in nearly unchanged cooling rates. Thus, the amorphous fraction remained the same or slightly decreased. Newly developed semi-empirical correlations to predict average cooling rates confirmed these results. Despite the fact that the cooling rate remained constant, hot gas atomization provided many advantages over conventional gas atomization. For instance, hot gas atomization is a promising design tool for the commercialization of bulk metallic glasses with the benefits of producing smaller amorphous powders, reducing gas consumption up to 50%, retaining the amorphous fraction, and increasing the amorphous yield by 20%. By contrast, particle shape factors decreased due to the attachment of smaller particles on larger semi-solidified droplets known as satellites. An increase in particle shape factors typically results in improved powder flowability.

List of publications and conference contributions

List of publications

[1] N. Ciftci, N. Ellendt, L. Mädler, V. Uhlenwinkel. Impact of Hot Gas Atomization on Glass Forming Alloys. Hamburg: World PM 2016, European Powder Metallurgy Association, ISBN: 978-1-899072-48-4, 2016.

[2] N. Ciftci, N. Ellendt, E. Soares Barreto, L. Mädler, V. Uhlenwinkel. Increasing the amorphous yield of $\{(Fe_{0.6}Co_{0.4})_{0.75}B_{0.2}Si_{0.05}\}_{96}Nb_4$ powders by hot gas atomization. Advanced Powder Technology, 29(2):380-385, 2018.

[3] N. Ciftci, N. Ellendt, G. Coulthard, E. Soares Barreto, L. Mädler, V. Uhlenwinkel. Novel Cooling Rate Correlations in Molten Metal Gas Atomization. Metallurgical and Materials Transactions B, 50(2):666-677, 2019.

[4] N. Ciftci, N. Yodoshi, S. Armstrong, L. Mädler, V. Uhlenwinkel. Processing soft ferromagnetic metallic glasses: on novel cooling strategies in gas atomization, hydrogen enhancement, and consolidation. Journal of Materials Science & Technology, 2020 (accepted for publication).

[5] V.C. Srivastava, G.K. Mandal, N. Ciftci, V. Uhlenwinkel, L. Mädler. Processing of High-Entropy $AlCoCr_{0.75}Cu_{0.5}FeNi$ Alloy by Spray Forming. Journal of Materials Engineering and Performance, 26(12):5906-5920, 2017.

[6] T. He, O. Ertuğrul, N. Ciftci, V. Uhlenwinkel, K. Nielsch, S. Scudino. Effect of particle size ratio on microstructure and mechanical properties of aluminum matrix composites reinforced with $Zr_{48}Cu_{36}Ag_8Al_8$ metallic glass particles. Materials Science and Engineering: A, 742:517-525, 2019.

[7] T. He, T. Lu, N. Ciftci, V. Uhlenwinkel, K. Nielsch, S. Scudino. Mechanical properties and tribological behavior of aluminum matrix reinforced with Fe-based metallic glass: Influence of particle size. Powder Technology, 361:12-19, 2019.

[8] J. Lehtoonen, Y. Ge, N. Ciftci, O. Heczko, V. Uhlenwinkel, S-P. Hannula. Phase structures of gas-atomized equiatomic CrFeNiMn high entropy alloy powder. Journal of Alloys and Compounds, 827(154142):1-6, 2020.

[9] N. Luo, C. Scheitler, N. Ciftci, F. Galgon, Z. Fu, V. Uhlenwinkel, M. Schmidt, C. Körner. Preparation of Fe-Co-B-Si-Nb bulk metallic glasses by selective laser melting: microstructure and properties. Materials Characterization, 162

(110206):1-9, 2020.

Conference contributions

[1] N. Ciftci, N. Ellendt, L. Mädler, V. Uhlenwinkel. Impact of Hot Gas Atomization on Glass Forming Alloys. World PM 2016 Congress & Exhibition, European Powder Metallurgy Association, Hamburg, Germany, 09-13 October 2016.

[2] N. Ciftci, N. Ellendt, L. Mädler, V. Uhlenwinkel. Cooling strategies for the droplet solidification of glass-forming alloys. 25th International Conference on Metastable, Amorphous, and Nanostructured Materials (ISMANAM 2018), Rome, Italy, 02-06 July 2018.

Acknowledgements

Writing a good acknowledgement is not as easy as you might think. Obviously, you do not want to be too emotional, but you also want to find the right words to say thank-you to the people who have accompanied you through your academic journey. I hope this note communicates what it means to have gone the extra mile to finalize this work, including the countless hours during long weekends that went into it, and that it reflects the spirit of dedication and support behind this thesis.

If someone asks me what I have personally learned the most, I would probably say learning from my mistakes, as it is the mistakes that lead to knowledge. I believe this outstanding characteristic can be attributed to my supervisor Prof. Dr.-Ing. habil. Lutz Mädler. My journey has always involved curiosity, which has sometimes turned into disappointment, as attempting great work can lead to failure. Prof. Lutz Mädler had the right intuition to turn frustration into lessons learned, but also for exploring alternatives and setting new research goals. I would also like to thank him for the fruitful scientific discussions and for his advice and feedback when preparing manuscripts for publications, which greatly improved their readability, structure, and scientific argumentation.

I would like to express my appreciation to Univ. Prof. Dr.-Ing. habil. Dr. h.c. Jürgen Eckert for being co-reviewer of my thesis. I also wish to thank him for the fruitful scientific and personal discussions during international conferences.

This work would never be a success without the substantial contribution of my direct supervisor Dr.-Ing. Volker Uhlenwinkel. I truly thank him for the opportunity to work in his research group including the use of modern atomization facilities and measurement instruments, as well as the financial and scientific freedom to try unconventional ideas that were not always successful. I am indebted to his patience, outstanding knowledge of atomization that he taught me, as well as for refining my thesis topic together. We have known each other for so many years, which has truly resulted in profound trust and constant scientific and personal support.

I am very grateful for the opportunity to work with Prof. Noriharu Yodoshi from Tohoku University in Sendai, Japan. During my stay, I had the chance to use his laboratories and discuss my research with him, resulting in substantial scientific progress. My stay was funded through two scholarships and I would like to thank the MAPEX Center for Materials and Processes at the University of Bremen and the Cooperative Research Center for Advanced Materials at Tohoku University for the financial support.

During this work, we had a joint collaboration with Prof. Dr. rer. nat. Ralf

Busch, Benedikt Bochtler, and Dr.-Ing. Simon Hechler from Lehrstuhl für Metallische Werkstoffe at Universität des Saarlandes. I am very thankful for the profound scientific discussions and the evenings we shared together before project meetings. A second collaboration was initiated with Prof. Livio Battezzati and Dario Gianoglio from the University of Turin. Dario joined our research group for three months and it was a pleasure working with him.

A thesis is always the product of many people setting the groundwork and for that I thank our technicians Stefan Evers, Rainer Lehmann, and Frank Peschel who helped me with experimental setups. Most of the experimental components were realized in the machine shop, and I am thankful to Dieter Brüns/Andreas Flunker and their teams. I thank Petra Witte for the SEM images, Dr. Michael Wendschuh for the help with the XRD measurements, and Ellen Matthaei-Schulz for the support with the hydrogen and oxygen measurements.

A big thank-you goes to the students who contributed to this thesis: Sarah Armstrong, Juliane Baumann, Malte Bloch, Evan Chow, Geoffrey Coulthard, Jasper Eitzen, Colm O'Fourthain, Zekiya Göktas, Sean Hickens, Philip Hopp, Luisa Ludwig, Waldemar Meinik, Viola Müller, Ronald Rosenberg, Patrik Sieverding, Nicole Temple, and Julian Wankelmann. I am grateful for your contribution as a student assistant, through a Bachelor/Master thesis, Master project, and UofA co-op program). All of you have found your way to my picture wall.

I am also very thankful for meeting and working with my colleagues in our Mechanische Verfahrenstechnik department, particularly to Prof. Dr.-Ing. habil. Udo Fritsching, Dr.-Ing. Nils Ellendt, and my closest peers: Erika Soares Barreto, Daniel Beckers, Eric Gärtner, Marcel Hesselmann, Shohag Hussain, Saeedeh Imani Moqadam, Farhad Mostaghimi, Dr.-Ing. Ilya Okulov, Lucas Barcelos Otani, Dustin Schröder and Anna Taruttis.

I would also like to thank the Friedrich-Ebert Foundation, which has supported me financially and personally through my entire studies. I am grateful for the beautiful personalities I have met during my time as a scholar and for the opportunity to learn what living in a free society means with the opportunities to participate on political, economic, social, and cultural levels regardless of one's origin, sex or religion.

Finally, this goes to my friends and family who were always supportive and have had unconditional trust and endless patience with me, especially when I canceled activities and family events at the last moment. I dedicate this work to all of you.

The last words are for a very special person in my life. I am really sorry for the late nights, early mornings, short weekends, and for all the things I missed that you personally enjoy. Thank you for being on my side, for your support and patience but also for reading drafts as well as accompanying and encouraging me through the toughest and most joyful moments. I owe you so much.

Contents

1. Prologue **1**
- 1.1. Introduction . . . 2
- 1.2. Statement of the problem and need for the study . . . 3
- 1.3. Aim . . . 4
- 1.4. Thesis outline and solution approach . . . 6
  - 1.4.1. Increasing the melt superheat temperature . . . 6
  - 1.4.2. Production of fine powder through hot gas atomization . . . 8
  - 1.4.3. Spray cone cooling . . . 9
  - 1.4.4. Liquid quenching . . . 9

2. From liquid metal to metallic glass **11**
- 2.1. Structure of metallic glasses . . . 11
- 2.2. Glass formation and thermodynamic considerations . . . 13
- 2.3. Criteria for the glass-forming ability . . . 15
- 2.4. Viscous slowdown and the fragility concept . . . 16
- 2.5. Time-temperature-transformation diagrams . . . 18
- 2.6. The role of oxygen and impurities on glass formation and properties 19

3. Atomization of glass-forming alloys **23**
- 3.1. Gas atomization . . . 23
  - 3.1.1. Free-fall atomization . . . 24
  - 3.1.2. Close-coupled atomization . . . 25
  - 3.1.3. Particle size and particle size distribution . . . 25
- 3.2. Thermal aspects during droplet solidification . . . 27
  - 3.2.1. Measuring the cooling rate . . . 28
  - 3.2.2. Modelling the cooling rate . . . 29
- 3.3. Atomization of glass-forming alloys . . . 34

4. Experimental methods and analyses **35**
- 4.1. Material selection . . . 35
- 4.2. Powder generation via gas atomization . . . 35
- 4.3. Spray cone cooling and liquid quenching experiments . . . 38
- 4.4. Melt Spinning . . . 38
- 4.5. Spark Plasma Sintering (SPS) . . . 39
- 4.6. Powder, ribbon and bulk characterization . . . 40

5. Results and Discussion **45**
- 5.1. Increasing the melt superheat temperature . . . 45
  - 5.1.1. Determination of enthalpy of crystallization . . . 45
  - 5.1.2. Particle size analyses . . . 48
  - 5.1.3. Particle shape analyses . . . 49
  - 5.1.4. The influence of thermophysical properties on the particle shape . . . 52

5.1.5. Conclusion of melt superheat temperature as a cooling strategy . . . 55
5.2. Hot gas atomization . . . 56
5.2.1. Gas mass flow rate and aspiration pressure . . . 56
5.2.2. Particle size analyses . . . 58
5.2.3. Determination of amorphous fraction . . . 60
5.2.4. Calculating the amorphous yield . . . 64
5.2.5. The influence of hot gas on cooling rate . . . 65
5.2.6. Conclusion of hot gas atomization as a cooling strategy . . . 70
5.3. Cooling rate correlations during molten metal atomization . . . 71
5.3.1. From secondary dendrites to average cooling rates . . . 75
5.3.2. From average cooling rates to cooling rate correlations . . . 77
5.3.3. Transferring the cooling rate correlation to different alloy systems . . . 81
5.3.4. Conclusion and review of the cooling rate calculations for the cooling strategy consideration . . . 82
5.4. Spray cone cooling and liquid quenching . . . 83
5.4.1. Safety consideration . . . 84
5.4.2. Powder characterization . . . 85
5.4.3. Conclusion of spray cone cooling and liquid quenching as a cooling strategy . . . 99
5.5. Combining the four cooling strategies together: a comparison . . . 100

6. Conclusion and outlook **105**
6.1. Conclusion . . . 105
6.1.1. Increasing the superheat temperature . . . 105
6.1.2. Production of fine powder through hot gas atomization . . . 106
6.1.3. Spray cone cooling and liquid quenching . . . 107
6.2. Outlook . . . 108

APPENDICES **110**

A. Experimental setups **111**

B. Thermophysical liquid and gas properties **113**

C. Process parameters **115**

Bibliography **119**

List of symbols **134**

CHAPTER 1

Prologue

We are surrounded by glass in our everyday lives. Natural glass itself is likely as old as our planet and is closely related to natural phenomena, such as the eruption of a volcano or a lightning strike, resulting in the formation of solidified glassy rock like *Obsidian* and *Fulgurite*. Even the ancient *Mesoamericans*[1] knew the benefits of naturally formed volcanic *Obsidian* glass. This material is fused within the earth and formed when felsic lava is extruded from a volcano, cooling rapidly during solidification. There is insufficient time for naturally contained mineralizing agents to enable atoms to arrange into a crystalline structure. Instead, the atomic structure of the liquid freezes into a glassy rock that has superior mechanical properties. Consequently, Obsidian was a highly integrated part of daily life and was considered as a valuable resource which may have made a significant contribution to *Mesoamerica's* lack of metallurgy.

It is unclear when our civilization began producing glass artificially. Some scientists have reported findings that go back to 5000 BC. Glass was originally a waste product from ceramic production. The ancient Egyptians continually developed glass production, while Roman glass specialists recognized the economic and technical significance of glass. Today, modern life would be inconceivable without glass as a technological material. This includes classic and modern application fields such as window glass, communication technology (glass fibers), medical techniques (endoscopes or microscopes), and tissue engineering (bioactive glasses) [2].

The modern scientific concept of amorphous materials encloses the material groups of polymers, glass ceramics, and amorphous metals. Amorphous metals or metallic glasses are newcomers to the field of engineering materials [3]. They possess fascinating properties that are unusual for solid metals [4]. Existing in a wide variety of compositions, they are relevant to many fields of research and practical applications [4]. The formation of glasses requires cooling to sufficiently low temperatures without the occurrence of crystallization [5]. Conventional oxide glasses such as window glass require a low critical cooling rate[2] during processing, making the cooling rate an unimportant production parameter [4]. By contrast, metallic glasses require higher cooling rates. Even when the cooling rate is sufficient, they rely mostly on expensive high purity materials and clean laboratory conditions to avoid crystallization. Because rapid solidification techniques are required to reach high cooling rates, metallic glasses are

[1] The ENCYCLOPAEDIA BRITANNICA describes the Mesoamerican civilization as an indigenous culture, and takes it origins from parts of Mexico and Central America prior to Spanish exploration and conquest in the 16th century [1]. The Mesoamerican civilization, along with the comparable Andean civilization, constitutes a New World counterpart to those of ancient Egypt, Mesopotamia, and China [1].

[2] The critical cooling rate is the minimum cooling rate for a particular alloy required to solidify into an amorphous state, resulting in superior material properties.

generally available only in small sizes. The tendency to crystallize impedes efforts to make commercially viable bulk samples by consolidating powder and chopped ribbons [4].

Since the first discovery of amorphous alloys made from a liquid in the 1960s [6], research on metallic glasses remains active, although commercial establishment and other potential applications are awaited [4]. Despite rapid development and the fact that many researchers believe metallic glasses are the ideal engineering material, appreciable access to the industrial market is still limited. It seems unlikely that we have achieved the largest possible dimensions or have found the ideal combination of properties. This may be an explanation for why research on metallic glasses has moved from production techniques to the exploration of new alloy compositions and presently to reassess our understanding of metallic glass formation [7].

1.1. Introduction

The selection and design of modern high-performance structural engineering materials is driven by combinations of mechanical properties such as strength, ductility, toughness, elasticity and the requirements for predictable and non-catastrophic failure in service [8]. The attainment of strength and toughness is a vital requirement for almost all engineering structural materials. Unfortunately, these properties are usually mutually exclusive [9, 10]. Most critical structures such as bridges, ships, and nuclear pressure vessels are manufactured from materials that are low in strength but high in toughness [11].

Crystalline materials exhibit features such as vacancies, interstitial atoms, impurities, dislocations, grain boundaries, surfaces or other interfaces which disrupts the periodicity and determines the physical properties of the crystal [12]. These microstructural defects propagate under stress, enabling plastic shielding that thus promotes high fracture toughness. However, the elastic-energy threshold is very low, resulting in rather low yield strengths [13]. For example, ductile crystalline materials such as low carbon steels exhibit high fracture toughness and a relatively low yield strength [13]. By contrast, ceramics typically have a higher strength, but low fracture toughness. This inherent trade-off between strength and toughness is the fundamental challenge in the quest for highly damage-tolerant materials [13].

Bulk metallic glasses (BMGs) bridge the gap between brittle and tough materials, attracting significant technological interest [8, 13, 14]. The lack of microstructural defects gives them unique properties: they are twice as strong as steel, have greater wear and corrosion resistance, and elasticity [13, 14]. Metallic glasses were found to have good soft magnetic properties, which is today the most successful application, considering commercial efforts [15]. Similar to thermoplastics, they are deformable between the glass transition and crystallization temperature [7]. Although there are significant challenges when scaling-up, metallic glasses are the materials of choice and are claimed to be closer than ever to a disruptive, cost-effective, and high-performance alternative with the advantage of replacing traditional materials and machining methods [16].

1.2. Statement of the problem and need for the study

The structural features of metallic glasses depend on alloy composition and cooling conditions during solidification. The liquid must be cooled quickly to circumvent crystallization, as exhibited in the time-temperature-transformation diagram (Fig.1.1). Rapid solidification techniques such as melt spinning or copper mold casting are commonly used to produce amorphous materials, as they provide the necessary cooling conditions. Transient cooling is often governed by time-dependent heat conduction where heat is extracted externally from the sample boundary. The cooling history is a function of location within the sample, being highest near the surface and lowest near the sample center [17]. When applied to the rapid quenching of metallic glasses, these conductive heat transfer conditions may cause crystallization due to limited cooling rates.

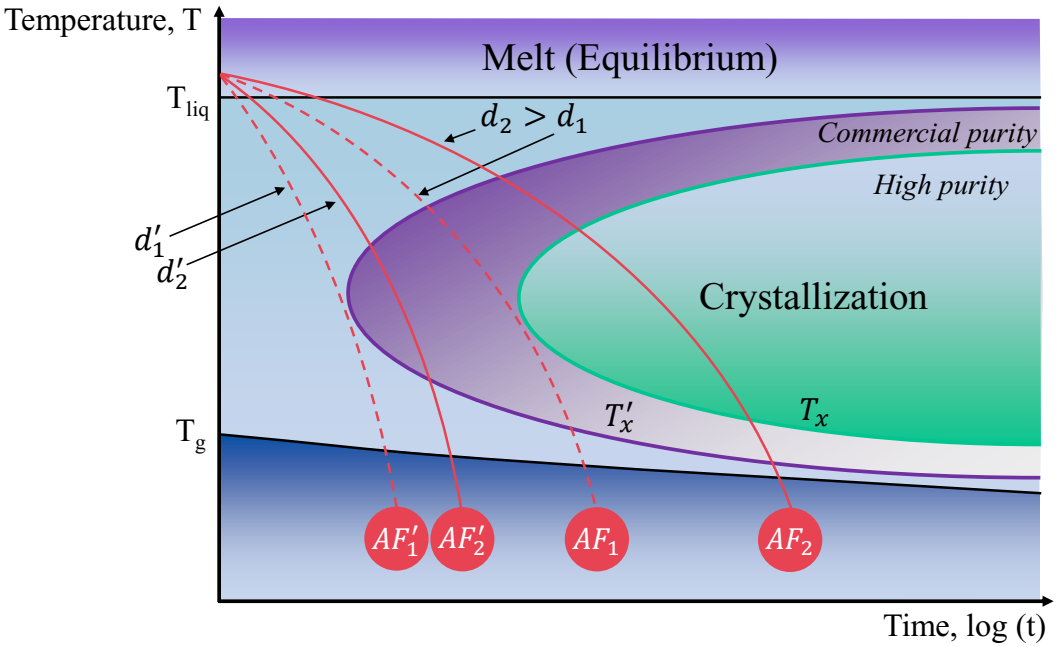

Fig. 1.1.: Schematic illustration of a time-temperature-transformation diagram showing the droplet cooling during gas atomization. Impurities and oxygen in commercial purity strongly promote crystallization which shift the crystallization nose to the left. The degree of impurities is related to the material's cost. A high cooling rate is necessary to avoid crystallization. Larger melt droplets ($d_2 > d_1$) experience lower cooling rates that lead to crystallization. The parameters $d_1^{'}$ and $d_2^{'}$ correspond to commerical purity material. The resulting amorphous phase for high and commercial purity are labelled as AF_i and $AF_i^{'}$. AF_1 and $AF_1^{'}$ represent 100% amorphous fraction, whereas AF_2 and $AF_2^{'}$ stand for partially-amorphous powders. To atomize even larger fully amorphous droplets that are produced from commercial purities, novel cooling strategies are required.

Glass formation depends mostly on high purity material, as impurities or oxygen can promote heterogenous crystal nucleation, creating a shift in the crystallization nose (Fig. 1.1) [7]. From an economic and ecological point of view, glass-forming alloys based on high purity are costly and rely on rare alloying elements, restricting commercial viability. Cheaper compositions with commercial purity such as ferrous metals (e.g. iron, nickel, and chromium) are far more attractive and would enable metallic glasses to truly compete with steels, titanium- and aluminum-based alloys [7]. However, there are more considerations than just the material cost for making metallic glass technologically competitive, as the fabricated part needs to have an appropriate combination of superior physical and mechanical properties. Thus, developing a low-cost metallic glass that meets performance requirements is key to success [7].

Crystallization of the liquid in even the most robust bulk metallic glass-formers is orders of magnitude faster than in many common polymers and silicate glass-forming liquids [18]. Ferrous glass-forming alloys are even more sensitive to crystallization, and their availability is virtually confined to wires, rods, and a few powder metallurgy products [19].

The industrial accessibility of modern new alloy systems has greatly improved. Recent work has demonstrated that the production of soft ferromagnetic glass-forming alloys with commercial purity and favourable processability as well as properties is possible. However, industry still depends on traditional metals to meet the accelerating requirements of worldwide power consumption. The rapid advancement in the performance and functionality of electronic and communication equipment (cellular phones, notebook PC's etc.) relies on the size, geometry, packing density, and weight of the devices for inductors, cores, choke coils, and transformers [20]. This field is dominated by traditional materials such as ferrites or Fe-Si alloys with less desirable material properties (e.g. high core losses) and a lack of freedom in size and geometry. The substitution of these traditional alloys with commercial purity soft ferromagnetic glass-forming alloys would be a great contribution to conserve energy, implying that we need to focus on alternative large-scale production methods.

1.3. Aim

The commercial viability of metallic glasses implies a basic understanding of controlling glass formation and processing routes. Geometric restrictions can be overcome by alternative production routes such as the combined use of powder production and consolidation. The production of amorphous bulk samples is possible as long as crystallization is avoided during powder consolidation. Various powder processing techniques have been applied to soft ferromagnetic glass-forming alloys and all require amorphous powders as a base material. Gas atomization is a suitable process for the production of amorphous powders. Smaller particles experience a higher cooling rate through a larger surface-to-volume ratio, resulting in fast heat extraction and thus in amorphous powders. Heat transfer during gas atomization occurs by radiation and convection. Droplet solidification depends on the droplet size, the temperature gradient between the

melt droplet and the surrounding inert gas, as well as the convective heat transfer coefficient, which is challenging to increase under regular gas atomization conditions [21]. Despite the use of high purity feedstock, gas atomization of soft ferromagnetic glass-forming alloys is often accompanied by nano-crystallization due to cooling rate limitations and their low glass-forming ability. Crystal nucleation and growth limitations can expose alloy metastability due to the suppression of an equilibrium phase or through the formation of a kinetically favored metastable phase [22]. The interaction between nucleation and growth control mechanisms is usually the limiting factor with respect to reaction characteristics [22]. Soft ferromagnetic glass-forming alloys are mostly synthesized under growth controlled kinetic conditions.

Miura et al. and Yodoshi et al. have demonstrated the production of iron-based amorphous powders with high purity feedstock and under laboratory conditions [23, 24], but the atomization of soft ferromagnetic glass-forming alloys on a commercial scale is virtually unknown. The production of atomized powders with commercial purity feedstock on an industrial scale requires alternative cooling strategies. The aim of this PhD thesis is therefore to extend the droplet cooling window beyond the common gas atomization range to produce amorphous powders as described in Fig. 1.1. This requires the development of novel cooling strategies to increase the heat transfer coefficient, to produce smaller melt droplets and to dissolve present heterogeneities acting as nucleation sites in the melt. The central research question can be derived for this PhD thesis as follows:

Central research question

Can the cooling rate of glass-forming alloys significantly be increased when applying innovative cooling strategies by increasing the heat transfer coefficient, producing smaller particles, and eliminating nucleation sites in the melt during gas atomization?

Higher cooling rates may result in fully amorphous particles even for droplets that would usually crystallize during solidification. Glass-forming alloys with a lower glass-forming ability such as commercial purity soft ferromagnetic glass-forming alloys can be atomized as glassy powders. The idea that cooling rates in gas atomization can be increased is based on the fact that heat transfer during gas atomization takes place through convection and radiation. The cooling rate depends on the droplet size, the properties of the surrounding fluid, the local heat transfer coefficient, and the temperature difference between the melt droplet and the surrounding fluid. This requires fine-tuning of the key parameters during gas atomization to increase the heat transfer coefficient, as the cooling rate is difficult to increase arbitrarily. Studies have shown that $\{(Fe_{0.6}Co_{0.4})_{0.75}B_{0.2}Si_{0.05}\}_{96}Nb_4$ particles atomized in a helium atmosphere can be cooled to achieve the same amorphous fraction as particles twice the size atomized in nitrogen [25]. A higher gas atomization pressure also produces finer amorphous powders [26]. These approaches can be considered as cooling strategies, but are limited to a small scale from an economic viewpoint,

as helium is roughly 10 times more expensive than nitrogen. The use of helium or higher gas pressures requires special gas reservoirs and increased safety regulations to meet industrial standards that are linked to higher costs. The implementation of innovative cooling strategies is therefore necessary and is key to success for the commercialization of soft ferromagnetic glass-forming alloys.

1.4. Thesis outline and solution approach

To achieve high cooling rates during gas atomization, innovative cooling strategies were developed and the impact on glass formation is discussed within the scope of this PhD thesis (Fig. 1.2). A reduction in droplet size, the dissolution of potent nucleation sites in the melt, and an increase in the heat transfer coefficient are also aimed in four different cooling strategies.

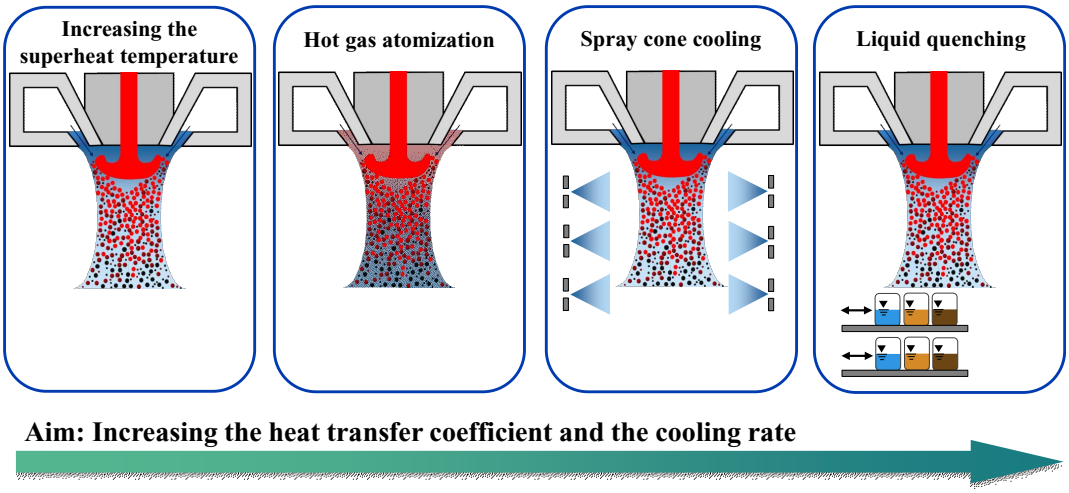

Fig. 1.2.: The aim of this PhD thesis is the development of novel cooling strategies during gas atomization to reduce droplet size, dissolve nucleation sites in the melt, and to increase the heat transfer coefficient. Increasing the heat transfer coefficient leads to an increased cooling rate, allowing the atomization of glass-forming alloys and particle sizes larger than 100 µm, such as for soft ferromagnetic glass-forming alloys with commercial purity, that normally tend to crystallize.

1.4.1. Increasing the melt superheat temperature

Increasing the melt superheat temperature may have two different effects:

(i) Eskin reported that an increased melt superheat temperature or cooling rate results in greater undercooling and supersaturation of the liquid [27]. He stated that an increased melt superheat temperature leads to an increased temperature gradient in the melt, deactivation of impurities, dissolution of intermetallic remains, increased diffusion coefficient, and decreased constitutional undercooling [27]. Other studies have shown that the amorphous fraction significantly increased when using containerless

droplet techniques [28–30]. However, the underlying mechanisms are rarely discussed in their studies, presenting an opportunity for further investigations. The variation of the melt superheat temperature is a complex process, as the presence of elevated temperatures may lead to chemical reactions with the crucible, triggering crystallization through the presence of additional heterogeneities in the melt [31].

The hypothesis is as follows: an increased melt superheat temperature influences the undercooling level and the crystallization times. This suggests that nucleation sites are dissolved above a certain threshold temperature. Impurities, acting as heterogenous nucleation sites, affect the nucleation process and may have a negligible influence on the growth process [32].

(ii) Spherical gas-atomized particles are desired for various industrial powder applications. In general, droplets are formed if a high velocity gas stream disintegrates a melt stream, resulting in solidified droplets with different sizes and shapes. Glass-forming alloys are characterized by a high melt viscosity that leads to the production of irregular particle shapes and fibers. The shape of the droplets formed is a result of a concurrent process between droplet solidification and spheroidization time. Thus, to obtain spherical droplets, the following condition must be satisfied [33]:

$$t_{sph} < t_{sol}, \tag{1.1}$$

where t_{sph} and t_{sol} are the spheroidization and solidification time, respectively. According to Nichiporenko, the spheroidization time can be estimated as follows [33]:

$$t_{sph} = 0.75 \cdot \frac{\pi^2 \cdot \eta_l}{V_d \cdot \sigma_l} \cdot \left(r_a^4 - r_b^4\right), \tag{1.2}$$

where η_l and σ_l are the dynamic viscosity and liquid surface tension of the melt droplet for a given droplet volume V_d. The parameters r_a and r_b represent the droplet radius after and before spheroidization. A solidification time can be estimated from the local solidification interval which is defined as: $t_{sol} = \left(T_{liq} - T_s/CR\right)$ where CR is the average cooling rate while T_{liq} and T_s are the liquidus and solidus temperature (for details, see sec. 3.2.2).

The hypothesis is as follows: an increased melt superheat temperature decreases the melt surface tension and viscosity, leading to a higher number of spherical droplets. The effect of liquid viscosity on particle size has been contradictorily reported in literature [34–37]. Smaller particles lead to a higher cooling rate. This research question will also be investigated in the context of a cooling strategy.

1.4.2. Production of fine powder through hot gas atomization

In the case where the thermal conductivity of a stagnant fluid is constant, a heated droplet cools without convection. Using Fourier's law, the heat flux is expressed as $Nu = \left(h \cdot d_p / k_g\right) = 2$ where Nu, h, d_p, and k represent the Nusselt number, heat transfer coefficient, droplet diameter, and thermal conductivity of the fluid [38]. From this equation, the heat transfer coefficient can be estimated as $h \sim 1/d_p$. Considering the cooling rate Eq. 3.13 in sec. 3.2.2 without convection and radiation (only conduction), the cooling rate is inversely proportional to the square of the diameter $\left(CR \propto 1/d_p^2\right)$. The rearranged Lubanska equation (Eq. 1.3) in sec. 3.1.3 gives a better understanding of the relationship between droplet diameter and process parameters as well as thermal properties:

$$d_{50,3} = K_{Lub} \cdot \sqrt{D_l} \cdot \frac{1}{u_{gl}} \cdot \sqrt{\frac{\nu_l}{\nu_g}} \cdot \sqrt{\frac{\sigma_l}{\rho_l}} \cdot \sqrt{1 + \frac{\dot{m}_L}{\dot{m}_G}}, \tag{1.3}$$

where $d_{50,3}$ is the mass median particle diameter, K is an atomizer geometry constant, D_l is the liquid stream diameter, u_{gl} is the gas velocity at impact with the liquid stream, ν_l and ν_g are the liquid and gas viscosity, ρ_l and σ_l are the liquid density and surface tension. The parameters $\dot{m}_L$ and $\dot{m}_G$ stand for the melt and gas mass flow rate. The following trends can be derived from Eq. 1.3:

- (i) The mass median particle diameter $d_{50,3}$ decreases with an increased gas velocity ($d_{50,3}$ is inversely proportional to the gas velocity).
- (ii) The $d_{50,3}$ decreases with a decreased nozzle outlet diameter (corresponding to the liquid stream diameter D_l).
- (iii) An increased liquid kinematic viscosity ν_l may result in larger droplet diameters (see sec. 5.1).
- (iv) An increased liquid surface tension σ_l may also result in larger droplet diameters (see sec. 5.1).

The strong relationship between gas velocity and droplet diameter can be seen in Eq. 1.3. Higher gas velocities lead to smaller droplets, but also to a higher gas consumption. Therefore, hot gas atomization is considered, as elevated gas temperatures reduce the gas density and thus gas consumption. Elevated gas temperatures also result in a higher sound velocity. The sound velocity c is calculated from the heat capacity ratio κ, the specific gas constant R_s, and the gas temperature T_G (assumed for the ideal gas law) [39]:

$$c = \sqrt{\kappa \cdot R_s \cdot T_G}. \tag{1.4}$$

The gas mass flow rate for a constant atomization pressure can be determined with following equation (assumed for the ideal gas law) [39]:

$$\dot{m}_G = \dot{m}_{G,0} \cdot \sqrt{\frac{T_a}{T_G}}, \tag{1.5}$$

where $\dot{m}_G$ and $\dot{m}_{G,0}$ represent the gas mass flow rate at ambient room temperature T_a and at elevated gas temperatures T_G, respectively [39].

The hypothesis is as follows: hot gas atomization promotes the production of finer powders, as a higher initial gas temperature introduces kinetic energy through a higher sound velocity (Eq. 1.4), and thus, to a higher gas velocity at the nozzle exit [40]. This in turn results in smaller droplets that cool faster, yielding a higher amorphous fraction of the atomized material. However, the effect of elevated gas temperatures on the final microstructure has yet to be investigated, which raises the following research question: Does the increased gas temperature result in crystalline particles, although smaller particles are produced?

1.4.3. Spray cone cooling

Spray quenching is an industrial process in which water is atomized with or without compressed air on a hot surface to increase the local heat transfer coefficient [41]. This approach will be taken and applied to the atomization of glass-forming alloys.

The hypothesis is as follows: the combined use of gas atomization and quenching the melt spray cone with a cooling medium increases the local heat transfer, resulting in higher cooling rates. Quenching a hot surface with a cooling medium such as water or oil introduces film boiling, which appears to be very sensitive to the local heat transfer coefficient and the cooling rate [41]. The extraction of heat by cooling water is quite complex and depends on the melt droplet temperature. Water and oil can act as potent nucleation sites, which raises the research question: If the quenching medium promotes heterogenous nucleation, will it result in crystalline particles?

1.4.4. Liquid quenching

Analogous to spray cone cooling, **the hypothesis** is as follows: quenching of melt droplets in a liquid medium leads to a higher heat transfer coefficient, and thus to higher cooling rates. Similar to spray cone cooling, the combined use of gas atomization and a quenching medium may promote an oxide layer around the melt droplets. The surrounding droplet oxide layer is likely sensitive to the cooling rate, leading to a decrease in mechanical and magnetic powder and bulk properties. Two research questions can be derived:

(i) Does quenching promote an oxide layer around the particles? If so, does the cooling rate decrease and therefore result in crystalline particles as well as alter the mechanical and magnetic properties?

(ii) If an oxide layer has formed, can the particles still be consolidated to a bulk material? The consolidation ability may depend on the process conditions during liquid quenching.

CHAPTER 2

From liquid metal to metallic glass

A glass is formed when a cooled liquid continuously hardens into the solid state without crystallization [42]. It is generally believed that glasses can be formed from materials with every type of bonding: covalent, ionic, metallic, Van der Waals, and hydrogen [5]. A crystalline solid represents the thermodynamically stable state of matter at low temperatures, but the formation of such solids requires the nucleation and growth of a new phase, and these processes take place over time [43]. If the cooling rate, relative to the kinetics of crystallization, is fast enough, the liquid phase can be cooled indefinitely without the occurrence of crystallization and a glass will be formed [5]. Recent research has proven that even pure, single-element liquid metals can be vitrified if quenched to low temperatures at ultrahigh cooling rates of 10^{12} - 10^{14} $\mathrm{K\,s^{-1}}$ [44, 45], while certain molten eutectic alloys form bulk metallic glasses at extremely low cooling rates $\sim$ 1 $\mathrm{K\,s^{-1}}$ or less [17, 46, 47]. The question of whether pure metals or eutectic alloys can form glasses includes more than just the cooling rate. The question then naturally arises: What are the important factors that determine the ability of materials to form a glass? [5]. The author addresses this question by paying attention to glass formation from the liquid state, with an emphasis on the atomistic structure, thermodynamics, and kinetics. It is beyond the scope of this PhD thesis to address all processing and consolidation techniques for metallic glasses and to catalogue the myriad of different materials that have been formed as glasses (for details, see Ref. [48]).

2.1. Structure of metallic glasses

Metallic glasses or amorphous solids, similiar to liquids, are considered as a congealed melt with a short-range order and a lack of translational and rotational structural symmetry (characteristic for crystalline solids). Although the structural composition determines the material properties, the term "disordered" would be a too simple description, as ordered atoms may arrange in clusters with localized order (e.g. short and/or medium-range order [49]). Short-range order refers to the nearest-neighbor atomic environment with an emphasis on geometric and chemical short-range order, while medium-range order refers to the second or third nearest-neighbor arrangement [50]. Research over the last three decades have shown that the medium-range order has a strong influence on glass-formation with corresponding material properties.

Research on structural order has tremendously evolved due to the acquisition of X-ray and Neutron Scattering data and computational methods, including the reverse Monte-Carlo method, molecular-dynamics simulations, as well as combined scattering and containerless leviated droplet experiments [51]. Cur-

rent models describe the atomic structure of metallic glasses with atom clusters, often described with an icosahedral short-range order. In geometry, an icosahedron is a 20-faced polyhedron. The modern concept of order originates from Frank's concept [52], guided by Turnbull's nucleation theory, where he proposed that the icosahedron is the most favorable local order in monatomic metallic liquids, successfully explaining how undercooling below the melting point can be achieved [53]. Due to its five-fold rotational symmetry, which is incompatible with the translational periodicity of normal crystalline phases, an icosahedral cluster would lose too much energy to form a crystal [49]. Bernal proposed the model of dense random packing of hard spheres in monoatomic metallic liquids [54, 55]. Since most metallic glasses consist of alloy elements with different atomic radii, his model excludes glass-forming systems such as metal-metalloid alloy elements with significant short-range order and it neglects multicomponent systems with short-range and medium-range order. However, it serves as a realistic model to treat metallic glasses as frozen liquids [56]. Gaskell proposed a stereo-chemically defined model of efficiently packed, solute-centered clusters incorporating metal-metalloid alloys [57]. His model included atoms of different sizes and gave a physical basis for chemical short-range order known to exist in metallic glasses [58]. Despite these benefits, it has a limited ability to explain the formation of medium-range order in metallic glasses and how efficiently packed clusters arrange to avoid packing frustration as well as which atomic size range/concentration is needed for the production of metallic glasses [58]. The characteristics of medium-range order remain one of the most important topics in metallic glass research, since the details of how densely-packed structural "units" are connected and arranged in three-dimensional space is still poorly understood.

Progress over the intervening decades has emphasized that maximizing packing density is a key factor governing the structure of metallic liquids and glasses [51]. Inoue recognized the importance of the packing density and stated in his empirical guidelines that the glass-forming ability (GFA) (sec.2.2) increases with efficient atomic packing [59]. Miracle's proposed model has recently inspired many researchers [60], as he modified the Gaskell model by considering efficiently packed solute-centered atom clusters to be structural building blocks, allowing for the quantitative prediction of density, short-range and medium-range order (Fig. 2.1) [58]. In his model, central solute atoms seek to be surrounded by solvent atoms, forming stable icosahedral clusters that are similar to a fcc structure. Due to the irregular cluster shape, secondary solute atoms are required in these interstitial spaces to achieve maximum atomic dense packing. The Miracle model is currently undoubtedly recognized as the most robust and accurate model, but it is limited in its ability to predict which atomic structure will have good glass-forming ability, often referring to the maximum fully amorphous diameter obtained from liquid quenching experiments. The atomic structure is important for the glass-forming ability, but is just one among many factors that affect how a metallic glass can be formed.

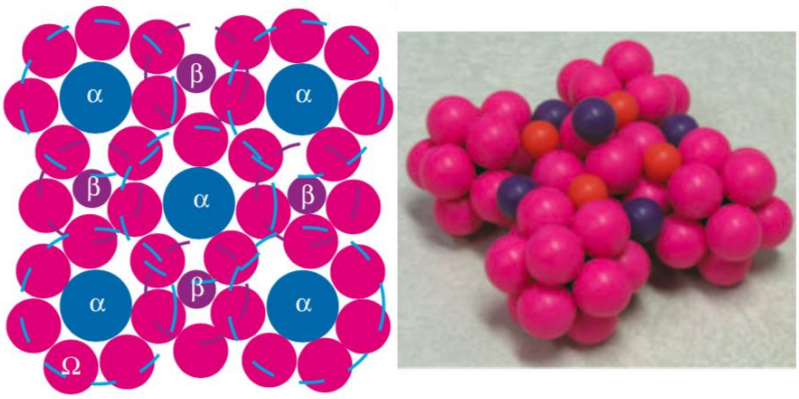

Fig. 2.1.: A 2D and 3D representation of Miracle's dense-cluster packing model. Reprinted from Ref. [60] with permission from Springer Nature. The 2D illustration shows a (110) fcc plane of clusters where Ω represents randomly packed solvents, α describes primary solutes, and β illustrates secondary solutes [50]. The solute-centered clusters are the basic building blocks for short-range order, while the connection between clusters through shared solvents result in medium-range order.

2.2. Glass formation and thermodynamic considerations

Thermodynamic equilibrium is defined by the Gibbs free energy of a system where stable equilibrium under constant pressure is at the lowest possible minimum, and thus, has the lowest possible free energy (Fig. 2.2a) [61]. There are many cases in which Gibbs free energy is in a relative minimum, resulting in a metastable state. When cooled below the equilibrium temperature, a liquid may undergo one of two solidification paths: a stable or a metastable crystalline phase (e.g. martensitic transformation). Turnbull suggested the concept of "configurationally frozen liquids", stating that metallic glasses are slowly undergoing internal rearrangements ("relaxation") to configurations with lower energy [62]. He pointed out that the rate of relaxation falls sharply with decreasing temperature, so that near the glass transition temperature, T_g, the liquid freezes into a solid configuration [62]. It is often assumed that a body is solid when the dynamic viscosity exceeds a somewhat arbitrarily defined value of $\eta \sim 10^{12}$ Pa s at the glass transition temperature. To become a glass, a liquid must be quenched through a wide temperature range of metastability in which crystal growth rates are extremely high [63]. Liquid undercooling can be achieved either by rapid solidification techniques or by controlling the most potent nucleation sites [64–66]. Undercooled samples can also be made via fluxing techniques or by containerless processing, where the removal of active nucleation sites requires a chemical treatment to deactivate possible catalytic sites or a physical separation of the container sites [64, 67, 68]. Fig. 2.2 summarizes the changes in properties which occur when a liquid solidifies either into a glassy or crystalline state.

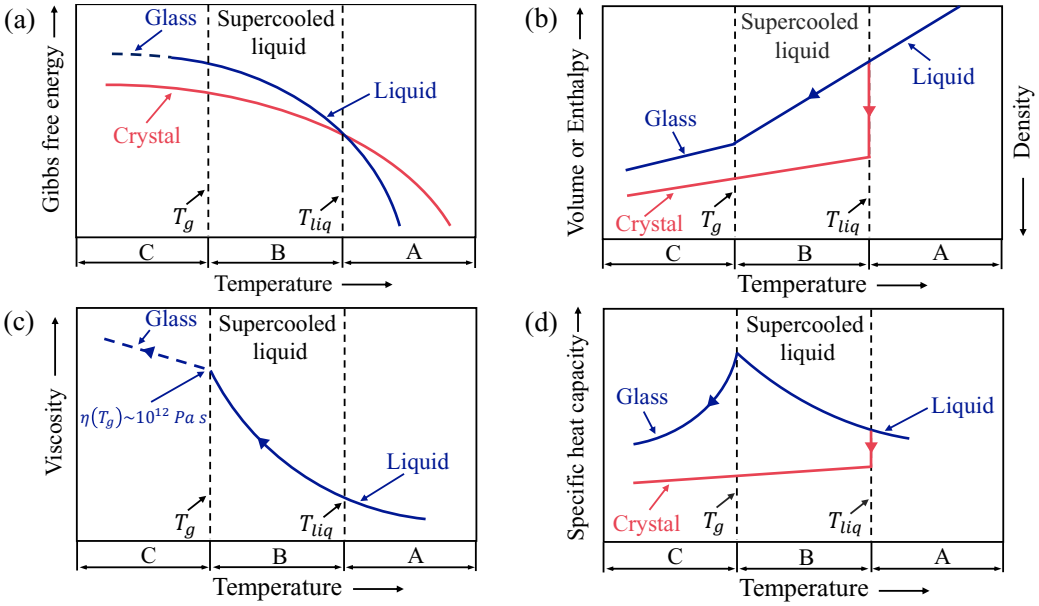

Fig. 2.2.: Illustration of properties such as (a) Gibbs free energy, (b) volume/enthalpy, (c) viscosity, and (d) specific heat capacity that change when a liquid melt solidifies into a glassy or crystalline state. The illustration was adapted from Ref. [61] with permission from Elsevier B.V. and modified in part. Solidification for a crystalline material is a first-order phase transformation where liquid and solid states coexist. This is in contrast to the properties of metallic glasses and many polymers that exhibit continuous change [69]. The melt is in equilibrium in range A and is thermodynamically undercooled in range B. A glass can be formed if crystallization is avoided in range B. Range C is defined by the glass transition temperature T_g where the liquid devitrifies into an amorphous state [61].

Crystallization is considered to be a first-order phase transformation and is often discussed by classical nucleation and growth theory [70, 71]. In range A, the superheated liquid is in equilibrium and cools down to the border between A and B. We define this border as the liquidus temperature T_{liq}, signifying the theoretical maximum temperature at which crystals can coexist in stable thermodynamic equilibrium with the liquid [49]. Upon cooling, the melt is thermodynamically undercooled and will crystallize rapidly if a nucleus is provided [61]. The liquid viscosity tends to increase rapidly with lowering temperature in region B, so that a glass can still be formed in the presence of nuclei, since the low atomic mobility stifles crystal growth [61]. The solidification of a crystalline alloy implies a discontinuous change in properties as can be seen in the enthalpy/volume and specific heat capacity. The border between B and C defines the glass transition temperature which is defined as a kinetic event. The properties of a glass exhibit a strong temperature dependence above glass transition temperature, reflecting the configurational changes in the liquid [61]. Below the glass transition temperature, the atomic motions in the melt are so slow that during solidification, configurational changes are prevented: the melt has become a rigid glass [61].

2.3. Criteria for the glass-forming ability

Since the first successful report of a metallic glass produced from a liquid with cooling rates above 10^6 K s^{-1} [6], and the formation of multicomponent bulk metallic glasses with a critical diameter larger than 1 mm at low cooling rates ($\sim$ 10 K s^{-1}) [47, 72], significant progress has been made in exploring new alloy systems with good glass-forming ability. The design for new bulk metallic glass compositions is tedious, time consuming, and costly, restricting the full exploration of the superior properties of metallic glasses. Great progress has been made over the last five decades in postulating glass-forming ability criteria, which describes the ability of how easy a liquid melt transforms into an amorphous state. The glass-forming ability is often referred to as the critical cooling rate R_c, and is defined by the temperature-dependent waiting time $t_x(T)$ for a detectable fraction of crystal(s) to nucleate and grow in a unit volume of liquid undercooled to a temperature $T < T_{liq}$ [17]. Between glass transition temperature and liquidus temperature, the $t_x(T)$-curve or time-temperature-transformation curve exhibits a sharp minimum (t_x^*) at an experimentally measurable nose temperature T^* [17]. To form a glass, a liquid must be cooled roughly from liquidus temperature to below T^* in a time less than t_x^* [17] (for details, see sec. 2.5) :

$$R_c \sim \frac{T_{liq} - T^*}{t_x^*}. \tag{2.1}$$

The critical cooling rate R_c is the minimum cooling rate required to obtain a fully amorphous sample and d_{max} is the maximum attainable amorphous diameter [73]. The smaller the R_c or the larger the d_{max}, the easier the glass-formation. Turnbull suggested the reduced glass transition temperature $T_{rg} = T_g/T_{liq}$ to be a characteristic parameter and argued that crystal nucleation rates should fall as the reduced glass transition temperature increases, becoming immeasurably small at $T_{rg} \sim 2/3$ [74]. This equation has been recognized as a valuable, albeit rough, guide to the development of bulk metallic glasses [74]. Quantitative studies [75, 76] have proven that a high reduced glass transition temperature is associated with low critical cooling rates [51]. It is also generally believed that good glass-forming ability is asscociated by a depression in the liquidus temperature (concept of deep eutectics[1]), which are more likely to be found in multicomponent alloys. Greer postulated the "confusion by design" principle and argued that the more constituent numbers involved, the lower the chance that the alloy can select viable crystal structures, and the greater the chance of glass formation [77]. This results in the "frustration" of the alloy's ability to crystallize, as the liquid phase is more stable relative to the crystalline phase. Inoue and co-workers systematically investigated several hundred multicomponent bulk metallic glasses, leading to the formulation of three basic empirical rules for glass formation in which he stated: (i) the selected alloys should be multicomponent alloys with at least three components, (ii) the constituent el-

[1] A deep eutectic is a system in which the eutectic temperature is significantly lower than the melting points of the individual components [48].

ements should have a significant difference in atomic size (> 12%), (iii) and the constituent elements should have a negative heat of mixing among each other [47]. Although most of the best glass-forming alloys found today follow the Inoue rules, the empirical rules represent only the bare essentials for glass formation and are insufficient for designing new alloys [78]. Numerous criteria have been developed since the formulation of three basic Inoue guidelines (for details, see Ref. [48]). All proposed parameters in these criteria align with their own experimental data, but none provide universal applicability. The search for new alloy systems is still a tedious "trial and error" approach even though computational, combinational or machine learning approaches are the subject of current research.

2.4. Viscous slowdown and the fragility concept

Monoatomic and binary metallic liquids have viscosities of about 10^{-3} Pa s at the melting point [79, 80]. The viscosity of metallic glasses is generally several orders of magnitude higher than that of pure metals or alloys [81]. Glass-forming alloys exhibit a drastic kinetic slowdown when cooled below the liquidus temperature, manifesting in measurable changes in shear viscosity, relaxation time, and in the self-diffusion constant [82]. The shear viscosity η in glass-forming alloys is a key parameter, changing by about 15 orders of magnitude upon cooling from high temperatures to the glass transition temperature [83]. The atomic mobility of some simple liquids is connected to viscosity via the Stokes-Einstein relation. If assuming steady-state nucleation (I_v), the nucleation rate is determined by the product of a thermodynamic and kinetic contribution [81]:

$$I_v = A \cdot D_{eff} \cdot exp\left(\frac{\Delta G^*}{k_B T}\right), \tag{2.2a}$$

$$\Delta G^* = \frac{16\pi\sigma_{sl}^3}{\Delta G^2}, \tag{2.2b}$$

where D_{eff} is the effective diffusivity, T is the temperature, A is a constant, and k_B is the Boltzmann constant. In the classical nucleation theory, ΔG^* is the activation barrier for nucleation, σ_{sl} is the interfacial energy between liquid and solid, and ΔG is the driving force for crystallization. The way viscosity changes with temperature, scaled to the glass transition temperature, is the basis for the widely-used fragility classification introduced by Angell (Fig. 2.3) [83, 84]. The temperature dependence of viscosity can vary considerably in which some liquids follow an Arrhenius law (e.g., SiO_2), while others such as bulk metallic glasses and polymeric systems, display highly non-Arrhenius behavior [85]. A quantitative description of the diversity of kinetic behavior is the notion of fragility as proposed by Angell, which quantifies the temperature dependence of viscosity and can be described by the Vogel-Fulcher-Tammann (VFT) equation [86]:

$$\eta = \eta_0 \cdot exp\left(\frac{D^* \cdot T_0}{T - T_0}\right), \tag{2.3}$$

where η_0 is the theoretical infinite-temperature limit of viscosity, calculated as $\eta_0 = \left(N_A \times h_p/V\right)$ [81]. N_A is the Avogadro constant, h_p is the Planck constant, and V is the molar volume [85]. D^* represents kinetic fragility and T_0 is the VFT temperature, where barriers with respect to flow approach infinity [81]. According to Angell, the viscosities of liquids at temperatures above the glass transition temperature can be plotted logarithmically as a function of the inverse temperature in an Arrhenius graph. For comparison with different liquids, the temperature is normalized with the corresponding glass transition temperature.

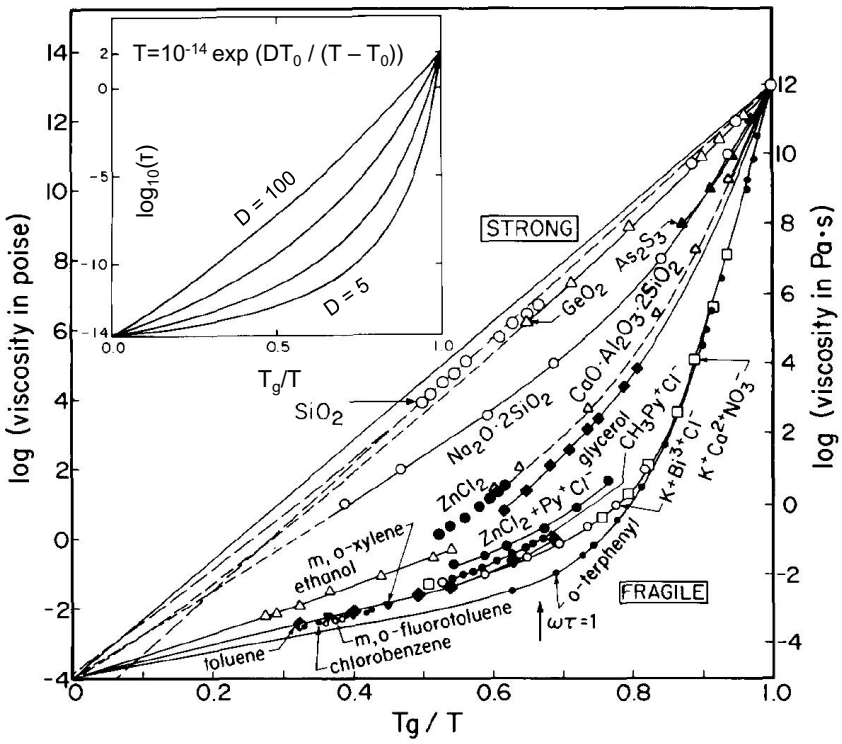

Fig. 2.3.: Arrhenius plot of viscosity scaled to the glass transition temperature for several liquids. The inset shows the dimensionless fragility parameter D^*, defining whether a glass is fragile or strong. Figure adapted from Ref. [87] with permission from Elsevier B.V.

D^* describes the deviation from Arrhenius behavior and smaller D^* values correspond to more fragile liquids. Fragility can also be represented by the dimensionless steepness index m, which is defined as the logarithms slope of viscosity at the glass transition temperature [86]:

$$m = \left.\frac{d log_{10}(\eta)}{d\left(T_g/T\right)}\right|_{T=T_g} \tag{2.4}$$

Glasses such as SiO_2 ($D^* > 100$) with low fragility show linear Arrhenius behavior and represent the strongest supercooled liquid with high viscosities over a wide temperature range. Higher fragility (smaller D^*) indicates more fragile behavior. Fragile liquids with low D^* values have lower viscosities, but increase greatly with a decreasing temperature at the glass transition temperature.

2.5. Time-temperature-transformation diagrams

The quantification for crystallization under isothermal conditions is given by a time-temperature-transformation (TTT) diagram (Fig. 2.4). These TTT diagrams are typically used to determine the temperature-dependent crystallization onset time to predict the critical cooling rates, and the processing time required to shape or consolidate glass-forming alloys[2] [89]. The distinctive "C-shape" results from temperature dependence governed by nucleation and growth rate. High temperatures favor diffusion and thus growth, while the nucleation rate increases with increasing undercooling. The superposition of these processes leads to the maximum transformation rate at a temperature T^* or critical nose time t_x^*.

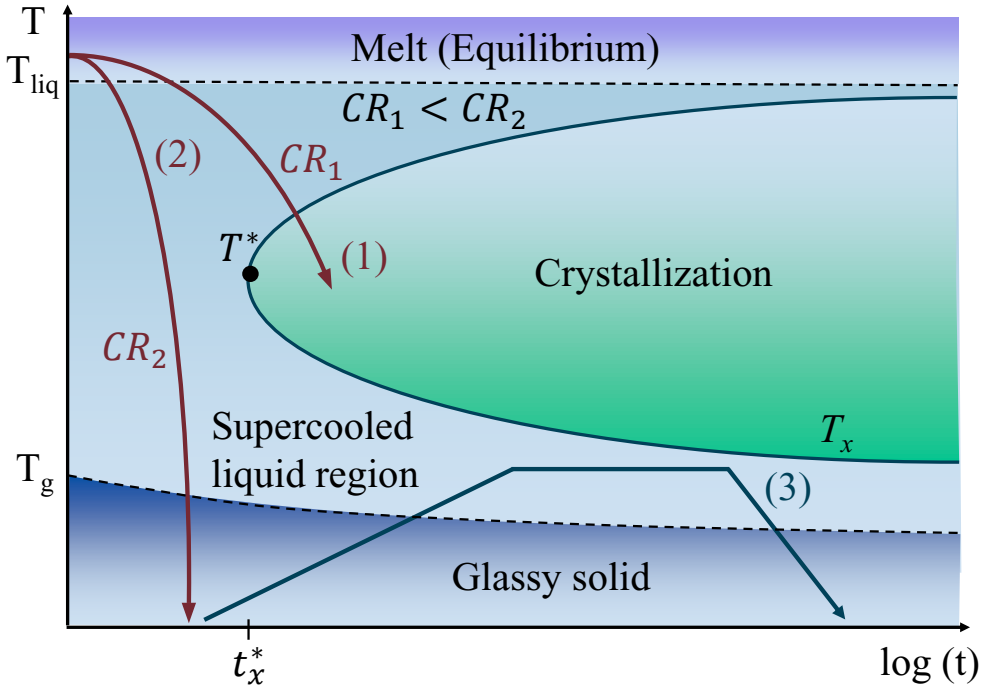

Fig. 2.4.: Schematic illustration of a time-temperature-transformation (TTT) diagram. A liquid may undergo one of two solidification paths. Path (1) crosses the crystallization nose due to slow cooling. This in turn leads to crystalline materials, whereas path (2) represents rapid solidification, where the crystallization nose is bypassed. Path (2) results in the formation of a glassy solid. The cooling rate CR_2 is larger than the cooling rate CR_1. Finally, path (3) illustrates a possible processing route where the glassy product is heated between crystallization temperature T_x and glass transition temperature T_g, given by $\Delta T_x = T_x - T_g$.

[2] The processability of bulk metallic glasses is related to the supercooled liquid region between the crystallization temperature T_x and the glass transition temperature T_g given by $\Delta T_x = T_x - T_g$. Bulk metallic glasses behave in this region in a highly viscous state and can be deformed in a way similar to that of plastics [88]. The supercooled region is also often used as a measure for the thermal stability and considered as a criterion for the glass-forming ability (sec. 2.3).

A liquid may undergo one of two solidification paths: a low cooling rate (CR_1) as illustrated in path (1) (Fig. 2.4) results in the formation of a crystalline solid due to the fact that the crystallization nose is crossed. In path (2), a large cooling rate (CR_2) results in amorphous solids, as the crystallization nose is bypassed. Path (3) shows a possible processing route for amorphous solids (e.g. bulk samples, ribbons, granules, and powders) where the amorphous product is heated in the supercooled liquid region, allowing for easy deformability.

The critical cooling rate can be estimated by constructing TTT curves corresponding to a just detectable degree of crystallinity taken as a volume fraction crystallized of 10^{-6} [90]. Such curves were constructed from kinetic approaches and have been extensively discussed by Davies or Uhlmann and co-workers [5, 43, 71, 75, 90]. The first complete TTT diagram was experimentally determined for a $Zr_{41}Ti_{14}Cu_{12}Ni_{10}Be_{23}$ glass-forming alloy using electrostatic levitation [91]. These measurements were limited to a few alloy systems, since only a few can be levitated and the cooling/heating rates provided by DSC measurements were too low to determine the complete TTT diagram. However, the recent development of chip-based calorimeters [92, 93], allowing cooling and heating rates of up to 10^4 $K\,s^{-1}$ [94], are promising advances in exploring full TTT diagrams for various alloy systems.

Most binary glass-forming alloys can only be produced by rapid solidification techniques with cooling rates larger than 10^6 $K\,s^{-1}$, whereas bulk metallic glasses with a pronounced glass-forming ability solidify into an amorphous state at cooling rates larger than 10^2 $K\,s^{-1}$ [95]. Modern glass-forming alloys such as the Vitreloy[3] family already show an amorphous microstructure at cooling rates less than 10 $K\,s^{-1}$ [72]. For example, when fluxed with B_2O_3, the Pd-Ni-Cu-P alloy solidifies into an amorphous state at lower cooling rates (≤ 0.1 $K\,s^{-1}$) [95–97]. Oxide glasses, on the other hand, can be produced at extremely low cooling rates of up to 10^{-5} $K\,s^{-1}$ [48].

2.6. The role of oxygen and impurities on glass formation and properties

The large-scale industrial commercialization of metallic glasses depends on material availability and cost as well as feedstock purity and the processing environment (e.g. vacuum or inert gas quality). The presence of impurities and oxygen is inevitable during fabrication, as laboratory conditions are rarely available. The formation of metallic glasses is a competing process between a stabilized supercooled liquid and the rivaling crystalline phase, as both processes strongly depend on the chemical alloy composition [98]. Small amounts of impurities or oxygen can affect the glass-forming ability, serving as heterogenous nucleants and lowering the energy barrier between an amorphous or crystalline phase [99].

[3] The name Vitreloy represents a class of Zr-based glass-forming alloys which were developed at California Institute of Technology, Pasadena, CA, United States, and were marketed by the Liquidmetal Technologies, Inc. company.

The impact of oxygen and impurities is controversially discussed and remains rather poorly understood. For instance, the critical casting thickness of fully amorphous Fe-C-Si-B-P-Cr-Mo-Al rods is reduced from 5 to 1 mm when a commercial Fe-Si pre-alloy is used instead of high purity Si [100]. The authors concluded that CaO and Al_2O_3 act as catalysts in the commercial Fe-Si pre-alloy, and therefore favor crystallization of the primary α-Fe phase, which leads to a reduced glass-forming ability. Other studies have shown that rare-earth oxides, acting as non-catalysts, can purify the melt by scavenging oxygen [101–104]. For example, microalloying of rare-earth elements improves the glass-forming ability. [105]. There is controversy in the literature about what can be considered as an impurity or a useful alloying addition [99]. It is common knowledge that fluxing agents (e.g. B_2O_3) [106–108], hydrogen inducement, and microalloying [109–111] are promising methods to improve the glass-forming ability and enhance the critical casting thickness, the supercooled liquid region, as well as the malleability and soft magnetic properties [112]. It is believed that B_2O_3 trap impurities at the surface and inside the melt, where the fluxing agent dissolves and deactivates present nuclei [112]. Flux-treatment approaches are restricted to systems that have a lower affinity to oxygen than boron, since more reactive elements such as Zr provoke a reduction of the fluxing agent so that a purification is impossible [112, 113].

Zr or Ti alloy systems are very sensitive to impurities and oxygen. Lin et al. have shown that the TTT diagram shifts to higher temperatures and shorter times when the investigated alloy is doped with oxygen (Fig. 2.5) [114]. Further studies concluded that oxygen impurities in Zr-based bulk metallic glasses alter the crystallization process from a single to a double-stage phenomena, and therefore reducing the supercooled liquid region [115, 116]. The glass-forming ability of Zr-based bulk metallic glasses strongly decreases when the oxygen impurity level is larger than 1000 appm. As a result, high purity and high-cost materials have to be used [117]. Other studies have reported that a critical level of oxygen could promote glass formation although the underlying reasons are still unclear [118–120].

Most of the existing studies deal with the impact of oxygen on Zr- or Pd-based glass-forming alloys, and limited work has been reported on other glass-forming systems such as Fe-based glass-forming alloys. The mechanisms that describe the effect of oxygen and other impurities are complex, insufficiently studied, and inapplicable for the generalization of different alloy systems.

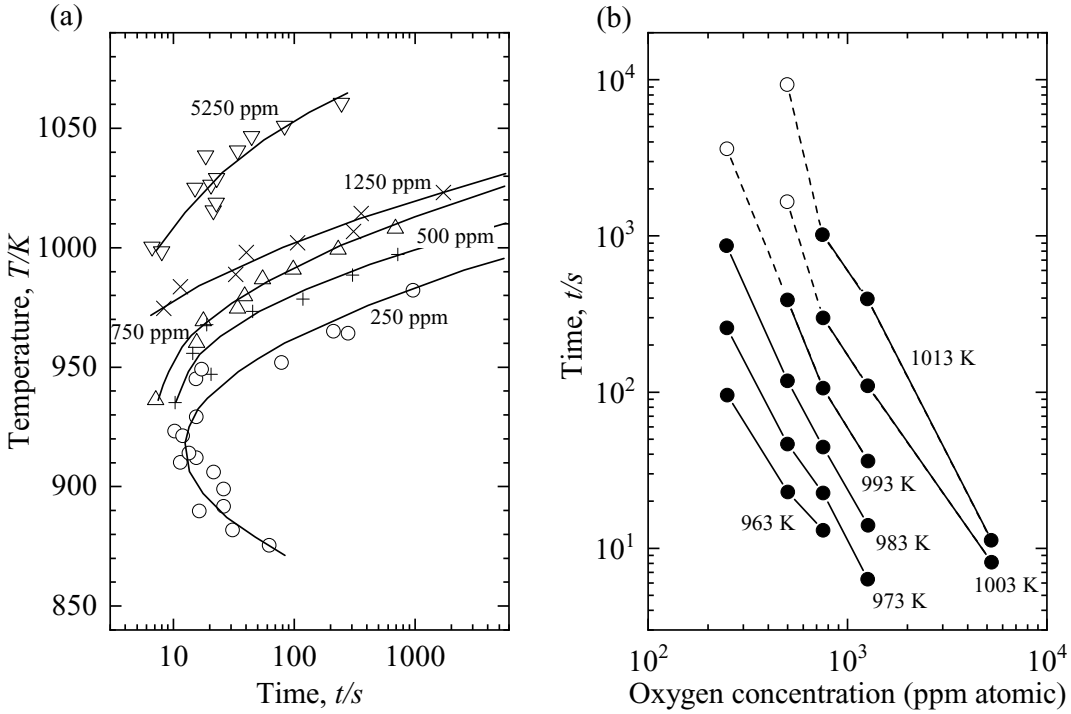

Fig. 2.5.: Effect of oxygen on crystallization of a $Zr_{52.5}Ti_5Cu_{17.9}Ni_{14.9}Al_{10}$ undercooled bulk glass-forming alloy. The data were retrieved and modified from Ref. [114] with permission from The Japan Institute of Metals and Materials. (a) The TTT diagram and the crystallization nose time were determined with a high temperature, high vacuum, electrostatic levitation processing technique. (b) A large amount of doped oxygen results in a shorter crystallization incubation time. The solid circles are measured values and the open circles are extrapolated data from the TTT diagram [114].

CHAPTER 3

Atomization of glass-forming alloys

Gas and water atomization are the most relevant industrial techniques to produce metal powders. Both techniques provide rapid solidification[1] conditions, extracting heat during the transition from a liquid state to a solid particle.

Gas atomization was selected to produce amorphous powders during this PhD project (for atomization details, see Ref. [126] and [127]). Gas atomization is suitable for the mass production of metallic glasses through powder synthesis and consolidation since geometric restrictions in conventional processing can be overcome [128]. The large surface-to-volume ratio of the melt droplets allows for rapid heat extraction, cooled by convection between the melt droplets and surrounding cooling gas, and by radiation. Present literature mainly covers only a few investigations dealing with the atomization of glass-forming alloys. The details of powder processing are mostly excluded from these reports, as powder consolidation is considered as the crucial step. A systematic investigation of fundamental and technical aspects of powder production is therefore desired, as powder quality determines final bulk properties. The science and technology behind gas-atomized glass-forming alloys will be described, focusing on solidification phenomena that determine whether amorphous powders can be produced. The mechanisms of melt disintegration, the design of atomization devices, thermal transport in atomized droplets, characteristics of particle size, size distribution, as well as particle shape will be briefly discussed, as they define final powder and thus bulk properties [129].

3.1. Gas atomization

The fundamental characteristic of gas atomization is the energetic disintegration of a liquid melt stream into micrometer-sized droplets [129]. During gas atomization, a molten metal stream is forced through an orifice and is subsequently disintegrated into droplets by the impingement of a gas jet [129]. The droplets are subsequently accelerated and allowed to cool in the presence of an inert gas during their flight inside the spray chamber. A schematic illustration of a gas atomization system including two different gas atomizer is presented in Fig. 3.1.

[1] Any solidification process with cooling rates ranging from 10^3 to 10^6 $\mathrm{K\,s^{-1}}$ is considered rapid solidification [40, 121]. The most commonly used rapid solidification techniques are molten metal atomization, melt spinning, copper mold casting, roller-quenching, plasma spraying, as well as laser or electron beam surface treatment [122]. For rapid solidification details, see Refs. [123–125].

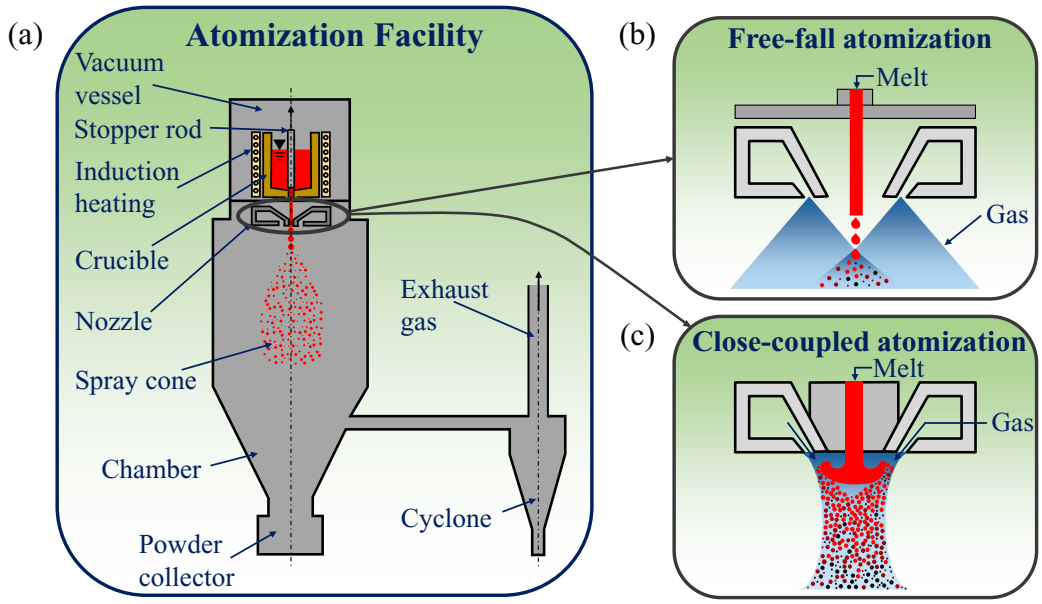

Fig. 3.1.: Schematic illustration of the gas atomization setup including close-coupled and free-fall atomization. The figures (b) and (c) were taken from [40] with permission from Springer Nature.

The melt disintegration process depends on the melt properties as well as the continuous delivery of the melt and gas stream. The atomization itself is influenced by the relative velocity, which in turn is caused by resultant shear and pressure differences between the supplied gas and the atomizing phase [130]. Ligaments and other irregular shapes, initially formed during disintegration and later during interaction with aerodynamic forces, are spheroidized [129]. The gas nozzle design is of particular interest, as the configuration determines the droplet break-up process and alters the cooling conditions. The gas acts as a heat sink and cools the melt droplets by convection and radiation, and hence, the rate of heat extraction from the melt droplet increases with increasing gas velocity and decreasing droplet diameter [131]. A slit jet configuration or a set of discrete gas jets is commonly used, allowing the gas to flow parallel or inclined towards the melt stream [132]. External mixing twin-fluid atomizers such as free-fall and confined/close-coupled atomizers are today the predominant industrial technologies when atomizing molten metal alloys. A brief discussion of the free-fall and close-coupled atomizer is presented. For further gas atomization details and different atomizer designs, see Ref. [132] and [133].

3.1.1. Free-fall atomization

The melt stream falls via gravity ($\sim$ 10 - 20 cm [134]) into the convergence of focused gas jets where it is disintegrated [133]. The simple, open and unconfined stream arrangement of the nozzle design requires about $\sim$ 5 cm between the melt stream and the gas outlet to protect the nozzle from melt splashing or melt film back flow ("lick-back") that cause a melt stream "freeze-off", and thus damaging the nozzle [133]. The nozzle is more robust in preventing melt

freezing when compared to close-coupled atomization due to the large distance between the melt stream and the exit location of each gas jet. However, this distance forces the gas jet to travel a longer way before hitting the melt stream, resulting in a reduced gas velocity and yielding in larger particles. This in turn leads to a reduced convective cooling effect, as cooling through expansion chilling in the gas occurs at a later position. [133].

3.1.2. Close-coupled atomization

For the industrial applications in which particles < 50 µm are required, close-coupled atomizers are often preferred, as they provide an energy intensive disintegration in the atomization zone. This is due to the close proximity of the high energy gas to the initial melt outlet tip, which produces a higher yield of fine powders [133]. Some studies report that the melt stream is distributed as a melt film, covering the outlet tip. However, our recently developed convergent-divergent close-coupled atomizer (CD-CCA-0.8), introduced by Schwenck et al. [135], shows a fallen melt stream without the occurrence of a melt film underneath the melt tube tip (Fig. 3.1c). This observation concludes that a successful atomization with respect to process stability and droplet size control can be performed without the presence of a melt film underneath the melt film tip. The melt mass flow rate depends on the metallostatic pressure in the crucible/tube cross-section and the aspiration pressure at the melt tube tip, which in turn depends on the relative position, geometry, and melt tube dimensions [136]. The local gas recirculation promotes a negative aspiration pressure, which results in suction and a stable melt delivery.

Close-coupled atomizers have a stronger tendency for melt "freeze-off" when compared with free-fall atomization if the melt tube surface is chilled by the cooling gas. [133]. This can be overcome through an increased melt superheat temperature (200 - 400 K). A strong melt superheat temperature may cause the vaporization of sensitive feedstock elements with a low vaporization temperature and may cause the melt to react with the crucible, leading to heterogenous nucleation. [133].

3.1.3. Particle size and particle size distribution

The cooling behavior or the cooling rate of melt droplets mainly depends on droplet size (for details, see sec. 1.4.2). The fundamental aspects of droplet formation and the most important empirical contributions to estimate the particle size as well as particle size distribution are presented.

Liquid stream disintegration phenomena and droplet formation have been the subject of theoretical and experimental considerations since Bidone's [137] and Savart's [138] pioneering experimental studies in 1829 and 1833, respectively. Rayleigh was the first to investigate the theoretical disintegration of a frictionless liquid stream emerging from a round orifice in 1879 [139]. His initial theoretical considerations neglected liquid viscosity and the impact of the ambient medium. His subsequent work considered liquid viscosity, but due to the complexity of his final equation, it was rarely used in subsequent literature.

Weber [140] presented a theoretical description of the stream disintegration process in 1931, guided by Haenlein's work [141], who first provided a quantitative description of the stability of a viscous stream [142]. Weber stated that the disintegration process depends on the stream velocity as well as on liquid properties such as surface tension, density, and viscosity. Because of his achievements, the relationship between inertial force and surface tension was named after him. The dimensionless liquid Weber number (We_l) is described as follows:

$$We_l = \frac{\rho_l \cdot u_l^2 \cdot D_l}{\sigma_l}, \tag{3.1}$$

where ρ_l describes the liquid density, u_l is the liquid stream velocity, D_l is the liquid stream diameter, and σ_l is the liquid surface tension. Dimensional considerations, incorporating the forces involved in the droplet disintegration process such as the inertial force, the ambient medium, the surface tension force, and the viscous force of the liquid melt were used to determine the maximum droplet size. The gas or aerodynamic Weber number $\left(We_g\right)$ is the decisive parameter:

$$We_g = \frac{\rho_g \cdot u_{rel}^2 \cdot d_p}{\sigma_l}, \tag{3.2}$$

and is a function of gas density ρ_g, droplet diameter d_p, relative velocity between the droplet and surrounding fluid u_{rel}, as well as the surface tension of the liquid melt σ_l. It is often assumed that $We_g > 10$ results in the disintegration of melt droplets [143]. The significance of the Weber number can be seen in numerous empirical equations that have been developed over the last four decades to estimate the droplet size [144]. The empirical correlation according to Lubanska [145] is the most common correlation used in gas atomization to predict the mass median particle diameter $d_{50,3}$:

$$\frac{d_{50,3}}{D_l} = K\left[\frac{\nu_l}{\nu_g}\frac{1}{We}\left(1+\frac{\dot{m}_L}{\dot{m}_G}\right)\right]^{0.5}, \tag{3.3a}$$

$$We = \frac{\rho_l \cdot u_{gl}^2 \cdot D_l}{\sigma_l}. \tag{3.3b}$$

Eq. 3.3a composes of the mass flow ratio (ratio of melt mass flow rate $\dot{m}_L$ and gas mass flow rate $\dot{m}_G$ which is often abbreviated as GMR), the Weber number as a function of the liquid density ρ_l, liquid stream diameter D_l, gas velocity at impact with the liquid stream u_{gl}, liquid surface tension σ_l, as well as the ratio of liquid viscosity ν_l to the gas viscosity ν_g. According to Lubanska, the constant K ranges from 40 - 50 and depends on the atomizer geometry. For a given nozzle and a fixed alloy, the particle size depends on the GMR, since a higher GMR yields finer powders. The GMR is often related to the economic efficiency of the process. Although the Lubanska correlation is often cited in literature, it should be noted that deviations between measurements and theoretical correlations of up to 50 % are common [143]. Another important aspect in gas atomization

is the particle size distribution, which is commonly described as a log-normal distribution. The geometric standard deviation σ_g is a key parameter, which describes how widely the powder is distributed.

$$\sigma_g = \frac{d_{84,n}}{d_{50,n}} = \frac{d_{50,n}}{d_{16,n}}, \tag{3.4a}$$

$$\sigma_g = \sqrt{\frac{d_{84,n}}{d_{16,n}}}. \tag{3.4b}$$

The index n represents the type of distribution, where zero, one, two, and three denote number-, length-, area-, and volume-based, respectively. Eq. 3.4a considers only the upper and lower distribution and provides an incomplete conclusion about the particle size distribution. Eq. 3.4b is preferred, as it provides an opportunity to describe the entire particle size distribution. Gas-atomized powders typically have a geometric standard deviation of 2 ± 0.3 [134].

3.2. Thermal aspects during droplet solidification

Most metallic glasses are produced via rapid solidification techniques. A fundamental feature of all rapid solidification processing techniques is that heat present in solidification is transferred to a heat sink with a high cooling rate [146]. This is accomplished by conductive heat transport, whereas radiative heat transport is for the most part too inefficient to permit the achievement of rapid solidification [147]. Rapid solidification can be achieved in three different ways by imposing (i) a high degree of undercooling prior to solidification, (ii) a high velocity of advance (solidification front velocity) during continuous solidification, and (iii) a high cooling rate during solidification [124]. A number of rapid solidification techniques have been developed. For a detail rapid solidification overview, see Refs. [122, 123, 125]. During rapid solidification, the amount of undercooling is important to determine microstructural development by controlling phase selection during nucleation and morphological evolution as well during crystal growth [148]. The dispersion of a liquid into small droplets effectively isolates the most potent nucleants from the melt droplets, that allows for deep undercooling ranging from 0.3 to 0.4 T_{liq} before the onset of nucleation [148]. Techniques such as the droplet emulsion technique, the drop tube process, and magnetic levitation are commonly used to minimize the probability of heterogenous nucleation through an elimination of crucible-induced nucleation and separation of heterogenous nucleation from the melt [124]. Method (ii) is achieved by withdrawing a sufficiently thin specimen at high velocity through a temperature gradient that is steep enough to constrain the solidification front from advancing the drawing velocity [124]. If considering a planar solidification front, the product of the planar solidification front times the thermal gradient is equal to the cooling rate, where an increase in both parameters favors rapid growth of the solid phase, promoting a refinement of the intrinsic microstructural features [124]. Method (iii) refers to the definition of cooling rates that

range from 10^2 to 10^5 $K s^{-1}$ for molten metal gas atomization [40].

3.2.1. Measuring the cooling rate

Direct and indirect measurements have been used to measure cooling rates with reasonable accuracy, allowing the comparison to theoretical heat flow considerations. Indirect measurements refer to microstructural features of the resulting crystalline alloy. Lamellar eutectic spacing [149], grain size [150], and dendrite arm spacing methods [151] are used to measure average cooling rates of crystalline alloys (Fig.3.2). Such a microstructural approach is unavailable when the product is a glass [61]. Cahn and Greer stated that: (i) indirect measurements can give an estimate only in the temperature range in which solidification takes place and neglects the subsequent cooling rate in the solid state, (ii) each family of alloys requires separate calibration, and (iii) the dendrites may coarsen after solidification and therefore yield misleading results [61].

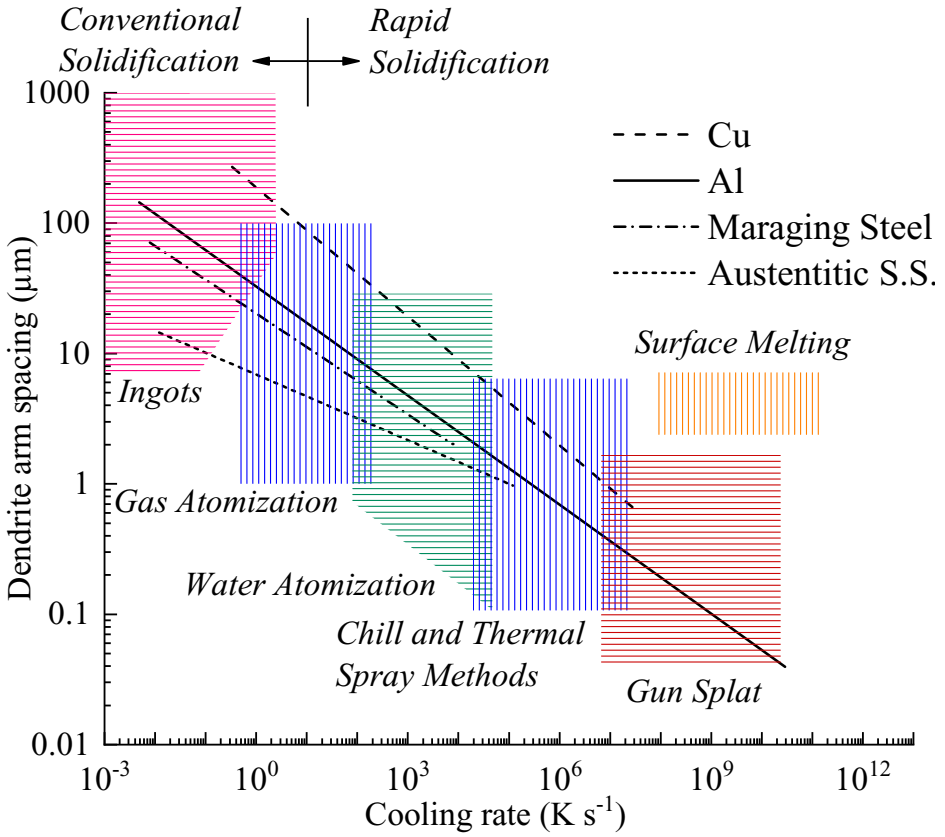

Fig. 3.2.: Relationship between dendrite arm spacing and cooling rate. The data was retrieved and modified according to Grant [152]. Permission for reuse was taken from Ref. [124] and granted by Springer Nature. The absolute cooling rate numbers are doubtful. For example, the cooling rate for gas atomization usually tends to range from 10^2 to 10^5 $K s^{-1}$. However, the diagram gives an excellent overview about experimentally derived cooling rates through secondary dendrites which were processed via different rapid solidification techniques.

Direct measurements with thermocouples or optical pyrometry would be preferred to measure the cooling rate of gas atomization processes. Direct measurements have been mainly used to measure the particle trajectory/thermal history and the gas flow field in the past, but were difficult to perform and the results deviated strongly due to the complexity and chaotic nature of the spray atomization process. Therefore, the dendrite arm spacing method has been the most trustful method to estimate cooling rates despite the drawbacks. The degree of microstructural refinement achieved during gas atomization is often measured with the primary (λ_1) or secondary dendrite arm spacing method ($SDAS, \lambda_2$) which rely on the relationship:

$$\lambda = a \cdot CR^{-n}, \tag{3.5}$$

where a and n are experimentally derived constants dependent on cooling rate CR and solidification time Δt [40]. Theoretical studies consider $n = 0.33$, but n often ranges from 0.3 to 0.5 due to experimental uncertainties and the limited range of cooling rate data [153].

3.2.2. Modelling the cooling rate

Levi and Mehrabian analyzed the solidification behavior of undercooled droplets with a Newtonian and a Non-Newtonian (Enthalpy) model [154]. A mathematical formulation that incorporated atomization process parameters, growth kinetics, interface velocity, undercooling, and other important solidification parameters was developed. The solidification paths of a given melt were graphically illustrated in a dimensionless Enthalpy-Temperature diagram (Fig. 3.3).

The graph is described by the following equation:

$$(H - H_{SM}) = \left[\Delta H_M + c_{p,l}\,(T - T_M)\right](1 - f_s) + c_{p,s}\,(T - T_M)\,f_s, \tag{3.6}$$

where H represents the enthalpy of the system at a given temperature T, f_s is the solid fraction, $c_{p,l}$ is the heat capacity of the liquid melt, $c_{p,s}$ is the heat capacity of the solid, ΔH_M is the latent heat of fusion, and H_{SM} represents the solid enthalpy at the melt temperature. By considering dimensionless numbers such as enthalpy, ψ, and temperature, θ, the equation can be arranged as follows:

$$\psi = (1 + \theta)(1 - f_s) + \left(c_{p,s}/c_{p,l}\right) f_s \theta, \tag{3.7a}$$

$$\psi = (H - H_{SM})/\Delta H_M, \tag{3.7b}$$

$$\theta = c_{p,l}\,(T - T_M)/\Delta H_M. \tag{3.7c}$$

The solidification path of the melt droplets can undergo different paths. Path (1) represents isothermal conditions where solidification takes place without notable undercooling ($\theta \sim 0$). Path (2) represents isenthalpic or adiabatic solidification, where nucleation is suppressed and the system undergoes complete solidification. ($\theta \geq 1$).

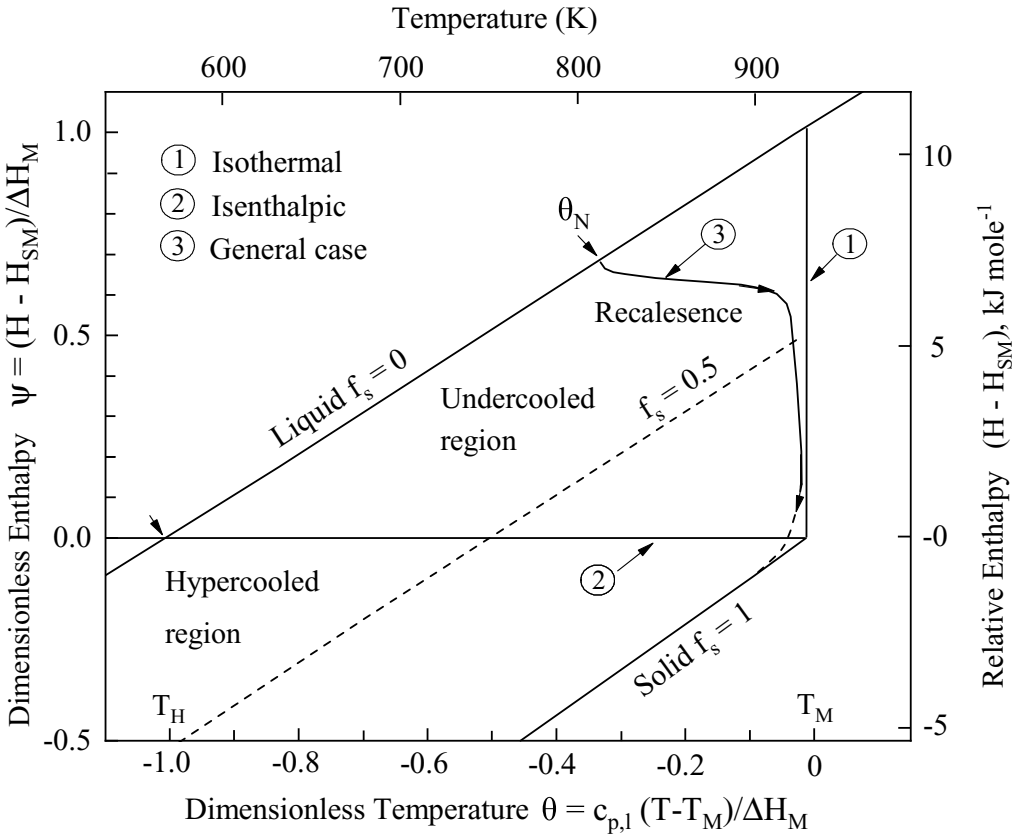

Fig. 3.3.: The dimensionless enthalpy-temperature diagram represents different solidification paths of undercooled melt droplets. Adapted from Levi and Mehrabian [154] with permission from Springer Nature.

The solidification behavior of undercooled liquids typically lies between path (1) and path (2) as seen in path 3. Path 3 shows adiabatic undercooling, followed by a rapid heat extraction of the latent heat. This results in a rapid increase of temperature, reaching almost the melt temperature (recalescence), where the liquid solidifies isothermally until solidification has been completed.

More recently developed models incorporate droplet dynamics and thermal profiles during molten metal atomization [155–157]. These mathematical models mainly have in common that they predict the size distribution, velocity, history, temperature, cooling rates, and the microstructural features with respect to secondary dendrites as a function of process conditions [124]. The process and cooling conditions of gas atomization can be summarized as seen in Fig.3.4. The atomization temperature depends on the melt superheat temperature and the heat loss from the melt stream running through the nozzle of the crucible. The thermal history of the melt droplets is governed by the distribution of the melt, impulse, enthalpy, particle size, particle velocity distribution and is determined by selected process conditions (nozzle geometry, inert gas, atomization pressure, gas velocity, initial gas temperature, and gas mass flow rate) [158].

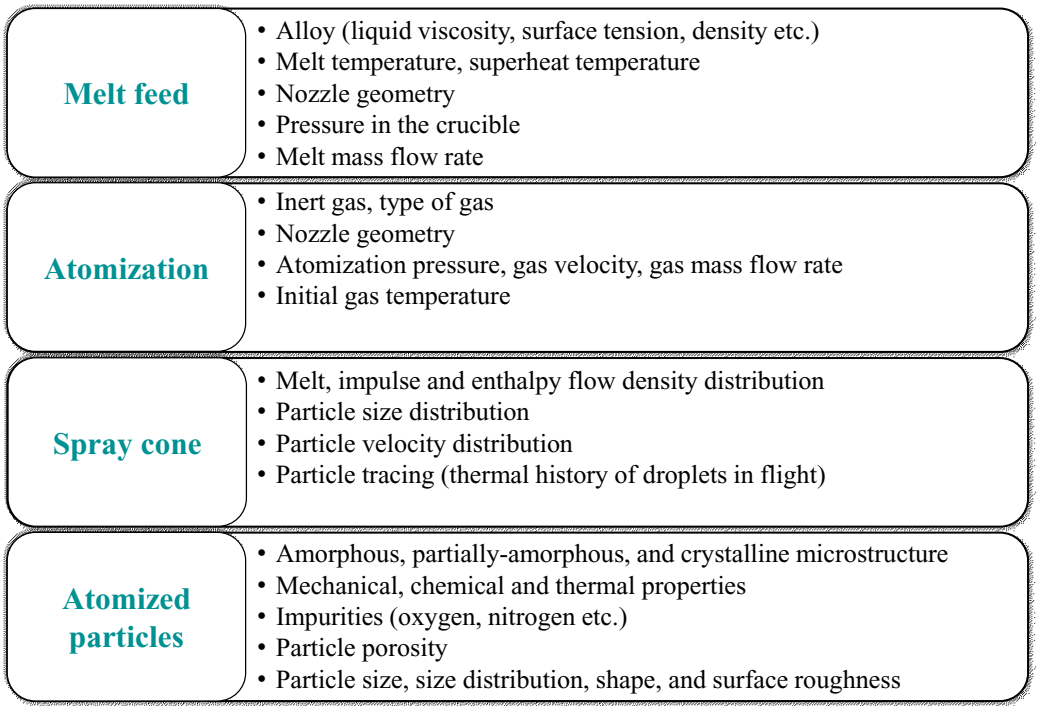

Fig. 3.4.: Process conditions during molten metal gas atomization determine the microstructure of the particles. The information was taken from Mathur et al. [159, 160] and updated according to current research for the atomization of glass-forming alloys.

Assumptions for the numerical droplet solidification model

The cooling behavior of rapidly solidified melt droplets, such as for binary crystalline alloys (e.g. Al-4.5wt%Cu), is divided into different solidification paths: (i) cooling in the liquid state, (ii) nucleation and recalescence, (iii) segregated solidification, (iv) eutectic solidification, and (v) cooling in the solid state. To estimate droplet temperature over different solidification paths, assumptions are required to set the boundary conditions for the differential equations, simplifying the gas atomization process. For instance, it is assumed that Newtonian cooling with forced convection is present. The droplets are spherical and formed at the impact point with the gas stream where the droplet velocity and flight distance is zero [26]. The droplets travel along the central axis of the chamber, and each droplet size considered is subjected to the same gas velocity profile [26]. The mean gas flow is usually taken in these studies [26]. Droplet-droplet collisions or continuous droplet contact, as well as droplet radiative transfer is mostly neglected. If the effect of the droplets on the quenching gas is included (two-way thermal coupling), the temperature of the gas would increase. Thus, the droplet cooling rate would be reduced, resulting in a smaller temperature gradient [161]. This is particularly relevant in the dense section of the spray cone where the relative velocity is highest. The spray cone generally consists of a dense and dilute section. A dense section is controlled by the droplet motion with respect to collisions and continuous contact, whereas the droplet motion of the dilute section is controlled by the fluid forces (drag and lift) [161].

Model description

Droplet solidification models for the gas atomization or spray forming process have been extensively described in literature [26, 156, 157, 160, 162–165], so only the most important relationships with respect to model droplet-gas interactions and heat transfer behavior are described. The model details with corresponding assumptions or equations are listed in the model developed by Grant et al. [156]. To calculate the droplet velocity, an analysis must be done on the gravitational, drag, and buoyant forces that act on the droplets. The governing differential equation for droplet motion is derived from the sum of the individual forces acting on the droplet:

$$\frac{du_p}{dt} = g - \frac{3}{4}\frac{\rho_g C_D}{\rho_p d_p}|u_p - u_g|\left(u_p - u_g\right) - \frac{\rho_g}{\rho_p}g, \tag{3.8}$$

where u_p, ρ_p, d_p are the droplet velocity, density and diameter, respectively. The variables u_g and ρ_g are the velocity and density of the gas, while C_D represents the drag coefficient. Most of the properties are constants, but the gas velocity is typically taken from experimental or simulation data, whereas C_D is related to the Reynolds number $Re = \rho_g \times u_{rel} \times d_p/\eta_g$. The parameter η_g is the dynamic viscosity of the gas and the relative velocity is described as $u_{rel} = u_p - u_g$. C_D has been determined empirically or theoretically by studying flow around spheres [159]. The drag coefficient for our developed numerical model was used according to Stoke's law [166], Schiller & Naumann correlation for the transition region [167], and Netwon's law [168]:

$$\begin{cases} C_D = 24/Re & \text{for} \quad Re < 1 \quad [166], & (3.9) \\ C_D = \dfrac{24}{Re}\left(1 + 0.15Re^{0.687}\right) & \text{for} \quad 1 \leq Re \leq 800 \quad [167], & (3.10) \\ C_D = 0.44 & \text{for} \quad Re > 800 \quad [168]. & (3.11) \end{cases}$$

It is often suggested that any temperature gradient within a molten metal droplet is uniform and may be neglected as the Biot number $Bi = h \times d_p/k_l$ is less than 0.1 (h represents the heat transfer coefficient, d_p is the droplet diameter, and k_l is the thermal conductivity of the melt droplet). Therefore, Newtonian cooling is assumed where the heat transfer coefficient is often described by the Nusselt number $Nu = h \times d_p/k_g$ (k_g is the thermal conductivity of the gas), according to the correlation introduced by Ranz and Marshall [169, 170]:

$$Nu = 2 + 0.6Re^{1/2}Pr^{1/3}, \tag{3.12}$$

where the Prandtl number is defined as $Pr = c_{p,g} \times \eta_g/k_g$ ($c_{p,g}$ is the specific heat capacity of the gas). The heat removed by convection and radiation at the droplet surface boundary layer can be equated to the change in droplet temperature, including a source term for the release of latent heat [156]:

$$\frac{dT_p}{dt} = \frac{-6\left[h\left(T_p - T_G\right) + \varepsilon k_{SB}\left(T_p^4 - T_w^4\right)\right]}{\rho_p d_p c_{p,l}}, \tag{3.13}$$

where T_p, T_G, T_w are the droplet, gas, and wall temperature, respectively. Other parameters are the specific heat capacity $c_{p,l}$ of the liquid melt droplet, ε is the emissivity, and k_{SB} is the Stefan-Boltzmann constant. Mehrabian and co-workers have shown that heat loss by radiation from melt droplets is at least an order of magnitude less than convective heat losses [171]. Most droplet cooling models neglect radiation, whereas the developed model in this work considers radiation. The consideration of radiation depends on initial melt temperature, gas and melt properties, and droplet size etc. Using the determined cooling curves, the cooling rate may be calculated with two different definitions:

(i) CR_{liq} describes the cooling rate of the melt just before crystallization starts and is obtained from the slope of the tangent line at a certain temperature above the liquidus temperature.

(ii) CR_{LS} is the average cooling rate over the entire local solidification process. The cooling rate in the local solidification interval can be calculated in three different ways depending on the cooling model used (see Fig. 3.5).

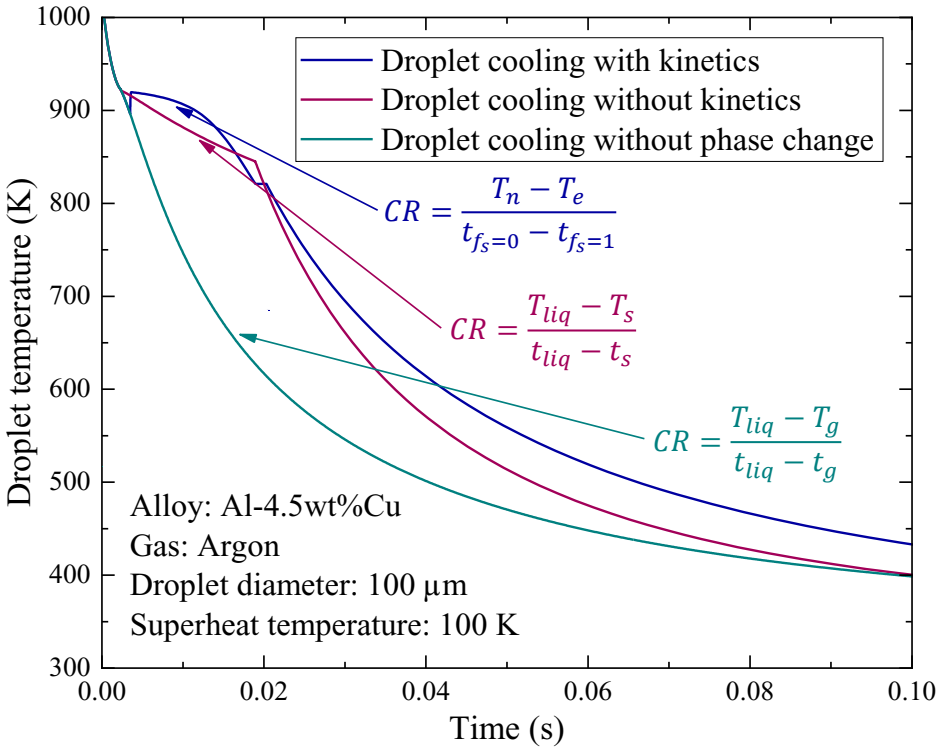

Fig. 3.5.: Three cooling models have been developed to calculate average cooling rates [172]. As an example, an Al-4.5wt%Cu alloy was considered with argon as the cooling gas, with a droplet diameter of 100 µm, and with a melt superheat temperature of 100 K. These models represent cooling with and without kinetics and cooling without phase change. Droplet cooling with kinetics refers to undercooling, recalescence, as well as segregated and eutectic solidification. Droplet cooling without kinetics is defined by the local solidification time under equilibrium conditions. Cooling without phase change is described by the absence of a solidification interval as in the case of an amorphous material.

3.3. Atomization of glass-forming alloys

A small number of studies on the atomization of glass-forming alloys have been reported [26, 31, 173–180]. These studies mainly focus on the microstructural evolution and magnetic properties of as-atomized powders. Further studies exclusively report on powder consolidation such as Layer Additive Manufacturing [181], Warm Hydrostatic Extrusion [182], Warm Rolling [183], Spark Plasma Sintering [184], Severe Plastic Deformation [185], Cold Spraying [186], and Thermoplastic Forming [187, 188]. The study by Zheng et al. is an exception [26, 31], as the authors reported the gas atomization of amorphous aluminum powders in detail. The powders were produced by means of close-coupled atomization at different process conditions: the atomization gas, melt superheat temperature, atomization pressure, and the crucible outlet diameter were changed in five experiments as well as the effect on powder properties were investigated. These results were supported by a droplet solidification model. The mass median particle diameter $d_{50,3}$ was measured to be 14 µm. The powders were partially-amorphous for all considered process conditions. A detailed examination of a particle size class < 25 μm showed amorphous fractions between 70% - 100%. An increased melt superheat temperature resulted in smaller particle sizes, but also in a significantly lower amorphous fraction for a particle size class < 25 µm. Zheng's work has provided many important findings, especially in the relationship between process parameters and final powder microstructure.

A fundamental analysis on the physical mechanisms that increase the cooling rate during molten metal gas atomization would be beneficial. Higher cooling rates are needed to obtain a higher amorphous yield and to produce amorphous powders that normally tend to crystallize. These amorphous powders may then be used for powder metallurgy processing techniques that were previously inaccessible, opening new commercial application fields. This can only be achieved if current boundary conditions in gas atomization are expanded. The question naturally arises: Have we already reached the limits with respect to increasing the cooling rate during molten metal gas atomization or is it possible to further increase the droplet cooling rate? Minimal knowledge on the relationship between the viscosity of glass-forming alloys and final particle shape is currently available. At the melting point, glass-forming alloys have viscosities that are usually two orders of magnitude higher than for pure elements or binary alloys, resulting in non-spherical particles. Methods to improve the particle shape would also be beneficial, as spherical particles are required for the subsequent consolidation such as for Metal Injection Molding and Layer Additive Manufacturing.

CHAPTER 4

Experimental methods and analyses

4.1. Material selection

Two soft ferromagnetic glass-forming alloys and one Cu-based glass-forming alloy with commercial purity, as well as one Zr-based glass-forming alloy with high purity have been atomized within the scope of this PhD thesis. The nominal composition of the alloys together with feedstock processing information are listed in Tab. 4.1. The selected alloys were considered for the different cooling strategies: (i) increasing the melt superheat temperature, (ii) hot gas atomization, (iii) spray cone cooling, and (iv) liquid quenching. For simplicity, the abbreviated nomenclature for all glass-forming alloys will be used.

To challenge the hypotheses in spray cone cooling (sec. 1.4.3) and liquid quenching (sec. 1.4.4), the two soft ferromagnetic glass-forming alloys have been chosen because of their low glass-forming ability. If conventional gas atomization is considered, nano-crystallization introduced by kinetically related growth (thermal stability) [19, 189] or cooling rate limitations inhibits the two soft ferromagnetic powders to become fully amorphous. The hypothesis is that an increased heat transfer coefficient will result in a higher cooling rate and in amorphous powders. Melt-spinning samples from the same feedstock have been produced and were chosen as reference materials.

A crystalline Cu-6wt%Sn alloy was taken for verifying the hot gas atomization results. This alloy was used as its thermophysical properties are well documented in literature, and correlations between secondary dendrite arm spacing and cooling rates are available [40]. To explore a greater viscosity range, the CuTiZrNiSiSn and ZrCuAlNb glass-forming alloys were exclusively taken for the melt superheat temperature study. A larger viscosity affects the droplet formation and break-up process during gas atomization, leading to different particle shapes (refers to the viscosity hypothesis in sec. 5.1).

4.2. Powder generation via gas atomization

Gas atomization was used to synthesize powders with different cooling conditions that vary with particle size. The schematic layout of the gas atomization tower is shown in Fig. 3.1. The system consists of three main components: (i) a vacuum vessel including an induction melting system which allows melt temperatures of up to 1870 K, (ii) a spray chamber with a particle falling distance of 4.8 m, and (iii) a gas atomizer.

Tab. 4.1.: Selected alloys including purity information. All alloys have been produced with commercial purity except the ZrCuAlNb alloy, which has a high tendency for crystallization if commercial purity is used.

Cooling strategy	Alloy (at%)	Nomenclature	Elements used (wt%)	Comments
Superheat temperature Spray cone cooling Liquid quenching	$\{(Fe_{0.6}Co_{0.4})_{0.75}B_{0.2}Si_{0.05}\}_{96}Nb_4$	FeCoBSiNb	Fe80.51B18.26 Fe33Nb65.5 Fe (99.97), Si (99.99) Co (99.8)	Binary alloys and raw elements were melted in the atomization tower (no master alloy was used).
Superheat temperature Spray cone cooling Liquid quenching	$Fe_{76}B_{10}Si_9P_5$	FeBSiP	Fe80.51B18.26 Fe75.92P23.23 Fe (99.97), Si (99.99)	Binary alloys and raw elements were melted in the atomization tower (no master alloy was used).
Superheat temperature	$Zr_{59.3}Cu_{28.8}Al_{10.4}Nb_{1.5}$	ZrCuAlNb	Zr Crystal bar (99.94) Cu (99.99), Al (99.99) Nb (99.99)	Master alloy was made via arc melting at LMW^*.
Superheat temperature	$Cu_{47}Ti_{33}Zr_{11}Ni_6Si_1Sn_2$	CuTiZrNiSiSn	Zr 702 (99.2) Ti Grade 1 (99.2) Cu (99.99), Ni (99.95) Si (99.9999) Sn (99.99)	Master alloy was made via arc melting at LMW^*.
Hot gas atomization	$\{(Fe_{0.6}Co_{0.4})_{0.75}B_{0.2}Si_{0.05}\}_{96}Nb_4$	FeCoBSiNb	Fe81.43B17.94 Fe31.4Nb65.2 Fe (99.99), Si (99.9) Co (99.0)	Binary alloys and raw elements were melted in the atomization tower (no master alloy was used).
Hot gas atomization	$Cu_{96.7}Sn_{3.3}$	Cu6Sn	$B16^*$	Pre-alloy was melted in the atomization tower.
Melt Spinning	$\{(Fe_{0.6}Co_{0.4})_{0.75}B_{0.2}Si_{0.05}\}_{96}Nb_4$	FeCoBSiNb	Fe80.51B18.26 Fe33Nb65.5 Fe (99.97), Si (99.99) Co (99.8)	Master alloy and melt-spun samples were made using an induction furnace and melt spinning, respectively (at IMR^*). Binary alloys and raw elements were used.
Melt Spinning	$Fe_{76}B_{10}Si_9P_5$	FeBSiP	Fe80.51B18.26 Fe75.92P23.23 Fe (99.97), Si (99.99)	Master alloy and melt-spun samples were made using an induction furnace and melt spinning, respectively (at IMR^*). Binary alloys and raw elements were used.

LMW: Lehrstuhl für Metallische Werkstoffe, Universität des Saarlandes, Saarbrücken, Germany.
IMR: Institute for Materials Research, Cooperative Research and Development Center for Advanced Materials, Tohoku University, Sendai, Japan.
B16: Is a commercially available rolled product (UNS: C51900) which is produced and traded by Wieland-Werke AG.

Al_2O_3 (CA97-GK80/20, MiTec Middeldorf) or graphite crucibles were placed into the vessel. The graphite crucibles were treated via halogen purfication (2120PT, Mersen) to reduce the amount of crucible impurities. Two kg of feedstock was used for the two soft ferromagnetic glass-forming alloys and 500 g was used for the CuTiZrNiSiSn and ZrCuAlNb glass-forming alloys[1]. The melt temperature was kept constant for 20 minutes for the two soft ferromagnetic glass-forming alloys and held for 5 minutes for the CuTiZrNiSiSn and ZrCuAlNb alloys. A stopper rod was placed into the crucible to prevent the melt from flowing through the nozzle outlet. Once the atomization temperature of interest was reached, the stopper rod was removed with a mechanical stroke, resulting in a controlled melt flow. A table with all process parameters is presented in Tab.C.1.

The spray chamber consisted of several electrolytically polished ring segments and a conical collector to capture the solidified particles. The spray chamber is connected to a cyclone with a filtration system to separate fine and coarse powders. The powder yield was typically above 95%. The remaining five percent corresponded to melt residues, splats or flakes/fibers from collisions between semi-solidified droplets and the chamber wall. The powders were sieved below 200 µm (CCA) or 300 µm (FFA) to remove unwanted flakes and fibers. The powders were divided with a vibratory feeder (DR100, Retsch) and a rotating powder divider (PT100, Retsch). The system divided the entire powder batch in a representative sample fraction (1/8 of the initial powder). 7/8 of the powder was air-classified into the following size classes: $<$ 20 or 25 µm, 20/25 - 45 µm, 45 - 63 µm, 63 - 90 µm, 90 -125 µm, 125 - 150 µm, 150 - 180 µm, 180 - 200 µm, 200 - 250 µm, and 250 - 300 µm[2].

The melt temperature was measured by a type B thermocouple located in the stopper rod. A second thermocouple (type K) was placed inside the graphite susceptor, located between the induction coil and crucible. The atomization pressure, chamber pressure, and the differential pressure between the spray chamber and the vacuum vessel were also recorded. A flow meter (Optiswirl 4200/C, Krohne Messtechnik) was used to measure the gas flow rate. A heat exchanger with elevated gas temperatures of up to 600 K was also connected to the gas atomization system. The gas temperature was measured with a type K thermocouple that was placed close to the gas nozzle. All experiments were performed with liquid argon 4.6 (Ar $\geq$ 99.996 with an oxygen content $\leq$ 4 ppm). The chamber and vessel were modified to reach a pressure of 10^3 Pa.

A free-fall atomizer with 20 holes (diameter of 1.1 mm) was used to produce larger particles for the hot gas atomization study. The close-coupled system is a convergent-divergent atomizer with an annular slit of 0.8 mm (CD-CCA-0.8) [135], performing stable atomization at low pressures of 0.8 MPa. The idea behind this atomizer is that the cross section initially narrows before widening, enabling the gas to accelerate to supersonic speed while minimizing the presence of shock waves [40].

[1] The master alloy was made using arc melting. Since the production of 2 kg of feedstock is very time consuming, down-scaled experiments were carried out. Five hundred gram is the amount required to ensure stable atomization.

[2] Particles larger than 200 µm were only considered for free-fall atomization, as close-coupled atomization typically produces powders below 200 µm.

4.3. Spray cone cooling and liquid quenching experiments

Experiments were carried out with distilled water for both cooling strategies. The FeCoBSiNb alloy was atomized and quenched in poly(ethylene glycol) provided by Sigma-Aldrich (PEG, BioUltra 200, CAS: 25322-68-3) for comparison. Poly(ethylene glycol) is a polymer quenchant with cooling properties typically ranging between that of water and mineral oils[3] [190].

Spray cone cooling experiments were performed with four dual argon/water (distilled H_20) nozzles (KL1, Diva Sprühtechnik) at an incident angle of 45°, a flow rate of $\sim$ 400 ml min^{-1}, and a preliminary pressure of 0.55 MPa. Experimental details are shown in Fig. A.1. The nozzles were placed 0.2 m away from the melt outlet and arranged 90° relative to each other, ensuring cooling from all angles. The impact between the water stream and the molten droplets resulted in an accelerated cooling rate during solidification. Liquid quenching experiments were carried out with 11 collectors at each falling distance (0.5 m and 0.7 m). Experimental details are shown in Fig. A.2. The head of the collectors were cone-shaped to ensure that a high amount of particles were collected while reducing the likelihood that the highly accelerated spray cone splashes the quenching medium out (the gas stream is accelerated up to 350 m s^{-1}, as computed in CFD simulations that are shown in Ref. [191]). A ledge was added to prevent the re-entry of contaminated particles that had already come in contact with the protective shield. The ledge was required, since the particles that impinged on the protection shield had a different thermal history than the liquid quenched particles, resulting in different cooling rates. Light microscopy and static particle imaging were used to estimate the amount of contaminated particles that came in contact with the protection shield. Particles that had impacted on the protection shields and liquid quenched particles were indistinguishable from each other, as almost all particles showed an irregular shape. It was assumed that the number of contaminated particles is negligible.

4.4. Melt Spinning

Reference samples of the two soft ferromagnetic glass-forming alloys were produced via melt spinning (NEV-A04, NISSIN GIKEN). The melt-spun samples were prepared at Institute for Materials Research, Tohoku University, Sendai, Japan. A sketch of the device is shown in Fig. 4.1. Ten grams of the master alloy (produced with a high frequency induction furnace: VMF-1-11, DIAVAC LIMITED) was placed in a quarz crucible with an outlet diameter of 0.5 mm. The vacuum level inside the chamber was reduced to 2×10^{-2} Pa. The rotation speed of the Cu-wheel was 4000 rpm.

[3] Quenching experiments with oil (DURIXOL V35, Burgdorf) were also performed. These experiments were discontinued due to high cleaning and maintenance time, as the oil vaporized and covered the entire atomization tower. In addition, the cooling rates between water and oil quenching yielded comparable results due to similar cooling capacities [21].

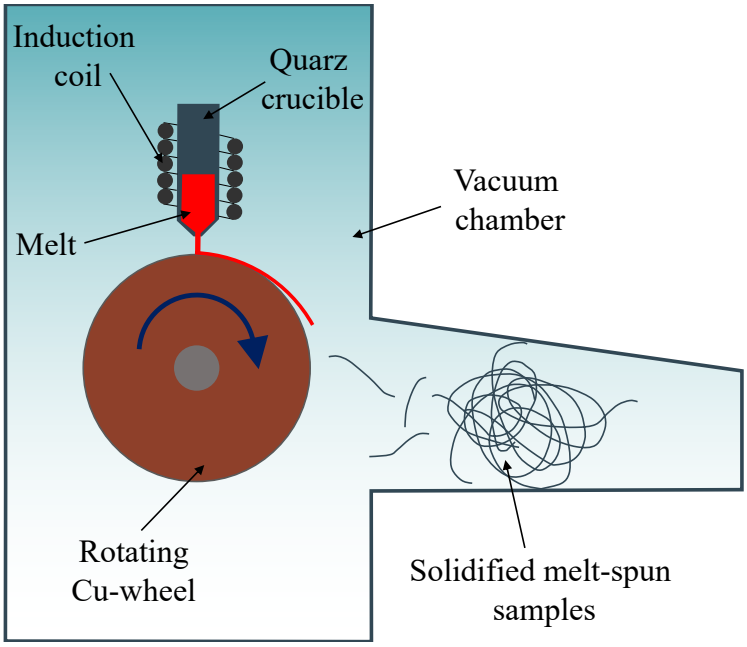

Fig. 4.1.: Sketch of the Melt Spinning device. The master alloy was initially produced with a high frequency induction furnace.

4.5. Spark Plasma Sintering (SPS)

Spark Plasma Sintering experiments were conducted with a Dr. Sinter, Sumitomo Coal Mining, SPS-1050 device (Fig. 4.2). The pressed samples were prepared at Institute for Materials Research, Tohoku University, Sendai, Japan. The Spark Plasma Sintering technique is a pressure-assisted pulsed-current process in which the powder samples were loaded in an electrically conducting die and sintered under an uniaxial pressure [192].

Approximately 1.6 g of as-atomized powders (particle size class: < 25 µm and 25 - 45 µm) were pressed in a tungsten carbide die, producing a ring with an outer and inner diameter of 13 and 8 mm, respectively. The ring height was $2.6^{\pm 0.15}$ mm, representing the required geometry to measure the magnetic properties. The experiments were carried under a pressure of $\sim$ 6 Pa. The powders were heated to the temperature(s) of interest (below the glass transition temperature). The applied force was set to 4.12 kN corresponding to a compression strength of 500 MPa. After a holding time of $\sim$ 30 - 45 s, the sintered samples were cooled with argon gas. The cooling rate was set to 25 $\mathrm{K\,min^{-1}}$ to reduce residual stresses, and thus to avoid micro-cracks. The relative density of the sintered samples was above 98%.

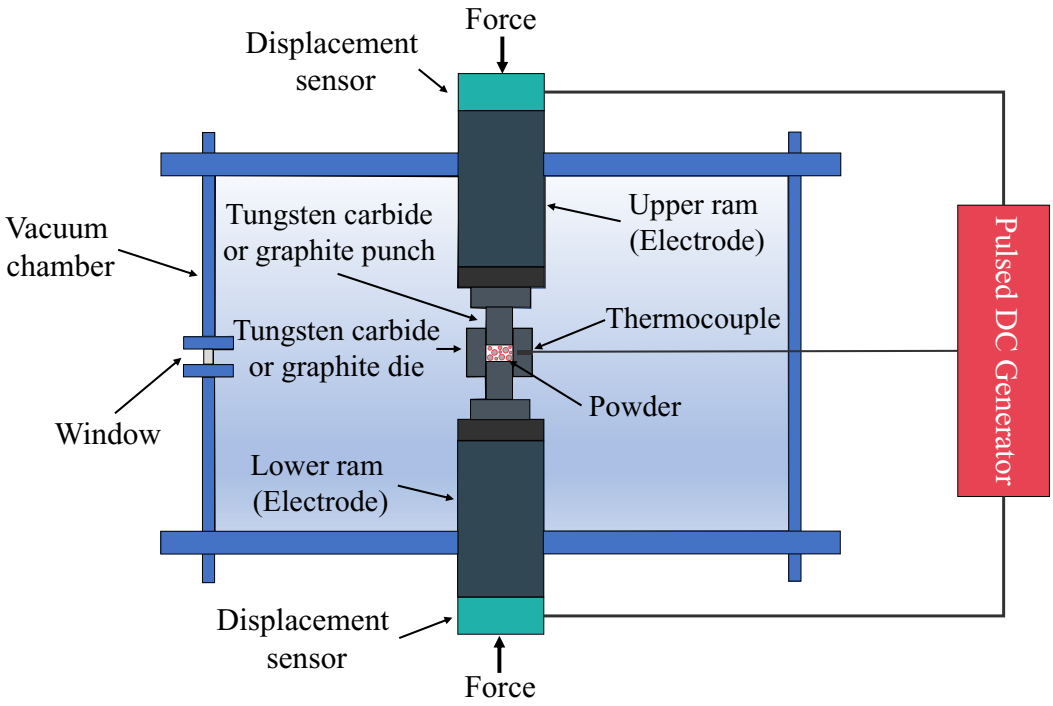

Fig. 4.2.: Schematic illustration of the Spark Plasma Sintering process. The experiments were performed at Tohoku University, Sendai, Japan.

4.6. Powder, ribbon and bulk characterization

Three different measurement systems were used to detect particle size, size distribution, and shape (Fig. 4.3). The as-atomized particles were measured with a laser diffraction system (Mastersizer 2000, Malvern). The powders were dispersed with water and delivered to the optical bench. The optical bench detects the scattering pattern of the particles. A detector array made up of many individual detectors within the optical bench collects the light scatter from a range of angles [193]. The detected information from each individual detector are combined in one measurement and analyzed by the Malvern software using the Fraunhofer or Mie theory. Despite the high accuracy and resolution, the system considers ideal spherical particles and can only be used to measure particle sizes or particle size distributions.

Static or dynamic particle imaging analysis can be used to measure the size and shape of non-spherical particles. A static particle imaging system (Morphologi G3, Malvern) was used. A small volume of particles (1 - 5 mm^3), which typically represents $\sim 10^3$ - 10^6 particles, was dispersed with air pressure on a glass plate. The microscope (2.5x and 10x objectives) automatically scans each three-dimensional particle in the form of a two-dimensional image and calculates particle sizes from the detected images [194]. The advantage of the system is the high resolution (down to submicrons). The measurement time ranges from minutes to days depending on the objectives. The particles lie in a fixed position on the glass plate, and overlapping particles must be separated/removed, manually or through computer algorithms, adding to the total analysis time.

A dynamic particle imaging analysis system (QICPIC, Sympatec) in combination with a dry dispersion unit (RODOS, Sympatec) was also used. The system has the advantage of short measurement times (within minutes), it enables arbitrary particle orientation, and due to the air transportation fluid the number of overlapped particles is reduced. The particles are dispersed and flow through an image plane. A special pulsed light source is used to ensure a high motion sharpness of the accelerated particles. A high-speed CMOS camera is used to detect submicron particles. Despite the great advantages of the dynamic analysis, the resolution of the particle shape images, and thus the quantitative results are different than in static imaging analysis. Only the combination of all three particle measurement systems allows for an accurate description of the particle size, distribution, and shape.

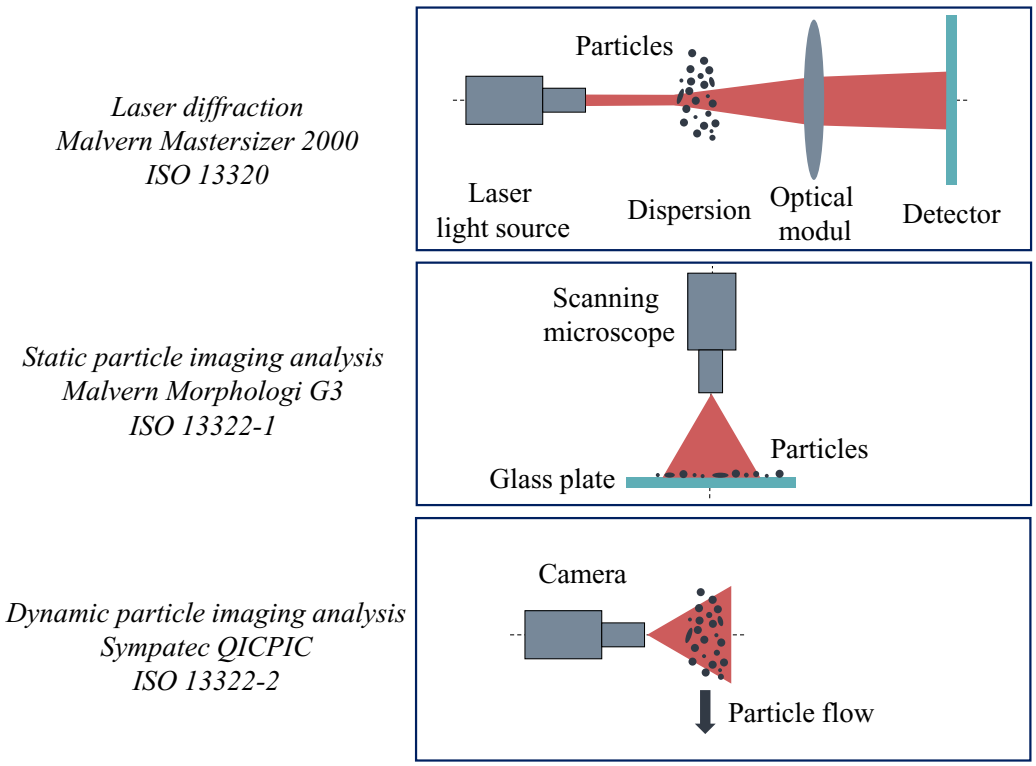

Fig. 4.3.: Schematic illustration of the three different measurement systems detecting the particle size, size distribution, and shape. A laser diffraction system can be used to measure the particle size and particle size distribution, whereas the dynamic and static particle image analysis also determine the particle shape.

X-ray diffraction analysis

The powders were initially placed on a single Si-crystal and mixed with ~ 1 ml 2-Propanol (C_3H_8O) to ensure that the powders were attached on a Si-crystal.

FeCoBSiNb powders for the hot gas atomization experiments were run with an omega-2-theta X-Ray powder diffractometer (D8 Advance, Bruker) equipped with a CuKα source and a fixed divergence slit. A primary monochromator (Ge)

was used to obtain Kα_1 emission. The powders were analyzed from 10 - 80° with a total measurement time of 6h:10 min. The discriminator was set to suitable values for Fe-based powders to restrict Fe fluorescence. After the acquisition of a new theta-theta X-Ray powder diffractometer (D8 Discover, Bruker) equipped with a CuKα source and a fixed divergence slit, it was used to collect the data for the melt superheat temperature, spray cone cooling, and liquid quenching experiments. Monochromization was electronically realized within the detector to obtain Kα_1 and Kα_2 emission. Fe fluorescence was electronically suppressed through the detector. The CuTiZrNiSiSn and ZrCuAlNb as well as the two soft ferromagnetic powders for the melt superheat temperature, spray cone cooling, and liquid quenching experiments were analyzed from 10 - 90° with a total measurement time of 3 hours. The structure analysis was performed with PANalytical - HighScore allowing for the identification of phases in the diffractogram.

Thermal analysis (DSC and DTA)

Continuous heating experiments on atomized powders and melt-spun ribbons were performed at a heating rate of 0.33 and 0.66 $K\,s^{-1}$ using a Mettler Toledo Differential Scanning Calorimetry instrument (TGA/DSC 3+). The instrument is equipped with a DTA sensor, allowing for the determination of thermophysical properties up to 1600 °C. The sample weight was 25 ± 0.5 mg (analyzed with an analytical balance; ME204T) and was placed in AlO_2 pans with a standard volume of 40 µl. The DSC/DTA instrument was initially calibrated with In, Zn, Al, as well as Au and Pd for the high temperature TGA/DSC 3+.

Microscopy and SEM analysis

The ground, polished, and etched particles were analyzed with an Olympus BX51 microscope equipped with an Olympus DP27 high-resolution camera to measure the SDAS for the Cu-6wt%Sn alloy. A SEM device was also used to determine the particle morphology and surface quality (Carl Zeiss, SUPRA 40 equipped with a Bruker XFlash 6/30 EDX detector).

Chemical composition analysis (ICP-OES)

Inductively Coupled Plasma-Optical Emission Spectroscopy (ICP-OES) was used to detect the chemical composition of the powders. The measurements were performed at Institute for Materials Research, Tohoku University, Sendai, Japan. The powders were initially prepared in an acidic solution. Twenty mg of powder was placed in sealed PFA vessels and diluted with 2 ml HNO_3 and 1 ml H_2O. The powders were subsequently heated to 423 K. After a holding time of 15 min, the samples were cooled to 288 K and 2 ml of hydrofluoric acid was added. The powders were heated for a second time to 373 K with a holding time of 15 min, followed by a cooling step to 288 K. The solution was finally mixed with Indium (1 mg/ml × 5 ml) and then filled with distilled water to 100 ml.

During ICP-OES, a plasma is formed by introducing argon gas that passes through a plasma torch. The powders are decomposed by the superheated inert

gas containing free atoms and ions of the elements [195]. The high temperature (plasma) excites the atoms and ions to emit light at particular wavelengths [196]. Once the atoms or ions are excited, they decay to lower states through thermal or radiative energy transitions [195]. The intensity of the emissions was measured and it corresponded to the concentration of the elements of interest.

Oxygen, Nitrogen, and Hydrogen analysis

An ELTRA ONH-2000 was used to measure the oxygen, nitrogen, and hydrogen powder content. ZrCuAlNb and CuTiZrNiSiSn powders with approximately 1 g were placed in Ni capsules (502-822, LECO Instruments), whereas 3 g of the soft ferromagnetic powders were placed in Sn capsules (90252, LECO Instruments). The Ni and Sn capsules were initially cleaned with acetone and dried on a heating plate. Graphite powder (501-073, LECO Instruments) was added to the CuTiZrNiSiSn and ZrCuAlNb powders to ensure homogenous melting. Three blank measurements with empty graphite crucibles were performed. The instrument was calibrated with oxygen steel standards (NIST), ranging from 1 to 1930 ppm. A steel standard with 7.4 ± 0.6 ppm was used for the hydrogen calibration. After calibration, five measurements with Sn or Ni capsules/graphite powder were performed to correct the final measurements (without capsule influence). The powders were subsequently placed in the sample drop mechanism and the furnace was purged with Helium 5.0 (also used as carrier gas). The powders covered by the capsule were dropped into an inner graphite crucible, which was placed in an outer graphite crucible. The outer graphite crucible was placed on an electrode tip. The sample started to melt due to an applied current, providing a power of 6 kW. The carrier gas extracted the oxygen and nitrogen from the sample. Carbon monoxide (CO) was produced through the reaction at the graphite crucible surface with the powder. The carrier and sample gas were pumped out and passed through a filter before entering a copper catalyst. CO is then converted to CO_2. Finally, carbon dioxide was detected by two infrared cells, determining the oxygen content. The nitrogen gas was measured by a thermal conductivity cell. Five measurements were performed in total.

Soft magnetic properties

The saturation magnetization B_S of powder and ribbons was measured with a Vibrating Sample Magnetometer at room temperature (VSM, VSM-5, Toei Industry). A schematic illustration is shown in Fig. 4.4.

Approximately 10-15 mg of powder and ribbons were carefully placed on adhesive tape and subsequently attached to a sample holder (glass rod). The Vibrating Sample Magnetometer system was initially calibrated with a Ni standard (purity of 99.99%, 7x7 mm, 230.49 mg, magnetic moment of 12.54 emu). A magnetic field H of ± 1600 $A\,m^{-1}$ (corresponding to 20 kOe) was applied by setting the sample within detecting coils. The magnetic field is generated by an electromagnet. The sample underwent a sinusoidal motion through vibration. This resulted in a change in magnetic flux within the sample and thus induced a voltage in the detection coil, proportional to the magnetic moment

of the sample. Three measurements were taken and averaged. The saturation magnetization was finally converted from the unit (emu) to the SI unit Tesla (T) by measuring the density of crushed pieces of the master alloy.

The properties with respect to saturation magnetization B_S, coercivity H_c, and permeability μ of the sintered parts were measured with a B-H curve tracer (BHH-50, Riken Denshi) as seen in Fig. 4.4. The samples were first covered in plastic capsules and then wound with two different wires to produce a toroidal coil. The toroidal shape is preferred for magnetic applications, as the magnetic flux is directed along its direction of coil (corners and air gaps are absent, resulting in low iron losses and high permeability) [197]. A magnetic field, detected by an integrated flux meter of up to ± 19 $kA\,m^{-1}$ (235 Oe) was applied by a given current. The current was converted from AC to DC through a pre-amplifier, resulting in a hysteresis loop. Similar to the Vibrating Sample Magnetometer measurements, three measurements were performed and averaged. Both techniques were used at Institute for Materials Research, Tohoku University, Sendai, Japan.

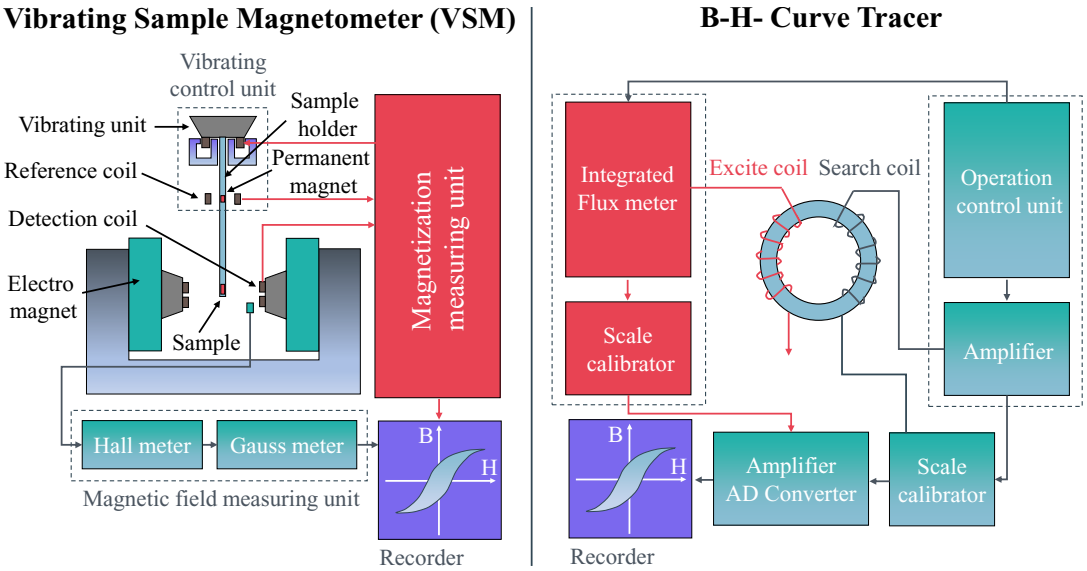

Fig. 4.4.: Schematic illustration of the Vibrating Sample Magnetometer and B-H Curve Tracer to measure the saturation magnetization of the as-atomized powders and ribbons. The B-H Curve tracer was also used to measure the saturation magnetization, coercivity, and permeability of the consolidated rings through Spark Plasma Sintering.

Density measurements

The density of the rings were measured by Archimedes' method with a Shimadzu AUW22D instrument and with n-Tridecane (Cat. No. 40265-00) as a working fluid to avoid corrosion. The measurements were performed at Institute for Materials Research, Tohoku University, Sendai, Japan. Ten pieces of the master alloy were measured in air and then soaked in n-Tridecane for one hour. The calculated density is the average value of ten measurements.

CHAPTER 5

Results and Discussion

5.1. Increasing the melt superheat temperature

Two hypotheses have been developed for this section. An increased melt superheat temperature may result in the dissolution of heterogeneities, acting as nucleation sites in the melt and thus leading to a higher amorphous fraction. The second hypothesis states that an increased melt superheat temperature decreases melt viscosity and leads to a higher number of spherical particles.

To challenge these hypotheses, FeCoBSiNb, FeBSiP, ZrCuAlNb, and CuTiZrNiSiSn glass-forming alloys were atomized and characterized with respect to their thermophysical properties, particle size, size distribution, and shape. Only the ZrCuAlNb and CuTiZrNiSiSn glass-forming alloys were used in the particle size and shape study, as their thermophysical properties such as the enthalpy of crystallization remained unaffected by different melt superheat temperatures.

5.1.1. Determination of enthalpy of crystallization

The effect of superheat temperature on the two soft ferromagnetic powders is shown in Fig. 5.1 and Fig. 5.2 with respect to XRD measurements. Three melt superheat temperatures were selected to be 250 K, 300 K, and 350 K.

A broad amorphous halo represents amorphous particles and reflection peaks describe crystalline or partially-crystalline powders. The FeCoBSiNb particles were fully amorphous up to 63 µm for the highest melt superheat temperature (350 K), whereas a lower superheat of 300 K or 250 K resulted in fully amorphous particles up to 45 µm. The same effect was observed for the FeBSiP glass-forming alloy. The lower the melt superheat temperature, the higher the number of pronounced peaks, concluding that the particle size classes were partially amorphous. Even the highest melt superheat temperature of 350 K and the smallest particle size class of < 25 µm showed crystalline peaks due to the low glass-forming ability. The lowest melt superheat temperature of 250 K for the FeBSiP alloy was too low to atomize the melt. A certain threshold superheat temperature is required in close-coupled atomization to avoid freezing the melt in the outlet nozzle. It is difficult to determine the mechanisms behind the melt freeze-off. For instance, heat dissipation determined by specific heat capacity deviates $< 10\%$ between the two glass-forming alloys [23, 198]. Melt viscosity could also be the cause for melt freeze-off, since a high viscosity slows down the melt flow rate, resulting in the inhomogeneous heating of the nozzle before atomization. This was supported by video recordings where the melt splashed out of the nozzle tip without flow and then froze. Contradicting the viscosity argument, the melt disintegration resulted in spherical particles for both alloys regardless of the melt superheat temperature used (e.g. 300 K and 350 K).

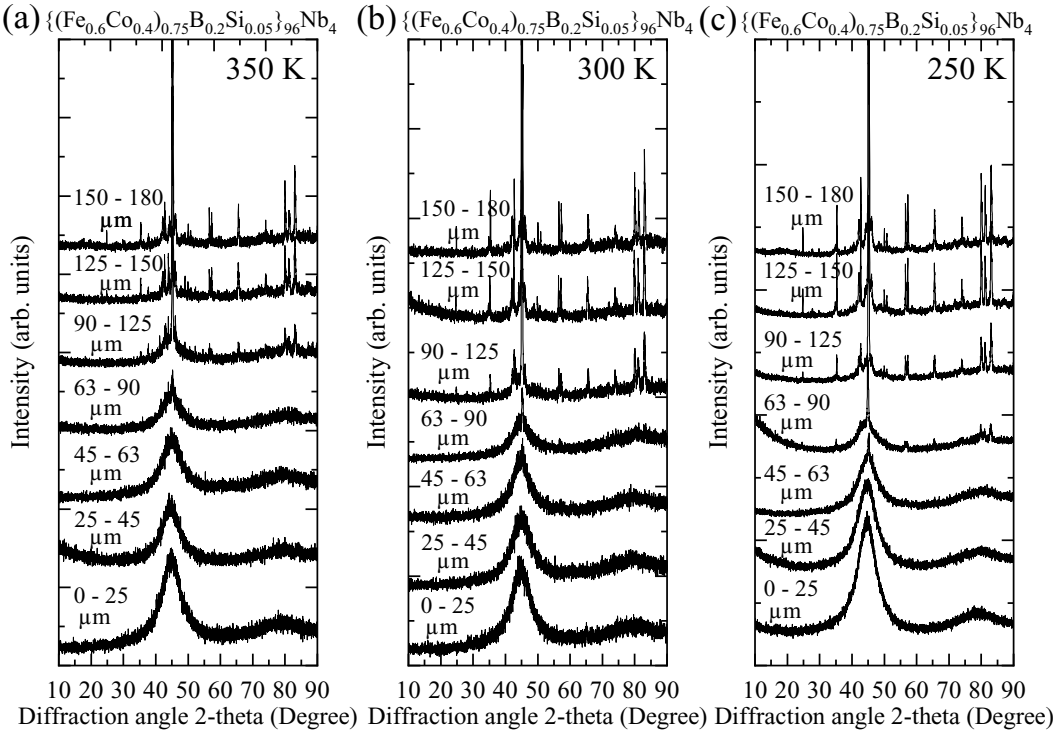

Fig. 5.1.: XRD analyses for $\{(Fe_{0.6}Co_{0.4})_{0.75}B_{0.2}Si_{0.05}\}_{96}Nb_4$ powders as a function of different particle size classes atomized at different melt superheat temperatures (350 K, 300 K, and 250 K).

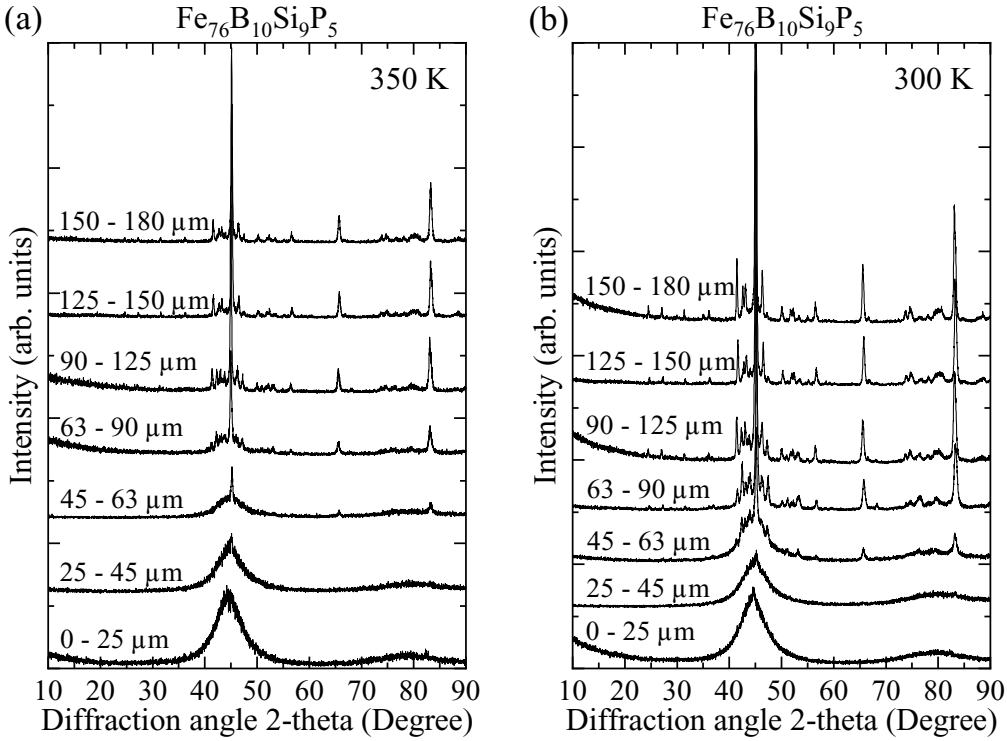

Fig. 5.2.: XRD analyses for $Fe_{76}B_{10}Si_9P_5$ powders as a function of different particle size classes atomized at different melt superheat temperatures (350 K and 300 K).

Although the ZrCuAlNb glass-forming alloy was atomized with high purity feedstock, using special halogen purified graphite crucibles to reduce the amount of impurities, and in an optimized vacuum environment, particles > 90 µm were partially-amorphous or fully crystalline regardless of the melt superheat temperature used (XRD analyses are not shown). The high oxygen affinity of Zr likely caused heterogenous nucleation and thus resulted in a lower amorphous fraction. The CuTiZrNiSiSn alloy was atomized in an amorphous state for the entire powder batch up to 200 µm regardless of the selected melt superheat temperature and the use of commercial purity (XRD analyses are not shown). The influence of melt superheat temperature on the enthalpy of crystallization and thus on the amorphous fraction as a function of particle size for the two soft ferromagnetic powders is shown in Fig. 5.3. The enthalpy of crystallization for the two soft ferromagnetic powders decreased with an increased particle size.

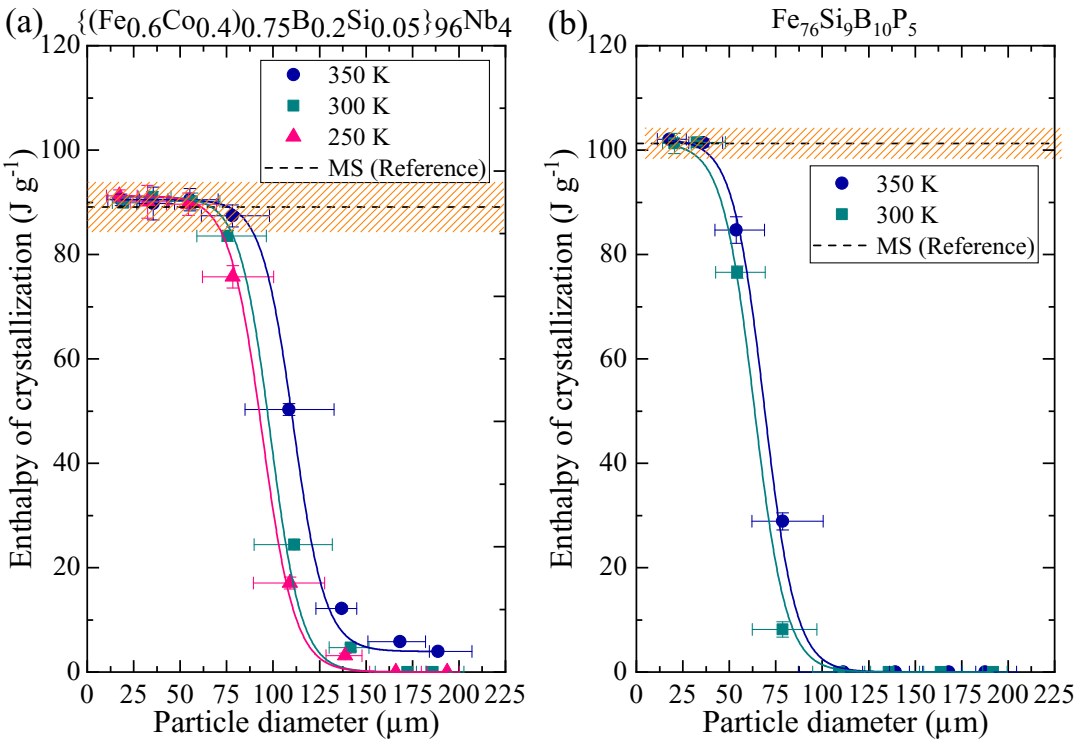

Fig. 5.3.: Enthalpy of crystallization as an indicator of amorphous fraction at different particle size classes, emphasizing the influence of the melt superheat temperature. The (a) $\{(Fe_{0.6}Co_{0.4})_{0.75}B_{0.2}Si_{0.05}\}_{96}Nb_4$ and (b) $Fe_{76}B_{10}Si_9P_5$ soft ferromagnetic glass-forming alloys were considered at three different melt superheat temperatures. The lowest melt superheat temperature (250 K) for the $Fe_{76}B_{10}Si_9P_5$ alloy was insufficient, since the melt froze at the nozzle outlet tip during gas atomization. The horizontal error bars represent particle laser diffraction measurements where the left and right error bars are the $d_{16,3}$ and $d_{84,3}$ percentiles. Measurements on melt spinning samples (MS) were also plotted for comparison (the dashed line refers to the average enthalpy of crystallization and the upper and lower edges of the orange area define the upper and lower standard deviation).

The results in Fig. 5.3 showed a systematic increase in enthalpy of crystallization when the melt superheat temperature is increased. The presented data were consistent with studies reported by Gillessen [29] and Dunst [30] where they performed containerless drop tube experiments on different glass-forming alloys. Both studies reported a substantial increase in amorphous fraction and undercooling if an appropriate melt superheat temperature was used [30]. The authors argued that the nucleation rate within the volume of the droplets was essentially influenced by the melt superheat temperature. They explained that an increased melt superheat temperature could destroy present clusters associated with intermetallic compound symmetry, and thus destroying potential nucleation sites [199, 200]. However, the influence of melt superheat temperature on the amorphous fraction in this study was found to be very small, likely caused by the crucible walls, as Gillessen and Dunst used a containerless technique under high vacuum conditions with high purity feedstock to synthesize amorphous particles. It is assumed that crystallization was favored due to impurities acting as heterogenous nucleants. The thermal stability, expressed as incubation time, of both soft ferromagnetic glass-forming alloys is very low and may have led to crystallization during atomization. All experiments were performed under industrial atomization conditions in a coarse vacuum (chamber pressure of 10^3 Pa) where oxygen was still present. Although soft ferromagnetic glass-forming alloys have a low affinity to oxygen, oxygen may still have had an effect on the crystallization kinetics.

5.1.2. Particle size analyses

The impact of melt superheat temperature on particle size during water or gas atomization is controversially reported in literature, as a decrease in particle size with an increased melt superheat temperature has been shown [34–36]. Other researchers have found that the final particle size is independent of the melt superheat temperature [37]. Fig. 5.4 shows the particle size distribution as a function of melt superheat temperature for the four different glass-forming alloys (FeCoBSiNb, FeBSiP, ZrCuAlNb, and CuTiZrNiSiSn). There was a weak correlation between melt superheat temperature and particle size, as the particle size of the two soft ferromagnetic powders showed only a small decrease for an increased melt superheat temperature. A more pronounced decrease in particle size was measured for the CuTiZrNiSiSn glass-forming alloy. The mass median particle diameter $d_{50,3}$ decreased from 49 to 43 µm, while the $d_{50,3}$ of the ZrCuAlNb glass-forming alloy decreased from 56 to 52 µm. The melt superheat temperature had a negligible effect on the geometric standard deviation (Tab. C.1).

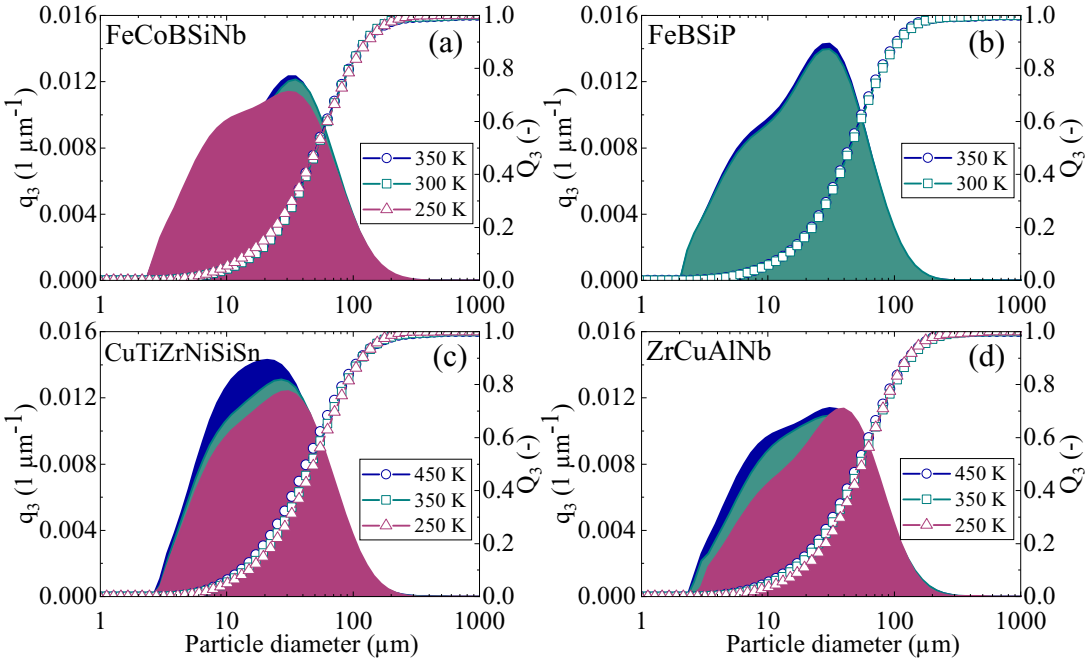

Fig. 5.4.: Density distributions (q_3) and cumulative mass distributions (Q_3) measured with laser diffraction for four glass-forming alloys atomized at different melt superheat temperatures: (a) $\{(Fe_{0.6}Co_{0.4})_{0.75}B_{0.2}Si_{0.05}\}_{96}Nb_4$, (b) $Fe_{76}B_{10}Si_9P_5$, (c) $Cu_{47}Ti_{33}Zr_{11}Ni_6Si_1Sn_2$, and (d) $Zr_{59.3}Cu_{28.8}Al_{10.4}Nb_{1.5}$.

5.1.3. Particle shape analyses

Particle morphology and surface roughness of four glass-forming alloys were qualitatively determined using scanning electron microscopy. Fig. 5.5 shows particles atomized at a melt superheat temperature of 350 K and with a particle size class of 25 - 45 µm.

The surface topography of the investigated particles were very smooth with the exception of the ZrCuAlNb glass-forming alloy, likely due to simultaneous crystallization and shrinkage. Sub-micrometer particles (satellites) were infrequently observed. Some larger particles were found to be partially covered by smaller, deformed particles (yellow frame). Satellites typically solidify faster due to the high surface-to-volume ratio, resulting in small spherical particles attached to larger particles. It appeared that these deformed particles passed through the supercooled liquid region up to the glass transition temperature, leading to droplets with a high viscosity. These droplets impacted on the larger particles, deformed, and covered the larger particles. Although a few undeformed particles or fibers can be observed in the FeCoBSiNb, FeBSiP, and CuTiZrNiSiSn powders, the majority of the particles were spherical. The ZrCuAlNb particles were much more irregular where a high amount of elongated fibers or "tadpole-shaped" particles were produced.

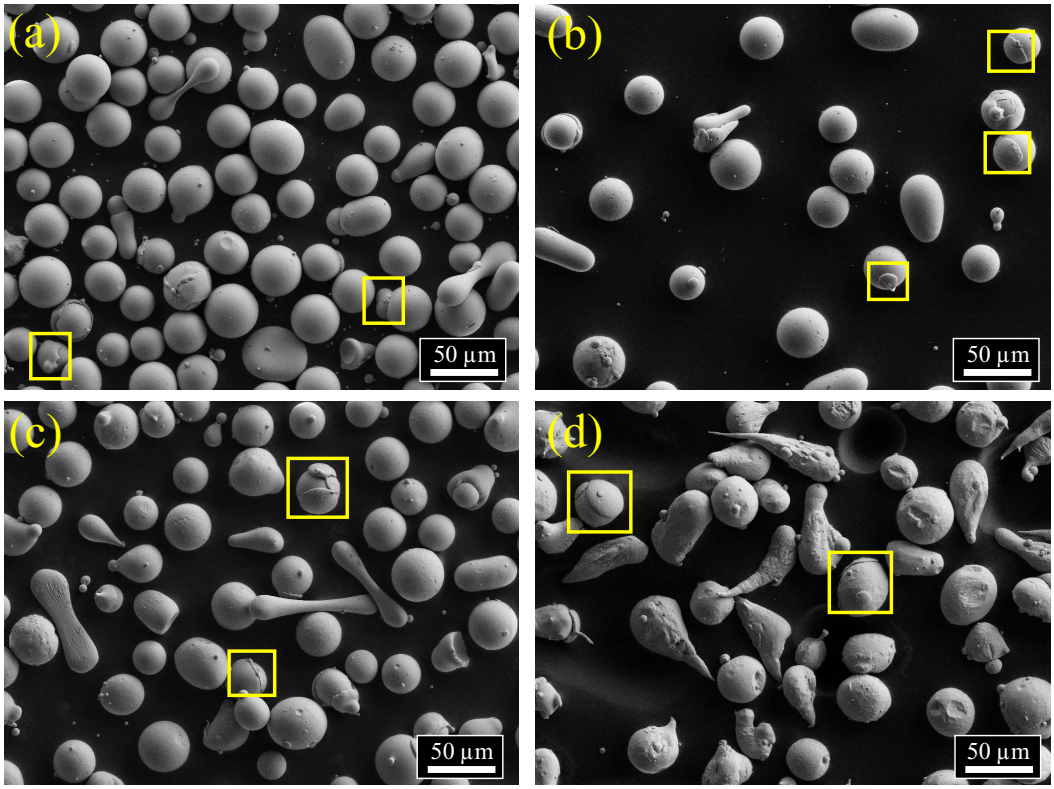

Fig. 5.5.: SEM images of (a)$\{(Fe_{0.6}Co_{0.4})_{0.75}B_{0.2}Si_{0.05}\}_{96}Nb_4$, (b) $Fe_{76}B_{10}Si_9P_5$, (c) $Cu_{47}Ti_{33}Zr_{11}Ni_6Si_1Sn_2$, and (d) $Zr_{59.3}Cu_{28.8}Al_{10.4}Nb_{1.5}$ as-atomized particles. Particles with a size class of 25 - 45 µm and a melt superheat temperature of 350 K are shown.

Particle shape analysis for the four different glass-forming alloys was performed using static particle imaging (Fig. 5.6). Two suitable particle shape factors were chosen to measure and describe the presented particle shapes in Fig. 5.5. HS-circularity, characterized by Malvern Panalytical Ltd., is known as sphericity (SPHT) and can be calculated using $SPHT_{0,2,3} = 4\pi A_p/P^2$ (ISO 9276-6) where A_p and P stand for the projected particle area and perimeter, respectively. The circle equivalent diameter calculation is based on a 2D image converted to a sphere of equivalent area. Sphericity will be considered instead of HS-circularity as per common convention in literature. The aspect ratio, $b/l_{0,2,3}$, represents the width-to-length ratio and is a measure of particle elongation. Both particle shape factors, sphericity and aspect ratio, have a value of 1 for ideal spherical particles.

Sphericity and aspect ratio for all glass-forming alloys decreased with an increased particle size. Large fluctuations seen in the curves at larger particle sizes resulted from the fewer number of particles, since the synthesized powders had a mass median particle diameter of 20 to 60 µm (Fig. 5.6). However, the amount of detected particles in these particle size classes were enough to accurately obtain particle shape information. The ZrCuAlNb glass-forming alloy had the lowest sphericity and aspect ratio values when compared to the three other glass-forming alloys, agreeing with the qualitative description in Fig. 5.5.

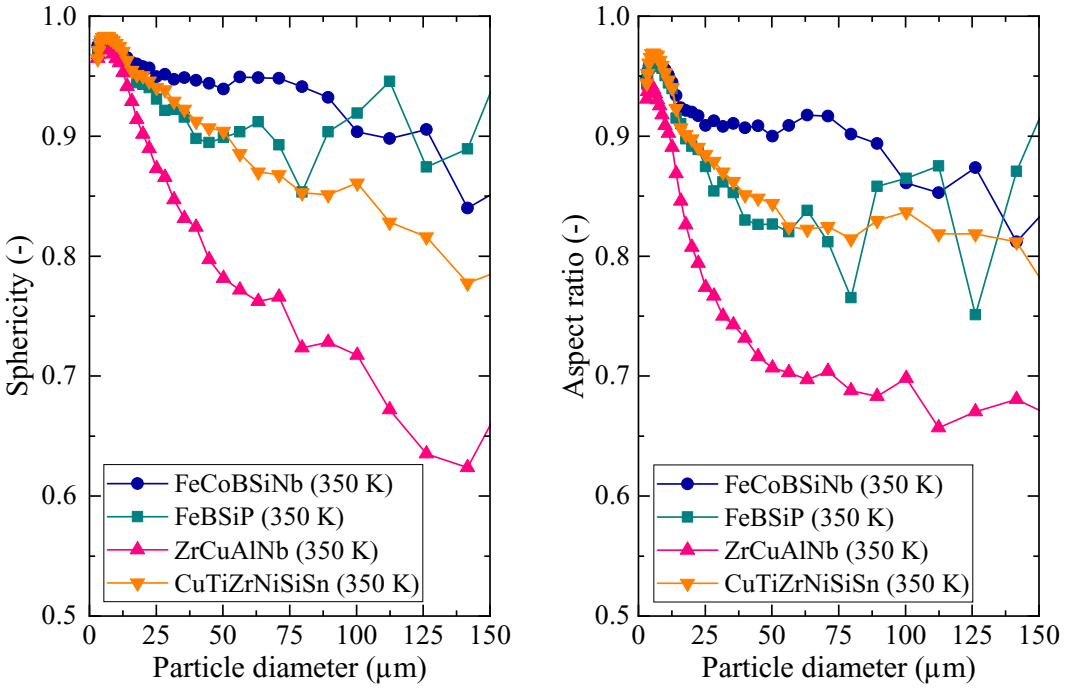

Fig. 5.6.: Particle shape analysis with respect to sphericity and aspect ratio for the four glass-forming alloys: (i) $\{(Fe_{0.6}Co_{0.4})_{0.75}B_{0.2}Si_{0.05}\}_{96}Nb_4$, (ii) $Fe_{76}B_{10}Si_9P_5$, (iii) $Cu_{47}Ti_{33}Zr_{11}Ni_6Si_1Sn_2$, and (iv) $Zr_{59.3}Cu_{28.8}Al_{10.4}Nb_{1.5}$. The particles were measured using static particle imaging. An average value for sphericity and aspect ratio was calculated between the lower and upper particle size classes. Ideal spherical particles typically have a sphericity and an aspect ratio of 1.

Fig. 5.7 shows the evaluation of sphericity and aspect ratio using static particle imaging analysis. A threshold value of k = 0.5 taken from the software corresponded to the ZrCuAlNb "tadpole-shaped" particles. A lower value of k indicates the presence of more irregularly shaped particles and a threshold value of k = 1 filters for ideal spherical particles. Spherical particles generally increase powder flowability, making them desirable for various powder metallurgy and Layer Additive Manufacturing processes. Both particle shape factors decreased with particle size, indicating that the number of irregularly shaped particles also increased with particle size. As melt superheat temperature for each glass-forming alloy increased, the number of irregular and "tadpole-shaped" particles decreased for a k value > 0.5. The number of spherical ZrCuAlNb particles distinctly increased with an increased melt superheat temperature, resulting in improved particle shape factors. The sphericity and aspect ratio for the other three glass-forming alloys only slightly increased. These results showed that spherical particles can be successfully produced using the melt superheat temperature method during gas atomization.

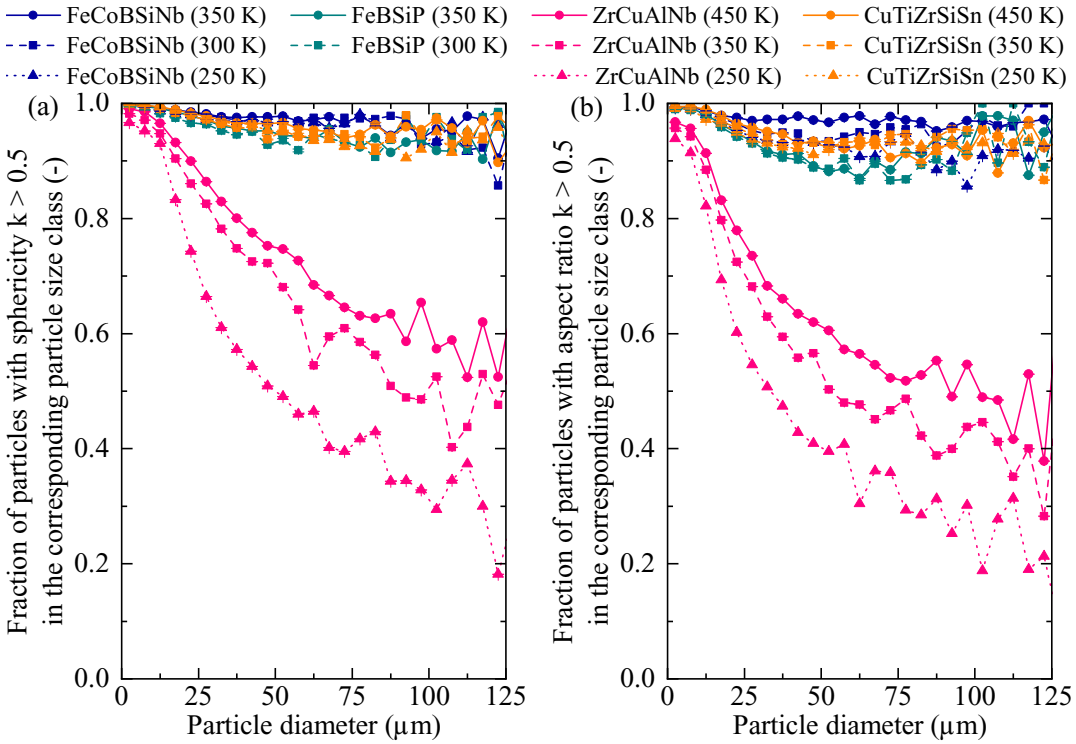

Fig. 5.7.: Evaluation of sphericity and aspect ratio using static particle imaging analysis. Three measurements were performed and averaged. Within each particle size class, the average particle diameter is plotted. Ideal spherical particles were represented by a k value of 1. A value > 0.5 was chosen as it represented the threshold for "tadpole-shaped" particles of the $Zr_{59.3}Cu_{28.8}Al_{10.4}Nb_{1.5}$ glass-forming alloy. A lower normalized value corresponded to an increase in irregular particles present in the powder. A higher melt superheat temperature increased the number of spherical particles.

5.1.4. The influence of thermophysical properties on the particle shape

A literature review has been performed to obtain liquid viscosity and surface tension data, since droplet formation and droplet break-up mainly depend on these thermophysical properties. The data were unattainable in literature for the two soft ferromagnetic glass-forming alloys. The viscosity data for the CuTiZrNiSiSn and ZrCuAlNb glass-forming alloys were measured at Lehrstuhl für Metallische Werkstoffe, Universität des Saarlandes, Saarbrücken, Germany and are provided in Fig.5.8 as part of a joint project. Since liquid density and surface tension data for the CuTiZrNiSiSn glass-forming alloy were unavailable, the data were taken from various literature sources for similar Vitreloy glass-forming alloys [82, 201, 202]. The density of the Vit101 glass-forming alloy was obtained from Ref. [202] between 740 and 1653 K. Mukherjee et al. provided surface tension data for the Vit1 glass-forming alloy ($Zr_{41.2}Ti_{13.8}Cu_{12.5}Ni_{10}Be_{22.5}$) [201] and a constant value was assumed for the considered melt superheat tempera-

ture range (∼ 1150 to 1280 K.). For the ZrCuAlNb glass-forming alloy, Hembree provided surface tension data and a constant value was applied to this study in the melt superheat temperature range from ∼ 1225 to 1350 K [82]. The determined values for liquid surface tension, density, and viscosity (calculated from the MYEGA fit as seen in Fig. 5.8) are summarized in Tab. B.4.

Tab. 5.1.: Thermophysical properties including liquid viscosity, surface tension, and density determined at liquidus temperature and different melt superheat temperatures.

Alloy -	T_{liq} K	ΔT_M K	η_l Pa s	σ_l N m^{-1}	ρ_l kg m^{-3}
Vitreloy family*	1160	0	0.042 (Fig. 5.8)**	1.47 [201]	6460 [202]
Vitreloy family*	1160	250	0.019 (Fig. 5.8)**	1.47 [201]	6325 [202]
Vitreloy family*	1160	350	0.018 (Fig. 5.8)**	1.47 [201]	6275 [202]
Vitreloy family*	1160	450	0.017 (Fig. 5.8)**	1.47 [201]	6225 [202]
$Zr_{59.3}Cu_{28.8}Al_{10.4}Nb_{1.5}$	1203	0	0.055 (Fig. 5.8)**	1.58 [82]	6460 [202]
$Zr_{59.3}Cu_{28.8}Al_{10.4}Nb_{1.5}$	1203	250	0.016 (Fig. 5.8)**	1.58 [82]	6385 [202]
$Zr_{59.3}Cu_{28.8}Al_{10.4}Nb_{1.5}$	1203	350	0.012 (Fig. 5.8)**	1.58 [82]	6355 [202]
$Zr_{59.3}Cu_{28.8}Al_{10.4}Nb_{1.5}$	1203	450	0.011 (Fig. 5.8)**	1.58 [82]	6325 [202]

T_{liq} = Liquidus temperature, ΔT_M = Melt superheat temperature, η_l = Liquid dynamic viscosity, σ_l = Liquid surface tension, ρ_l = Liquid density.

* Surface tension and density data for $Cu_{47}Ti_{33}Zr_{11}Ni_6Si_1Sn_2$ were unavailable in literature. The Vit101 glass-forming alloy was considered for liquid density and the Vit1 glass-forming alloy for surface tension was used instead, as they are quite similar to the $Cu_{47}Ti_{33}Zr_{11}Ni_6Si_1Sn_2$ glass-forming alloy.

** The liquid viscosity data were measured at Lehrstuhl für Metallische Werkstoffe, Universität des Saarlandes, Saarbrücken, Germany.

Viscosities around the glass transition temperature for both glass-forming alloys were measured using three-point-beam bending on amorphous bulk samples (Netzsch, TMA 402). Experimental details can be found in Ref. [203]. Liquid viscosities for the ZrCuAlNb glass-forming alloy were measured with electrostatic levitation [204], whereas viscosities for the CuTiZrNiSiSn glass-forming alloy were measured via couette rheometry. Experimental details are reported in Ref. [205]. A few three-parameter viscosity models such as the standard Vogel-Fulcher-Tammann (VFT) model [206], the Adam-Gibbs equation [207], and the Avramov-Milchev model [208] have been developed to determine the viscosity in high and low temperature regimes [209]. The recently proposed Mauro-Yue-Ellison-Gupta-Allan (MYEGA) model allows for the determination of viscosity up to 15 orders of magnitude and was therefore taken to accurately predict viscosities between the glass transition and the liquidus temperature [209].

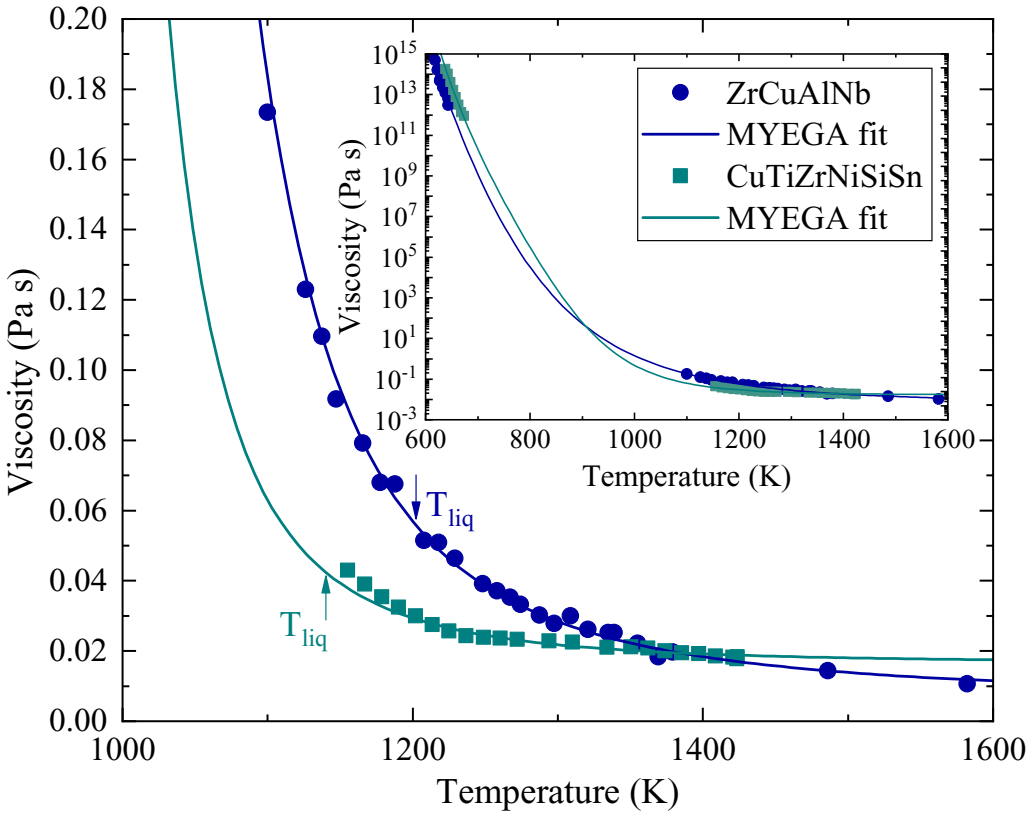

Fig. 5.8.: Viscosity as a function of temperature for the $Cu_{47}Ti_{33}Zr_{11}Ni_6Si_1Sn_2$ and $Zr_{59.3}Cu_{28.8}Al_{10.4}Nb_{1.5}$ glass-forming alloys. The experimental data were fitted with the Mauro-Yue-Ellison-Gupta-Allan (MYEGA) model [209, 210]. The viscosity data for both glass-forming alloys were measured with three-point beam bending at the glass transition temperature. The viscosity data for $Zr_{59.3}Cu_{28.8}Al_{10.4}Nb_{1.5}$ taken from Ref. [204] were measured using electrostatic levitation, whereas the viscosity for the $Cu_{47}Ti_{33}Zr_{11}Ni_6Si_1Sn_2$ glass-forming alloy was measured via couette rheometry. The figure inset shows the viscosity data from the glass transition temperature to the liquidus temperature. The experimental viscosity data and subsequent evaluation were provided by Lehrstuhl für Metallische Werkstoffe, Universität des Saarlandes, Germany.

The viscosity of the ZrCuAlNb glass-forming alloy was ∼ 30 % higher compared to the CuTiZrNiSiSn glass-forming alloy at liquidus temperature. The viscosity values converged when passing through the supercooled liquid region, leading to a higher viscosity for the CuTiZrNiSiSn glass-forming alloy (the intersection occurred at ∼ 908 K). A second intersection point was detected at ∼ 1385 K where the viscosity of the ZrCuAlNb glass-forming alloy decreased to lower values than that of the CuTiZrNiSiSn glass-forming alloy. The data suggested that droplet formation was mainly affected by viscosity in a narrow temperature range around the liquidus temperature. An increased melt superheat temperature decreased liquid viscosity, resulting in a higher number of spherical droplets as seen in Fig. 5.7. It was assumed that the solidification and

atomization zones were de-coupled, meaning that droplets had more time to spheroidize before solidification was complete (Fig. 5.9).

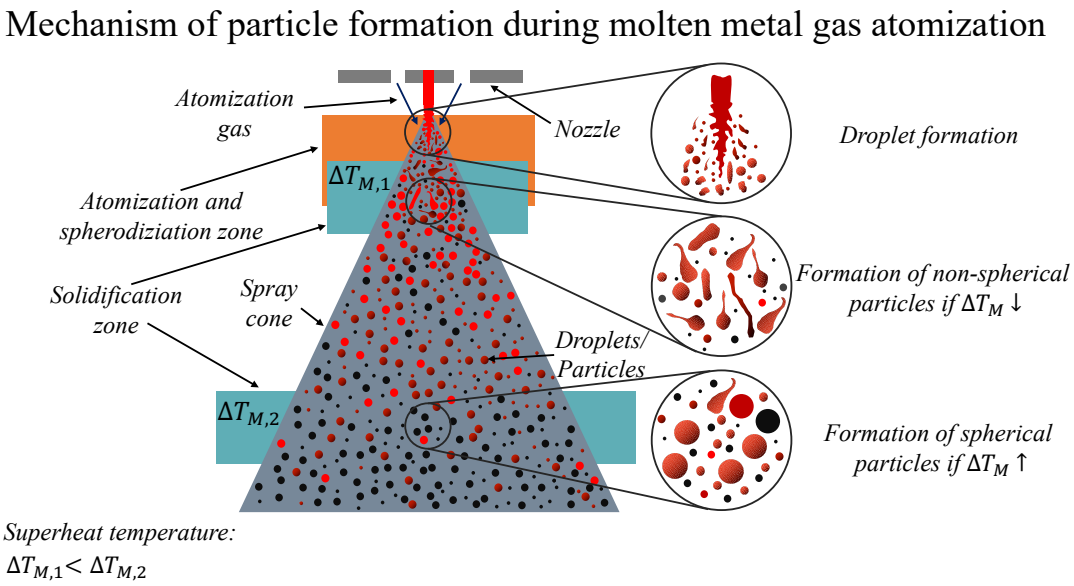

Fig. 5.9.: Phenomenological model describing droplet formation and solidification considering different melt superheat temperatures for the atomization of glass-forming alloys. An increased melt superheat temperature ($\Delta T_{M,2}$) shifted droplet solidification to a later time and decoupled the solidification as well as spheroidization zones, and thus spherical droplets were formed.

5.1.5. Conclusion of melt superheat temperature as a cooling strategy

The effect of an increased melt superheat temperature on amorphous fraction and particle shape are summarized as follows:

- The amorphous fraction of the two soft ferromagnetic glass-forming alloys ($\{(Fe_{0.6}Co_{0.4})_{0.75}B_{0.2}Si_{0.05}\}_{96}Nb_4$ and $Fe_{76}B_{10}Si_9P_5$) slightly increased with melt superheat temperature. The impact was relatively small when compared with literature in which containerless droplet techniques with high purity feedstock were used instead.
- The particle size was nearly unaffected by the melt superheat temperature. This effect was partially in agreement with literature studies where some reported a decrease in particle size, while other studies showed that particle size was independent of the melt superheat temperature used.
- A higher number of spherical particles were produced when increasing the melt superheat temperature as the liquid viscosity decreased. The particle shape study was extended to two additional glass-forming alloys ($Cu_{47}Ti_{33}Zr_{11}Ni_6Si_1Sn_2$, and $Zr_{59.3}Cu_{28.8}Al_{10.4}Nb_{1.5}$). The ZrCuAlNb glass-forming alloy showed the highest number of irregular particles due to the high viscosity at liquidus temperature.

5.2. Hot gas atomization

The hypothesis was to demonstrate if hot gas atomization provides smaller particles that lead to a higher cooling rate and thus to a higher amorphous powder yield. A higher amorphous yield is required for a few powder metallurgy techniques such as sintering and Molten Injection Molding etc. The effect of elevated gas temperatures on the final microstructure has yet to be investigated, as an increase in gas temperature may result in crystalline particles although smaller particles are produced.

5.2.1. Gas mass flow rate and aspiration pressure

Fig. 5.10 shows the gas mass flow rate as a function of atomization pressure for close-coupled atomization (CD-CCA-0.8). Measured gas flow rates were compared with calculated gas mass flow rates. The theoretical calculation of the gas mass flow rate $\dot{m}_{G,theo}$ required simplifications in order to estimate gas consumption. For this purpose, the atomization system was assumed to be a vessel at constant pressure and the orifice cross-section was treated as an annular gas nozzle [39]. Considering isentropic conditions, the theoretical gas mass flow rate was calculated with the following equation:

$$\dot{m}_{G,theo} = A_n \cdot \Psi_{max} \cdot \sqrt{2 \cdot \rho_g \cdot p} \quad \text{for} \quad p_i > p_{crit}, \tag{5.1}$$

where A_n represents the area of flow and the parameters Ψ_{max}, ρ_g, and p describe the outflow function, gas density, and atomization pressure. The parameter Ψ_{max} corresponds to p_{crit}, which is a function of the isentropic exponent κ ($\Psi_{max} = 0.514$ for argon). For instance, irrecoverable losses associated with gas consumption are expressed in the discharge coefficient C_d, which is the ratio of the experimentally determined gas mass flow rate $\dot{m}_{G,exp}$ to the theoretically calculated gas mass flow rate $\dot{m}_{G,theo}$:

$$\dot{m}_{G,exp} = C_d \cdot \dot{m}_{G,theo}, \tag{5.2}$$

An increasing linear relationship between atomization pressure and gas mass flow rate is shown in the upper plot of Fig. 5.10, where a higher atomization pressure resulted in an increased gas mass flow rate. Hot gas atomization resulted in lower gas consumption than in atomization at ambient temperature, caused by the lower gas density. The gas density depends on temperature. For instance, gas consumption decreased by one third for a typical atomization pressure of 1.6 MPa using hot gas atomization, demonstrating that hot gas atomization is a valuable tool to reduce gas consumption. Atomization at elevated gas temperatures require a higher energy consumption that need to be considered for commercial viability. The solid line in the upper plot of Fig. 5.10 represents the calculated values describing ideal isentropic flow conditions without disturbances. The individual C_d values were averaged over the entire atomization range, resulting in discharge coefficients of $C_{d,RT} = 0.88$ and $C_{d,HG} = 0.84$. The C_D values account for influences such as inertial forces and viscosity that affect the gas mass flow rate. According to these C_d values, it appeared that gas

outflow was unaffected by elevated gas temperatures.

The lower figure shows the aspiration pressure as a function of atomization pressure (Fig. 5.10). Hot gas and ambient temperature atomization were both stable over the entire aspiration pressure range as exhibited in the negative pressure values. Atomization under hot gas conditions provided a slightly higher aspiration pressure that was above 1.5 MPa. This enhanced the stability of the melt mass flow rate, as 1.6 MPa was used for our convergent-divergent close-coupled atomizer (CD-CCA-0.8). A higher aspiration pressure generally resulted in a higher melt mass flow rate that changed the GMR. The measured aspiration pressures for argon gas were in agreement with the measured nitrogen aspiration pressures presented by Schwenck et al. [135], demonstrating that the melt mass flow rate for nitrogen gas also increased using hot gas atomization.

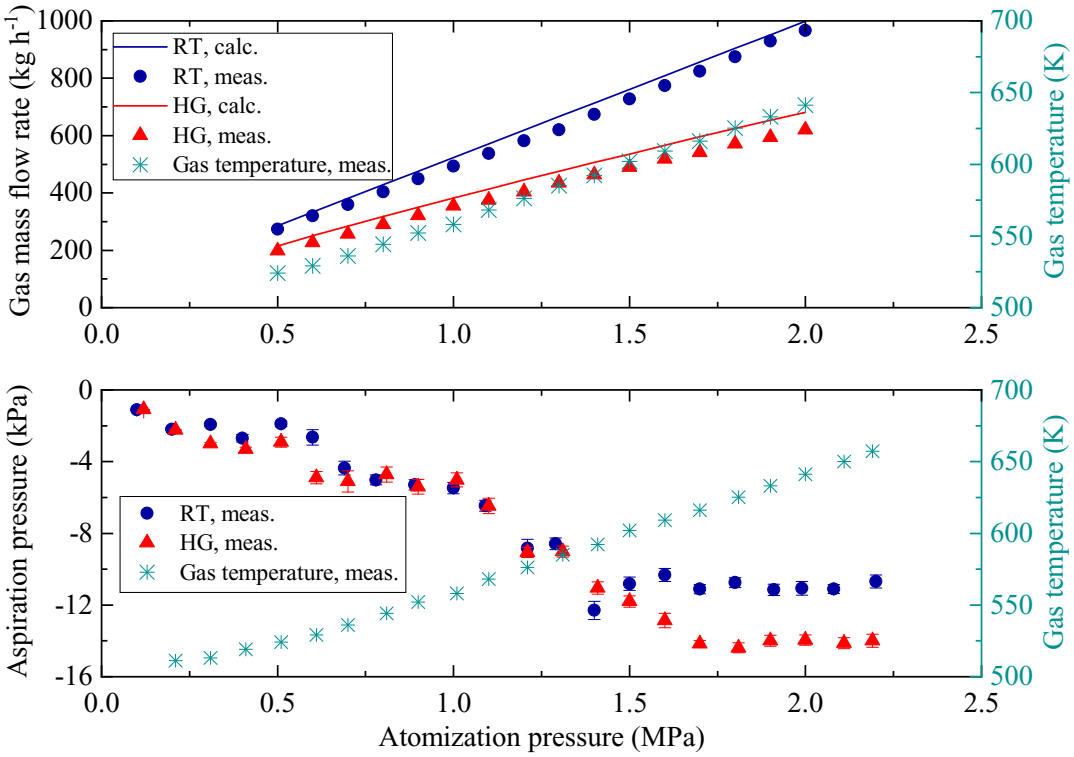

Fig. 5.10.: The upper figure shows the gas mass flow rate $\dot{m}_G$ as a function of atomization pressure (relative pressure p_u). HG and RT stand for hot gas atomization and atomization at ambient temperature. Measured (meas.) and calculated (calc.) gas mass flow rates at ambient temperature were compared with gas mass flow rates at elevated gas temperatures. Argon was used as the process gas. The theoretical gas mass flow rate was calculated according to Eq. 5.1. Gas temperatures were also plotted. The lower figure presents aspiration pressure p_{asp} as a function of atomization pressure. The investigated convergent-divergent (CD-CCA-0.8) nozzle has an outlet section area A_n of 4.52 × 10^{-5} m^2. Reprinted and modified in part from Ref. [39] with permission from Elsevier B.V.

5.2.2. Particle size analyses

The hypothesis was to investigate if hot gas atomization provides smaller particles. It was assumed that elevated gas temperatures introduce a higher kinetic energy as a result of the higher sound velocity $c = \sqrt{\kappa \cdot R_s \cdot T_G}$, where κ is the isentropic exponent, R_s is the specific gas constant, and T_G is the gas temperature.

The cumulative mass distributions Q_3 for FeCoBSiNb powders are presented in Fig. 5.11. The data show the influence of GMR and elevated gas temperatures on the particle size.

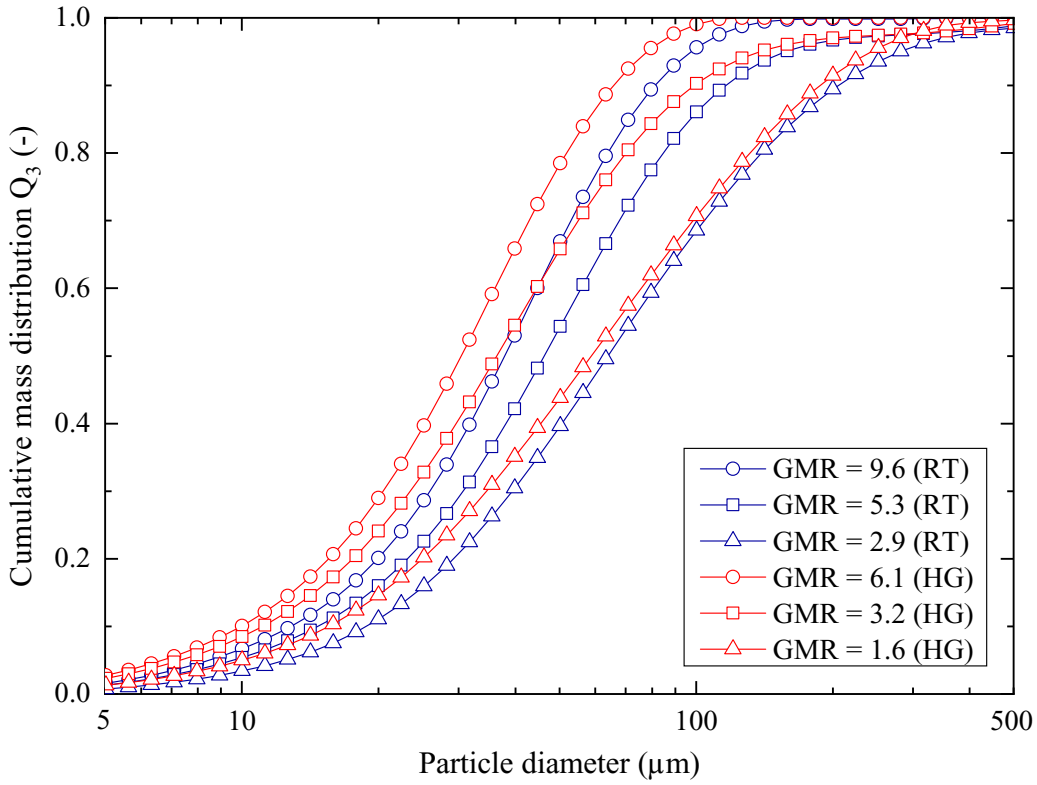

Fig. 5.11.: Cumulative mass distributions (Q_3) for $\{(Fe_{0.6}Co_{0.4})_{0.75}B_{0.2}Si_{0.05}\}_{96}Nb_4$ powders atomized using hot gas (HG) and ambient temperature atomization (RT). A higher gas-to-melt mass flow ratio (GMR) and hot gas atomization resulted in finer powders.

An increase in GMR resulted in smaller particles, which was consistent with present literature. Altering the melt mass flow rate changed the GMR while the gas flow rate was kept constant. Hot gas atomization led to smaller particles, supporting the hypothesis that elevated gas temperatures result in finer powders. These findings were in agreement with other in-house studies where Cu-6wt%Sn [211] and Cu-15.5wt% Sn [135] crystalline alloys were atomized using hot gas atomization. Both studies showed that elevated gas temperatures decreased particle size. The relationship between particle size and cooling rate as well other process parameters is explored extensively in sec. 5.3. Hot gas atomization produced smaller particles through a higher gas velocity that is caused

by a higher sound velocity. The sound velocity can be altered using different atomization gases. For instance, helium gas has a sound velocity 2.5 times higher than nitrogen, resulting in an increased gas velocity and thus yielding in finer particles. The mass median particle diameter $d_{50,3}$ is inversely proportional to the gas velocity ($d_{50,3} \sim 1/u_g$) [212].

A decrease in particle size can be seen when considering the mass median particle diameter as a function of melt mass flow rate or GMR (Fig. 5.12).

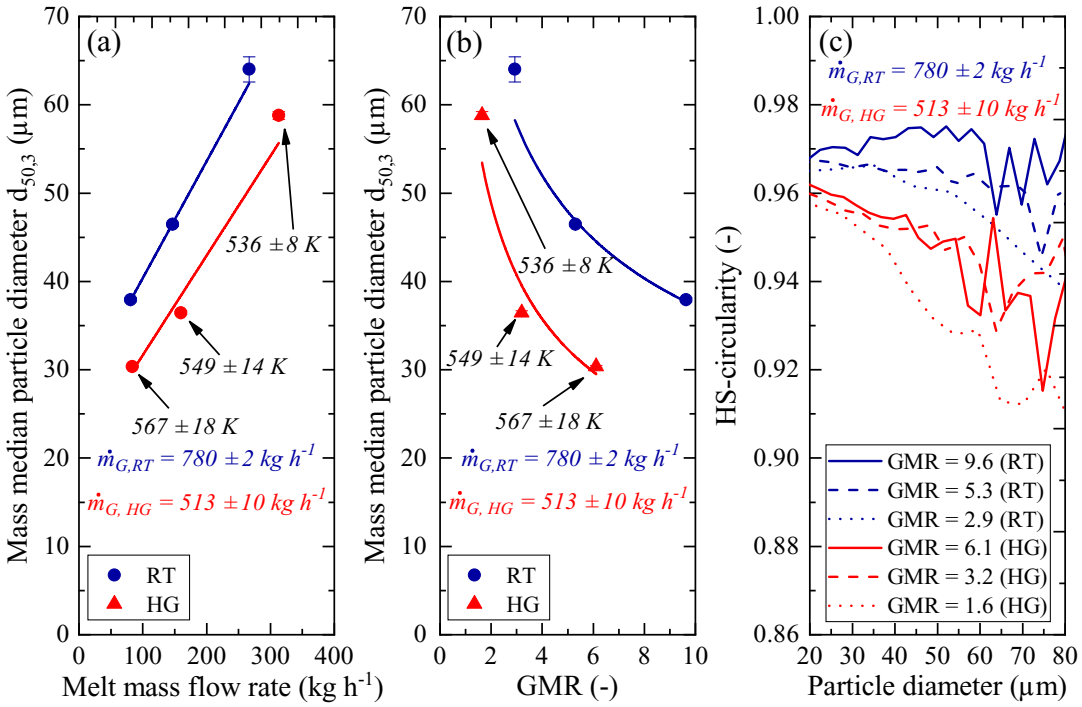

Fig. 5.12.: The mass median particle diameter $d_{50,3}$ of $\{(Fe_{0.6}Co_{0.4})_{0.75}B_{0.2}Si_{0.05}\}_{96}Nb_4$ powders as a function of (a) melt mass flow rate $\dot{m}_L$ as well as (b) gas-to-melt mass flow ratio (GMR). The averaged hot gas temperatures and gas mass flow rates are also listed. The lines serve only as visual guides. An increased GMR and gas temperature resulted in smaller $d_{50,3}$ values. (c) Compared to atomization at ambient temperature, hot gas atomization decreased the circularity of the powders due to smaller droplets that attached to semi-solidified droplets (satellites). Reprinted and modified in part from Ref. [39] with permission from Elsevier B.V.

At a constant gas mass flow rate, increasing the melt mass flow rate resulted in an increased GMR and thus in a decreased mass median particle diameter. Present literature and additional in-house studies for Cu-6wt%Sn [211] and Cu-15.5wt%Sn [135] crystalline alloys were consistent with these results. Analogous to the melt mass flow rate and GMR, elevated gas temperatures resulted in significantly smaller mass median particle diameters, demonstrating that hot gas atomization is a promising design tool for the production of smaller particles required for various powder consolidation techniques.

A higher amount of small, solidified particles that attached to partially or

fully liquid molten droplets (satellites) during gas atomization increased the frequency of non-spherical particles. This may reduce powder flowability and packing density of the powder. To improve powder flowability, Mostaghimi et al. recently reported an anti-satellite system using a tangential and secondary gas to reduce particle re-circulation into the dense atomization area [213]. They reported that the particle re-circulation of small, solidified droplets resulted in a higher frequency of particle collisions. This resulted in increased particle deformation and satellite formation. Preliminary results have shown that the anti-satellite system improved the particle shape although gas consumption increased.

5.2.3. Determination of amorphous fraction

The impact of GMR and gas temperature on cooling rate and thus on amorphous fraction was qualitatively investigated using XRD analyses. Fig. 5.13a and Fig. 5.13b show XRD traces as a function of GMR atomized at ambient and elevated gas temperatures for two different particle size classes (45 - 63 µm and 63 - 90 µm). For a size class of 45 - 63 µm, particles atomized at ambient temperature showed broad amorphous halos for all GMR values. A small crystalline peak was observed for particles in a size class of 63 - 90 µm atomized at ambient temperature and with a GMR of 2.9, suggesting that these particles were partially-crystalline. A quantitative description of the influence of GMR on the cooling rate is given in sec. 5.3.4. The particles atomized at elevated gas temperatures showed less pronounced amorphous halos except for at the highest GMR, suggesting that hot gas atomization slightly decreased the cooling rate and thus the amorphous fraction. The highest GMR resulted in similar XRD traces as seen in atomization at ambient temperature, demonstrating that the cooling rate and the amorphous fraction were similar. An increased GMR resulted in a more pronounced amorphous halo, concluding that the GMR may have increased the cooling rate and the amorphous fraction.

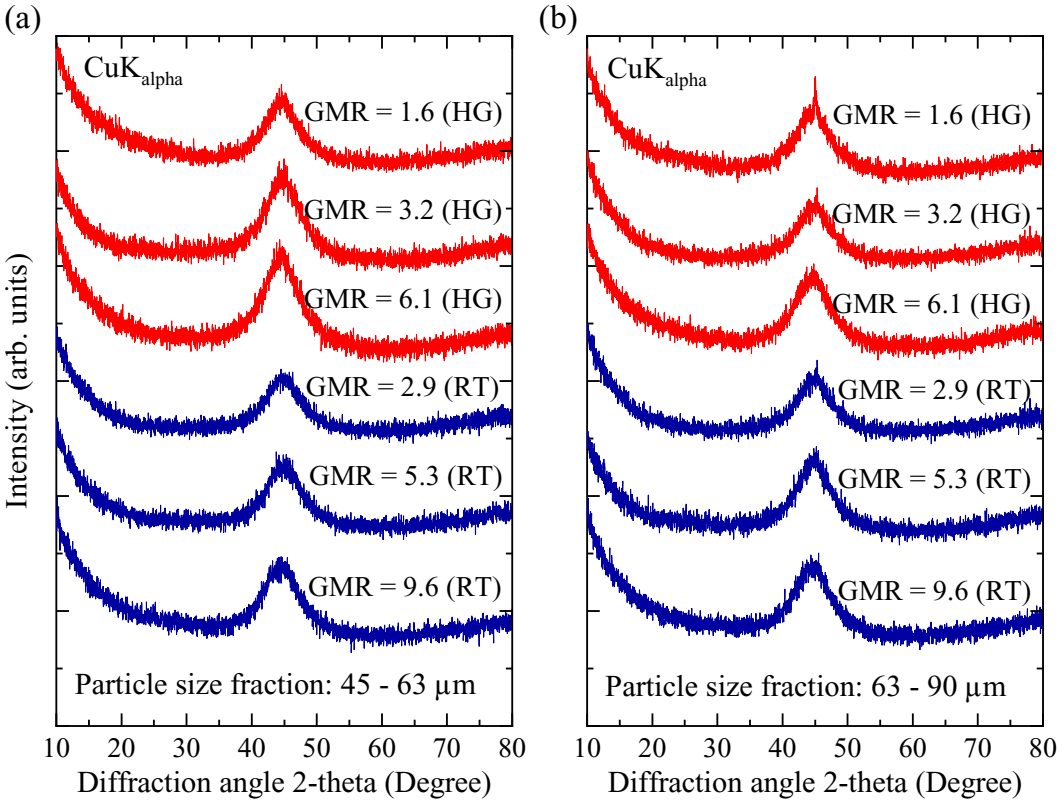

Fig. 5.13.: XRD traces are shown as a function of gas-to-melt mass flow ratio (GMR) for $\{(Fe_{0.6}Co_{0.4})_{0.75}B_{0.2}Si_{0.05}\}_{96}Nb_4$ powders that were atomized at ambient temperature (RT) and at elevated gas temperatures (HG). To investigate the effect of GMR and elevated gas temperatures on powder microstructure, two different particle size classes were considered. Broad amorphous halos were obtained for most powders atomized at RT, while some small crystalline peaks were detected for powders atomized at HG, concluding that hot gas atomization slightly decreased the cooling rate and thus the amorphous fraction. In addition, a decreased GMR resulted in small crystalline peaks, concluding that the cooling rate and the amorphous fraction decreased. Reprinted from Ref. [39] with permission from Elsevier B.V.

The largest GMR values (RT = 9.6 and HG = 6.1) from Fig.5.13a and Fig.5.13b were plotted as a function of particle size class in Fig. 5.14a. Particles atomized under ambient temperature conditions were fully amorphous up to a particle size class of 63 - 90 µm. Particles > 90 µm showed some minor crystalline peaks, suggesting that the particles were partially-amorphous due to the lower cooling rate during gas atomization. Minor crystalline peaks were already detected for a particle size class of 63 - 90 µm at elevated gas temperatures. More pronounced peaks were detected in a particle size class of 90 - 125 µm when compared with particles atomized at ambient temperature. These findings concluded that cooling rate and thus amorphous fraction slightly decreased using hot gas atomization. DSC measurements in Fig. 5.14b were performed on the same particle size classes. The measured enthalpy of crystallization confirmed

the XRD observations. The enthalpy of crystallization decreased with an increased particle size. DSC curves for a particle size class of 63 - 90 µm qualitatively agreed with the reference powder that was confirmed to be amorphous using different characterization techniques [25]. The amorphous fraction of the reference powder was then determined to be 100% from the measured enthalpy of crystallization. The enthalpy of crystallization for different particle size classes were measured and divided by the enthalpy of crystallization of the reference powder $\left(\Delta H_x/\Delta H_{x,ref}\right)$, leading to the amorphous fraction for each particle size class.

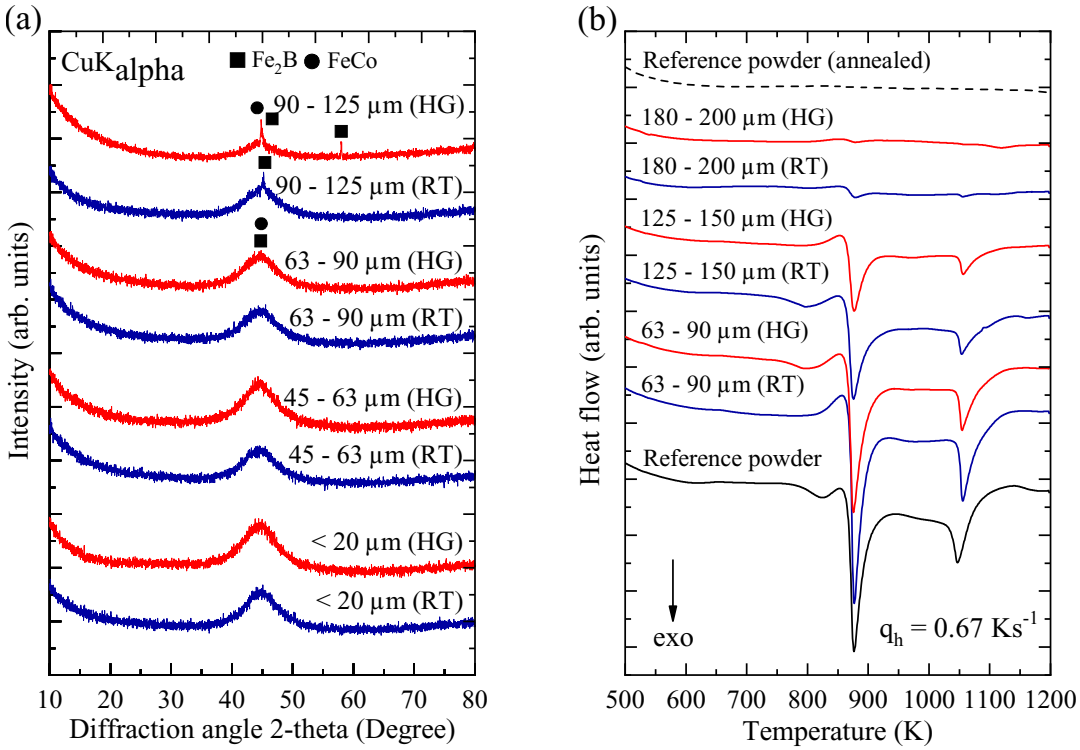

Fig. 5.14.: $\{(Fe_{0.6}Co_{0.4})_{0.75}B_{0.2}Si_{0.05}\}_{96}Nb_4$ powders for a given GMR (RT = 9.6 and HG = 6.1) were analyzed using (a) XRD and (b) DSC. The powders atomized at ambient temperature (RT) were fully amorphous up to 90 µm, whereas crystalline peaks were observed for particles atomized under hot gas atomization (HG) for the same particle size class. This concluded that hot gas atomization had only a small effect on cooling rate. Increasing the particle size resulted in lower enthalpy of crystallization values that confirmed XRD results. A fully amorphous reference powder [25] was plotted for comparison. Reprinted from Ref. [39] with permission from Elsevier B.V.

Fig. 5.15 shows the calculated amorphous fraction determined from the enthalpy of crystallization as a function of mean particle diameter from corresponding particle size classes. Particles atomized at ambient temperature were fully amorphous up to 90 µm, confirming XRD results in Fig. 5.14. Particles atomized at elevated gas temperatures were fully amorphous up to 63 µm only for the highest GMR (HG = 6.1) while lower GMR values resulted in lower amor-

phous fractions. The influence of elevated gas temperatures on cooling rate and amorphous fraction was very small, since comparable GMR values of 2.9 (RT) and 3.2 (HG) yielded similar amorphous fractions.

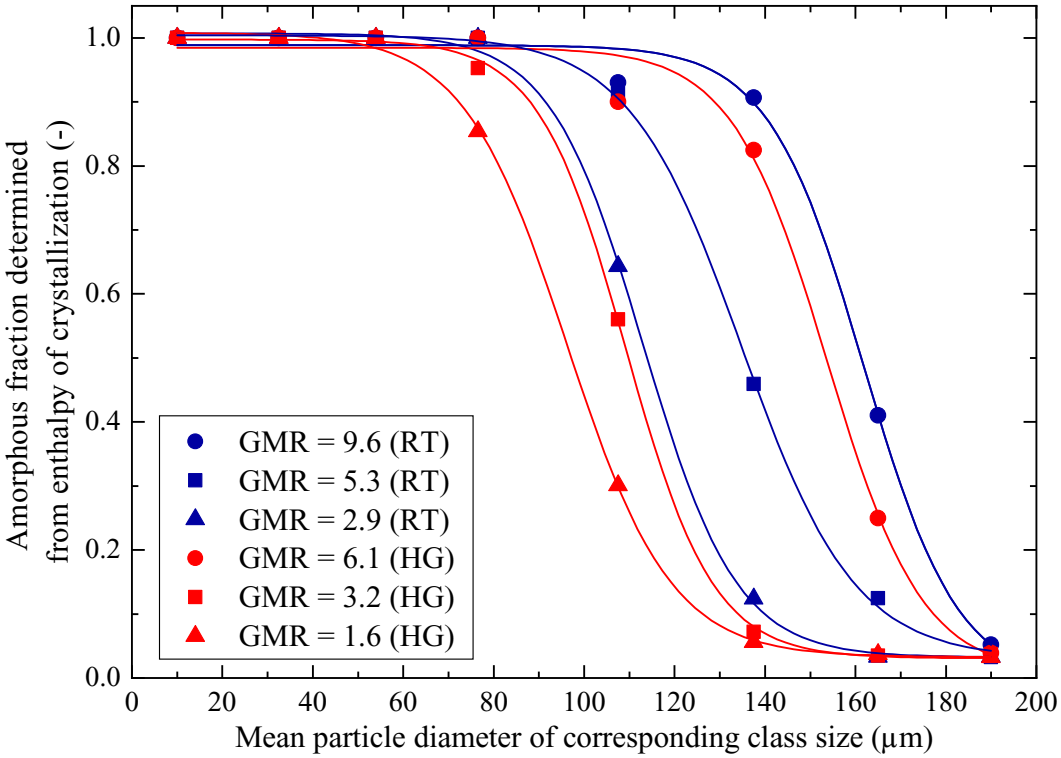

Fig. 5.15.: Amorphous fraction as a function of corresponding particle size classes for $\{(Fe_{0.6}Co_{0.4})_{0.75}B_{0.2}Si_{0.05}\}_{96}Nb_4$ powder. The influence of hot gas atomization as well as gas-to-melt mass flow ratio (GMR) was investigated. Reprinted from Ref. [39] with permission from Elsevier B.V.

The effect of elevated gas temperatures on cooling rate and amorphous fraction was determined from the experimental data presented in Fig. 5.15. An application-oriented graph was plotted to show the relationship between amorphous fraction and cooling rate based on particle diameter and how it can be changed by considering different GMR values as well as elevated gas temperatures (Fig. 5.16). Three different cases of amorphous fractions were considered that may be applicable in different industrial applications [39]:

(i) 5% amorphous fraction,

(ii) 50% amorphous fraction,

(iii) 95% amorphous fraction.

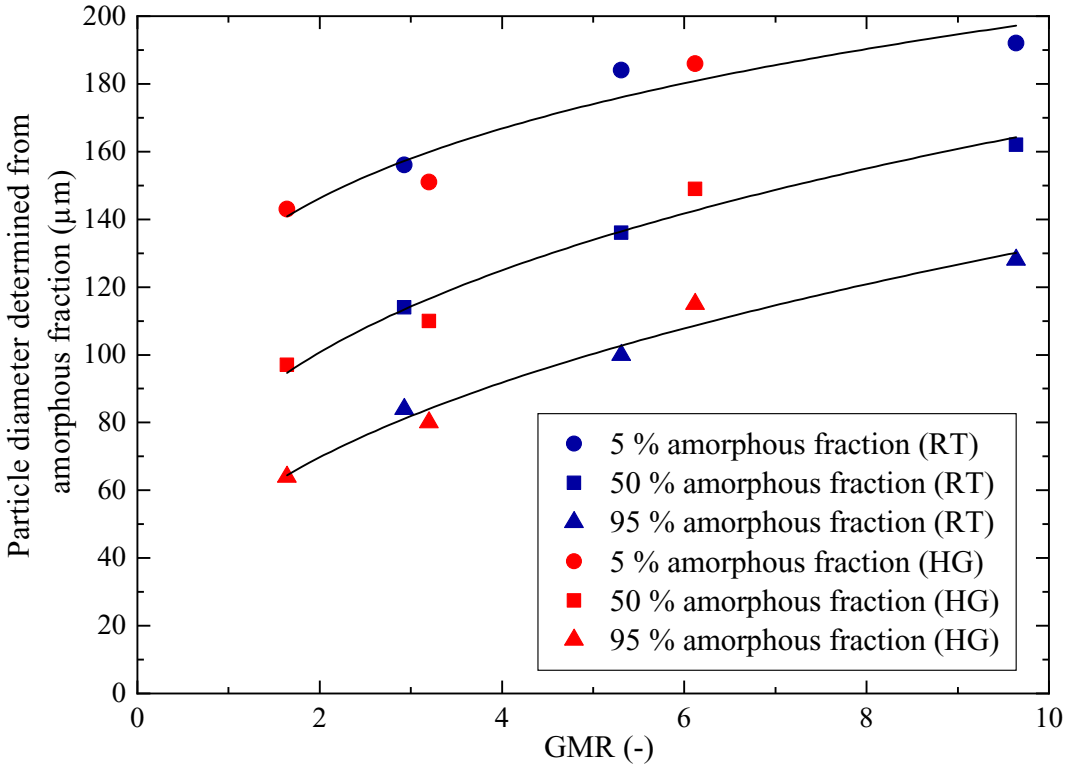

Fig. 5.16.: Particle diameter correlated to amorphous fraction as a function of gas-to-melt mass flow ratio (GMR) for the $\{(Fe_{0.6}Co_{0.4})_{0.75}B_{0.2}Si_{0.05}\}_{96}Nb_4$ powder. Three different cases of amorphous fractions are plotted that have industrial relevance. The lines serve only as visual guides. Reprinted from Ref. [39] with permission from Elsevier B.V.

5.2.4. Calculating the amorphous yield

The following Eq. 5.3 allows for the calculation of amorphous yield from the data in Fig. 5.15 and Fig. 5.11:

$$\sum_{i=1}^{n} \Delta Q_{3_i} \cdot AF_i. \tag{5.3}$$

This equation represents the amorphous fraction (AF) and the accumulated mass distribution of each particle size class (ΔQ_3). Applying Eq. 5.3 resulted in the amorphous yield of each individual particle size class that are represented by variable i. The sum of all individual particle size classes resulted in the final amorphous yield as a function of GMR (Fig. 5.17). Two effects can be observed: an increased GMR and elevated gas temperatures resulted in a higher amorphous yield.

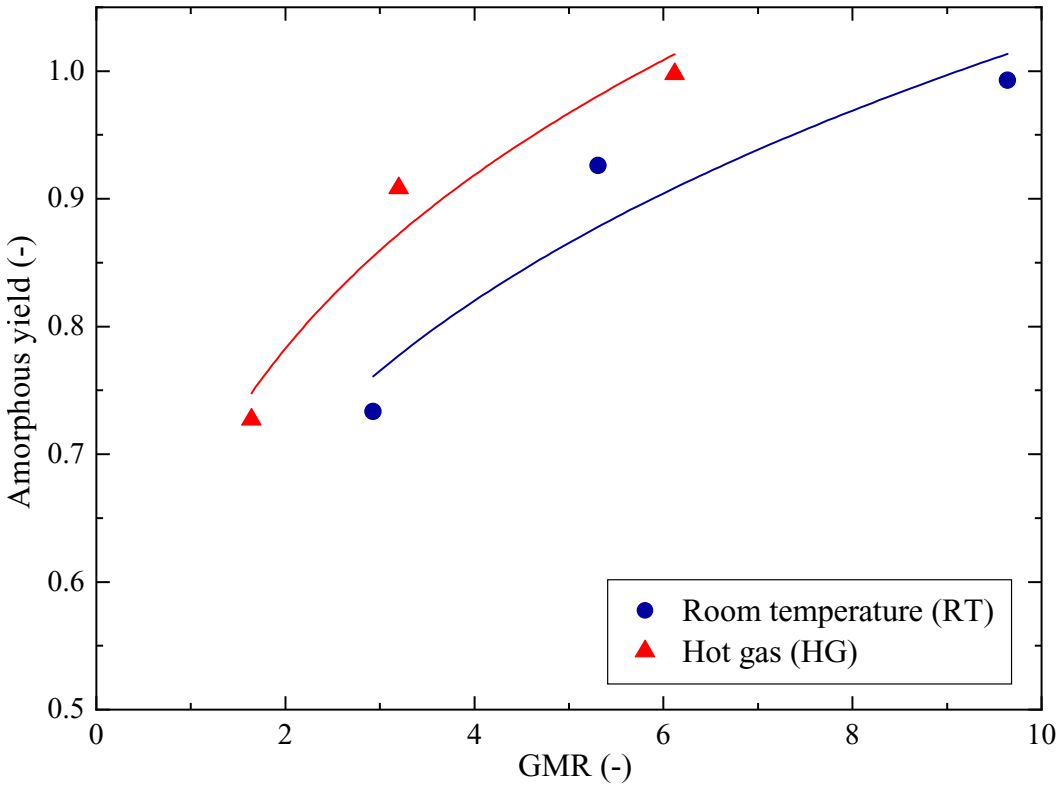

Fig. 5.17.: Amorphous yield as a function of gas-to-melt mass flow ratio (GMR) for $\{(Fe_{0.6}Co_{0.4})_{0.75}B_{0.2}Si_{0.05}\}_{96}Nb_4$ powder. The lines serve only as visual guides. The influence of gas temperature on the amorphous yield was investigated. Reprinted from Ref. [39] with permission from Elsevier B.V.

5.2.5. The influence of hot gas on cooling rate

Experimental results have shown that the amorphous fraction was nearly unaffected using hot gas atomization, suggesting that hot gas atomization had a negligible effect on cooling rate. In order to understand the physical mechanisms of why hot gas atomization provided nearly the same cooling rate as in atomization at ambient temperature, a simplified one-dimensional model was used (described in sec. 3.2.2). Developed in MathWorks MATLAB R2019b, it predicts the gas, droplet and relative velocity as well as the gas temperature, Nusselt number, heat transfer coefficient, and droplet cooling history as a function of atomization time t and distance z_d. Due to the lack of thermophysical properties for the two soft ferromagnetic glass-forming alloys, a Cu-6wt%Sn crystalline alloy was used to demonstrate the effect of elevated gas temperatures on droplet solidification. The thermophysical properties of the melt droplets and cooling gas are listed in Appendix B. This alloy can also be compared to experimental cooling rate correlations in sec. 5.3.4. The model is based on the following assumptions and simplifications:

- The model simulates the cooling of a single particle under an argon atmosphere that is traveling along the center axis of the spray chamber.

- The droplets have an initial velocity of 1 $\mathrm{m\,s^{-1}}$ at a starting position of 0.12 m below the nozzle tip.
- The gas velocities for both temperature cases were calculated with a two-dimensional model in Comsol Multiphysics 5.3a at an atomization pressure of 1.6 MPa with a corresponding gas mass flow rate of 691 $\mathrm{kg\,h^{-1}}$. These values were in good agreement with gas velocity measurements [191]. Gas velocity fit functions were computed in a two-dimensional simulation for both temperature cases and are as follows:

$$v_{g_{RT}} = 354771(1000z_d)^{-1.385}, \tag{5.4a}$$
$$v_{g_{HG}} = 23.159(z_d)^{-1.584}. \tag{5.4b}$$

- Gas temperature was calculated according to Grant [156] using the following equation:

$$T_G = T_{G,f} - \left(T_{G,f} - T_{G,i}\right) \cdot exp\left(-\frac{z_d}{\lambda_T}\right). \tag{5.5}$$

  where $T_{G,f}$ and $T_{G,i}$ are the final and initial gas temperatures, z_d is the position along the center axis, and λ_T is a constant in molten metal gas atomization assumed to be 0.1 [156]. The initial hot gas temperature was set to 573 K, while the ambient gas temperature was set to 298 K. The final gas temperature was assumed to be 350 K for both cases. In the case of atomization at ambient temperature, it was assumed that the molten droplets heated the surrounding gas over time (one-way thermal coupling).
- The melt superheat temperature was selected to be 350 K.
- Maximum radiation with an emissivity value of $\varepsilon = 1$ was assumed.
- Solidification under equilibrium conditions is calculated with apparent specific heat capacity $c_{p,apparent}$, while the respective solid and liquid specific heat capacities were used for a fully solid and a fully liquid droplet.

$$c_{p,Lat} = \frac{\Delta H_M}{T_{liq} - T_s}, \tag{5.6a}$$
$$c_{p,apparent} = c_{p,Lat} + \frac{c_{p,l} + c_{p,s}}{2}, \tag{5.6b}$$

  where ΔH_M is the latent heat of fusion, T_{liq} and T_s are the liquidus and solidus temperatures, while $c_{p,l}$ and $c_{p,s}$ are the specific heat capacities of the material in a liquid and solid state.

The gas, droplet, and relative velocity as well as the gas temperature for atomization at ambient temperature and hot gas atomization is shown in Fig.5.18.

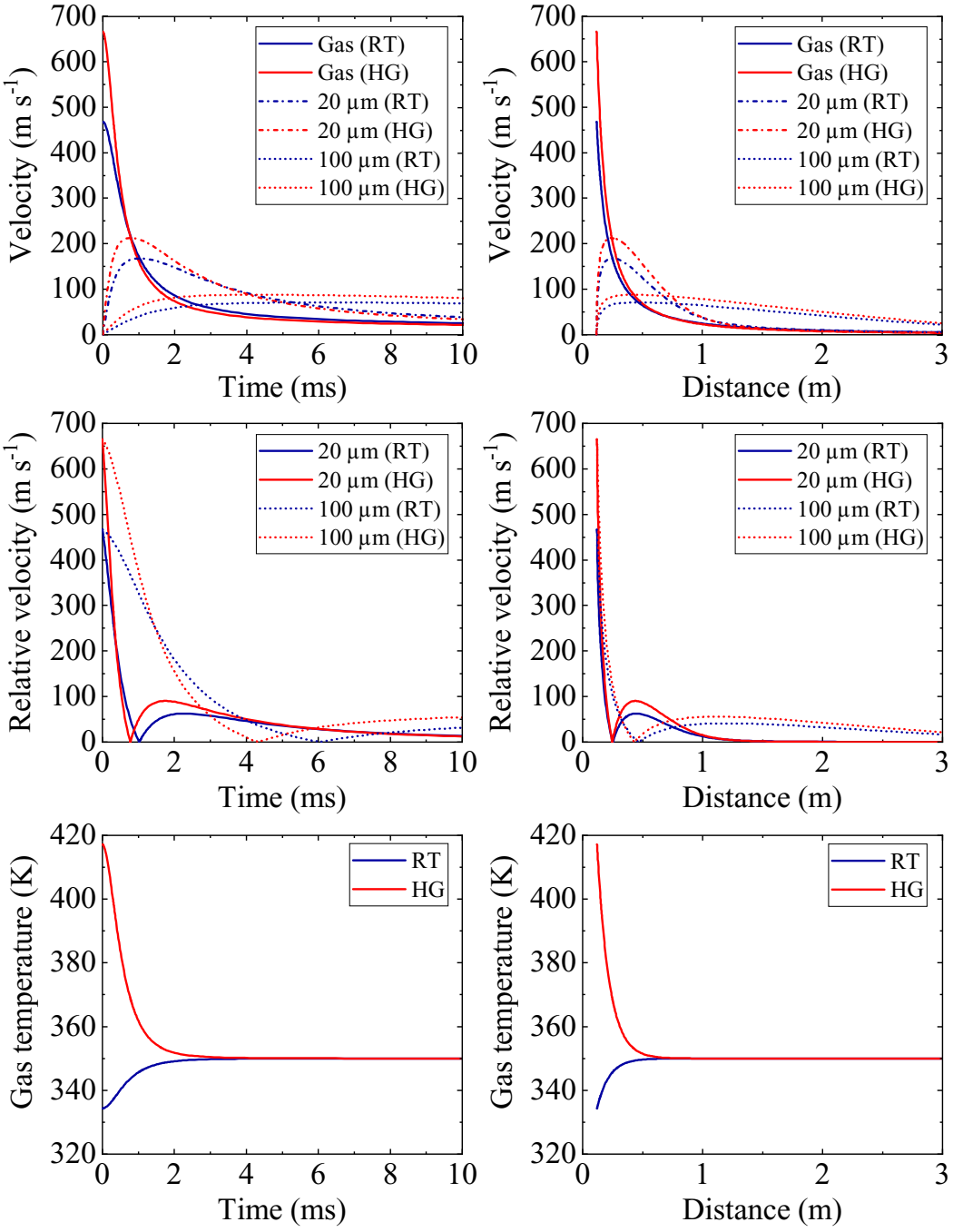

Fig. 5.18.: Gas, droplet and relative velocity as well as gas temperature as a function of atomization time and distance for 20 µm and 100 µm Cu-6wt%Sn droplets. The abbreviations HG and RT stand for hot gas atomization (573 K) and atomization at ambient temperature (298 K). Gas, droplet, and relative velocities were calculated with the equations in sec. 3.2.2. Argon was selected as the cooling gas. An initial droplet velocity of 1 $m\,s^{-1}$, a droplet starting position of 0.12 m with maximum radiation (emissivity $\varepsilon = 1$) and a superheat temperature of 350 K was assumed. The gas temperature was calculated with Eq. 5.5. Model details can be found in [156, 172].

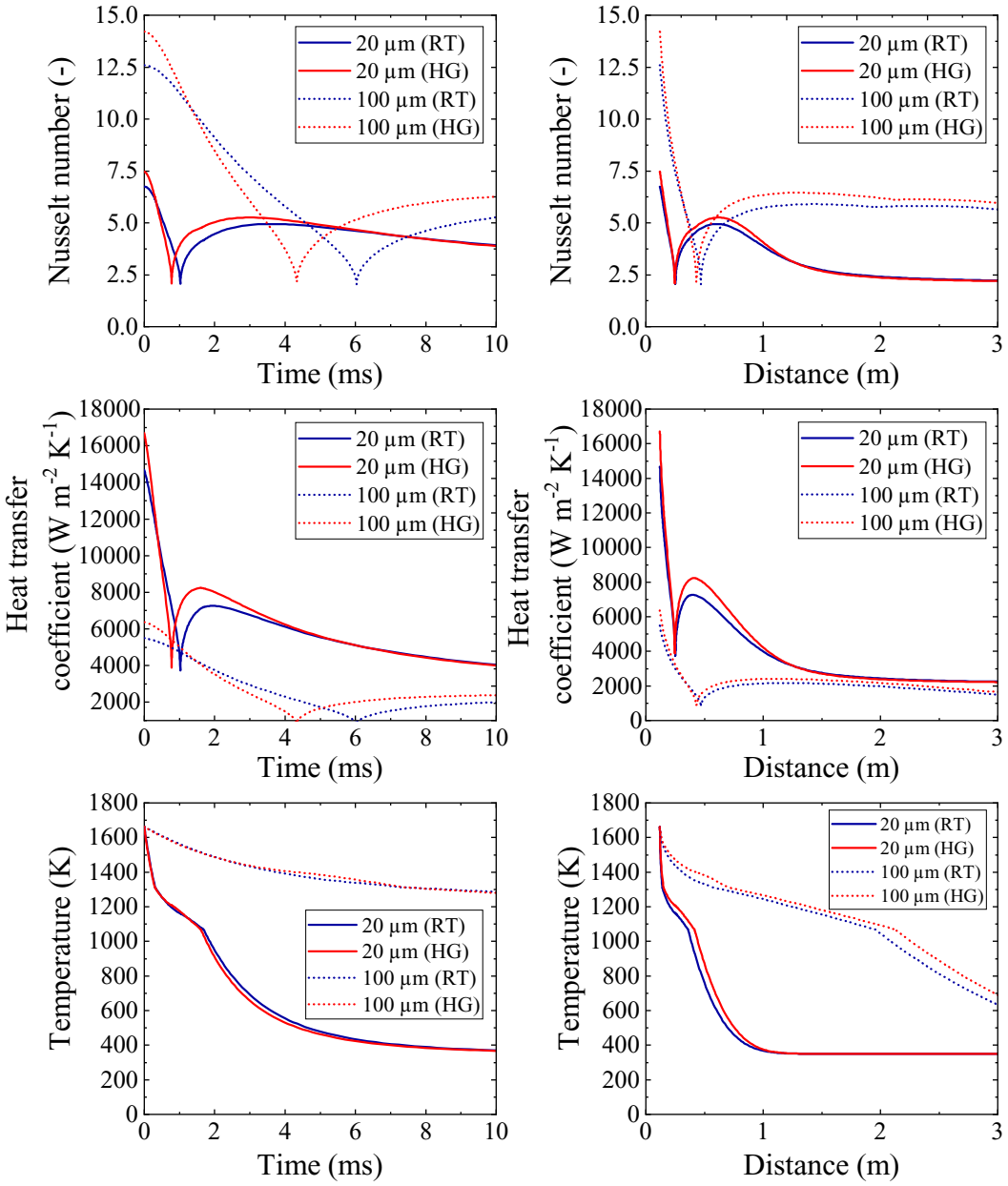

Fig. 5.19.: Nusselt number, heat transfer coefficient and droplet temperature as a function of atomization time and distance for 20 µm and 100 µm Cu-6wt%Sn droplets. The abbreviations HG and RT stand for hot gas atomization (573 K) and atomization at ambient temperature (298 K). The values were calculated with the equations presented in sec. 3.2.2. Argon was used as the cooling gas. An initial droplet velocity of 1 m s^{-1}, a droplet starting position of 0.12 m with maximum radiation (emissivity $\varepsilon = 1$) and a superheat temperature of 350 K was assumed. The apparent specific heat capacity approach was used to model the droplet solidification interval without undercooling, recalescence, and without segregated, eutectic, and peritectic solidification. Model details can be found in [156, 172].

Elevated gas temperatures resulted in higher gas and droplet velocities and therefore to higher relative velocities. This was in agreement with in-house studies where the particle velocity of AISI 52100 steel powders (particle size class: 63 - 90 µm) was experimentally measured using Laser Doppler Anemometry [214]. Compared to atomization at ambient temperature, Hussain et al. reported that the mean particle velocity at elevated temperatures was higher by a factor of ~ 1.6 with a gas mass flow rate of 150 $\mathrm{kg\,h^{-1}}$.

In the case of hot gas atomization, the gas temperature decreased exponentially and reached the final temperature after ~ 2 ms. The gas temperature for atomization at ambient temperature increased exponentially until the final temperature was reached after ~ 2 ms. This is due to the assumption that the molten metal droplets heat the gas over time through one-way thermal coupling.

The Nusselt number and the heat transfer coefficient depend on relative velocity as seen in Eq.3.12. Hence, an increased relative velocity resulted in higher Nusselt numbers and heat transfer coefficients as shown in the case of elevated gas temperatures (Fig. 5.19). According to the model, hot gas atomization resulted in similiar droplet cooling due to the high relative velocity. The average cooling rate $CR = \left(T_{liq} - T_s/\Delta t\right)$ as a function of particle size was calculated without undercooling, recalesence, as well as without segregated, eutectic, and peritectic solidification (Fig. 5.20). The calculated average cooling rates for hot gas atomization and atomization at ambient temperature deviated slightly from each other. Hot gas atomization provided slightly higher cooling rates than for atomization at ambient temperature. This was inconsistent with experimental findings as hot gas atomization provided a similiar or slightly lower cooling rate than for atomization at ambient temperature. Predicted average cooling rates were compared with a semi-empirical correlation for the Cu-6wt%Sn alloy (for correlation details, see sec. 5.3.2). The average cooling rates determined from the semi-empirical equation were lower by a factor of 2.8 to 4 depending on particle size. This is due to the simplified assumptions in the one-dimensional model, as the influence of GMR and two-way thermal coupling was neglected. Two or three-dimensional models would be a powerful tool to compute droplet cooling histories at different positions in the simulated gas stream. These models allow for particle tracing to determine droplet thermal history. A more realistic model would also consider heat exchange between the heated gas and the melt droplets (two-way thermal coupling). A two-dimensional two-way thermal coupling model was developed [191], but failed due to the complexity of solving non-linearities for an increased GMR in the defined equations with respect to momentum and heat exchange. Although the one-dimensional model relies on a few simplifications as stated in sec. 3.2.2, this type of model is commonly used in literature to predict droplet solidification in gas atomization [26, 156].

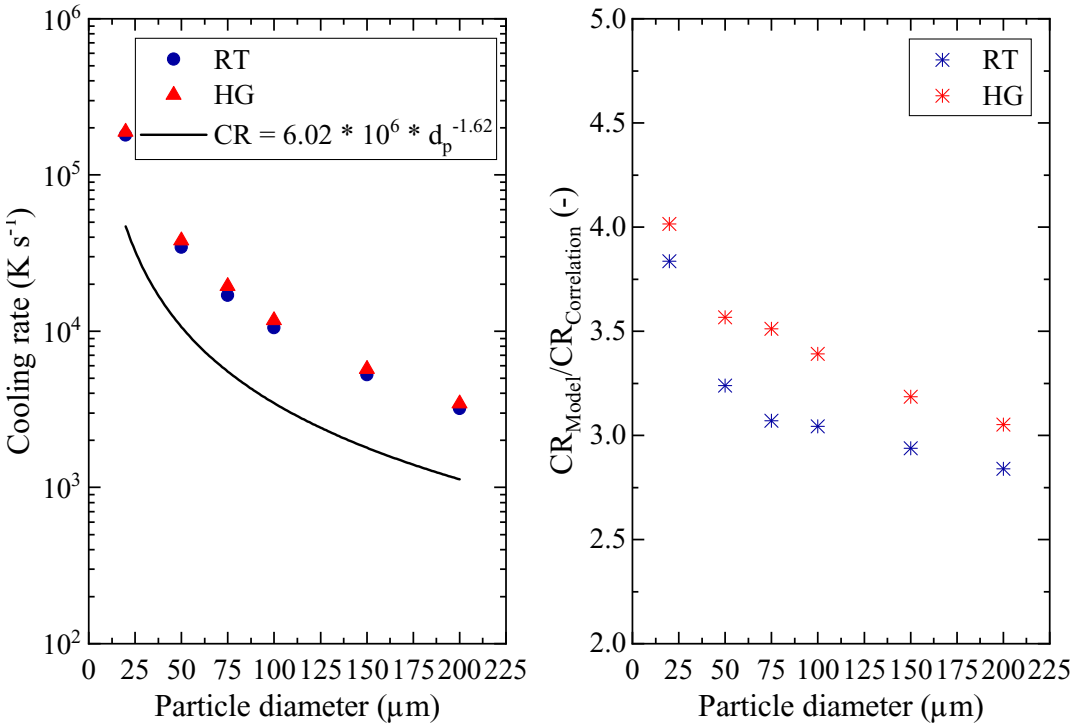

Fig. 5.20.: Average cooling rates as a function of particle size for a Cu-6wt%Sn binary crystalline alloy. The abbreviations HG and RT stand for hot gas atomization (573 K) and atomization at ambient temperature (298 K). The values were calculated with the equations presented in sec. 3.2.2. Argon was used as the cooling gas. An initial droplet velocity of 1 $m\,s^{-1}$, a droplet starting positon of 0.12 m with maximum radiation (emissivity $\varepsilon = 1$) and a melt superheat temperature of 350 K was assumed. The apparent specific heat capacity approach was used to model the droplet solidification interval without undercooling, recalesence, and without segregated, eutectic, and peritectic solidification. Model details can be found in [156, 172]. The predicted average cooling rates were compared with cooling rates derived from a semi-empirical correlation that has been presented in sec. 5.3.

5.2.6. Conclusion of hot gas atomization as a cooling strategy

Hot gas atomization is a promising design tool for the commercialization of fine, amorphous powders. The main findings can be summarized as follows:

- Hot gas atomization produced smaller particles, reduced gas consumption, nearly maintained the amorphous fraction and significantly increased the amorphous yield. However, particle shape factors slightly decreased due to the attachment of smaller droplets on larger semi-solidified droplets.
- Although hot gas atomization provided many advantages over conventional gas atomization, the cooling rate was unaffected or slightly de-

creased. This is due to changes in the relative velocity and in the temperature gradient between the cooling gas and melt droplets. An increased gas velocity affected the relative velocity and thus the heat transfer coefficent. Elevated gas temperatures resulted in a reduced temperature gradient between the melt droplets and the surrouding cooling gas. It is assumed that both effects compensated for each other, leading to a nearly unchanged cooling rate. This can be expressed by the general heat convection equation:

$$Q = h \cdot A_p \cdot \left(T_p - T_G\right), \tag{5.7}$$

where h is the heat transfer coefficient and A_p is the droplet surface area. T_p and T_G are the droplet and gas temperature, respectively. This compensation effect was seen in the XRD and DSC measurements where the amorphous fraction was nearly unchanged. These experimental findings were also confirmed by a one-dimensional droplet solidification model.

5.3. Cooling rate correlations during molten metal atomization

This section discusses cooling rate calculations and correlations for molten metal gas atomization, as the cooling rate is the determining factor for the microstructure of crystalline and amorphous powders. Cooling rates are generally estimated via analytical/numerical [155, 156, 163] and experimental [215, 216] approaches. The average cooling rate is typically correlated with droplet diameter through a power function:

$$CR\left(K\,s^{-1}\right) = a_0 \cdot d_p\,(\mu m)^{a_1}, \tag{5.8}$$

where a_0 is a pre-exponential factor describing the material/gas properties and a_1 is a constant taking droplet diameter into account [40]. A literature review regarding cooling rate correlations and their validity have been summarized for single droplet and molten metal gas atomization processes [40]. In the case of single droplets, it is assumed that the cooling rate is a function of droplet diameter, heat transfer coefficient, as well as the temperature difference between the droplet surface and surrounding fluid (ΔT). Melt and gas properties (Ψ) also need to be considered to calculate the cooling rate. The GMR is zero during single droplet synthesis due to the absence of an atomization gas. The surrounding gas temperature is constant, allowing for the determination of the cooling rate that is dependent only on droplet diameter and material/gas properties as seen in Eq. 5.8 and Fig. 5.21.

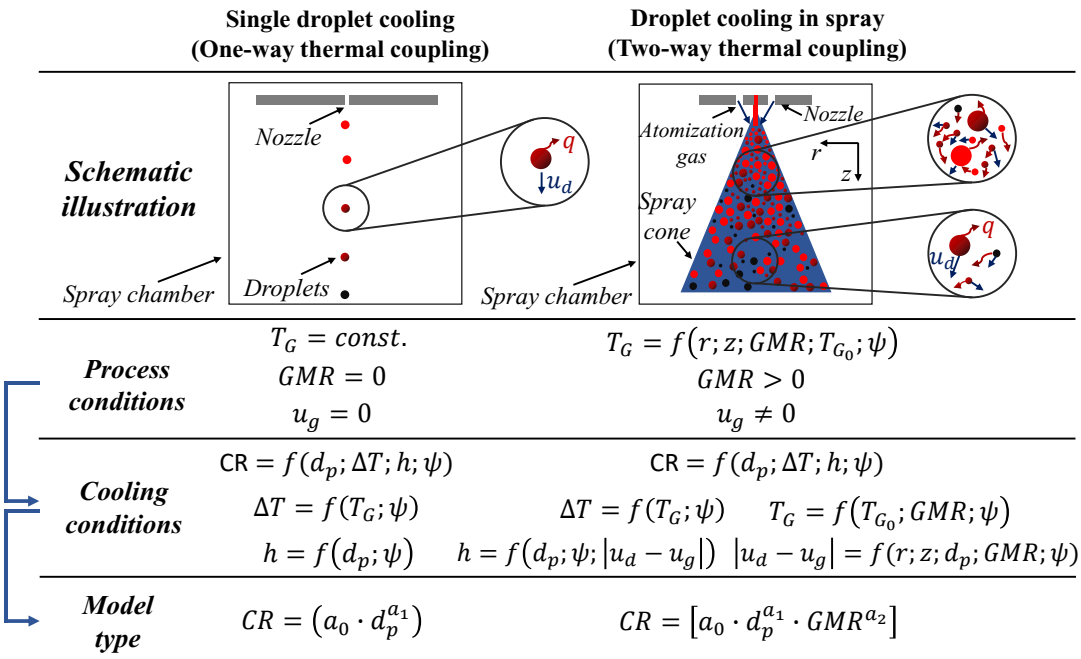

Fig. 5.21.: This illustration describes the relationship between single droplet synthesis and gas atomization [40]. The cooling rate correlation changes as cooling conditions of solidifying droplets are affected by process conditions. Gas atomization is characterized by a GMR > 0 and $u_g \neq 0$, resulting in different cooling conditions that are more complex than in the case of single droplet synthesis. Reprinted from Ref. [40] with permission from Springer Nature.

The interaction between molten metal droplets and surrounding gas flow in gas atomization is more complex than in single droplet synthesis, as more process parameters are involved. For instance, the GMR and the initial gas temperature (GMR > 0 and $u_g \neq 0$) affect cooling conditions that resulted in an extended cooling rate correlation:

$$CR\left(K\,s^{-1}\right) = a_0 \cdot d_p\,(\mu m)^{a_1} \cdot GMR\,(-)^{a_2}\,. \tag{5.9}$$

The cooling rate during molten metal gas atomization depends on droplet diameter, heat transfer coefficient, temperature gradient between the molten metal droplets and the surrounding gas, as well as the material and gas properties. The GMR characterizes the initial load of the droplets that can be adjusted by altering the melt mass flow rate. A larger melt mass flow rate results in a lower GMR which in turn decreases the cooling rate, as a higher number of molten droplets interact with each other. A higher frequency of droplet interaction leads to a smaller temperature gradient between molten metal droplets and the surrounding gas. A higher initial gas temperature also affects the temperature difference between the molten metal droplets and the surrounding gas. The GMR and the initial gas temperature $\left(u_g = f\left(T_{G,0}\right)\right)$ are dependent on each other (sec. 5.3.4) where an increase in the initial gas temperature $T_{G,0}$ resulted in smaller GMR values with a reduced particle size. Smaller droplets have an impact on the relative velocity between melt droplets in flight and gas velocity

u_{rel}. Spray cones in molten metal gas atomization typically consist of a dense section (shown by the enlarged circle on the top right in Fig. 5.21) and a dilute section (shown by the enlarged circle on the top right in Fig. 5.21) [40]. The relative velocity has a direct influence on the heat transfer coefficient and the particle trajectory in the dense section [40]. These considerations make numerical and theoretical cooling rate calculations very challenging. Therefore, most of the present studies in literature rely on experimental methods. Similar to most studies, this PhD work used the secondary dendrite arm spacing method (SDAS) to estimate cooling rates and to investigate the influence of process parameters on cooling rate. For this purpose, a Cu-6wt%Sn alloy was atomized with close-coupled and free-fall atomization and its microstructure was subsequently analyzed to estimate average cooling rates. Secondary dendrites strongly depend on local solidification time [217, 218]. Choi's relationship[1] [219] between SDAS and cooling rate has been used to estimate the cooling rate for Cu-6wt%Sn powders as a reference sample:

$$SDAS\,(\mu\mathrm{m}) = 69.5 \cdot CR_L^{-0.34}\left(\mathrm{K\,s^{-1}}\right), \tag{5.10a}$$

$$SDAS\,(\mu\mathrm{m}) = 34 \cdot CR_{SL}^{-0.323}\left(\mathrm{K\,s^{-1}}\right). \tag{5.10b}$$

Fig. 5.22 shows micrographs of Cu-6wt%Sn particles with a particle size class of 63 - 90 µm. The particles were initially embedded, ground, polished, and subsequently etched for 7 s in 10 g ammonium persulfate ($[NH_4]_2S_2O_8$) and 100 ml distilled water. The particle microstructure consisted of primary and secondary dendrites. Elevated gas temperatures resulted in the same spacing as seen for particles atomized at ambient temperature, concluding that hot gas atomization had a minor effect on the cooling rate and final microstructure of the particles. Small differences were seen for particles atomized under close-coupled conditions compared to those in free-fall atomization, as the microstructure of close-coupled atomized particles consisted of smaller dendrites.

According to DIN EN 1706, ten particles for each particle size class were taken and five dendrites per particle were measured, allowing for the determination of at least 50 dendrites for each particle size class. The SDAS were determined from the following equation:

$$SDAS\,(\mu\mathrm{m}) = \frac{L\,(\mu\mathrm{m})}{n_{arms} - 1}, \tag{5.11}$$

where L represents the distance between the first and last adjacent arm, and n_{arms} describes the number of counted secondary dendrites [40]. Fig. 5.23 shows measured SDAS as a function of mean particle diameter for each corresponding particle size class.

[1] Choi measured cooling curves in an arc melter and induction oven by pouring ~ 0.1 - 3 g of the melt on thin thermocouples (125 μm thick and 50 ms response time) and analyzed the signals with a storage oscilloscope and line recorder. The cooling rates were measured up to 10^4 $\mathrm{K\,s^{-1}}$ and extrapolated up to 10^8 $\mathrm{K\,s^{-1}}$ [40].

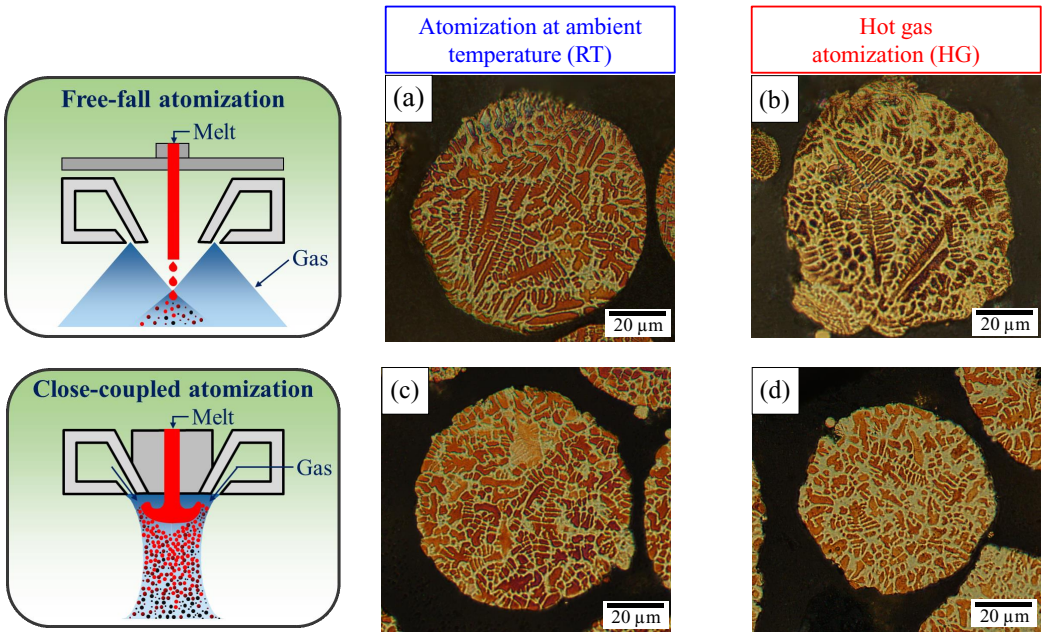

Fig. 5.22.: The microstructure of Cu-6%wtSn particles at a particle size class of 63 - 90 µm atomized with close-coupled (CCA) and free-fall (FFA) atomization. The impact of elevated gas temperatures (HG) and atomization at ambient temperature (RT) is also shown. The particles were etched for 7 s in 10 g ammonium persulfate ($[NH_4]_2S_2O_8$) and 100 ml distilled H_2O. Reprinted from Ref. [40] with permission from Springer Nature.

The GMR widely ranged from 1.4 to 8.3, corresponding to a factor of six between the lowest and highest value. This analysis was performed in a wider GMR range than in literature, allowing for the determination of a wide variety of cooling rates.

An increasing linear relationship between particle size and SDAS is shown in Fig.5.23. Larger particles resulted in lower cooling rates due to the longer solidification time, and thus, in larger SDAS. The measured SDAS values ranged from 1 to 5 µm and were consistent with other literature studies that considered rapid solidification processes such as molten metal gas atomization [220–223]. Each melt droplet had a different particle trajectory during solidification, resulting in different thermal histories and thus in relatively large standard deviations. The maximum measured standard deviation for a mean particle diameter of corresponding particle size class ranged from ± 0.15 to ± 0.65 µm. To provide a statistically accurate average SDAS and thus average cooling rate, the number of dendrites studied should be maximized. In this study at least 50 dendrites per particle size class were measured, satisfying DIN EN 1706 standards. The standard deviation is typically the product of the following effects [40]:

(i) the inherent SDAS measurement method,

(ii) different thermal histories of the melt droplets, resulting in different microstructures,

(iii) and the variation of the particle size class range.

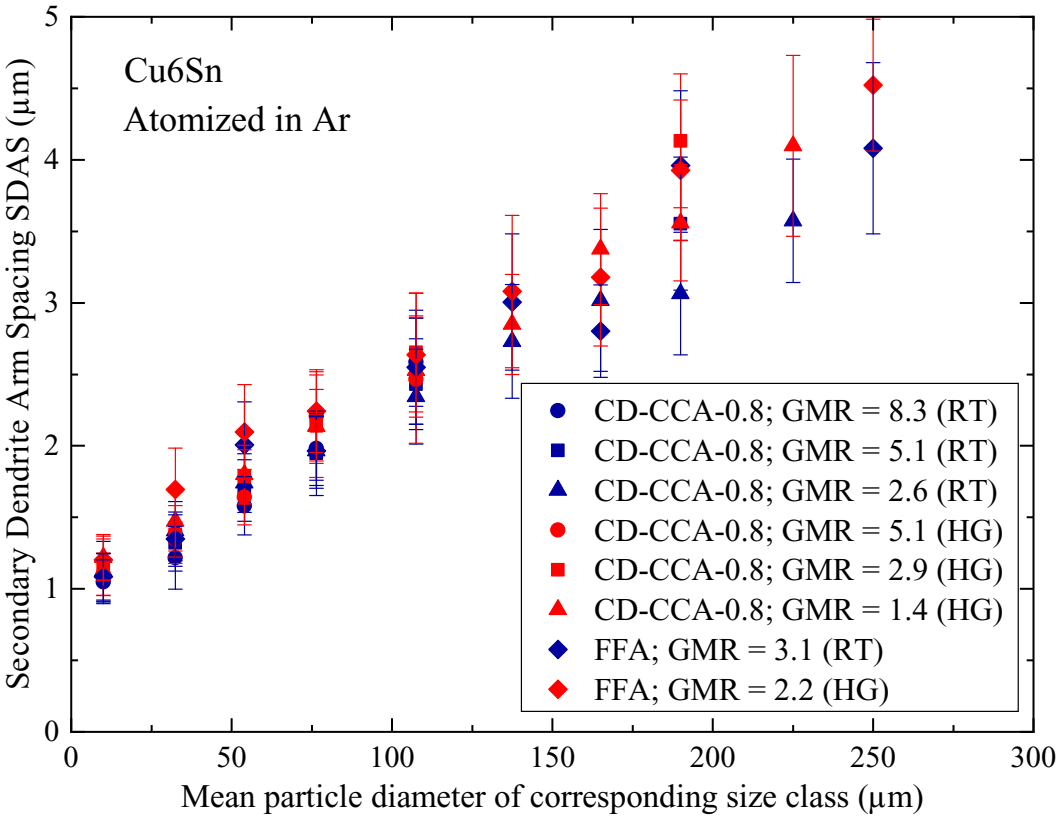

Fig. 5.23.: Measured secondary dendrite arm spacing (SDAS) for Cu-6wt%Sn particles as a function of the mean particle diameter of corresponding particle size class. Particles atomized at elevated gas temperatures (HG) and at ambient temperature (RT) as well as different gas-to-melt mass flow ratios (GMR) were investigated. The hot gas temperature was varied from 525 K to 571 K. Reprinted from Ref. [40] with permission from Springer Nature.

5.3.1. From secondary dendrites to average cooling rates

Fig. 5.24 shows the average cooling rate calculation based on SDAS using Choi's empirical equation (Eq. 5.10b). The average cooling rate decreased with an increasing particle size that was consistent with hot gas atomization findings presented in sec. 5.2.3. Hot gas atomization had a minor influence on cooling rate. The calculated cooling rate values, ranging from 5×10^2 to 5×10^4 K s^{-1}, were independent of the gas temperature. These values were in good agreement with present literature, as the cooling rate for molten metal gas atomization is typically classified in a range from 10^2 to 10^6 K s^{-1}.

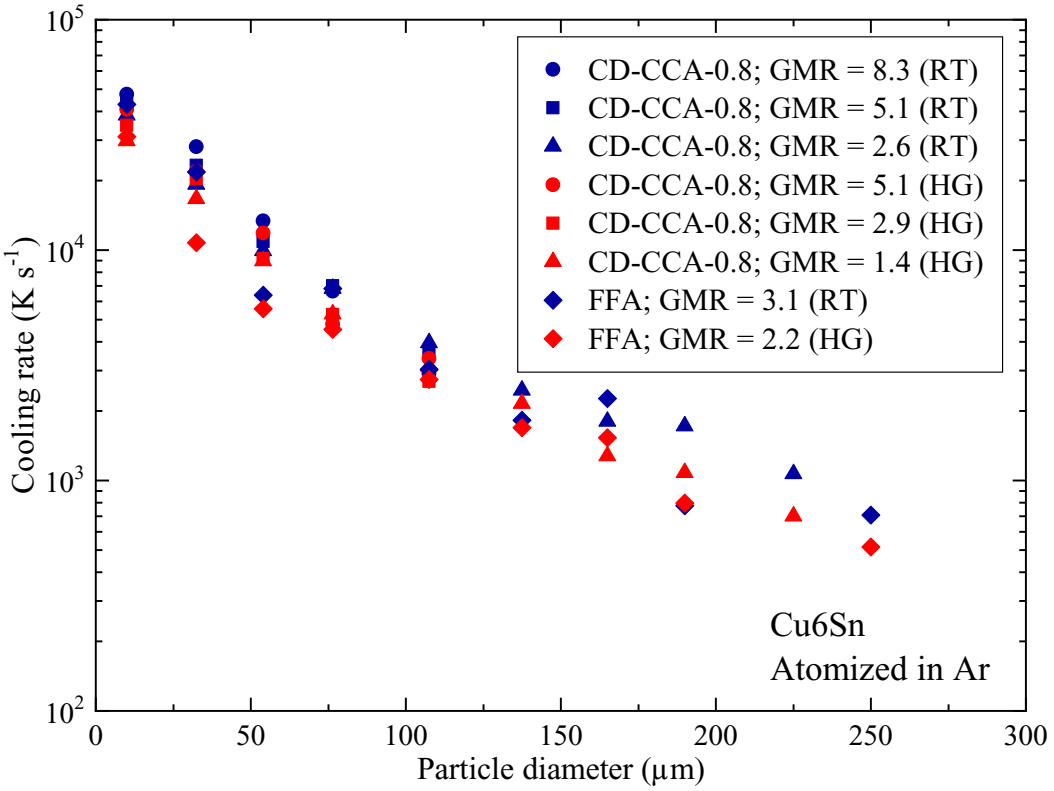

Fig. 5.24.: The average cooling rate during molten metal gas atomization was calculated using Choi's empirical correlation (Eq. 5.10b). Hot gas atomization had a minor influence on cooling rate. The hot gas temperature was varied from 521 K to 571 K. Reprinted from Ref. [40] with permission from Springer Nature.

To understand the influence of the process parameter GMR on cooling rate, calculated average cooling rates are shown as a function of GMR at different particle size classes (Fig. 5.25). For particles < 45 µm, the cooling rate significantly increased with an increased GMR. This investigated effect was attributed to the initial load of the particles, as a larger GMR resulted in fewer particle interactions. Particles ranging from 45 - 63 µm exhibited similar characteristics, but the observed effect for particles > 63 µm was less pronounced as cooling rates were nearly constant. Elevated gas temperatures provided virtually the same cooling rates when compared with atomization at ambient temperature, except for particles < 20 µm.

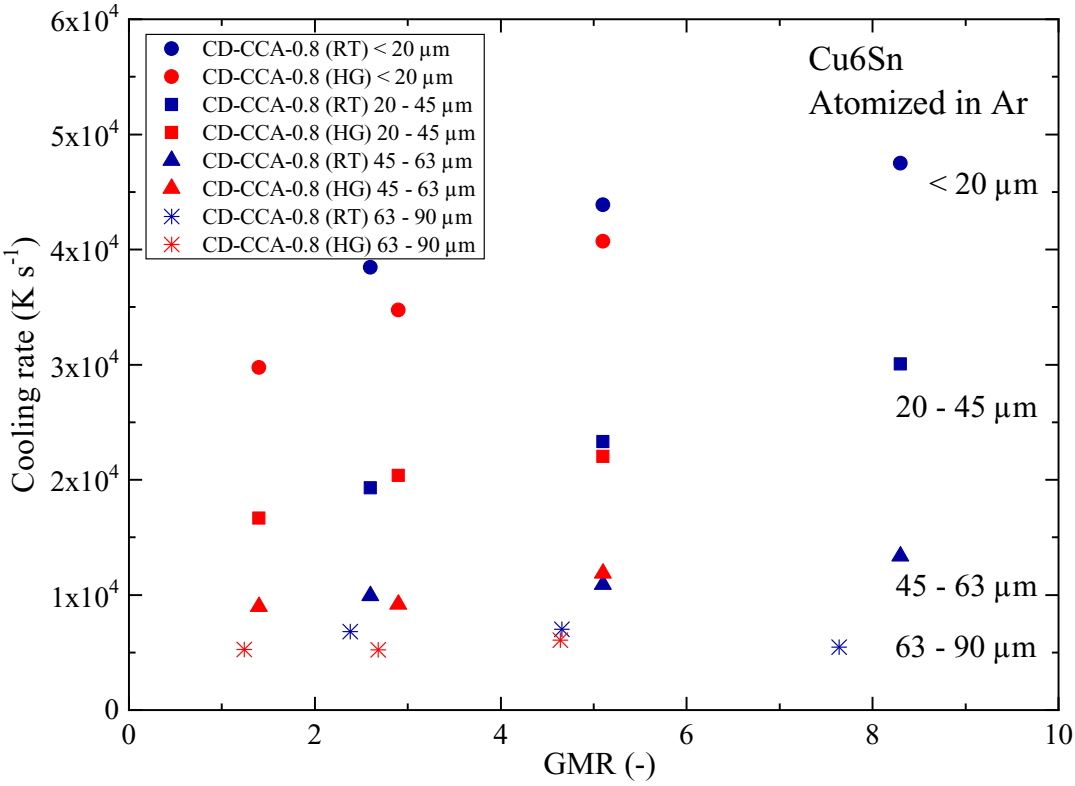

Fig. 5.25.: Calculated average cooling rate as a function of the gas-to-melt mass flow ratio (GMR) at different particle size classes. The cooling rate significantly increased with an increased GMR for particles < 45 µm. The effect of hot gas atomization on cooling rate was only visible for particles < 20 µm, concluding that elevated gas temperatures had a minor effect on cooling rate. Reprinted from Ref. [40] with permission from Springer Nature.

5.3.2. From average cooling rates to cooling rate correlations

Cooling rate correlations were developed (Eq. 5.8 and Eq. 5.9) to estimate average cooling rates as well as to investigate main process parameters that alter cooling rates during molten metal gas atomization. The constants a_i in Eq. 5.8 and Eq. 5.9 were determined with a Nelder-Mead optimization algorithm that was implemented in MATLAB R2017a. The Nelder-Mead algorithm was used to minimize the following residuum [40]:

$$R = \sum_{i=j}^{n} \left(1 - \frac{CR_{Model,j}(a_i)}{CR_{Experiment,j}} \right), \tag{5.12}$$

where CR_{Model} described the calculated average cooling rate and $CR_{Experiment}$ was the calculated average cooling rate based on SDAS analyses. The cooling rate was calculated using Choi's empirical formula (Eq. 5.10b). An investigation of process parameters with respect to proposed cooling rate correlations is presented in Fig. 5.26.

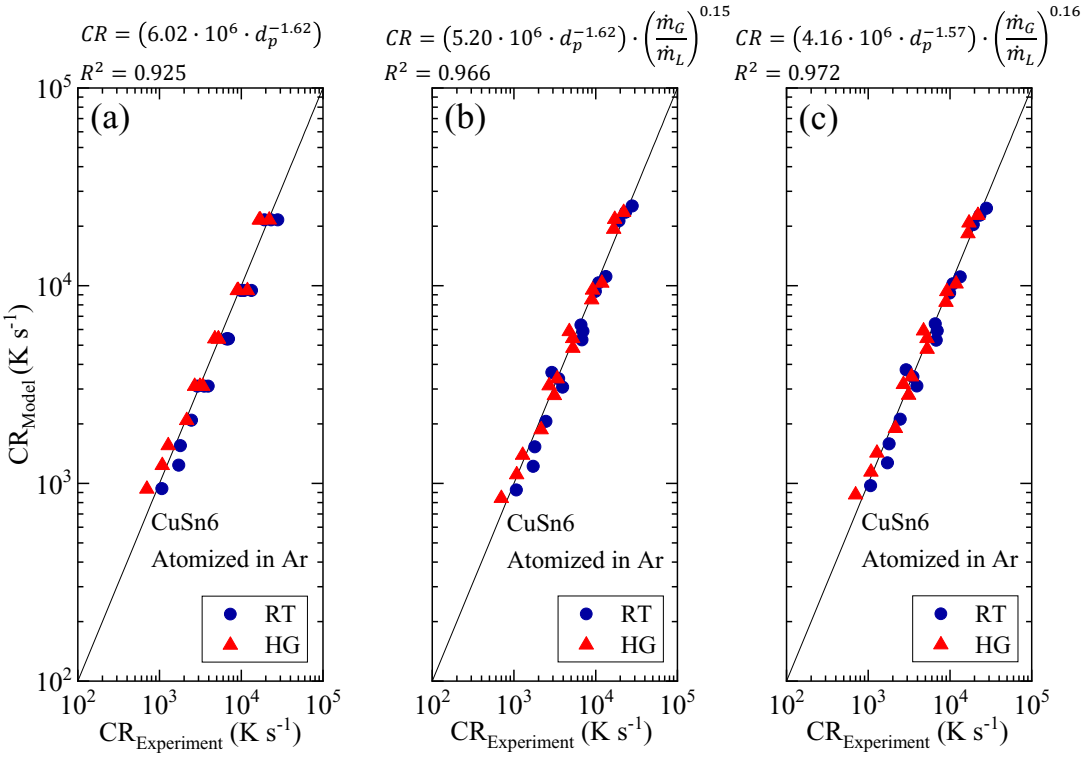

Fig. 5.26.: The three subplots compared estimated average cooling rates derived from the new proposed cooling rate correlation (Eq. 5.9) and calculated average cooling rates derived from the secondary dendrite arm spacing method (SDAS). Subplot (a) shows the mathematical optimization of the data to find the optimum constants considering only droplet diameter. Case (b) represents the influence of the gas-to-melt mass flow ratio (GMR) using the same droplet exponent as in case (a). This allowed for the direct evaluation of the influence of process parameters. Subplot (c) demonstrates the mathematical optimization considering GMR and droplet diameter. The abbreviations RT and HG stand for atomization at ambient temperature and hot gas atomization. All three models were valid for GMR values ranging from 1.3 to 8.3 and temperatures from 293 K to 571 K [40]. Reprinted and modified in part from Ref. [40] with permission from Springer Nature.

The proposed semi-empirical cooling rate correlation was valid for GMR and temperature values ranging from 1.3 to 8.3 and 293 K to 571 K, respectively [40]. Present literature provides studies describing the relationship between secondary dendrites and cooling rates during molten metal gas atomization [28, 29, 224–227]. Studies describing the analytical relationships between cooling rate and key process parameters that alter solidification behavior are rarely available. Therefore, three different cases to estimate average cooling rates based on a Cu-6wt%Sn alloy have been developed. Case (a) represents the mathematical optimization with the aim to find the optimum constants a_i, resulting in a calculated droplet constant of $a_1 = -1.62$. Smaller particles with high cooling rates in case (a) deviated systematically, as the cooling rate for smaller

particles was also a function of GMR (described in Fig. 5.25). The droplet exponent found in this study was consistent with the experimentally determined droplet exponent provided by Mullis et al. (a_1 = -1.67) [225]. The authors atomized an Al-4wt%Cu alloy and analyzed the microstructure through secondary dendrite arm spacing that led to a cooling rate correlation which was only a function of droplet diameter.

The study by Mullis et al. [225] was used as a reference. Although the material selected was different, the authors used the same atomization method (close-coupled atomization), the same inert gas (argon), a similar particle size range, and used SDAS analysis. While the droplet exponent (a_1 = -1.62) was consistent with Mullis et al. (a_1 = -1.67), the pre-exponential factor a_0 was different due to the alloys investigated [40]. The incorporation of the process parameter GMR modified the correlation as seen in case (b). The droplet exponent was maintained at a_1 = -1.62, allowing for a direct comparison with case (a) [40]. This resulted in an improved cooling rate correlation, demonstrated by $R^2 = 0.966$. Therefore, the GMR had a significant influence on cooling rate in addition to droplet diameter [40]. Case (c) represented a mathematical optimization as performed in case (a) and was used to find the optimum constants for case (b) that led to slightly different constants and a $R^2 = 0.972$.

An attempt was made to incorporate the initial gas temperature in the proposed cooling rate correlation Eq. 5.9. Analogous to the results in sec. 5.3.4, elevated gas temperatures had a small but quantitative influence on the cooling rate, supported by the data in Tab.5.2. The R^2 values were almost unchanged regardless of whether hot gas atomization or atomization at ambient temperature was considered. Incorporating initial gas temperature into the proposed cooling rate correlation would be a valuable scientific contribution to the molten metal gas atomization community. However, the present data available from our experiments and from literature were insufficient to fully understand the influence of initial gas temperature on average cooling rate [40]. This presents an interesting opportunity for future scientific inspiration and exploration. The contribution of GMR to the proposed cooling rate correlation is already a unique study when considering cooling rate estimations during molten metal gas atomization [40].

Tab. 5.2.: Proposed cooling rate correlations from Fig.5.26. The R^2 values were listed individually for hot gas atomization (HG) and atomization at ambient temperature (RT), as well HG + RT together.

Model	R^2 (HG + RT)	R^2 (RT)	R^2 (HG)
(a) $6.02 \cdot 10^6 \cdot d_p^{-1.62}$	0.925	0.925	0.922
(b) $5.20 \cdot 10^6 \cdot d_p^{-1.62} \cdot GMR^{0.15}$	0.966	0.977	0.946
(c) $4.16 \cdot 10^6 \cdot d_p^{-1.57} \cdot GMR^{0.16}$	0.972	0.975	0.966

To verify Eq. 5.9, FFA experiments were performed. The difference of FFA and CCA nozzle geometry generally leads to different particle sizes and thermal droplet histories. According to Fig. 5.24, the cooling rate for both atomization

systems was in the same order of magnitude. The initial proposed model was extended with FFA data and the residuum was modified as follows:

$$R = \frac{n_{FFA}}{n_{FFA}+n_{CCA}} \sum_{j=1}^{n_{CCA}} \left[1 - \frac{CR_{Model,j}\left(a_{0_{CCA;a_i>0}}\right)}{CR_{Experiment,CCA,j}} \right] + \frac{n_{CCA}}{n_{FFA}+n_{FFA}} \sum_{j=1}^{n_{CCA}} \left[1 - \frac{CR_{Model,j}\left(a_{0_{FFA;a_i>0}}\right)}{CR_{Experiment,FFA,j}} \right]. \tag{5.13}$$

For a given a_{0_i}, the residuals were individually calculated and the values of $a_{0_{CCA}}$ and $a_{0_{FFA}}$ were adjusted [40]. The number of data points varied, as FFA provided larger particle sizes, allowing for the inclusion of additional particle size classes. The different number of data points for FFA and CCA required weighing the residuals by their relative numbers to determine the regression independent of the number of data points [40]. The comparison between cooling rates based on the proposed model and experimentally derived cooling rates from SDAS analyses for CCA and FFA data are shown in Fig. 5.27.

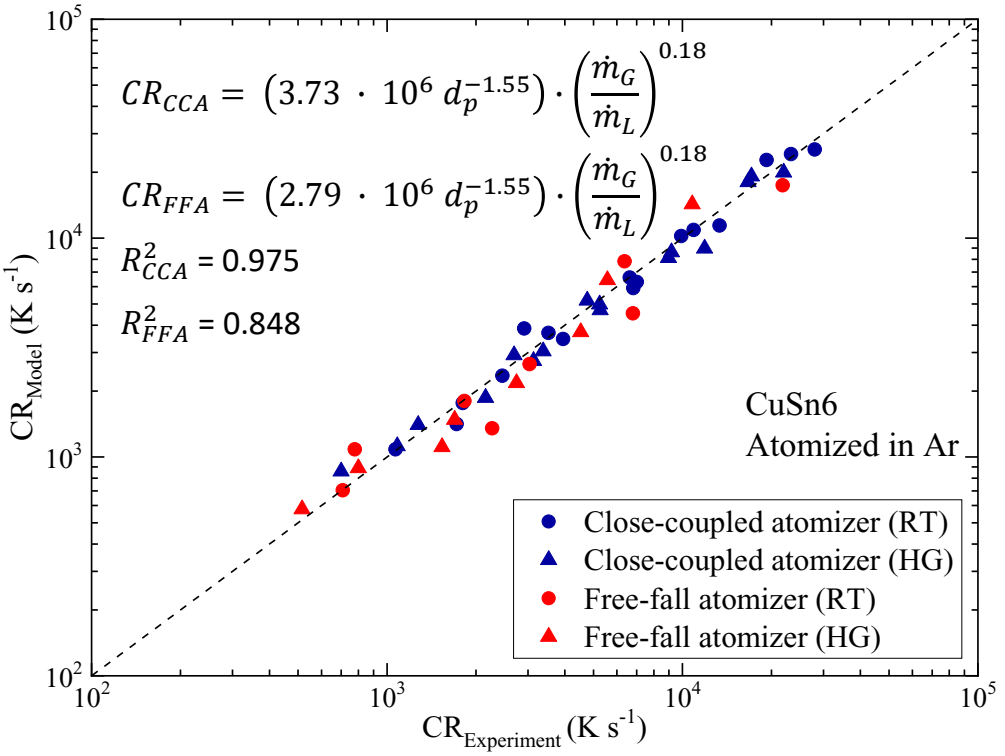

Fig. 5.27.: The cooling rate correlation (Eq.5.9) was extended to a second study in which free-fall atomization was considered. Calculated average cooling rates based on the proposed Eq. 5.9 were compared to experimentally derived cooling rates based on SDAS for close-coupled and free-fall atomization. The proposed semi-empirical cooling rate correlation was valid for GMR and temperature values ranging from 1.3 to 8.3 and 293 K to 571 K, respectively [40]. Reprinted from Ref. [40] with permission from Springer Nature.

To compare the influence of droplet diameter and GMR on the proposed cooling rate correlation, the exponent on droplet diameter and GMR was fixed to the same value for FFA and CCA as seen in Fig. 5.27. CCA and FFA data were in good agreement despite the lower R^2 value. Therefore, the proposed cooling rate correlation may be applicable to different atomization systems. The pre-exponential factor for the CCA atomizer was slightly higher than for the FFA atomizer, likely due to the higher relative velocity in CCA. Based on these calculations, a cooling rate correlation independent of the atomizers used was proposed to calculate the average cooling rate. The pre-exponential factor a_0 describing the material and gas properties was determined to be 3.73×10^6 for CCA and 2.79×10^6 for FFA.

5.3.3. Transferring the cooling rate correlation to different alloy systems

The proposed semi-empirical cooling rate correlation was applicable for a Cu-6wt%Sn binary alloy. To apply the equation to different alloys, it was necessary to know the pre-exponential factor, which averaged the influence of material and gas properties on droplet history for the entire droplet size distribution [40]. An attempt was made to transpose the Cu-6wt%Sn data (ref) to a different alloy system (x). For this purpose, the following equation was developed [40]:

$$\frac{a_{0_x}}{a_{0_{ref}}} = \frac{\rho_{f_x} \cdot \left(c_{p,l_x}\left[T_{liq_x} - T_{s_x}\right] + \Delta H_{M_x}\right)}{\rho_{f_{ref}} \cdot \left(c_{p,l_{ref}}\left[T_{liq_{ref}} - T_{s_{ref}}\right] + \Delta H_{M_{ref}}\right)} \cdot \frac{\left(T_{liq_x} - T_{s_x}\right) \cdot \left(T_{m_x} - T_a\right)^{-1}}{\left(T_{liq_{ref}} - T_{s_{ref}}\right) \cdot \left(T_{m_{ref}} - T_a\right)^{-1}} \tag{5.14}$$

$$\text{with} \quad T_m = \frac{T_{liq} + T_s}{2}. \tag{5.15}$$

The proposed Eq. 5.14 and Eq. 5.15 represented the ratio between the reference alloy (Cu-6wt%Sn atomized with argon inert gas) and a desired alloy (x). The purpose of this equation was to provide a physical relationship for the thermal droplet behavior by considering thermophysical properties of the melt to estimate average cooling rates without additional gas atomization experiments. The proposed Eq. 5.14 and Eq. 5.15 incorporated thermodynamic properties by considering Choi's SDAS equation (Eq. 5.10). Note that Eq. 5.14 and Eq. 5.15 were invalid to predict microstructure. The equations used to calculate the pre-exponential factor consisted of three terms: (i) the heat release $\rho_f \cdot \left(c_{p,l} \times \left[T_{liq} - T_s\right] + \Delta H_M\right)$, (ii) the solidification interval $\left(T_{liq} - T_s\right)$, and (iii) the mean temperature between the droplet and surrounding gas $(T_m - T_a)$. Eq. 5.14 and Eq. 5.15 included the following thermophysical properties: droplet density ρ_f at a solid fraction f_s of 0.5, liquid specific heat capacity of the molten metal droplet $c_{p,l}$, latent heat of fusion ΔH_M, liquidus temperature T_{liq}, and solidus temperature T_s. The parameter T_m represented the mean solidification temperature with a solid fraction of $f_s = 0.5$ at ambient temperature T_a.

Currently, the proposed equation can only be compared and applied to a few

studies. While most of the present literature provides relationships between SDAS and cooling rates, few studies provide values for the pre-exponential factor. Therefore, the study by Mullis et al. [225] was again used to verify the proposed equation for the pre-exponential factor describing the material and gas properties. The material properties used to calculate the pre-exponential factor for the reference alloy Al-4wt%Cu, together with the required data for the Cu-6wt%Sn alloy, are listed in Tab. 5.3.

Tab. 5.3.: Material properties used to calculate the pre-exponential factor for the Cu-6wt%Sn (CuSn6) reference alloy as well as the Al-4wt%Cu alloy (Al4Cu).

Material properties	**Unit**	**CuSn6 (Our Study)**	**Al4Cu (Mullis et al.) [225]**
Liquidus temperature T_{liq}	K	1323	921
Solidus temperature T_s	K	1173	845
Density at solid fraction $f_s = 0.5$	$\mathrm{kg\,m^{-3}}$	7870	2540
Specific heat capacity $c_{p,s}$ (Solid)	$\mathrm{J\,kg^{-1}\,K^{-1}}$	422	910
Specific heat capacity $c_{p,l}$ (Liquid)	$\mathrm{J\,kg^{-1}\,K^{-1}}$	475	1178
Latent heat of fusion ΔH_M	$\mathrm{J\,kg^{-1}}$	187 890	321 000

Li et al. reported a pre-exponential factor for a Fe-6.5wt%Si alloy, but their SDAS analysis was not independently validated by other researchers. Therefore, this study was excluded from the calculation of the pre-exponential factor. Applying Eq. 5.14 and Eq. 5.15 yielded a pre-exponential factor for the Al-4wt%Cu alloy of 2.32×10^6 instead of the value of 1.87×10^6 reported by Mullis et al.[225]). The calculated a_0 value agreed well with the experimentally determined pre-exponential factor considering the large variation in critical cooling rates of different alloys. These findings supported the hypothesis that the proposed model was valid for more than just CCA and FFA, but may also be applied to other atomization systems [40]. Melt droplet cooling by radiation was neglected in the proposed equation, but should be considered if the degree of radiation is significant in alloy systems with a high liquidus temperature. In the case of the Al-4wt%Cu alloy, the effect of radiation was neglected due to a relatively low liquidus temperature and an initial melt atomization temperature of $T_M = 1021\,\mathrm{K}$ [40]. The proposed cooling rate correlation is invalid to predict microstructure, since SDAS analysis is only able to estimate average cooling rates. The results can also be applied to glass-forming alloys if thermophysical property data are available.

5.3.4. Conclusion and review of the cooling rate calculations for the cooling strategy consideration

A new mathematical cooling rate correlation was developed to estimate average cooling rates during molten metal gas atomization. For this purpose, a crystalline Cu-6wt%Sn alloy was atomized using close-coupled as well as free-fall atomization and was subsequently analyzed with secondary dendrite arm

spacing (SDAS). The SDAS was used to calculate average cooling rates and to investigate critical process parameters. The results are summarized as follows:

- An independent atomizer cooling rate correlation was proposed. The cooling rate CR is a function of droplet diameter d_p and gas-to-melt mass flow ratio (GMR). These findings were a progressive development compared to current cooling rate correlations available in literature that only consider droplet diameter. The proposed semi-empirical cooling rate correlation is valid for GMR and temperature values ranging from 1.3 to 8.3 and 293 K to 571 K, respectively.

$$CR = a_0 \cdot d_p^{-1.55} \cdot GMR^{0.18} \tag{5.16}$$

- Initial gas temperature was incorporated into the cooling rate correlation. However, experimental and literature data are currently incomplete, excluding the determination of the influence of initial gas temperature on cooling rate. This presents room for future studies to improve the cooling rate correlation. Nonetheless, first results showed that cooling rate was independent of initial gas temperature. This was consistent with experimental hot gas atomization results as described in sec. 5.2, demonstrating that elevated gas temperatures had a minor effect on cooling rate.

- The cooling rate correlation was applied to different alloy systems without additional gas atomization experiments. A pre-exponential material and gas property factor a_0, transferable to different alloy systems, was predicted. Calculated results agreed remarkably well with literature data ($< 20\%$), suggesting that the proposed cooling rate correlation may be applicable to different atomization systems.

5.4. Spray cone cooling and liquid quenching

One part of this research was to increase the heat transfer coefficient for droplet solidification during melt atomization, as it was shown that the two soft ferromagnetic glass-forming alloys were difficult to atomize in an amorphous state during gas atomization (sec. 5.1.1). In particular, gas atomization resulted in partially-amorphous particles for the FeBSiP glass-forming alloy even at the smallest particle size class (< 25 µm), likely due to their low glass-forming ability and cooling rate limitations (Fig. 5.30a). The atomized FeCoBSiNb particles were fully amorphous up to 63 µm (Fig. 5.29a). Bulk sample consolidation techniques require powders that are entirely amorphous. To satisfy this requirement, cooling strategies for the atomization of the two soft ferromagnetic glass-forming alloys have been developed.

Two cooling strategies were considered: spray cone cooling and liquid quenching (sec. 1.4.3 and sec. 1.4.4). Both methods included distilled water as a liquid quench medium. The combined use of quench media and gas atomization provided higher cooling rates, but also promoted an oxide layer around the melt

droplets. Liquid quenching may introduce hydrogen in the water-quenched particles and alter the material properties. In the production of quenched steel, for instance, hydrogen trapping is a common phenomena. Material properties are typically deteriorated and cracks can be observed due to hydrogen embrittlement [228]. Although metallic glasses become embrittled when induced with hydrogen, the embrittlement is less severe than in crystalline materials. In metallic glasses, hydrogen may be absorbed and desorbed many times without spontaneous material disintegration that often occurs for crystalline materials [229]. Hydrogen is typically introduced from the gas phase, electrochemically, and by ion implantation [229]. The effect of hydrogen in metallic glasses regarding transport processes, structural changes, glass formation, and material properties [110, 230–235] is controversially reported in literature. The following section discusses the benefits of alternative cooling strategies, the influence of hydrogen, and subsequent powder processability. To investigate the feasibility of powder consolidation, Spark Plasma Sintering was used. This section also discusses the extent to which produced powders influence consolidated bulk properties with a focus on magnetic properties.

5.4.1. Safety consideration

The developed cooling techniques resulted in vapor formation inside the spray chamber, since distilled water was used as the primary cooling medium. An attempt was made to predict the increase in pressure caused by vapor formation. However, the melt enthalpy data from our experiments were insufficient to predict this pressure increase. The estimation of the pressure increase would be a powerful tool in the design of atomization facilities, as it is a safety-related process parameter. It becomes more critical when atomization is scaled up to an industrial size, as the length of operation time in these facilities is typically longer, increasing the risk of producing oxyhydrogen gas (a mixture of oxygen and hydrogen).

Fig. 5.28 shows the measured pressure increase as a function of time during gas atomization and the developed cooling strategies. A maximum pressure increase corresponded to the onset of the melt mass flow due to the volumetric expansion of the melt. The higher the melt mass flow rate, the higher the pressure increased. This was followed by a decrease to a constant pressure regardless of the cooling strategy used. Significant vapor formation was only observed in liquid quenching. However, the values were far below the maximum pressure, showing that the developed cooling strategies can be safely applied. An internally defined safety limit of 30 kPa was set using a relief valve. Due to experimental limitations, the total weight of collected powders for liquid quenching was typically < 100 g and far less than in conventional and spray cone cooling (corresponding to 2 kg feedstock).

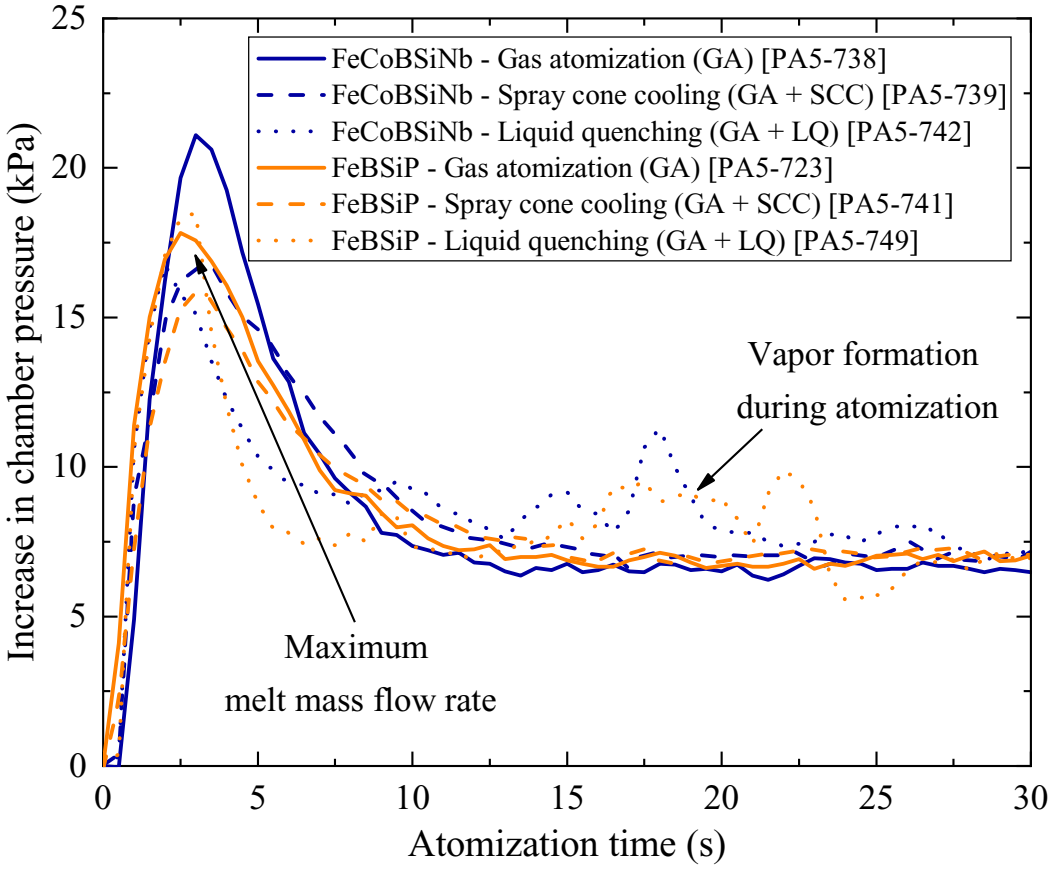

Fig. 5.28.: Increase in chamber pressure as a function of atomization time for spray cone cooling and liquid quenching experiments. The onset of the melt mass flow caused a pressure increase, followed by a decrease and a stationary stage. The cooling strategies led to an increased pressure due to vapor formation. However, this pressure was relatively small compared to the pressure increase caused by the onset of the melt mass flow. Chamber pressure must remain below a maximum of 30 kPa as defined by internal safety regulations.

5.4.2. Powder characterization

In Fig. 5.29 and Fig. 5.30, XRD traces of FeCoBSiNb and FeBSiP powders are shown for conventional cooling, spray cone cooling, and liquid quenching. All cooling strategies were carried out under the same process conditions as seen in Tab. C.1. As discussed in sec. 5.1.1, the FeCoBSiNb powders were fully amorphous up to 63 µm for the highest melt superheat temperature (350 K) during gas atomization (Fig. 5.1a), whereas melt superheat temperatures of 250 K and 300 K resulted in fully amorphous FeCoBSiNb particles up to 45 µm (Fig. 5.1a and Fig. 5.1b). FeBSiP particles showed minor crystalline peaks even for the smallest particle size class and for the highest melt superheat temperature of 350 K, demonstrating that the particles were partially-amorphous due to the use of commercial purity feedstock (Fig. 5.30a). In the case of both soft ferromagnetic powders, the number of crystalline reflections and their intensity in-

creased with particle size. This indicated that larger particles experienced lower cooling rates. These results showed that alternative cooling strategies were required. Spray cone cooled particles for the FeCoBSiNb and FeBSiP powders were fully amorphous up to 125 µm and 45 µm, respectively. These results showed the improvement in amorphous fraction during spray cone cooling when compared to gas atomization with conventional cooling. Liquid quenching resulted in fully amorphous particles that were independent of particle size class and falling distance (0.5 m and 0.7 m) for both soft ferromagnetic powders. Different particle size classes were considered, as the amount of collected particles were lower in conventional gas atomization. The collectors were modified to increase the amount of quenched particles captured. After modifying the collectors, the amount of powder collected was significantly higher, although the amount of post-processing such as cleaning increased. (Fig. A.2).

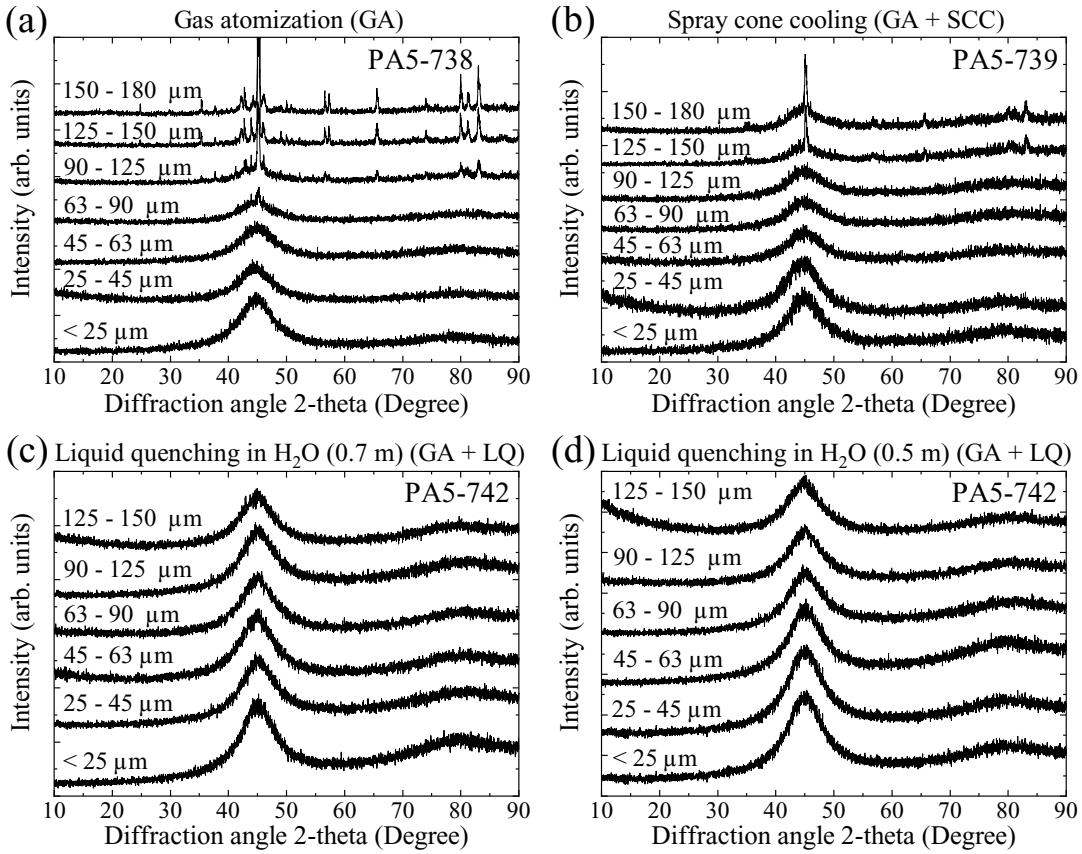

Fig. 5.29.: XRD traces for $\{(Fe_{0.6}Co_{0.4})_{0.75}B_{0.2}Si_{0.05}\}_{96}Nb_4$ powders atomized with conventional gas atomization and different cooling strategies. All powders were atomized under the same process conditions (Tab. C.1). Conventional gas atomization and liquid quenching performed at collection distances of 0.5 m and 0.7 m resulted in the highest cooling rates and in fully amorphous particles. Particle size classes > 125 µm showed a slightly sharper amorphous halo, likely due to the presence of minor crystals. The second highest cooling rate was achieved by spray cone cooling, followed by conventional gas atomization.

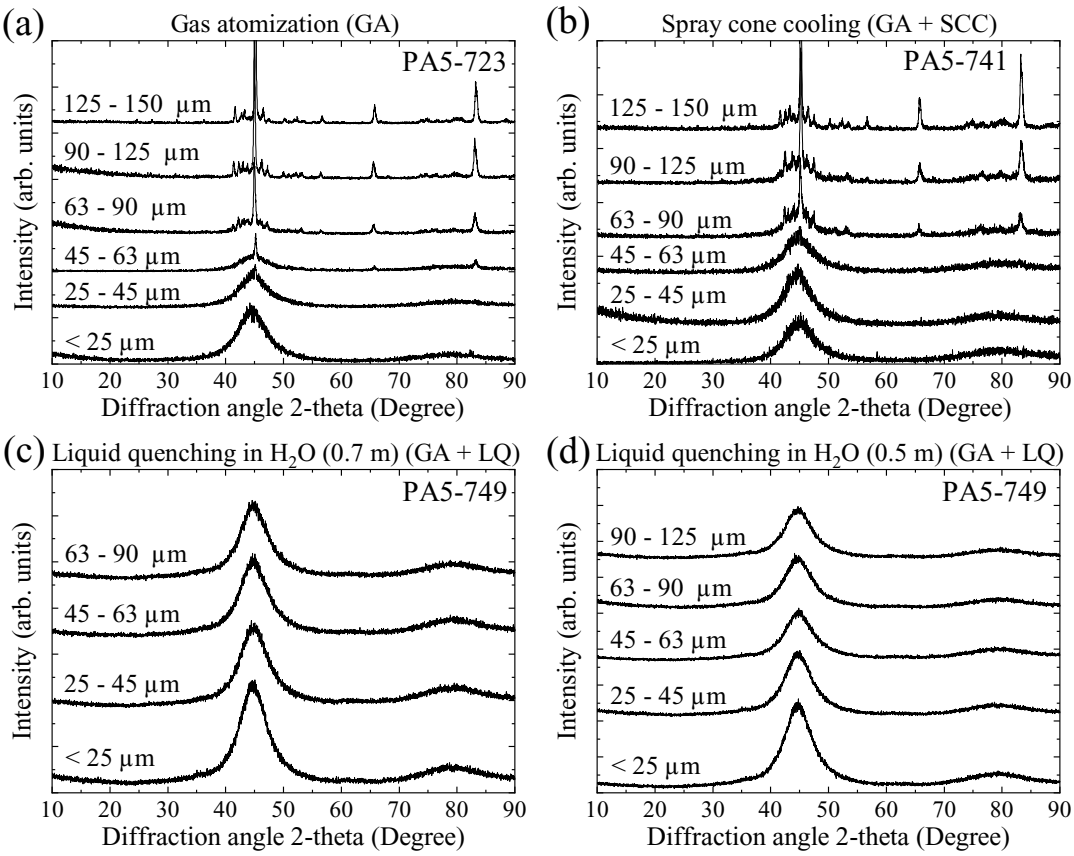

Fig. 5.30.: XRD traces for $Fe_{76}B_{10}Si_9P_5$ powders atomized with conventional gas atomization and different cooling strategies. All powders were atomized under the same process conditions (Tab. C.1). Conventional gas atomization and liquid quenching performed at collection distances of 0.5 m and 0.7 m resulted in the highest cooling rates and in amorphous particles. The second highest cooling rate was achieved by spray cone cooling, followed by conventional gas atomization.

Fig. 5.31a and Fig. 5.31b present DSC measurements for the two soft ferromagnetic powders at particle size classes of 25 - 45 µm and 125 - 150 µm. The DSC measurements for the FeCoBSiNb alloy were consistent with XRD measurements exhibited in Fig. 5.29, as the enthalpy of crystallization for particles atomized under gas atomization and spray cone cooling decreased with an increased particle size due to a lower cooling rate. For comparison, DSC measurements for both melt spinning reference samples were plotted. The shape of the crystallization event for the smallest particle size class (25 - 45 µm) was similar to that of the melt spinning reference curves, demonstrating that this particle size class was fully amorphous. The water-quenched FeCoBSiNb particles were fully amorphous regardless of the investigated particle size class and collection distance. These results were consistent with the presented XRD measurements. The FeBSiP particles exhibited the same behavior as seen for FeCoBSiNb particles and were in agreement with the presented XRD measurements in Fig. 5.30. However, a distinct difference between the two soft ferromagnetic powders were observed: water-quenched FeBSiP particles showed a second exothermic event

at temperatures around 1073 - 1078 K, which is reported for this alloy system for the first time. For instance, for a $Ti_{50}Ni_{25}Cu_{25}$ glass-forming alloy, Yamaura et al. reported a second exothermic peak after producing melt-spun ribbons [236]. They explained that hydrogen resulted in a broad exothermic peak due to hydrogen desorption, followed by a secondary exothermic peak corresponding to the crystallization of hydride, and finally to a sharp endothermic peak due to hydrogen desorption. Kováč et al. reported that hydrogen absorption corresponded to the sign of the enthalpy. An exothermic peak is typically detected for hydride-forming systems (e.g. Zr, Ti, V, and rare elements), whereas an endothermic peak is observed for metals and alloys that form hydrides at room temperature [235].

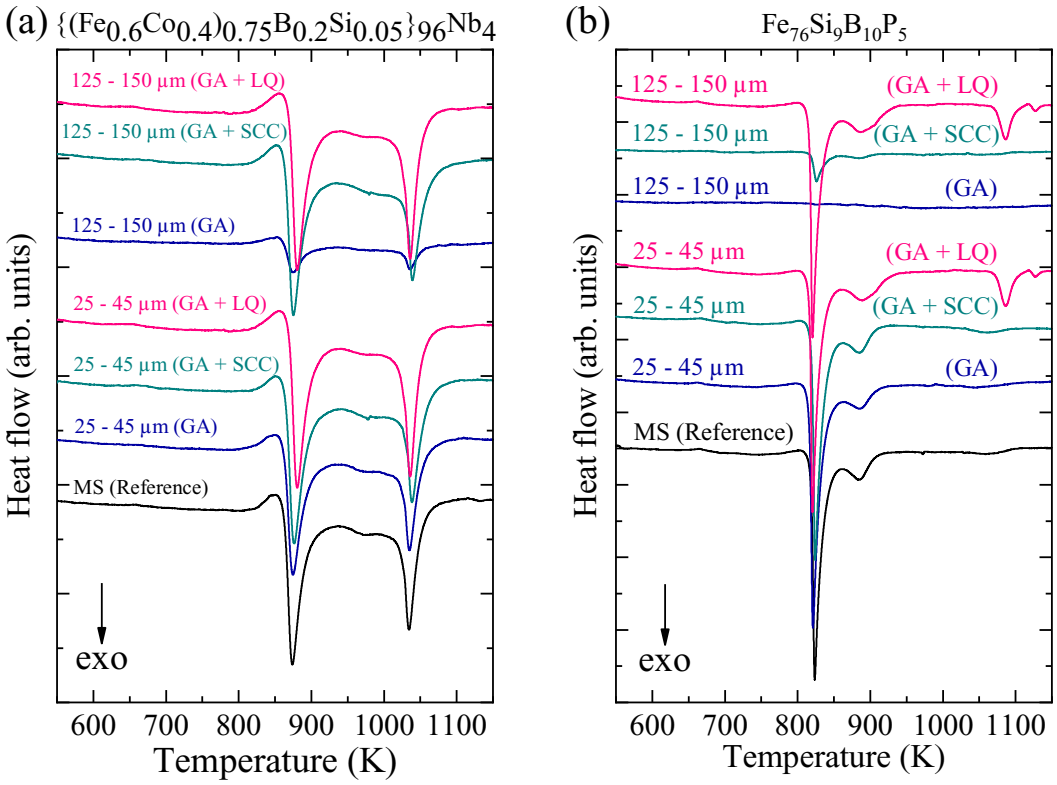

Fig. 5.31.: DSC measurements on (a) $\{(Fe_{0.6}Co_{0.4})_{0.75}B_{0.2}Si_{0.05}\}_{96}Nb_4$ and (b) $Fe_{76}B_{10}Si_9P_5$ soft ferromagnetic powders for the following particle size classes: 25 - 45 µm and 125 - 150 µm. The abbreviations GA, GA + SCC, and GA + LQ stand for conventional gas atomization, conventional gas atomization with spray cone cooling, and conventional gas atomization with liquid quenching, respectively.

The enthalpy of crystallization (ΔH_x) as a function of particle size for conventional gas atomization and the different cooling strategies determined from the corresponding DSC measurements in Fig. 5.31 are shown in Fig. 5.32. The enthalpy of crystallization for the melt spinning reference samples are included in Fig. 5.32 for comparison. The dashed line represents the average enthalpy of crystallization and the upper and lower edges of the orange area defines the standard deviation. FeCoBSiNb particles up to 63 µm atomized under con-

ventional gas atomization showed the same enthalpy of crystallization values as the melt spinning reference. The enthalpy of crystallization values for the FeCoBSiNb glass-forming alloy also decreased with particle size. Spray cone cooled particles showed the same trend as particles atomized under conventional gas atomization conditions. However, the decrease in enthalpy of crystallization was less pronounced, demonstrating that spray cone cooling is an effective method to increase the cooling rate and thus the amorphous fraction. The highest enthalpy of crystallization was achieved for liquid quenched particles, followed by spray cone cooling, where the measured enthalpy of crystallization values were consistently higher than for the FeCoBSiNb melt spinning reference. This behavior was unexpected, as measured or calculated cooling rates during melt spinning (10^4 - 10^6 Ks^{-1}) [237, 238] are generally larger than in gas atomization (10^2 - 10^5 Ks^{-1}) [40]. The DSC measurements were carefully checked and the liquid quenching experiments were repeated using distilled water as well as poly(ethylene glycol) (PA5-754 and PA5-761). The original measurements were validated (PA5-742). The chemical composition of the powders were measured with ICP-OES, but only slight deviations from the nominal composition were observed (Tab. 5.4 and Tab. 5.5). These validations led to the assumption that hydrogen had a strong effect on the enthalpy of crystallization for the liquid quenching experiments.

Tab. 5.4.: ICP-OES measurements on $\{(Fe_{0.6}Co_{0.4})_{0.75}B_{0.2}Si_{0.05}\}_{96}Nb_4$ powders using conventional gas atomization and the developed cooling strategies. ICP-OES values deviated slightly from the nominal composition.

Cooling strategy -	Particle size class µm	Fe wt%	Co wt%	B wt%	Si wt%	Nb wt%
Nominal composition		50	35.2	4.3	2.8	7.7
Gas atomization	45 - 63	49.95	35.75	4.49	2.75	7.94
Spray cone cooling	45 - 63	50.15	36	3.37	2.75	8.02
Liquid quenching	45 - 63	50.55	36.05	4.23	2.45	7.8

Tab. 5.5.: ICP-OES measurements on $Fe_{76}B_{10}Si_9P_5$ powders using conventional gas atomization and the developed cooling strategies. ICP-OES values deviated slightly from the nominal composition.

Cooling strategy -	Particle size class µm	Fe wt%	B wt%	Si wt%	P wt%
Nominal composition		89.17	2.27	5.31	3.25
Gas atomization	45 - 63	89.25	2.50	5.04	3.36
Spray cone cooling	45 - 63	88.55	2.41	4.97	3.31
Liquid quenching	45 - 63	88.85	2.35	5.04	3.23

The FeBSiP particles followed the same trend as the FeCoBSiNb particles for conventional gas atomization and spray cone cooling. For water-quenched FeB-

SiP particles, the enthalpy of crystallization was almost identical to the enthalpy of crystallization of the FeBSiP melt spinning reference. This was contradictory to the FeCoBSiNb water-quenched particles, where the enthalpy of crystallization was significantly higher than for the corresponding melt spinning reference. For the FeBSiP and the FeCoBSiNb glass-forming alloy, the enthalpy of crystallization was independent of collection distance (0.5 m and 0.7 m), demonstrating that both distances provided nearly the same cooling rates and thus an identical amorphous fraction. For the FeCoBSiNb water-quenched particles, the enthalpy of crystallization values taken at a collection distance of 0.7 m were not shown for the sake of readability (Fig. 5.32).

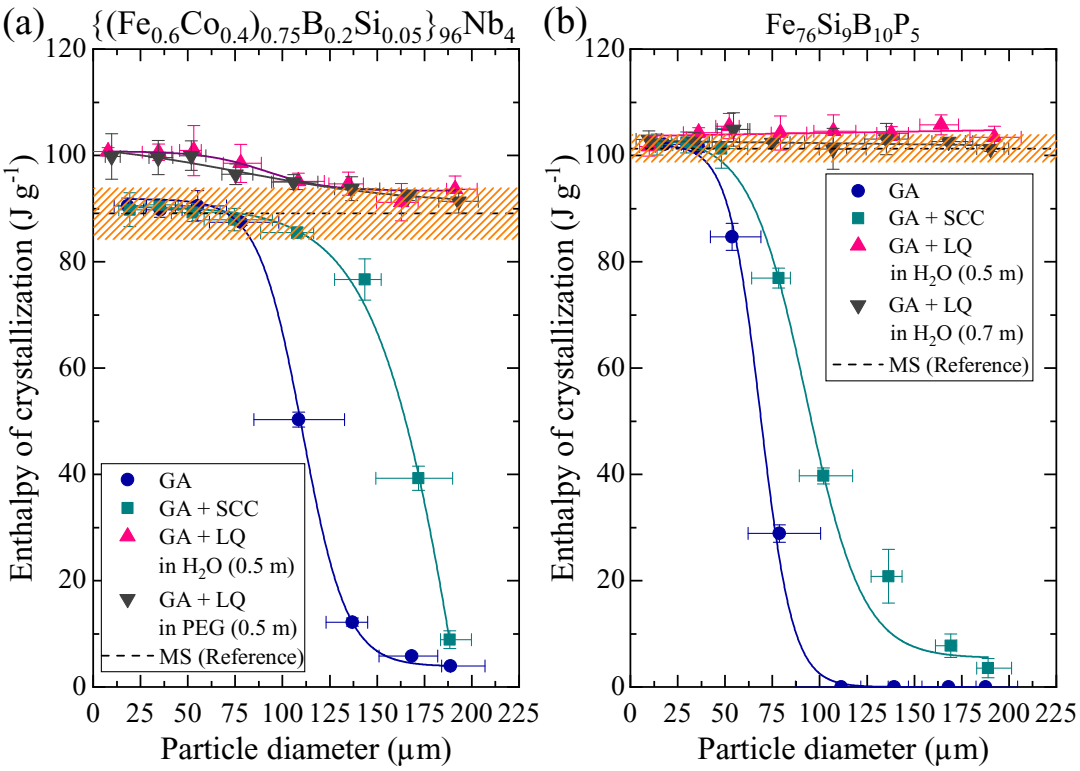

Fig. 5.32.: Enthalpy of crystallization as an indicator of amorphous fraction was plotted as a function of particle size. The values were determined for $\{(Fe_{0.6}Co_{0.4})_{0.75}B_{0.2}Si_{0.05}\}_{96}Nb_4$ and $Fe_{76}B_{10}Si_9P_5$ powders. The $\{(Fe_{0.6}Co_{0.4})_{0.75}B_{0.2}Si_{0.05}\}_{96}Nb_4$ particles were also quenched in poly(ethylene glycol) (PEG). The $d_{16,3}$ and $d_{84,3}$ percentiles were determined from laser particle diffraction measurements and are denoted by the horizontal error bars. The enthalpy of crystallization values for the powders atomized under conventional gas atomization and different cooling strategies were compared with melt spinning (MS) reference samples. The dashed line represents the average enthalpy of crystallization and the upper and lower edges of the orange area defines the standard deviation. The abbreviations GA, GA + SCC, and GA + LQ stand for conventional gas atomization, conventional gas atomization with spray cone cooling, and conventional gas atomization with liquid quenching, respectively.

The increase in amorphous fraction achieved by applying these cooling strategies has the potential to make significant contributions to the commercialization of metallic glasses with commercial purity, considering amorphous powder synthesis and subsequent consolidation. These novel cooling techniques allow manufacturers to overcome limitations introduced by conventional gas atomization that prevents the production of bulk amorphous samples.

A second exothermic DSC peak was observed for water-quenched FeBSiP particles, the enthalpy of crystallization of water-quenched FeCoBSiNb particles were significantly higher than the corresponding melt spinning reference, and the saturation magnetization of water-quenched FeCoBSiNb particles distinctly increased (results will be discussed later). These findings can be attributed to hydrogen inducement. To prove this assumption, the hydrogen and oxygen levels in the powders were measured. Molten or partially-solidified droplets impinging on the quench medium may have underwent structural changes caused by internal stresses from hydrogen inducement [110, 234, 235]. Liquid quenched particles showed more irregularities when compared to nearly spherical gas-atomized or spray cone cooled particles, demonstrating that the particles were liquid before impinging on the quench medium (Fig. 5.33). Hence, partially-solidified or molten droplets may have been influenced by hydrogen, as the large temperature differential between the hot melt droplets and the quench medium enhanced hydrogen inducement.

Fig.5.34 shows the measured hydrogen and oxygen levels for the two soft ferromagnetic powders at different particle size classes. The lowest oxygen level for both powders were found in the largest particle size class and can be attributed to the surface-to-volume effect, in which more relative surface area for smaller particles was available to be covered by an oxide film. Gas-atomized powders are typically subjected to slow oxidation after they have successfully been synthesized in an inert gas atmosphere. This resulted in an oxide film with a thickness dependent on alloy composition, production method, and passivation [239]. For instance, micro- or nano-sized Al or Zr powders are pyrophoric and need to be passivated in order to stabilize them from spontaneous ignition.

From conventional gas atomization to spray cone cooling, the oxidation level for the FeBSiP particles increased by nearly one order of magnitude and increased again by nearly another order of magnitude for water-quenched particles. The oxygen level of the FeCoBSiNb particles increased to a lower extent, confirming that the FeBSiP alloy was more prone to oxidation due to the high Fe and P content in the alloy. For particles that were in contact with water, the hydrogen and oxygen levels were independent of particle size and almost constant, concluding that these particles were dominated by mass diffusion. The hydrogen level of both alloy systems was typically an order of magnitude lower than the oxygen level. A pronounced increase in hydrogen was observed for spray cone cooled and liquid quenched particles compared to particles atomized under conventional cooling conditions, suggesting that hydrogen was responsible for the improvement in saturation magnetization and for the aforementioned effects with respect to DSC measurements. The hydrogen level was nearly unaffected when poly(ethylene glycol) was used, since it is a water-soluble polymer.

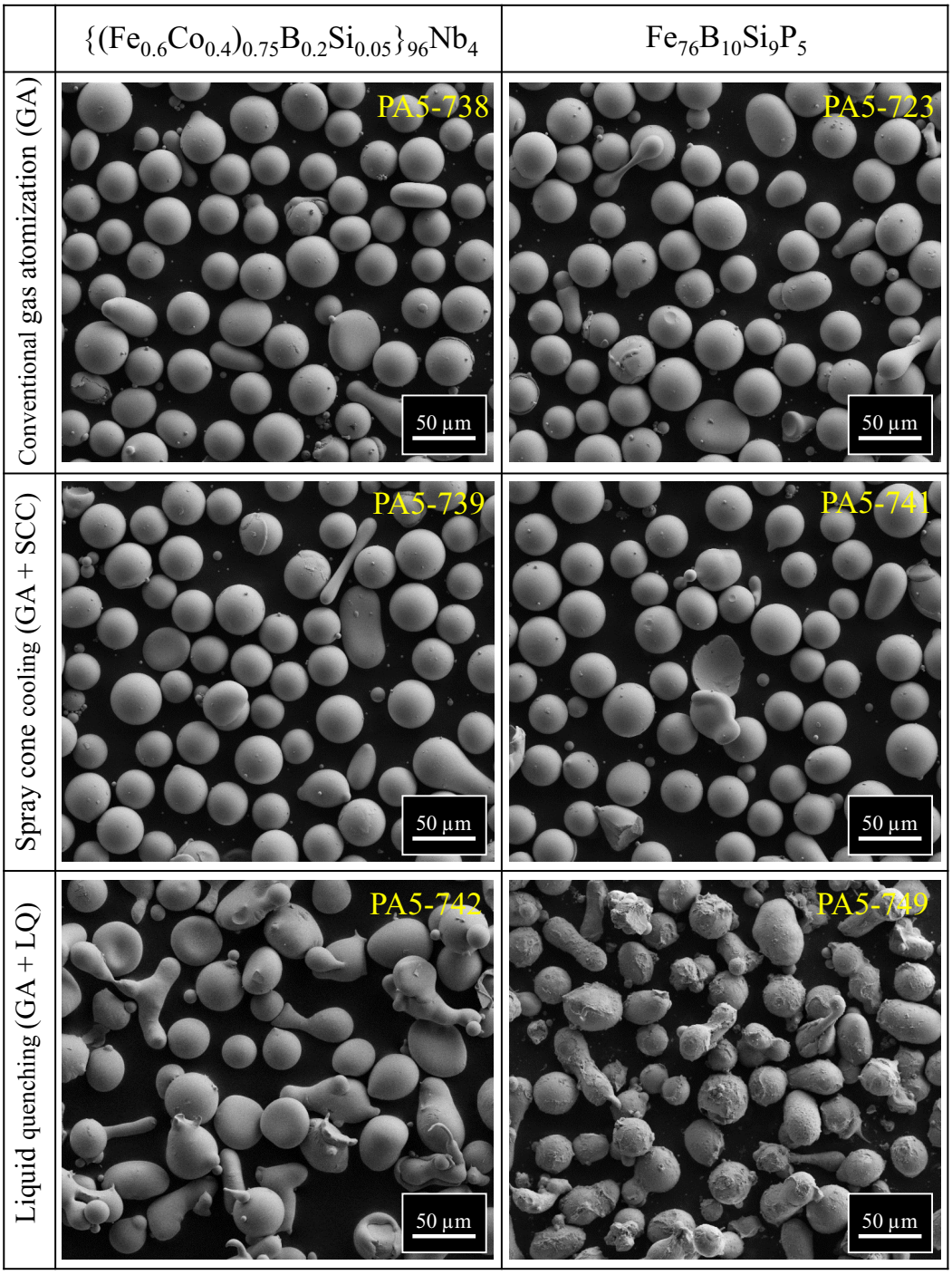

Fig. 5.33.: SEM images of $\{(Fe_{0.6}Co_{0.4})_{0.75}B_{0.2}Si_{0.05}\}_{96}Nb_4$ and $Fe_{76}B_{10}Si_9P$ particles are shown for a particle size class of 25 - 45 µm atomized at a melt superheat temperature of 350 K. Water-quenched particles were collected at a falling distance of 0.5 m. Particles atomized under conventional gas atomization and spray cone cooling conditions showed a nearly spherical particle morphology and a smooth surface topography, whereas water-quenched particles had a higher number of non-spherical particles, agglomerates, and rough surfaces. Water-quenched $Fe_{76}B_{10}Si_9$ particles were also covered by a thin oxide film due to corrosion.

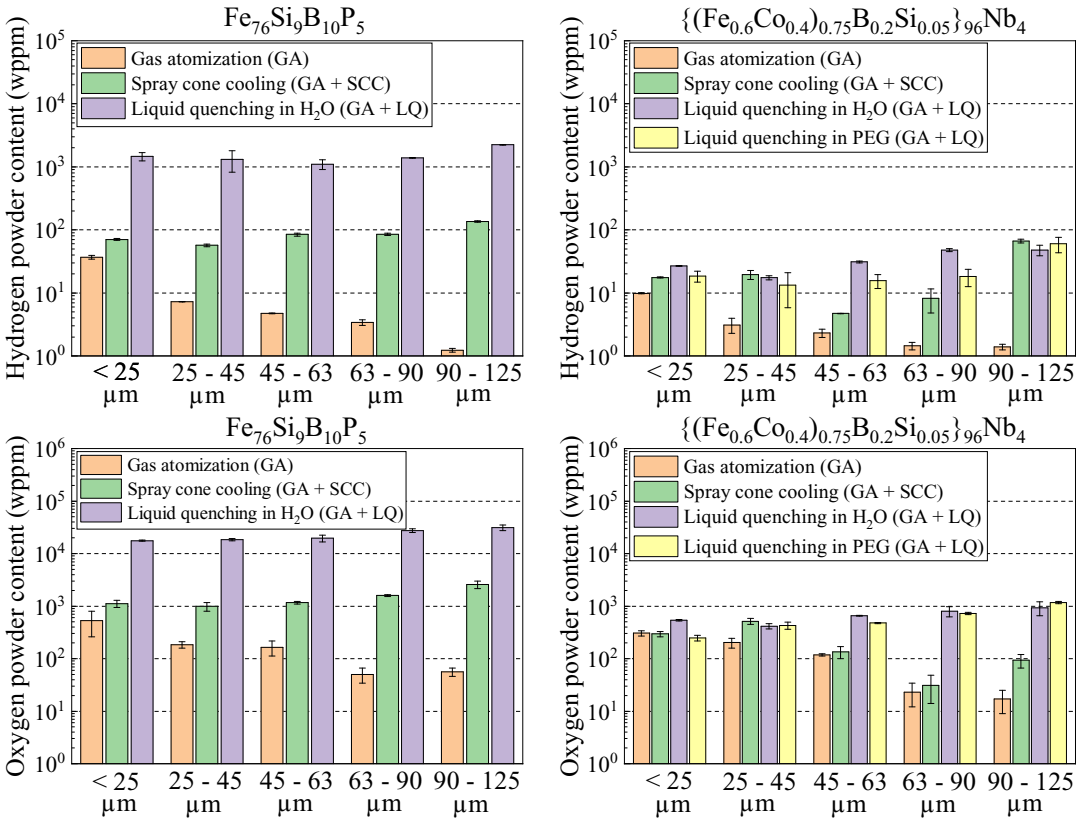

Fig. 5.34.: Hydrogen and oxygen measurements for the two soft ferromagnetic powders ($\{(Fe_{0.6}Co_{0.4})_{0.75}B_{0.2}Si_{0.05}\}_{96}Nb_4$ and $Fe_{76}B_{10}Si_9P_5$) at different particle size classes. The powders were initially dried at 423 K and then measured. The hydrogen and oxygen levels for the $Fe_{76}B_{10}Si_9P_5$ particles were typically an order of magnitude higher than in the $\{(Fe_{0.6}Co_{0.4})_{0.75}B_{0.2}Si_{0.05}\}_{96}Nb_4$ particles. The hydrogen level in poly(ethylene glycol) (PEG)-quenched $\{(Fe_{0.6}Co_{0.4})_{0.75}B_{0.2}Si_{0.05}\}_{96}Nb_4$ particles was nearly the same as for that of water-quenched particles.

DSC measurements recorded for water-quenched FeBSiP particles showed a second exothermic peak (Fig. 5.31). Two particle size classes (25 - 45 µm and 125 - 150 µm) were used to evaluate the cause of the peak. The powder samples were heated to two temperatures lying before (1023 K) and after (1353 K) the exothermic DSC peak. To demonstrate the effect of heat treatment, Fig. 5.35 shows XRD measurements for the particle size class of 125 - 150 µm, heated to the aforementioned temperatures. The XRD traces for the particle size class of 25 - 45 µm were excluded, since the results were in good agreement with the particle size class of 125 - 150 µm. Phase identification was performed to assess whether any phases containing hydrogen or oxygen had formed. Although additional phases were present at the lower temperature (1023 K), the determined phases for both temperatures were in agreement with Santhaweesuk [240] and were unaffected by the presence of hydrides or oxides. This concluded that improved properties such as the glass-forming ability and saturation magnetization were independent of hydrides and oxides.

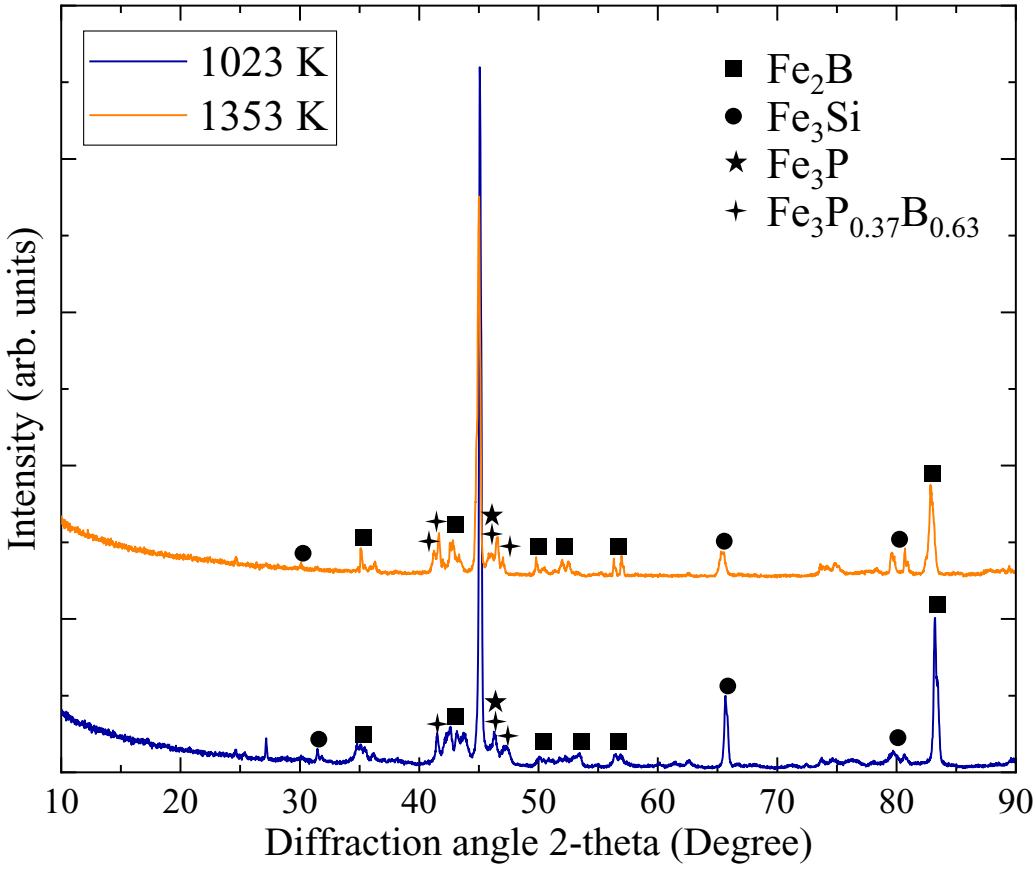

Fig. 5.35.: XRD measurements of $Fe_{76}B_{10}Si_9P_5$ powder at a particle size class of 125 - 150 µm after heating to 1023 K and 1353 K. To evaluate if the second peak was caused by hydrogen formation, a temperature before and after the exothermic DSC peak was chosen, corresponding to the DSC measurements in Fig. 5.31. The phase identification was consistent with the study by Santhaweesuk [240].

Hydrogen and oxygen measurements for the FeBSiP glass-forming alloy were performed for both particle size classes at the chosen temperatures corresponding to the exothermic DSC peak. At both temperatures, the oxygen content was nearly constant, whereas the hydrogen level for the heat-treated FeBSiP powder at 1353 K decreased from 2230 ± 15 ppm to 5 ± 1 ppm. At the lower temperature of 1023 K, the hydrogen level remained constant at 2099 ± 47 ppm. These values verified that the second peak could be attributed to the presence of hydrogen. To confirm the formation of hydrogen during liquid quenching, the hydrogen and oxygen levels were similarly measured for the heated FeCoBSiNb powders at the same particle size classes. Only one crystallization event was seen when the FeCoBSiNb glass-forming alloy was heated using the DSC technique (Fig. 5.31). The samples were heated above the crystallization event to a temperature of 1273 K. Similar to the FeBSiP results, the oxygen level remained unchanged, while the hydrogen level decreased only slightly from 60 ± 5 ppm to 40 ± 4 ppm.

Another important aspect was the evaluation of the soft magnetic properties, as it was shown in literature that the soft magnetic properties can be positively

influenced through hydrogen inducement. Fig. 5.36 shows the saturation magnetization as a function of particle size for the two soft ferromagnetic glass-forming alloys. Huang et al. reported that saturation magnetization is affected by local short-range order and can be altered by increasing the cooling rate and by hydrogen inducement [241]. Thus, the saturation magnetization was considered as an indicator of cooling rate and hydrogen content in this study. Saturation magnetization was measured in the electromagnetic unit emu g^{-1}. The widely used SI unit Tesla was calculated from the measured emu g^{-1} values using the bulk density of the two soft ferromagnetic glass-forming alloys.

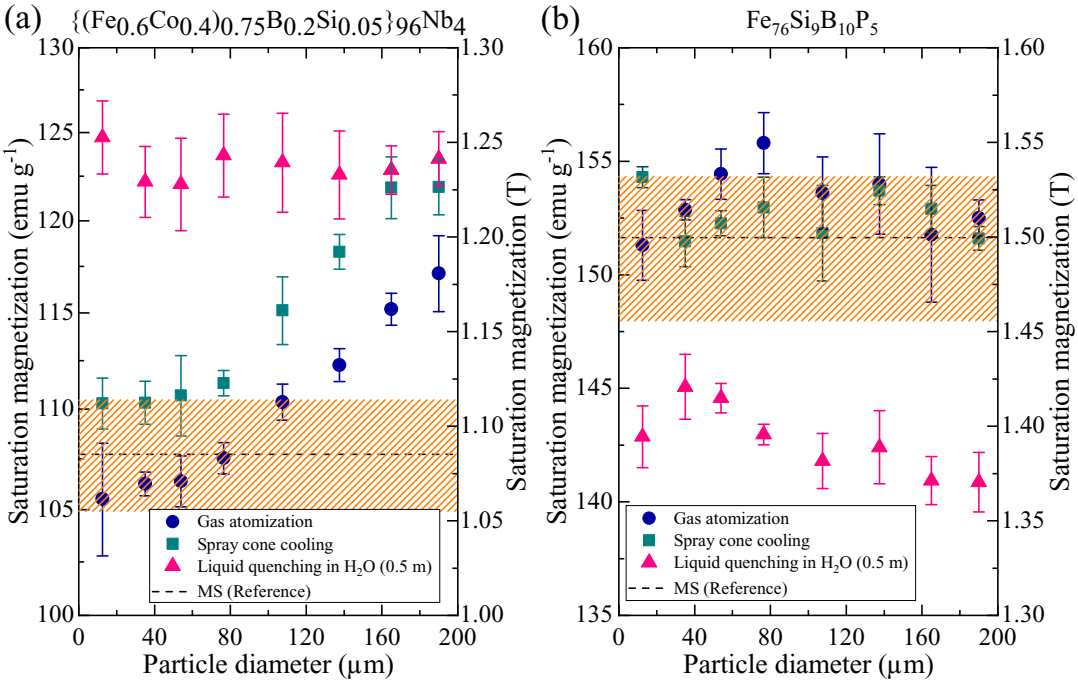

Fig. 5.36.: Saturation magnetization determined from Vibrating Sample Magnetometer measurements as a function of particle size for (a) $\{(Fe_{0.6}Co_{0.4})_{0.75}B_{0.2}Si_{0.05}\}_{96}Nb_4$ and (b) $Fe_{76}B_{10}Si_9P_5$ powders. Conventional gas atomization and the two developed cooling strategies were considered for this study. The saturation magnetization values for gas-atomized powders and different cooling strategies were compared with melt spinning (MS) reference samples. The dashed line represents the average saturation magnetization values and the upper and lower edges of the orange area defines the standard deviation.

The saturation magnetization for the FeCoBSiNb glass-forming alloy atomized under conventional gas atomization and spray cone cooling conditions increased with particle size. This resulted from the lower cooling rate experienced by larger particles, likely due to the presence of minor crystals in the amorphous matrix. Precipitated nano-crystals increased the soft magnetic properties. The saturation magnetization for water-quenched particles was significantly higher than for gas atomization or spray cone cooling and can be attributed to hydrogen inducement. Regardless of particle size, the saturation magnetization values

were nearly constant for the water-quenched FeCoBSiNb particles. The saturation magnetization values for the gas-atomized powders and different cooling strategies were compared with melt spinning references. The dashed line represents the average saturation magnetization values and the upper and lower edges of the orange area defines the standard deviation. The measured saturation magnetization values were compared with literature. For the melt spinning reference sample, the saturation magnetization values were consistent with high purity monolithic bulk samples [242], demonstrating that water-quenched particles with commercial purity can be produced with a similar or an improved saturation magnetization value.

Due to the lower corrosion resistance, the saturation magnetization of water-quenched FeBSiP particles was distinctly lower than that of the melt spinning reference and lower than particles atomized with conventional gas atomization as well as spray cone cooling. Particles atomized under conventional gas atomization and spray cone cooling conditions were consistent with the melt spinning reference. The values for these commercial purity powders and the melt spinning reference were also in good agreement with literature for high purity monolithic bulk samples and ribbons.

Densification of soft ferromagnetic powders primarily depends on the particle size distribution and the presence of an oxide layer around the particles [243]. Experiments have shown that particles in contact with water had a higher hydrogen and oxygen level (Fig. 5.34), potentially influencing the ability of the particles to mechanically bond during consolidation due to the large oxide layers around the particles. To determine the consolidation ability of the water-quenched particles, binder-free consolidation was performed using Spark Plasma Sintering on two particle size classes (< 25 µm and 25 - 45 µm). The particles sintered into toroidal rings resulted in a relative density $> 98\%$ (Tab.4.1) and were fully amorphous (Fig.5.37). Although an attempt was made to consolidate particles > 63 µm, the rings cracked during Spark Plasma Sintering. The sintered rings also fractured during handling and thus prevented mechanical testing. The consolidation ability and magnetic properties of the water-quenched particles were of primary interest in this investigation, while the mechanical properties were beyond the scope of this thesis. Recent research has demonstrated that the mechanical properties of soft ferromagnetic glass-forming alloys can be distinctly increased using a second metallic glass powder as a binder [244]. Powder consolidation generally requires a polymer binder that increases mechanical strength, but causes large core losses. For instance, Luan et al. reported a yield strength of ~ 500 MPa for nano-crystalline soft ferromagnetic glass-forming alloys that is typically sufficient for most industrial magnetic applications [244].

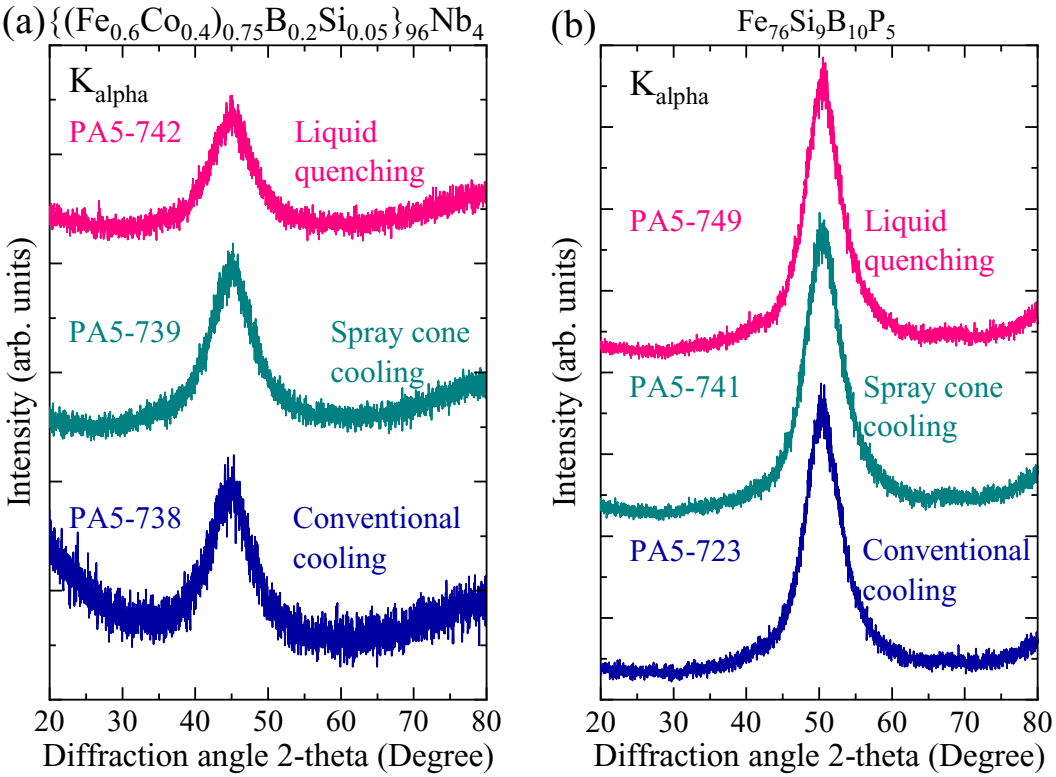

Fig. 5.37.: XRD measurements for the two soft ferromagnetic sintered rings: (a) $\{(Fe_{0.6}Co_{0.4})_{0.75}B_{0.2}Si_{0.05}\}_{96}Nb_4$ and (b) $Fe_{76}B_{10}Si_9P_5$. According to the XRD measurements, the sintered rings for a particle size class of 25 - 45 µm were fully amorphous after Spark Plasma Sintering, regardless of the cooling strategy applied.

The saturation magnetization values between as-atomized powders and sintered toroidal rings were compared in Fig. 5.38. Powders at two different particle size classes (< 25 µm and 25 - 45 µm) were atomized under gas atomization conditions and different cooling strategies. The sintered rings are represented by the green data points, while the blue data points are analogous to the data points as shown in Fig. 5.36. After consolidation of water-quenched FeCoBSiNb particles, the saturation magnetization slightly decreased. Since saturation magnetization values were slightly below the melt spinning reference, it was concluded that consolidation had a minor effect on the final saturation magnetization of this alloy system. For the FeBSiP sintered rings, the saturation magnetization of gas-atomized particles slightly decreased, while the saturation magnetization for particles that were in contact with water such as spray cone cooling and liquid quenching significantly decreased due to the presence of oxides.

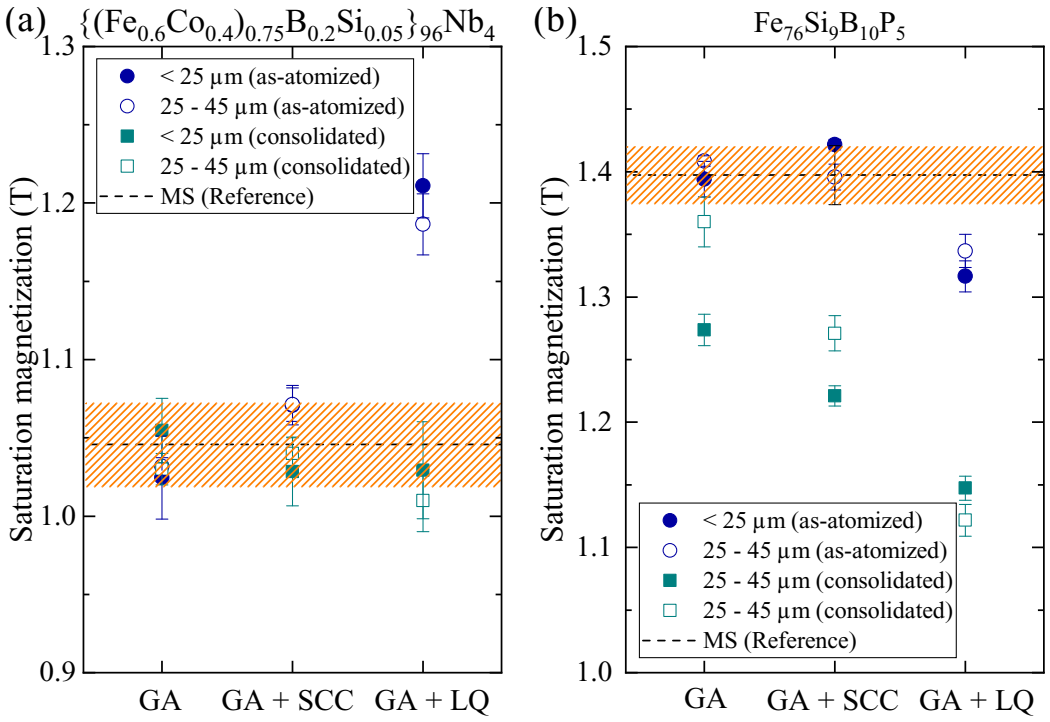

Fig. 5.38.: Saturation magnetization measured using a B-H curve tracer for (a) $\{(Fe_{0.6}Co_{0.4})_{0.75}B_{0.2}Si_{0.05}\}_{96}Nb_4$ and (b) $Fe_{76}B_{10}Si_9P_5$ as-atomized powders and sintered rings (after Spark Plasma Sintering) at two particle size classes (< 25 µm and 25 - 45 µm). The saturation magnetization values for the gas-atomized powders and different cooling strategies were compared with melt spinning (MS) reference samples. The dashed line represents the average saturation magnetization and the upper and lower edges of the orange area defines the standard deviation. GA, GA + SCC, and GA + LQ stand for conventional gas atomization, conventional gas atomization with spray cone cooling, and conventional gas atomization with liquid quenching, respectively.

For the powders that were in contact with water, further magnetic properties such as coercivity H_c and permeability μ were measured for the sintered rings (Fig.5.39). In the case of water-quenched particles, the coercivity of the sintered FeCoBSiNb rings slightly decreased, while the sintered FeBSiP rings showed a strong increase. The permeability of the FeCoBSiNb and FeBSiP sintered rings distinctively decreased for both spray cone cooling and liquid quenching.

The powder consolidation ability of water-quenched particles was also investigated. It was expected that a strong oxide film would form during liquid quenching, deteriorating the particle bonding ability during consolidation. Regardless of the cooling strategies used, fully amorphous toroidal rings were produced with a relative density of 98% using Spark Plasma Sintering. The saturation magnetization was nearly unchanged after consolidation. However, the coercivity slightly increased and the permeability decreased significantly.

This study focused on the development of novel cooling strategies and powder consolidation, including the determination of soft magnetic properties. Im-

proving the mechanical and magnetic properties was beyond the scope of this research. For instance, research over the last three decades has already shown that soft magnetic properties can be successfully improved by the introduction of nano-crystals [245–249]. This study showed that soft ferromagnetic powders with commercial purity could be successfully produced and subsequently consolidated while retaining an amorphous structure. These new insights provide an opportunity for the commercialization of soft ferromagnetic glass-forming alloys with commercial purity through the application of the developed cooling strategies.

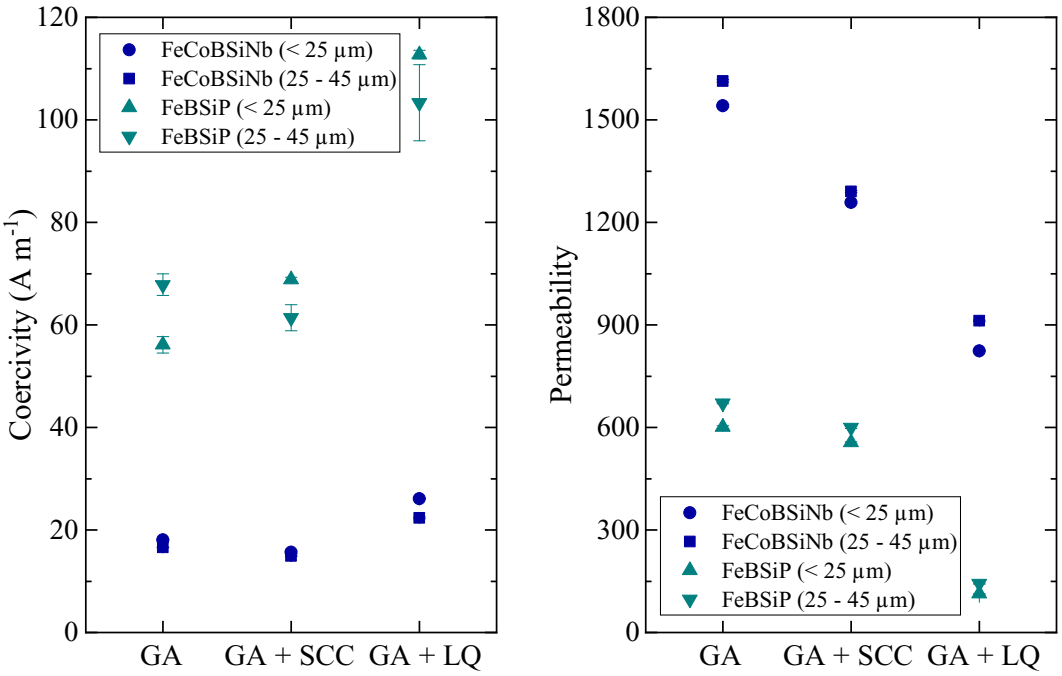

Fig. 5.39.: Coercivity and permeability was measured using a B-H curve tracer for (a) $\{(Fe_{0.6}Co_{0.4})_{0.75}B_{0.2}Si_{0.05}\}_{96}Nb_4$ and (b) $Fe_{76}B_{10}Si_9P_5$ sintered toroidal rings at two particle size classes (< 25 µm and 25 - 45 µm). GA, GA + SCC, and GA + LQ stand for conventional gas atomization, conventional gas atomization with spray cone cooling, and conventional gas atomization with liquid quenching, respectively.

5.4.3. Conclusion of spray cone cooling and liquid quenching as a cooling strategy

In powders produced with commercial purity, an increased amorphous fraction is required for subsequent powder consolidation. Many soft ferromagnetic glass-forming alloys with commercial purity are challenging to atomize into amorphous powders due to their low glass-forming ability and cooling rate limitations. The aim of this section was therefore to develop novel cooling strategies to increase the heat transfer coefficient and thus to increase the cooling rate during melt atomization. The results can be summarized as follows:

- Spray cone cooling was an improvement compared to conventional gas

atomization, as the cooling rate could be significantly increased for both soft ferromagnetic powders. The FeCoBSiNb particles were fully amorphous up to 125 µm, whereas particles atomized under conventional gas atomization were fully amorphous up to 63 µm. FeBSiP particles were partially-crystalline even for the smallest particle size class (< 25 µm) under conventional gas atomization, while spray cone cooled particles were synthesized into an amorphous state up to 45 µm.

- Liquid quenching extended the process window of conventional gas atomization, resulting in the highest cooling rate for both soft ferromagnetic glass-forming alloys. The particles were fully amorphous for the entire powder range (< 200 µm) regardless of particle collection distance and quench media used.

- Some new results were found in experiments performed with distilled water. A second exothermic DSC peak was observed for water-quenched FeBSiP particles. The enthalpy of crystallization of water-quenched FeCoBSiNb particles was distinctly higher than the melt spinning reference and the saturation magnetization significantly increased. These findings can be attributed to the presence of hydrogen, as heat treatment experiments showed that hydrogen in the powder disappeared after the sample was heated to a temperature above the second exothermic peak. Hydrogen in metallic glasses is rarely explored in literature. A few studies reported that hydrogen led to structural changes in metallic glasses with improved glass-forming ability and soft magnetic properties.

- Amorphous torodial rings with a relative density of 98% using Spark Plasma Sintering were produced independent of the cooling strategy applied.

5.5. Combining the four cooling strategies together: a comparison

During melt atomization, the highest cooling rates were found in the following decreasing order: liquid quenching, spray cone cooling, and in the increase of the melt superheat temperature. The cooling rate in hot gas atomization remained constant or slightly decreased. These experimental findings were supported with a one-dimensional model where cooling curves for the two soft ferromagnetic glass-forming alloys are compared in one diagram (Fig. 5.40). Model equations are described in sec. 3.2.2 and assumptions as well as simplifications are listed in sec. 5.2.5. In the case of the two soft ferromagnetic glass-forming alloys, droplet solidification occurred without phase change. Conventional cooling curves are labelled as GA, while liquid quenching experiments are labelled as GA + LQ. All data were generated with a variable gas temperature as presented in Eq. 5.5. Ambient temperature cooling curves (RT) were computed with an initial gas temperature T_{G_i} of 300 K and a final gas temperature T_{G_f} of 350 K, while the hot gas atomization cooling curves (HG) were computed

with a T_{G_i} of 600 K and a T_{G_f} of 350 K. For the sake of readability, a melt superheat temperature of 350 K was only considered, as it has been shown that a higher melt superheat temperature had a minor influence on cooling rate. A few other assumptions in the model were required for liquid quenched particles than for conventional cooling. An identical solidification path was followed in the case of liquid quenching until the droplets reached the particle collection distance. The distances in the model were 0.5 m and 0.7 m that corresponded to the experimental setup. For the droplet velocity, the final term that accounts for buoyant forces in the differential equation (Eq. 3.8) needed to be considered. After the particle collection distance was reached, the effects of cooling in water were considered through a different Nusselt number correlation. The Nusselt number was critical in the simulation of liquid quenching. The following equation that incorporates film boiling reported by Dhir et al. [250] was implemented in the model to describe the liquid quenching effects:

$$Nu = 0.8 \cdot \left[\frac{g\rho_v (\rho_l - \rho_v) h_{fg} d_p^3}{\eta_v k_v \left(T_p - T_{sat}\right)} \right]^{1/4} + 0.8 \left(Re\right)^{1/2} \tag{5.17}$$

where ρ_v, η_v, k_v are the density, dynamic viscosity, and thermal conductivity of the vapor film. The variables ρ_l, h_{fg}, T_p and T_{sat} are the density, latent heat of vaporization, molten droplet temperature and saturation temperature of the quench medium.

Eq. 5.17 calculates the Nusselt number as a function of droplet velocity and is valid for Reynolds numbers between 1200 and 29000. Eq. 5.17 was developed for droplets with a diameter of 19 mm and 25.4 mm which may have affected the accuracy of the droplet solidification model. Most Nusselt number correlations for spheres moving through a liquid are accurate for diameters $>$ 19 mm, making it difficult to find an appropriate correlation that can be used for liquid quenching in gas atomization. Although Eq. 5.17 has limitations when applied to gas atomization, it was used to qualitatively show the effect of liquid quenching on droplet solidification. For a 100 µm droplet, results in Fig. 5.40 have shown that liquid quenching yielded in faster cooling compared to conventional cooling. By contrast, a 20 µm droplet already solidified before reaching the liquid quench medium regardless of particle collection distance. Liquid quenching provided a great opportunity to produce amorphous particles. Droplets larger $>$ 100 µm were fully liquid before impacting the liquid quench medium. This increased the possibility that these molten droplets solidified into an amorphous state through the higher cooling rate experienced. This was consistent with experimental results where both soft ferromagnetic powders were fully amorphous up to 200 µm. The alignment of the hot gas atomization cooling curve (red) and the ambient temperature cooling curve (dark blue) confirmed that hot gas atomization provided comparable cooling rates to atomization at ambient temperature regardless of droplet diameter. For a 20 µm droplet, fluctuations in the cooling curves at both quenching distances are seen. Currently, these fluctuations are challenging to interpret and need to be investigated further. Although these fluctuations existed, they were only present below the glass transition temperature, meaning that the droplets already devitrified into an amorphous

state and were unaffected by the deviations.

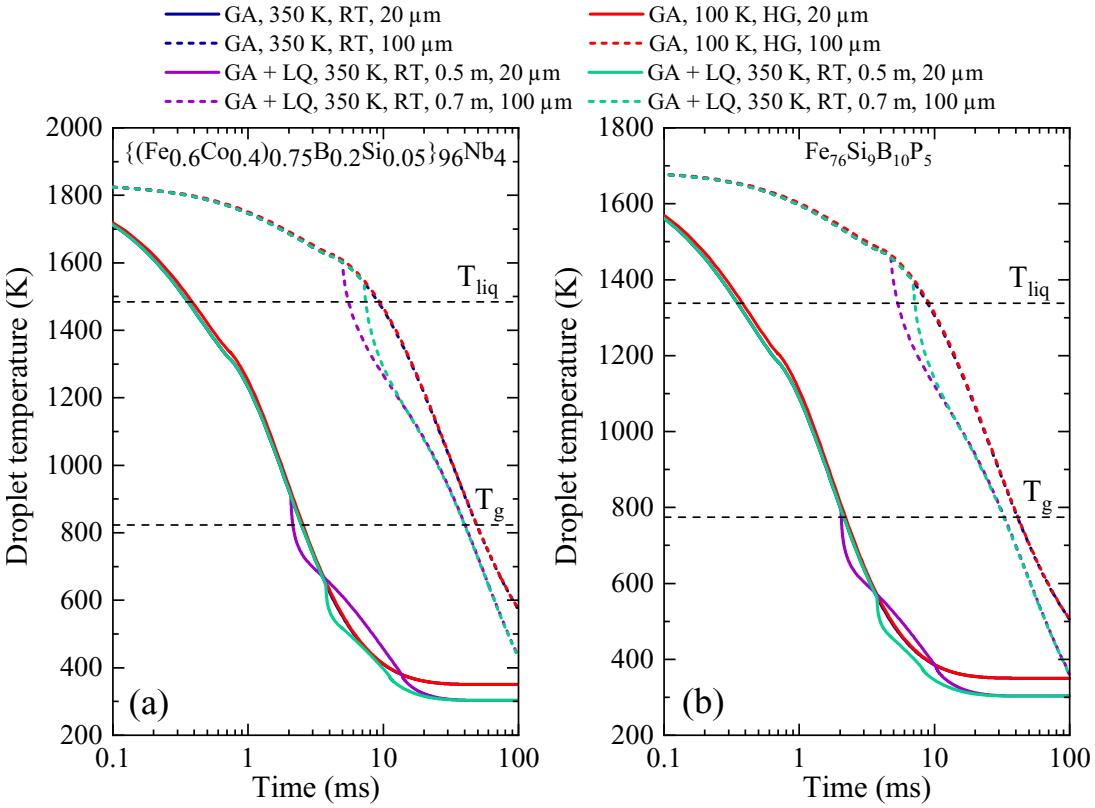

Fig. 5.40.: Droplet temperature as a function of atomization time for (a) $\{(Fe_{0.6}Co_{0.4})_{0.75}B_{0.2}Si_{0.05}\}_{96}Nb_4$ and (b) $Fe_{76}B_{10}Si_9P_5$ droplets. The abbreviations HG and RT stand for hot gas atomization (600 K) and atomization at ambient temperature (300 K). GA and GA + LQ stand for conventional gas atomization and conventional gas atomization with liquid quenching at falling distances of 0.5 m and 0.7 m. The Nusselt number for the liquid quenching case was determined with Eq. 5.17. The amorphous droplets were modeled without phase change. The temperature values were calculated with the equation presented in sec. 3.2.2. Argon was used as the cooling gas. An initial droplet velocity of 1 $m\,s^{-1}$, a droplet starting position of 0.12 m with maximum radiation (emissivity $\varepsilon = 1$) and a melt superheat temperature of 350 K was assumed. Model details can be found in sec. 3.2.2.

Process parameters depended on the cooling strategies used that led to different cooling conditions and thus to different cooling rates and amorphous fractions. The main findings have been combined in one diagram to compare results from each cooling technique as well as to compare results with common cooling methods in use today (Fig. 5.41). For various gas atomization factors, the table describes the effectiveness of each method to dissolve potent nucleation sites, reduce particle size, and increase the heat transfer coefficient. The green and red arrows indicate positive and negative effects on gas atomization

factors. The symbols demonstrate enhanced (↑), decreased (↓), and neutral (o) effects. The number of arrows indicates the magnitude of the effect on the presented parameters. A strong correlation between particle size and cooling rate was seen, as smaller particles led to higher cooling rates. An increased melt superheat temperature led to a slight decrease in particle size. This contradicted literature, as some authors reported an unaffected particle size, while others presented a strong decrease with particle size (denoted as an asterisk * in the diagram). Since some droplets agglomerated during liquid quenching, particle size evaluation was inaccurate (seen in the diagram as two asterisks **). The cooling rate depended on droplet diameter and gas-to-melt mass flow ratio (GMR).

From Fig. 5.41, it was apparent that even the developed cooling strategies were unable to achieve all desired particle characteristics. A balanced set of process parameters need to be developed in order to obtain ideal powder properties. The ideal gas atomization process would produce a high yield of fine, amorphous and spherical particles.

Factors/Parameters	Current knowledge based on gas atomization			New knowledge based on cooling strategies			
	Increasing gas pressure	Mixing of gas (e.g. He in Ar)	Increasing GMR ($\dot{m}_L \uparrow; \dot{m}_G = \text{const}$)	Increasing superheat temperature	Increasing gas temperature (Hot gas atomization	Applying spray cone cooling	Applying liquid quenching
Gas consumption	↑	o	o	o	↓↓	o	o
Energy consumption	o	o	o	↑	↑	o	o
Melt viscosity	-	-	-	↓	-	-	-
Particle size	↓	↓	↓	o *	↓↓	o	↑**
Particle shape factors	↓	↓	↓	↑	↑	o	↓
Relative velocity	↑	↑	o	o	↑	-	-
Temperature difference (melt droplet/gas)	↑	↑	↑	↑	↓	↑↑	↑↑↑
Heterogeneous nucleation	-	-	-	o	-	-	-
Heat transfer coefficient	↑	↑↑	↑	o	o	↑↑	↑↑↑
Cooling rate	↑	↑↑	↑	o	o	↑↑	↑↑↑
Amorphous fraction	↑	↑↑	↑	o	o	↑↑	↑↑↑
Amorphous yield	↑	↑↑	↑	o	↑	↑↑	↑↑↑

Fig. 5.41.: Key gas atomization factors/parameters are divided into two categories: the latest atomization strategies in use today and the presented novel cooling strategies. The green and red arrows indicate positive and negative effects and the number of arrows describe the intensity of the effect. The symbols demonstrate enhanced (↑), decreased (↓), and neutral (o) effects. The hyphen (-) represents factors that have no relationship to the strategies. One asterisk (*) denotes results that are inconsistent with literature, and two asterisks (**) represent innacurate particle size measurements (see sec. 5.5).

CHAPTER 6

Conclusion and outlook

This PhD thesis provided new process guidelines for the atomization of soft ferromagnetic glass-forming alloys with commercial purity feedstock and bridges the gap between glass-forming alloys and melt atomization for the first time. Most studies relating to amorphous powders are only focused on subsequent powder consolidation, frequently ignoring the fact that powder synthesis is the critical process step for final material bulk properties. Therefore, a fundamental understanding of amorphous powder properties is key to success for the large-scale commercialization of metallic glasses.

6.1. Conclusion

Soft ferromagnetic glass-forming alloys are generally used in critical components such as electric motors, generators, transformers, batteries, notebook PC's, and cellular phones etc. These alloys may have a global societal impact on reducing power consumption and CO_2 emissions [251, 252]. The atomization of commercial purity soft ferromagnetic glass-forming alloys is very challenging and may lead to crystallization due to cooling rate limitations and low glass-forming ability. The production of high purity soft ferromagnetic glass-forming alloys has been successfully demonstrated, but is undesirable from an ecological and economic point of view. To successfully atomize commercial purity soft ferromagnetic glass-forming alloys, a process window in gas atomization was extended to allow for the production of amorphous powders that are typically inaccessible through conventional gas atomization. For this purpose, four different cooling strategies were developed to dissolve potent nucleation sites in the melt, reduce particle size, and increase heat transfer coefficient. The following cooling strategies were considered: (i) increasing the melt superheat temperature, (ii) hot gas atomization, (iii) spray cone cooling, and (iv) liquid quenching.

6.1.1. Increasing the superheat temperature

In sec.5.1, the influence of an increased melt superheat temperature on thermophysical properties, as well as particle size, size distribution, and shape on four different glass-forming alloys was discussed: (i) $\{(Fe_{0.6}Co_{0.4})_{0.75}B_{0.2}Si_{0.05}\}_{96}Nb_4$, (ii) $Fe_{76}B_{10}Si_9P_5$, (iii) $Cu_{47}Ti_{33}Zr_{11}Ni_6Si_1Sn_2$, and (iv) $Zr_{59.3}Cu_{28.8}Al_{10.4}Nb_{1.5}$. To extend the range of thermophysical properties, a Zr-based and Cu-based glass-forming alloy were also considered for the particle shape study.

Crystalline vs. amorphous state

Results showed that an increased melt superheat temperature led to a higher amorphous fraction for the two soft ferromagnetic powders. However, the effect was relatively small compared to studies on containerless droplet techniques. A melt superheat temperature of 350 K was recommended for both soft ferromagnetic powders, as it was shown that an increase in melt superheat temperature had a minimal effect on amorphous fraction. The particle size and particle size distribution was independent of melt superheat temperature. Although a decrease in particle size was demonstrated, the change in particle size was relatively small for all glass-forming alloys.

Production of spherical particles

An increased number of spherical particles was achieved by increasing the melt superheat temperature. A strong increase in sphericity and aspect ratio for the ZrCuAlNb glass-forming alloy was observed, whereas the other three glass-forming alloys showed only a small improvement in particle shape. The ZrCuAlNb glass-forming alloy showed by far the highest amount of non-spherical particles. A high number of non-spherical particles is generally undesirable for subsequent powder consolidation due to a reduced powder flowability (e.g. in Molten Injection Molding and Layer Additive Manufacturing). The amount of irregular ZrCuAlNb particles was attributed to the high melt viscosity, preventing the formation of spherical droplets. A melt superheat temperature of 450 K was recommended for all four glass-forming alloys to achieve powders with a high fraction of spherical particles.

Increasing the melt superheat temperature can only be regarded as a cooling strategy to a limited extent, as the amorphous fraction only slightly increased. However, it is a valuable design method to improve particle shape.

6.1.2. Production of fine powder through hot gas atomization

For the large scale commercialization of metallic glasses, hot gas atomization is a promising design tool. Gas consumption was reduced up to $\sim$ 50%, particle size was significantly decreased, amorphous fraction was retained, and the amorphous yield was increased up to $\sim$ 20% for the same gas-to-melt mass flow ratio (GMR) (sec. 5.2). For instance, the mass median particle diameter of the FeCoBSiNb glass-forming alloy decreased from 44 µm (GMR = 5.3) to 39 µm (GMR = 3.2) using hot gas atomization, while the mass median particle diameter of the Cu-6wt%Sn alloy decreased from 30 µm (GMR = 5.1) to 22 µm (GMR = 2.9). However, the particle shape slightly decreased ($\sim$ 5%) due to the attachment of semi-solidified droplets on larger droplets (satellites).

According to XRD and DSC analyses, the amorphous fraction of the FeCoBSiNb glass-forming alloy was nearly unaffected by hot gas atomization when compared to ambient temperature atomization, concluding that the cooling rate

was similar for both cases. The cooling rate depended on heat transfer coefficient and droplet size. The heat transfer coefficient was mainly affected by the relative velocity and temperature gradient between the melt droplet and surrounding gas. Hot gas atomization yielded in a higher relative velocity due to the higher gas velocity, caused by a decrease in gas density. Elevated gas temperatures simultaneously resulted in a smaller temperature gradient. These two effects compensated for each other, leading to a nearly unchanged cooling rate. These assumptions were supported by cooling rate correlations for molten metal gas atomization. Analytical approaches have shown that the cooling rate mainly depended on droplet size and on GMR (sec.5.3). The effect of initial gas temperature on cooling rate was negligible.

6.1.3. Spray cone cooling and liquid quenching

The FeCoBSiNb particles were fully amorphous up to 125 µm using spray cone cooling, while particles atomized under conventional gas atomization were only fully amorphous up to 63 µm. The spray cone cooled FeBSiP particles were fully amorphous up to 45 µm, whereas even the smallest particle size class atomized under conventional gas atomization was partially-crystalline. The spray cone cooling method was characterized by easy handling and low costs, demonstrating its potential use in commercial powder manufacturing. The highest amorphous fraction was achieved using liquid quenching. The particles were fully amorphous for the entire powder range (< 200 µm), regardless of the quench media and particle collection distance used.

Most of the liquid quenching experiments were performed using distilled water. A second exothermic DSC peak was detected for water-quenched FeBSiP particles. The enthalpy of crystallization of water-quenched FeCoBSiNb particles were significantly higher than for the melt spinning reference, while the saturation magnetization significantly increased. These new findings were attributed to hydrogen, as heat treatment experiments showed that hydrogen content disappeared after the powder sample was heated to a temperature above the second exothermic peak. Some studies have reported on the positive effect of hydrogen, as it can lead to structural changes with improved glass-forming abilities and soft magnetic properties.

The powder consolidation ability was also validated, as it was assumed that an oxide layer was formed around the particles during liquid quenching. Consolidation experiments via Spark Plasma Sintering demonstrated that the production of fully amorphous toroidal rings was feasible even though the oxygen content in the powders ranged from $\sim 10^2$ to 10^4 ppm. The effect of the cooling strategies on the soft magnetic properties were investigated. The saturation magnetization after consolidation remained nearly constant while the coercivity slightly increased and the permeability decreased significantly. Dense, amorphous toroidal rings with commercial feedstock purity were produced. These sintered rings may be used for widespread commercialization in various electronic applications in the future.

The central research question of this PhD thesis was to investigate whether the

cooling rates of glass-forming alloys could be significantly increased by applying innovative cooling strategies during gas atomization. Liquid quenching was the most efficient method to increase the cooling rates and thus the amorphous fraction.

6.2. Outlook

The melt superheat temperature experiments have shown that the atomization of the ZrCuAlNb glass-forming alloy resulted in a higher amount of non-spherical droplets compared to the other glass-forming alloys. The data suggested that non-spherical particles were the result of a high melt viscosity or of a surface oxide layer that formed around the melt droplets. These droplets are undesirable for use in processes such as Layer Additive Manufacturing as they reduce powder flowability. The question then naturally arises: How many of these non-spherical particles are permissible in Layer Additive Manufacturing and how do they alter the final bulk properties?

Another method to increase the cooling rate and the particle shape may be the development of high-velocity combustion flame atomization. The implementation of a high velocity combustion flame (e.g. a mixture of kerosene and air) can provide a flame speed of up to 1600 $\mathrm{m\,s^{-1}}$ and a temperature of up to 1900 K as commonly seen in turbine technologies. The high flame velocity and temperature would result in small, spherical droplets with a decreased melt viscosity and surface tension at the melt stream point of impact.

The hot gas temperature study was limited to temperatures of around 600 K due to a maximum temperature restriction from the heat exchanger ($\sim$ 825 K) and isolation issues. Since studies have shown that an increased gas temperature significantly improved particle shape for highly viscous melts, gas temperatures of up to 1300 K may be beneficial for the production of spherical and amorphous powders [130, 253]. Applying elevated gas temperatures to glass-forming alloys raises two questions: Will the particle size decrease or can we expect an asymptotic particle size limit, and will the particle shape factors continue to decrease due to satellite formation?

Further experiments carried out at elevated gas temperatures are required to extend the proposed cooling rate correlation in sec. 5.3. Cooling rate calculations were supported by CFD simulations [191]. A one-way thermal coupling model was developed for crystalline alloys and extended to a two-way thermal coupling model. The two-way thermal coupling model considered heat transfer between the surrounding gas and the melt droplets in both directions. These calculations failed to converge with increasing GMR due to non-linearities in the defined equations with respect to momentum and heat exchange. One of the conclusions drawn was that the finite element method (FEM) was inadequate for this particular fluid flow and heat transfer problem. The finite volume method (FVM) could be used instead. Although this model is not inherently superior to FEM with respect to computational time and accuracy, it may be able to solve these non-linearities. A successful model mainly depends on the

efficient and stable handling of time-stepping to accurately solve large systems of linear equations. Why is this important? In addition to the prediction of CCT/TTT curves, the estimation of critical cooling rates is required to compute amorphous fractions. Powder manufacturers would greatly benefit from these numerical models as process and cooling conditions can be adjusted to customize the amorphous powder fraction. These droplet solidification calculations are still in embryonic stages, since thermophysical properties such as specific heat capacity and viscosity in the supercooled liquid region are rarely available.

Strategies to increase the amorphous fraction could also include the use of fluxing agents to improve the glass-forming ability [254]. Impurities can be trapped by B_2O_3 if the major constituent elements in the melt have an affinity to oxygen lower than that of boron [88, 106, 254]. For instance, the critical cooling rate for a $Fe_{40}Ni_{40}P_{14}B_6$ glass-forming alloy decreased by three orders of magnitude and the supercooled liquid region could be increased up to $\sim$ 30 K when fluxed with B_2O_3 [254, 255]. Recently, molten salts have become the subject of extensive research [256]. Chloride salts such as NaCl, KCl, $MgCl_2$, and $CaCl_2$ can be selected based on certain thermodynamic considerations. These salts typically increase the wettability of the melt, enhancing the separation of oxide inclusions [254]. Chloride fluxing agents are capable of floating on the surface of the melt and subsequently absorbing oxide impurities via agglomeration [254]. They then decompose to generate cationic ions, forming new low-density oxides. The new oxides combine with residual oxides to form clathrate compounds, leading to the removal of additional oxide impurities in the melt, and thus to a cleaner alloy [254].

Since hydrogen had a positive effect on the glass-forming ability and soft magnetic properties of soft ferromagnetic powders, reactive gases could be a valuable tool to increase the cooling rate and thus the amorphous fraction. A mixture of argon and hydrogen gas (forming gas) is useful if safety regulations are met. The hydrogen content should be below a value of 5.5%, as it is highly flammable and explosive. A combination of 2-3% hydrogen and argon could be used as a reducing agent to minimize the presence of moisture and oxygen. Hydrogen is the lightest element and thus would increase the gas velocity, producing smaller particles with a higher amorphous yield.

The fundamental mechanisms of hydrogen enhancement are iinsufficiently understood at present and require further scientific study. It is unclear whether hydrogen inducement is governed by adsorption, absorption or even diffusion. Hydrogen diffusion occurs through internal stresses at the melt droplet interface when the droplets impinge on the quench medium. The potential for hydrogen adsorption and absorption may increase with decreasing liquid quench media temperature. It would be reasonable to calculate the droplet temperature when impinging on the liquid, as the temperature of the droplet surface determines the physical mechanisms of hydrogen inducement. An attempt has been made to incorporate such calculations into a developed droplet solidification model. Correlations for the heat transfer coefficient are difficult to obtain

in literature [250, 257–259]. Droplet temperature calculations were run, but provided inaccurate heat transfer coefficient values due to an invalid Reynolds number regime. Numerical models incorporating experimentally determined film boiling correlations would be beneficial to estimate the droplet cooling behavior when impinging on a quench medium.

Liquid water quenching with respect to vapor explosion can be used to further increase the cooling rate. Water vapor explosion typically occurs in industries such as nuclear energy if hot molten metal accidentally makes contact with water [260]. This process is safety sensitive, since water vaporizes at an explosive rate whereby a cloud of water vapor generated can attain very high pressures in fully unconfined locations [260]. Quenching of molten droplets is regarded as 'fine-fragmentation' that must take place for rapid water vapor formation where particle sizes are usually < 10 µm. Due to safety issues, it is recommended to synthesize amorphous droplets with the single droplet technique, allowing for small-scale experiments. It is expected that 'fine-fragmentation' occurs if the water temperature is heated to 353 K and is in contact with salt additives as a cooling medium. Possible solutions could be chloride, calcium, and magnesium chloride solutions. For instance, it has been shown that the cooling rate of Al89Si11 (wt%) droplets ranged from 10^7 to 10^8 $K\,s^{-1}$ for corresponding particle sizes between $\sim$ 15 - 250 µm if lithium chloride is used as a coolant [261]. The heat transfer coefficient during film boiling significantly increased, causing an unstable vapor film, thus leading to a film collapse and subsequent spontaneous vapor explosion.

A last thought is the consideration of different quench media such as ionic liquids [262, 263], water-soluble polymers [264], and mineral oils [265]. It is expected that these quench media would provide almost the same cooling rates and amorphous fractions, as shown in previously reported in-house experiments on $Cu_{47}Ti_{33}Zr_{11}Ni_6Si_1Sn_2$, and $Zr_{59.3}Cu_{28.8}Al_{10.4}Nb_{1.5}$ glass-forming alloys using impulse atomization [266]. Previous results showed that the amorphous fraction was constant regardless of the quench media used. It is also expected that the oxygen level will decrease, leading to lower corrosion rates for soft ferromagnetic powders and finally improving the consolidation ability.

APPENDIX A

Experimental setups

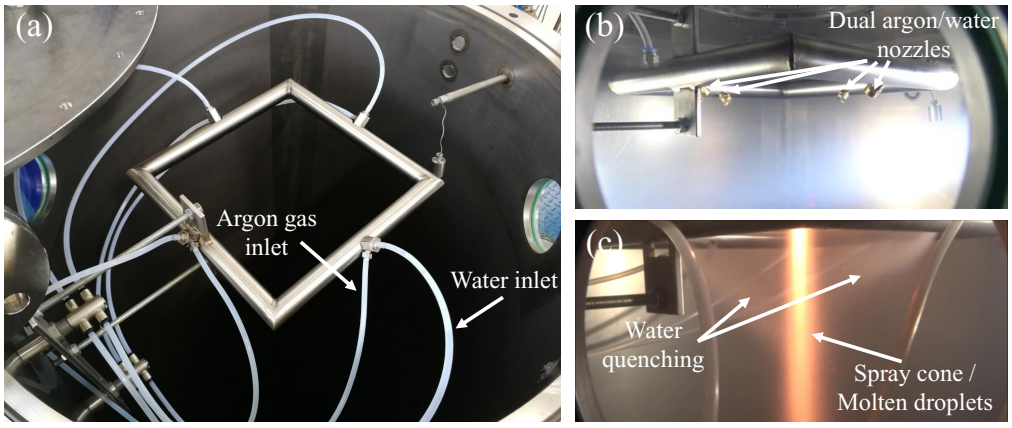

Fig. A.1.: Experimental setup for the spray cone cooling strategy: (a) top view of the attached setup in the spray chamber, (b) nozzle configuration for the dual argon/water nozzles (KL1, DIVA Sprühtechnik GmbH), and (c) melt atomization under real conditions. Four nozzles at an incident angle of 45° were used. The nozzles were arranged at 90° relative to each other, allowing spray cone cooling from all angles. The blurred image in (c) is due to vapor formation.

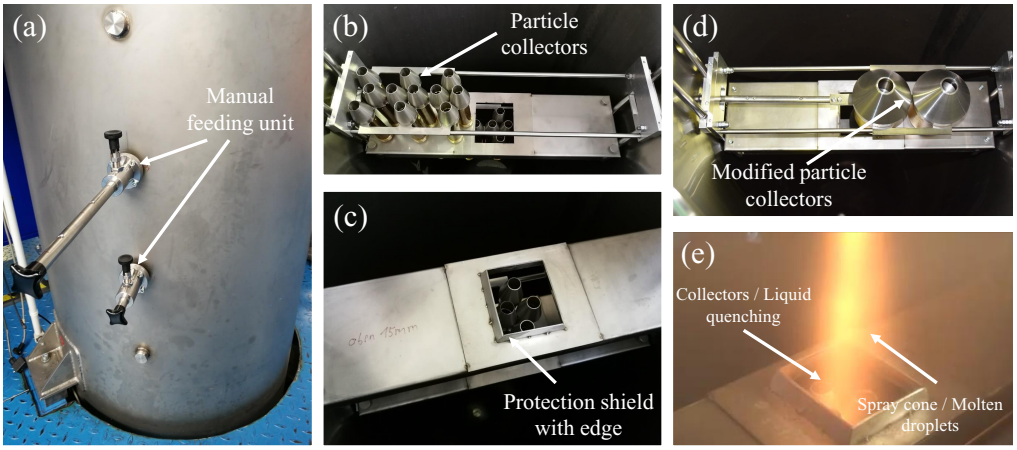

Fig. A.2.: Experimental setup for the liquid quenching cooling strategy: (a) manual feed unit to control particle collectors containing different quench media at two collection distances of 0.5 m and 0.7 m, (b) collector arrangement, (c) protective shield with ledge to prevent particle re-entry, (d) modified particle collectors to increase the numbers of particles collected, and (e) melt atomization under real process conditions. The blurred image is due to vapor formation.

APPENDIX B

Thermophysical liquid and gas properties

Tab. B.1.: Thermophysical properties for a Cu-6wt%Sn (CuSn6) and an Al-4.5wt%Cu (Al4.5Cu) crystalline alloy. The Al4.5Cu and CuSn6 thermophysical property values were used in sec. 3.2.2 and sec. 5.2.5, respectively.

Parameter	Unit	AlCu4.5	Cu6Sn
Liquidus temperature T_{liq}	K	921 [267]	1312 [40]
Solidus temperature T_s	K	845 [225]	1173 [40]
Eutectic temperature T_e	K	821 [267]	
Liquid density ρ_l	$kg\,m^{-3}$	2540 [225]	8849*
Specific heat capacity (Liquid) $c_{p,l}$	$J\,kg^{-1}\,K^{-1}$	1178 [225]	475 [40]
Specific heat capacity (Solid) $c_{p,s}$	$J\,kg^{-1}\,K^{-1}$	910 [225]	422 [40]
Latent heat of fusion ΔH_M	$J\,kg^{-1}$	381 774 [267]	187 890 [40]
Equilibrium partition coefficient y	-	0.17 [156]	0.20*
Wetting angle Θ_l	°	24.6 [267]	138 [268]
Solid-liquid interfacial energy γ	$J\,m^{-2}$	0.1634 [267]	0.064*

* Data were taken from Wieland-Werke AG.

Tab. B.2.: Thermophysical properties for a $\{(Fe_{0.6}Co_{0.4})_{0.75}B_{0.2}Si_{0.05}\}_{96}Nb_4$ (FeCoBSiNb) and a $Fe_{76}B_{10}Si_9P_5$ (FeBSiP) glass-forming alloy. The values for the two soft ferromagnetic glass-forming alloys were used in sec. 5.5.

Parameter	Unit	FeCoBSiNb	FeBSiP
Liquidus temperature T_{liq}	K	1484 [23]	1338 [198]
Glass transition temperature T_g	K	823*	774*
Liquid density ρ_l	$kg\,m^{-3}$	7710 [23]	7197 [198]
Specific heat capacity (Liquid) $c_{p,l}$	$J\,kg^{-1}\,K^{-1}$	742 [23]	680 [198]

* DSC measurements performed by author.

Tab. B.3.: Thermophysical properties and velocity fit functions taken from a two-dimensional CFD simulation for argon as a cooling gas [191]. Thermophysical properties were taken from Ref. [269].

Parameter	Unit	Fit function/value
Density ρ_g	$\mathrm{kg\,m^{-3}}$	$101\,325/(208 \times \mathrm{T})$
Viscosity η_g	Pa s	$6.38^{-2} + 8.87^{-2} \times \mathrm{T} - 5.08^{-5} \times \mathrm{T}^2$ $+ 2.14^{-8} \times \mathrm{T}^3 - 3.64^{-12} \times \mathrm{T}^4/1\,000\,000$
Specific heat capacity $c_{p,g}$	$\mathrm{J\,kg^{-1}\,K^{-1}}$	520
Thermal conductivity k_g	$\mathrm{W\,m^{-1}\,K^{-1}}$	$1.21^{-2} + 6.98^{-2} \times \mathrm{T} - 4.03^{-5} \times \mathrm{T}^2$ $+ 1.7^{-8} \times \mathrm{T}^3 - 2.87^{-12} \times \mathrm{T}^4/1\,000$
Velocity (RT) $u_{g,RT}$	$\mathrm{m\,s^{-1}}$	$354\,771 \times (\mathrm{z}_d \times 1\,000)^{-1.385}$
Velocity (HG) $u_{g,HG}$	$\mathrm{m\,s^{-1}}$	$23.159 \times \mathrm{z}_d^{-1.584}$

Tab. B.4.: Thermophysical properties for liquid water and water vapor. The data were taken for the liquid quenching model presented in sec. 5.5.

Parameter	Unit	Value
Initial liquidus temperature $T_{liq,i}$	K	303 (This work)
Saturation temperature T_{sat}	K	373 (This work)
Density (Liquid) ρ_l	$\mathrm{kg\,m^{-3}}$	997 [270]
Density (Vapor) ρ_{vap}	$\mathrm{kg\,m^{-3}}$	0.5975 [270]
Specific heat capacity (Vapor) $c_{p,vap}$	$\mathrm{J\,kg^{-1}\,K^{-1}}$	2042 [270]
Latent heat of fusion (Vapor) $\Delta H_{M,vap}$	$\mathrm{J\,kg^{-1}}$	2 256 700 [270]
Thermal conductivity (Vapor) k_{vap}	$\mathrm{W\,m^{-1}\,K^{-1}}$	0.05476 [270]
Dynamic viscosity (Liquid) η_l	Pa s	0.0008891 [270]
Dynamic viscosity (Vapor) η_{vap}	Pa s	0.000012 [270]

APPENDIX C

Process parameters

Tab. C.1.: Process conditions used during molten metal gas atomization for the four different cooling strategies, including some experimental results with respect to atomization characteristics and particle size analysis.

Cooling strategy	Run	Alloy	Atomizer	D	$T_{G,0}$	T_{liq}	T_M	ΔT_M	p	$\dot{m}_L$	$\dot{m}_G$	GMR	$d_{50,3}$	σ_g
-	-	at%	-	mm	K	K	K	K	MPa	kg h^{-1}	kg h^{-1}	-	µm	-
Superheat temperature	PA5-738	$Fe_{43.2}Co_{28.8}B_{19.2}Si_{4.8}Nb_4$	CD-CCA-0.8	2	293 (RT)	1484	1834	350	1.6	149	780 ± 2	5.2	51	2.16
Superheat temperature	PA5-726	$Fe_{43.2}Co_{28.8}B_{19.2}Si_{4.8}Nb_4$	CD-CCA-0.8	2	293 (RT)	1484	1784	300	1.6	160	780 ± 2	4.9	52	2.13
Superheat temperature	PA5-727	$Fe_{43.2}Co_{28.8}B_{19.2}Si_{4.8}Nb_4$	CD-CCA-0.8	2	293 (RT)	1484	1734	250	1.6	148	780 ± 2	5.3	53	2.23
Superheat temperature	PA5-723	$Fe_{76}B_{10}Si_9P_5$	CD-CCA-0.8	2	293 (RT)	1338	1688	350	1.6	142	780 ± 2	5.5	44	2.15
Superheat temperature	PA5-724	$Fe_{76}B_{10}Si_9P_5$	CD-CCA-0.8	2	293 (RT)	1338	1638	300	1.6	150	780 ± 2	5.2	45	2.14
Superheat temperature	PA5-725	$Fe_{76}B_{10}Si_9P_5$	CD-CCA-0.8	2	293 (RT)	1338	1588	250	1.6	Experiment failed				
Superheat temperature	PA5-735	$Cu_{47}Ti_{33}Zr_{11}Ni_6Si_1Sn_2$	CD-CCA-0.8	2	293 (RT)	1160	1610	450	1.6	152	780 ± 2	5.1	43	2.32
Superheat temperature	PA5-736	$Cu_{47}Ti_{33}Zr_{11}Ni_6Si_1Sn_2$	CD-CCA-0.8	2	293 (RT)	1160	1510	350	1.6	144	780 ± 2	5.4	47	2.25
Superheat temperature	PA5-737	$Cu_{47}Ti_{33}Zr_{11}Ni_6Si_1Sn_2$	CD-CCA-0.8	2	293 (RT)	1160	1410	250	1.6	153	780 ± 2	5.1	49	2.21
Superheat temperature	PA5-733	$Zr_{59.3}Cu_{28.8}Al_{10.4}Nb_{1.5}$	CD-CCA-0.8	2	293 (RT)	1203	1653	450	1.6	149	780 ± 2	5.2	52	2.29
Superheat temperature	PA5-744	$Zr_{59.3}Cu_{28.8}Al_{10.4}Nb_{1.5}$	CD-CCA-0.8	2	293 (RT)	1203	1553	350	1.6	145	780 ± 2	5.4	54	2.28
Superheat temperature	PA5-745	$Zr_{59.3}Cu_{28.8}Al_{10.4}Nb_{1.5}$	CD-CCA-0.8	2	293 (RT)	1203	1453	250	1.6	139	780 ± 2	5.6	56	2.08
Hot gas atomization	PA5-567	$Fe_{43.2}Co_{28.8}B_{19.2}Si_{4.8}Nb_4$	CD-CCA-0.8	1.5	293 (RT)	1484	1834	350	1.6	81	780 ± 2	9.6	35	1.96
Hot gas atomization	PA5-535	$Fe_{43.2}Co_{28.8}B_{19.2}Si_{4.8}Nb_4$	CD-CCA-0.8	2	293 (RT)	1484	1834	350	1.6	147	780 ± 2	5.3	44	2.13
Hot gas atomization	PA5-534	$Fe_{43.2}Co_{28.8}B_{19.2}Si_{4.8}Nb_4$	CD-CCA-0.8	3	293 (RT)	1484	1834	350	1.6	267	780 ± 2	2.9	68	2.66
Hot gas atomization	PA5-560	$Fe_{43.2}Co_{28.8}B_{19.2}Si_{4.8}Nb_4$	CD-CCA-0.8	1.5	567 (HG)	1484	1834	350	1.6	84	513 ± 10	6.1	35	1.97
Hot gas atomization	PA5-559	$Fe_{43.2}Co_{28.8}B_{19.2}Si_{4.8}Nb_4$	CD-CCA-0.8	2	549 (HG)	1484	1834	350	1.6	160	513 ± 10	3.2	39	1.98
Hot gas atomization	PA5-558	$Fe_{43.2}Co_{28.8}B_{19.2}Si_{4.8}Nb_4$	CD-CCA-0.8	3	536 (HG)	1484	1834	350	1.6	313	513 ± 10	1.6	57	2.21
Cooling rate calculation	PA5-537	$Cu_{96.7}Sn_{3.3}$	CD-CCA-0.8	1.5	293 (RT)	1323	1673	350	1.6	94	780 ± 2	8.3	24	2.18
Cooling rate calculation	PA5-538	$Cu_{96.7}Sn_{3.3}$	CD-CCA-0.8	2	293 (RT)	1323	1673	350	1.6	154	780 ± 2	5.1	30	2.32
Cooling rate calculation	PA5-539	$Cu_{96.7}Sn_{3.3}$	CD-CCA-0.8	3	293 (RT)	1323	1673	350	1.6	301	780 ± 2	2.6	42	3.09
Cooling rate calculation	PA5-564	$Cu_{96.7}Sn_{3.3}$	CD-CCA-0.8	1.5	571(HG)	1323	1673	350	1.6	101	513 ± 10	5.1	18	2.11
Cooling rate calculation	PA5-565	$Cu_{96.7}Sn_{3.3}$	CD-CCA-0.8	2	549 (HG)	1323	1673	350	1.6	175	513 ± 10	2.9	22	2.26
Cooling rate calculation	PA5-566	$Cu_{96.7}Sn_{3.3}$	CD-CCA-0.8	3	525 (HG)	1323	1673	350	1.6	379	513 ± 10	1.4	37	2.57

Continued on next page

Tab. C.1 – *Continued from previous page*

Cooling strategy	Run	Alloy	Atomizer	D	$T_{G,0}$	T_{liq}	T_M	ΔT_M	p	$\dot{m}_L$	$\dot{m}_G$	GMR	$d_{50,3}$	σ_g
-	-	at%	-	mm	K	K	K	K	MPa	kg h^{-1}	kg h^{-1}	-	µm	-
Cooling rate calculation	PA5-567	$Cu_{96.7}Sn_{3.3}$	FFA	2	293 (RT)	1323	1673	350	2	111	338 ± 10	3.1	90	1.83
Cooling rate calculation	PA5-566	$Cu_{96.7}Sn_{3.3}$	FFA	2	521 (HG)	1323	1673	350	2	113	250 ± 10	2.2	93	1.80
Spray cone cooling	PA5-739	$Fe_{43.2}Co_{28.8}B_{19.2}Si_{4.8}Nb_4$	CD-CCA-0.8	2	293 (RT)	1484	1834	350	1.6	146	780 ± 2	5.3	48	2.09
Spray cone cooling	PA5-740	$Fe_{43.2}Co_{28.8}B_{19.2}Si_{4.8}Nb_4$	CD-CCA-0.8	2	293 (RT)	1484	1834	350	1.6	151	780 ± 2	5.2	55	2.13
Spray cone cooling	PA5-741	$Fe_{76}B_{10}Si_9P_5$	CD-CCA-0.8	2	293 (RT)	1338	1688	350	1.6	142	780 ± 2	5.5	51	2.17
Spray cone cooling	PA5-750	$Fe_{76}B_{10}Si_9P_5$	CD-CCA-0.8	2	293 (RT)	1338	1688	350	1.6	149	780 ± 2	5.2	44	2.19
Liquid quenching	PA5-742	$Fe_{43.2}Co_{28.8}B_{19.2}Si_{4.8}Nb_4$	CD-CCA-0.8	2	293 (RT)	1484	1834	350	1.6	175	780 ± 2	4.5	33	1.99
Liquid quenching	PA5-754	$Fe_{43.2}Co_{28.8}B_{19.2}Si_{4.8}Nb_4$	CD-CCA-0.8	2	293 (RT)	1484	1834	350	1.6	168	780 ± 2	4.7	35	2.08
Liquid quenching	PA5-761	$Fe_{43.2}Co_{28.8}B_{19.2}Si_{4.8}Nb_4$	CD-CCA-0.8	2	293 (RT)	1484	1834	350	1.6	141	780 ± 2	5.5	29	2.03
Liquid quenching	PA5-749	$Fe_{76}B_{10}Si_9P_5$	CD-CCA-0.8	2	293 (RT)	1338	1688	350	1.6	144	780 ± 2	5.4	37	2.17
Liquid quenching	PA5-759	$Fe_{76}B_{10}Si_9P_5$	CD-CCA-0.8	2	293 (RT)	1338	1688	350	1.6	148	780 ± 2	5.3	33	2.01

D = Nozzle outlet diameter, $T_{G,0}$ = Initial gas temperature, T_{liq} = Liquidus temperature, T_M = Melt temperature, ΔT_M = Melt superheat temperature, p = Atomization pressure, $\dot{m}_L$ = Melt mass flow rate, $\dot{m}_G$ = Gas mass flow rate, GMR = Gas-to-melt mass flow ratio, $d_{50,3}$ = Mass median particle diameter, and σ_g = Geometric standard deviation.

Tab. C.2.: Spark Plasma Sintering parameters including final ring properties after consolidation. The abbreviations FeCoBSiNb and FeBSiP stand for the $\{(Fe_{0.6}Co_{0.4})_{0.75}B_{0.2}Si_{0.05}\}_{96}Nb_4$ and $Fe_{76}B_{10}Si_9P_5$ glass-forming alloys, respectively.

Experiment	1	2	3	4	5	6
Cooling strategy	Conventional cooling	Conventional cooling	Spray cone cooling	Spray cone cooling	Liquid quenching	Liquid quenching
Alloy	FeCoBSiNb	FeCoBSiNb	FeCoBSiNb	FeCoBSiNb	FeCoBSiNb	FeCoBSiNb
Particle size (µm)	< 25	25 - 45	< 25	25 - 45	< 25	25 - 45
Powder weight (g)	1.6	1.6	1.6	1.6	1.6	1.6
Vacuum (mbar)	0.06	0.06	0.06	0.06	0.06	0.06
Applied force (kN)	4.12 kN	4.12 kN	4.12 kN	4.12 kN	4.12 kN	4.12 kN
Compression strength (MPa)	500	500	500	500	500	500
Heating procedure	in 4 min to 450 °C in 2 min to 548 °C	in 4 min to 450 °C in 2 min to 548 °C	in 4 min to 450 °C in 2 min to 548 °C	in 4 min to 450 °C in 2 min to 548 °C	in 4 min to 450 °C in 2 min to 546 °C	in 4 min to 450 °C in 2 min to 546 °C
Overshoot temperature (°C)	550	550	550	550	548	548
Pressing time (min)	0.75	0.75	0.75	0.75	0.75	0.75
Cooling / purging gas	Argon	Argon	Argon	Argon	Argon	Argon
Cooling rate after SPS (K/min)	25	25	25	25	25	25
Sample thickness (mm)	2.55	2.58	2.50	2.64	2.60	2.62
Relative bulk density (%)	98.4	98.3	98.5	98.2	98.1	98.0
Experiment	1	2	3	4	5	6
Cooling strategy	Conventional cooling	Conventional cooling	Spray cone cooling	Spray cone cooling	Liquid quenching	Liquid quenching
Alloy	FeBSiP	FeBSiP	FeBSiP	FeBSiP	FeBSiP	FeBSiP
Particle size (µm)	< 25	25 - 45	< 25	25 - 45	< 25	25 - 45
Powder weight (g)	1.6	1.6	1.6	1.6	1.6	1.6
Vacuum (mbar)	0.06	0.06	0.06	0.06	0.06	0.06
Applied force (kN)	4.12 kN	4.12 kN	4.12 kN	4.12 kN	4.12 kN	4.12 kN
Compression strength (MPa)	500	500	500	500	500	500
Heating procedure	in 4 min to 400 °C in 2 min to 496 °C	in 4 min to 400 °C in 2 min to 496 °C	in 4 min to 400 °C in 2 min to 496 °C	in 4 min to 400 °C in 2 min to 496 °C	in 4 min to 400 °C in 2 min to 495 °C	in 4 min to 400 °C in 2 min to 495 °C
Overshoot temperature (°C)	499	499	499	499	498	498
Pressing time (min)	0.75	0.75	0.75	0.75	0.75	0.75
Cooling / purging gas	Argon	Argon	Argon	Argon	Argon	Argon
Cooling rate after SPS (K/min)	25	25	25	25	25	25
Sample thickness (mm)	2.58	2.58	2.71	2.61	2.64	2.73
Relative bulk density (%)	98.2	98.2	98.1	98.2	98.1	97.9

Bibliography

[1] *Retrieved from: https://www.britannica.com/topic/Mesoamerican-civilization (2019, March 2)*.

[2] P. Lunkenheimer, U. Schneider, R. Brand, and A. Loidl. Relaxationsdynamik in Gläsern. *Physikalische Blätter*, 56(6):35–41, 2000.

[3] M.K. Miller and P. Liaw, editors. *Bulk Metallic Glasses: An Overview*. Springer Science+Business, LLC, Luxembourg, 2008.

[4] A.L. Greer. Metallic Glasses. *Science*, 267(5206):1947–1953, 1995.

[5] D.R. Uhlmann. Glass Formation, a Contemporary View. *Journal of the American Ceramic Society*, 66(2):95–100, 1983.

[6] W. Klement, R.H. Willens, and P. Duwez. Non-Crystalline Structure in Solidified Gold-Silicon Alloys. *Nature*, 187(4740):869–870, 1960.

[7] W.L. Johnson and J. Plummer. Is metallic glass poised to come of age? *Nature*, 14(6):553–555, 2015.

[8] D.C. Hofmann, J.-Y. Suh, A. Wiest, G. Duan, M.-L. Lind, M. Demetriou, and W.L. Johnson. Designing metallic glass matrix composities with high thoughness and tensile ductility. *Nature*, 451(7182):1085–1089, 2008.

[9] R.O. Ritchie. The conflicts between strength and toughness. *Nature Materials*, 10(11):817–822, 2011.

[10] U.G.K. Wegst, H. Bai, E. Saiz, A.P. Tomsia, and R.O. Ritchie. Bioinspired structural materials. *Nature Materials*, 14(1):23–36, 2015.

[11] R.O. Ritchie. The Quest for Stronger, Tougher Materials. *Science*, 320(5875):448, 2008.

[12] Y.-T. Cheng and W.L. Johnson. Disordered Materials: A Survey of Amorphous Solids. *Science*, 235(4792):997–1002, 1987.

[13] M.D. Demetriou, M.E. Launey, G. Garrett, J.P. Schramm, D.C. Hofmann, W.L. Johnson, and R.O. Ritchie. A damage-tolerant glass. *Nature Materials*, 10(2):123–128, 2011.

[14] M. Telford. The case for bulk metallic glass. *Materials Today*, 7(3):36–43, 2004.

[15] D.B. Miracle. A Physical Model for Metallic Glass Structures: An Introduction and Update. *JOM*, 64(7):846–855, 2012.

[16] Nature Materials Editorial. Crystallizing glassy issues. *Nature Materials*, 14(6):541, 2015.

[17] W.L. Johnson, J.H. Na, and M.D. Demetriou. Quantifying the origin of metallic glass formation. *Nature Communications*, 7(10313):1–7, 2016.

[18] W.L. Johnson, G. Kaltenboeck, M.D. Demetriou, J.P. Schramm, X. Liu, K. Samwer, C.P. Kim, and D.C. Hofmann. Beating Crystallization in Glass-Forming Metals by Millisecond Heating and Processing. *Science*, 332(6031):828–833, 2011.

[19] P. Ramasamy, A. Szabo, S. Borzel, J. Eckert, M. Stoica, and A. Bárdos. High pressure die casting of Fe-based metallic glass. *Scientific Reports*, 6(35258):1–11, 2016.

[20] S. Yoshihiro, Y. Hideaki, and T. Tsubasa. The "MPCG Series" of Large-Current Choke Coils Using the Low-Loss Metallic Magnetic Material "Senntix". *NEC Technical Journal*, 4(1):71–75, 2009.

[21] N. Ellendt, N. Ciftci, C. Goodreau, V. Uhlenwinkel, and L. Mädler. Solidification of single droplets under combined cooling conditions. *IOP Conference Series: Materials Science and Engineering*, 117(012057):1–7, 2016.

[22] J.H. Perepezko. Nucleation-controlled reactions and metastable structures. *Progress in Materials Science*, 49(3-4):263–284, 2004.

[23] A. Miura, W. Dong, M. Fukue, N. Yodoshi, K. Takagi, and A. Kawasaki. Preparation of Fe-based monodisperse spherical particles with fully glassy phase. *Journal of Alloys and Compounds*, 509(18):5581–5586, 2011.

[24] N. Yodoshi, S. Ookawa, R. Yamada, N. Nomura, K. Kikuchi, and A. Kawasaki. Effects of nanocrystallisation on saturation magnetisation of amorphous $Fe_{76}Si_9B_{10}P_5$. *Materials Research Letters*, 6(1):100–105, 2018.

[25] N. Ciftci, N. Ellendt, R. von Bargen, H. Henein, L. Mädler, and V. Uhlenwinkel. Atomization and characterization of a glass forming alloy $\{(Fe_{0.6}Co_{0.4})_{0.75}B_{0.2}Si_{0.05}\}_{96}Nb_4$. *Journal of Non-Crystalline Solids*, 394-395:36–42, 2014.

[26] B. Zheng, Y. Lin, Y. Zhou, and E.J. Lavernia. Gas Atomization of Amorphous Aluminum: Part I. Thermal Behavior Calculations. *Metallurgical and Materials Transactions A*, 40(5):768–778, 2009.

[27] D.G. Eskin. *Physical Metallurgy of Direct Chill Casting of Aluminum Alloys*. CRC Press Taylor & Francis Group, Boca Raton, London, New York, 1st edition, 2008.

[28] A.J. Drehman and D. Turnbull. Solidification behavior of undercooled $Pd_{83}Si_{17}$ and $Pd_{82}Si_{18}$ liquid droplets. *Scripta Metallurgica*, 15(5):543–548, 1981.

[29] F. Gillessen, D.M. Herlach, and B. Feuerbacher. Glass formation by containerless solidification of metallic droplets in drop tube experiments. *Journal of the Less Common Metals*, 145(1-2):145–152, 1988.

[30] A. Dunst, D.M. Herlach, and F. Gillessen. Formation of glassy spheres of Fe-Ni-P-B by containerless processing. *Materials Science and Engineering A*, 133:785–789, 1991.

[31] B. Zheng, Y. Lin, Y. Zhou, and E.J. Lavernia. Gas Atomization of Amorphous Aluminium Powder: Part II. Experimental Investigation. *Metallurgical and Materials Transactions B*, 40:995–1004, 2009.

[32] S. Mukherjee, Z. Zhou, J. Schroers, W.L. Johnson, and W.K. Rhim. Overheating threshold and its effect on time-temperature-transformation diagrams of zirconium based bulk metallic glasses. *Applied Physics Letters*, 84(24):5010–5012, 2004.

[33] O.S. Nichiporenko. Role of melt viscosity in the formation of powder particles during atomization. *Soviet Powder Metallurgy and Metal Ceramics*, 7(12):931–933, 1968.

[34] J.J. Dunkley and J.D. Palmer. Factors Affecting Particle Size of Atomized Metal Powders. *Powder Metallurgy*, 29(4):287–290, 1986.

[35] S. Özbilen, A. Ünal, and T. Sheppard. Influence of Superheat on Particle Shape and Size of Gas Atomised Copper Powders. *Powder Metallurgy*, 34(1):53–61, 1991.

[36] H.-W. Ouyang, X. Chen, and B.-Y. Huang. Influence of melt superheat on breakup process of close-coupled gas atomization. *Transactions of Nonferrous Metals Society of China*, 17(5):967–973, 2007.

[37] M. Pasupathy, J.M. Martín, A. Rivas, I. Iturriza, and F. Castro. Effect of the solidification time on the median particle size of powders produced by water atomisation. *Powder Metallurgy*, 59(2):128–141, 2016.

[38] R.B. Bird, W.E. Stewart, and E.N. Lightfoot. *Transport Phenomena*. Jon Wiley & Sons, Inc. New York, 2nd edition, 2002.

[39] N. Ciftci, N. Ellendt, E. Soares Barreto, L. Mädler, and V. Uhlenwinkel. Increasing the amorphous yield of $\{(Fe_{0.6}Co_{0.4})_{0.75}B_{0.2}Si_{0.05}\}_{96}Nb_4$ powders by hot gas atomization. *Advanced Powder Technology*, 29(2):380–385, 2018.

[40] N. Ciftci, N. Ellendt, G. Coulthard, E. Soares Barreto, L. Mädler, and V. Uhlenwinkel. Novel Cooling Rate Correlations in Molten Metal Gas Atomization. *Metallurgical and Materials Transactions B*, 50(2):666–677, 2019.

[41] U. Alam. *Experimental Study of Local Heat Transfer during Quenching of Metals by Spray and Mutiple Jets*. PhD thesis, Fakültät für Verfahrens- und Systemtechnik, Otto-von-Guericke-Universität Magdeburg, 2011.

[42] A.L. Greer. New horizons for glass formation and stability. *Nature Materials*, 14(6):542–546, 2015.

[43] D.R. Uhlmann. Kinetics of Glass Formation and Devitrification Behavior. *Le Journal de Physique Colloques*, 43(9):175–190, 1982.

[44] L. Zhong, J. Wang, H. Sheng, Z. Zhang, and S.X. Mao. Formation of monatomic metallic glasses through ultrafast liquid quenching. *Nature*, 512(7513):177–180, 2014.

[45] Q. An, S-N. Luo, W.A. Goddard III, W.Z. Han, B. Arman, and W.L. Johnson. Synthesis of single-component metallic glasses by thermal spray of nanodroplets on amorphous substrates. *Applied Physics Letters*, 100(041909):1–4, 2012.

[46] W.L. Johnson. Bulk Glass-Forming Metallic Alloys: Science and Technology. *MRS Bulletin*, 24(10):42–56, 1999.

[47] A. Inoue. Stabilization of metallic supercooled liquid and bulk amorphous alloys. *Acta Materialia*, 48(1):279–306, 2000.

[48] C. Suryanarayana and A. Inoue, editors. *Bulk Metallic Glasses*. CRC Press Taylor & Francis Group, Boca Raton, London, New York, 2nd edition, 2017.

[49] Z.J. Evenson. *On the thermodynamic and kinetic properties of bulk glass forming metallic systems*. PhD thesis, Naturwissenschaftlich-Technische Fakultät III Chemie, Pharmazie und Werkstoffwissenschaften, Universität des Saarlandes, 2012.

[50] X. Yue, A. Inoue, C-T. Liu, and C. Fan. The Development of Structure Model in Metallic Glasses. *Materials Research*, 20(2):326–338, 2017.

[51] A.L. Greer. Metallic glasses...on the threshold. *Materials Today*, 12(1-2):14–22, 2009.

[52] F.C. Frank. Supercooling of liquids. *Proceedings of the Royal Society A: Mathematical, Physical and Engineering Sciences*, 215(1120):43–46, 1952.

[53] A. Hirata, L.J. Kang, T. Fujita, B. Klumov, K. Matsue, M. Kotani, A.R. Yavari, and M.W. Chen. Geometric Frustration of Icosahedron in Metallic Glasses. *Science*, 341(6144):376–379, 2013.

[54] J.D. Bernal. Geometry of the Structure of Monatomic Liquids. *Nature*, 185(4706):68–70, 1960.

[55] J.D. Bernal and J. Mason. Packing of Spheres: Co-ordination of Randomly Packed Spheres. *Nature*, 188(4754):910–911, 1960.

[56] G. Kaur. *Bioactive Glasses: Potential Biomaterials for Future Therapy*. Number 10. Springer International Publishing AG, Basel, Switzerland, 1st edition, 2017.

[57] P.H. Gaskell. A new structural model for transition metal-metalloid glasses. *Nature*, 276(5687):484–485, 1978.

[58] K.J. Laws, D.B. Miracle, and M. Ferry. A predictive structural model for bulk metallic glasses. *Nature Communications*, 6(8123):1–10, 2015.

[59] A. Inoue, T. Negishi, H.M. Kimura, T. Zhang, and A.R. Yavari. High Packing Density of Zr- and Pd-Based Bulk Amorphous Alloys. *Materials Transactions, JIM*, 39(2):318–321, 1998.

[60] D.B. Miracle. A structural model for metallic glasses. *Nature Materials*, 3(10):697–702, 2004.

[61] R.W. Cahn and A.L. Greer. *Physical Metallurgy*, chapter Metastable states of alloys, pages 1723–1830. Oxford, North Holland, 4th edition, 1996.

[62] D. Turnbull. Thermodynamics and Kinetics of Laser-Induced Structure Changes. In M. Bertolotti, editor, *Physical Processes in Laser-Materials Interactions*, volume 84, pages 117–142. New York and London, Plenum Press, 1980.

[63] F. Spaepen and D. Turnbull. Atomic Transport and Transformation Behavior in Metallic Glasses. techreport 1, Division of Engineering and Applied Physics, Harvard Univeristy, Cambridge, Massachusetts, 1976.

[64] H.J. Fecht. Thermodynamic Properties of Amorphous Solids - Glass Formation and Glass Transition - (Overview). *Materials Transactions, JIM*, 36(7):777–793, 1995.

[65] D. Turnbull. Kinetics of Solidification of Supercooled Liquid Mercury Droplets. *The Journal of Chemical Physics*, 20(3):411–424, 1952.

[66] J.H. Perepezko. In R. Mehrabian, B.H. Kaer, and M. Cohen, editors, *Proceedings of the Second International Conference on Rapid Solidification Processing: Principles and Technologies*, pages 56–. Baton Rouge, LA, Claitor's Publishing Division, 1980.

[67] L. Battezzati and A.L. Greer. Thermodynamics of $Te_{80}Ge_{20-x}Pb_x$ glass-forming alloys. *Journal of Materials Research*, 3(3):570–575, 1988.

[68] D. Herlach and D.M. Matson, editors. *Solidification of Containerless Undercooled Melts*. Wiley-VCH Verlag, Weinheim, Germany, 1st edition, 2012.

[69] F.X. Tanner. *Handbook of Atomization and Sprays*, chapter Droplet Freezing and Solidification, pages 327–338. Springer Science+Business, LLC, Luxembourg, 1st edition, 2011.

[70] D. Turnbull. Under what conditions can a glass be formed? *Contemporary Physics*, 10(5):473–488, 1969.

[71] D.R. Uhlmann. A kinetic treatment of glass formation. *Journal of Non-Crystalline Solids*, 7(4):337–348, 1972.

[72] A. Peker and W.L. Johnson. A highly processable metallic glass: $Zr_{41.2}Ti_{13.8}Cu_{12.5}Ni_{10.0}Be_{22.5}$. *Applied Physics Letters*, 63(17):2342–2344, 1993.

[73] S. Guo, Z.P. Lu, and C.T. Liu. Identify the best glass forming ability criterion. *Intermetallics*, 18(5):883–888, 2010.

[74] J.H. Na, M.D. Demetriou, M. Floyd, A. Hoff, G.R. Garrett, and W.L. Johnson. Compositional landscape for glass formation in metal alloys. *Proceedings of the National Academy of Sciences of the United States of America*, 111(25):9031–9036, 2014.

[75] H.A. Davies. Formation of metallic glasses. *Physics and Chemistry of Glasses*, 17(5):159–173, 1976.

[76] A. Inoue, T. Ochiai, Y. Horio, and T. Masumoto. Formation and mechanical properties of amorphous Al-Ni-Nd alloys. *Materials Science and Engineering A*, 179-180, Part 1:649–653, 1994.

[77] A.L. Greer. Confusion by design. *Nature*, 366:303–304, 1993.

[78] M. Chen. A brief overview of bulk metallic glasses. *NPG Asia Materials*, 3:82–90, 2011.

[79] T. Iida and R.I.L. Guthrie, editors. *The Physical Properties of Liquid Metals*. Clarendon Press, Oxford University Press, Oxford, 1st edition, 1988.

[80] A. Masuhr, T.A. Waniuk, R. Busch, and W.L. Johnson. Time Scales for Viscous Flow, Atomic Transport, and Crystallization in the Liquid and Supercooled Liquid States of $Zr_{41.2}Ti_{13.8}Cu_{12.5}Ni_{10.0}Be_{22.5}$. *Physical Review Letters*, 82(11):2290–2293, 1999.

[81] R. Busch. The thermophysical properties of bulk metallic glass-forming liquids. *JOM*, 52(7):39–42, 2000.

[82] W. Hembree. *High temperature rheology of Zr-based bulk metallic glass forming liquids*. PhD thesis, Naturwissenschaftlich-Technische Fakultät III Chemie, Pharmazie und Werkstoffwissenschaften, Universität des Saarlandes, 2015.

[83] M.E. Blodgett, T. Egami, Z. Nussinov, and K.F. Kelton. Proposal for universality in the viscosity of metallic liquids. *Scientific Reports*, 5(13837):1–8, 2015.

[84] C.A. Angell. Formation of Glasses from Liquids and Biopolymers. *Science*, 267(5206):1924–1935, 1995.

[85] I. Gallino. On the Fragility of Bulk Metallic Glass Forming Liquids. *Entropy*, 19(9):483, 2017.

[86] S. Wei, M. Stolpe, O. Gross, Z. Evenson, I. Gallino, W. Hembree, J. Bednarcik, J.J. Kruzic, and R. Busch. Linking structure to fragility in bulk metallic glass-forming liquids. *Applied Physics Letters*, 106(181901):1–5, 2015.

[87] C.A. Angell. Structural instability and relaxation in liquid and glassy phases near the fragile liquid limit. *Journal of Non-Crystalline Solids*, 102(1-3):205–221, 1988.

[88] J. Schroers and W.L. Johnson. Highly processable bulk metallic glass-forming alloys in the Pt-Co-Ni-Cu-P system. *Applied Physics Letters*, 84(18):3666–3668, 2004.

[89] L. Perrière, Y. Champion, and F. Bernard. *Spark Plasma Sintering of Materials: Advances in Processing and Applications*, chapter Spark Plasma Sintering of Metallic Glasses, pages 291–335. P. Cavaliere, 1st edition, 2019.

[90] D.R. Uhlmann. Nucleation, crystallization and glass formation. *Journal of Non-Crystalline Solids*, 38-39, Part 2:693–698, 1980.

[91] Y.J. Kim, R. Busch, W.L. Johnson, A.J. Rulison, and W.K. Rhim. Experimental determination of a time-temperature-diagram of the undercooled $Zr_{41}Ti_{14}Cu_{12}Ni_{10}Be_{23}$ alloy using the containerless electrostatic levitation processing technique. *Applied Physics Letters*, 68(8):1057–1059, 1996.

[92] E. Zhuravlev and C. Schick. Fast scanning power compensated differential scanning nano-calorimeter: 1. The device. *Thermochimica Acta*, 505(1-2):1–13, 2010.

[93] E. Zhuravlev and C. Schick. Fast scanning power compensated differential scanning nano-calorimeter: 2. Heat capacity analysis. *Thermochimica Acta*, 505(1-2):14–21, 2010.

[94] S. Pogatscher, P.J. Uggowitzer, and J.F. Löffler. In-situ probing of metallic glass formation and crystallization upon heating and cooling via fast differential scanning calorimetry. *Applied Physics Letters*, 104(251908):1–5, 2014.

[95] J.Heinrich. *Massivglasbildende metallische Legierungen als Konstruktionswerkstoff - Materialoptimierung und Technologieentwicklung zur Herstellung und Verarbeitung*. PhD thesis, Naturwissenschaftlich-Technische Fakultät III Chemie, Pharmazie und Werkstoffwissenschaften, Universität des Saarlandes, 2012.

[96] A. Inoue and N. Nishiyama. Extremely low critical cooling rates of new Pd-Cu-P base amorphous alloys. *Materials Science and Engineering A*, 226-228:401–405, 1997.

[97] J. Schroers and W.L. Johnson. Crystallization kinetics of the bulk-glass-forming $Pd_{43}Ni_{10}Cu_{27}P_{20}$ melt. *Applied Physics Letters*, 77(8):1158–1160, 2000.

[98] J.S. Yu, Y.Q. Zeng, T. Fujita, T. Hashizume, A. Inoue, T. Sakurai, and M.W. Chen. On the effect of impurities in metallic glass formation. *Applied Physics Letters*, 96(141901):1–3, 2010.

[99] M. Stoica. *Fe-Based Bulk Metallic Glasses: Understanding the Influence of Impurities on Glass Formation*. Springer Fachmedien Wiesbaden GmbH, 1st edition, 2017.

[100] H. Li, Z. Lu, and S. Yi. Estimation of the glass forming ability of the Fe-based bulk metallic glass $Fe_{68.8}C_{7.0}Si_{3.5}B_{5.0}P_{9.6}Cr_{2.1}Mo_{2.0}Al_{2.0}$ that contains non-metallic inclusions. *Metals and Materials International*, 15(1):7–14, 2009.

[101] C.Y. Luo, Y.H. Zhao, X.K. Xi, G. Wang, D.Q. Zhao, M.X. Pan, W.H. Wang, and S.Z. Kou. Making amorphous steel in air by rare earth microalloying. *Journal of Non-Crystalline Solids*, 352(2):185–188, 2006.

[102] S.F. Guo, L. Liu, and X.Lin. Formation of magnetic Fe-based bulk metallic glass under low vacuum. *Journal of Alloys and Compounds*, 478(1-2):226–228, 2009.

[103] N. Chen, L. Martin, D.V. Luzguine-Luzgin, and A. Inoue. Role of Alloying Additions in Glass Formation and Properties of Bulk Metallic Glasses. *Materials*, 3(12):5320–5339, 2010.

[104] J. Heinrich, R. Busch, F. Müller, S. Grandthyll, and S. Hüfner. Role of aluminum as an oxygen-scavenger in zirconium based bulk metallic glasses. *Applied Physics Letters*, 100(071909):1–3, 2012.

[105] H.X. Li, Z.C. Lu, S.L. Wang, Y.Wu, and Z.P. Lu. Fe-based bulk metallic glasses: Glass formation, fabrication, properties and applications. *Progress in Materials Science*, 103:235–318, 2019.

[106] H.W. Kui, A.L. Greer, and D. Turnbull. Formation of bulk metallic glass by fluxing. *Applied Physics Letters*, 45(6):615–616, 1984.

[107] N. Nishiyama and A. Inoue. Flux Treated Pd-Cu-Ni-P Amorphous Alloy Having Low Critical Cooling Rate. *Materials Transactions, JIM*, 38(5):464–472, 1997.

[108] D. Granata, E. Fischer, V. Wessels, and J.F. Löffler. Fluxing of Pd-Si-Cu bulk metallic glass and the role of cooling rate and purification. *Acta Materialia*, 71:145–152, 2014.

[109] D. Suh and R.H. Dauskardt. The effects of hydrogen on deformation and fracture of a Zr-Ti-Ni-Cu-Be bulk metallic glass. *Materials Science and Engineering A*, 319-321:480–483, 2001.

[110] Y. Su, F. Dong, L. Luo, J. Guo, B. Han, Z. Li, B. Wang, and H. Fu. Bulk metallic glass formation: The positive effect of hydrogen. *Journal of Non-Crystalline Solids*, 358(18-19):2606–2611, 2012.

[111] D. Granata, E. Fischer, and J.F. Löffler. Hydrogen microalloying as a viable strategy for enhancing the glass-forming ability of Zr-based bulk metallic glasses. *Scripta Materialia*, 103:53–56, 2015.

[112] D. Granata. *Effects of fluxing, microalloying and composition in bulk metallic glass design*. PhD thesis, ETH Zürich, 2015.

[113] H.J.T. Ellingham. Reducibility of oxides and sulfides in metallurgical processes. *Journal of the Society of Chemical Industry, London*, 63(5):125–133, 1944.

[114] X.H. Lin, W.L. Johnson, and W.K. Rhim. Effect of Oxygen Impurity on Crystallization of an Undercooled Bulk Glass Forming Zr-Ti-Cu-Ni-Al Alloy. *Materials Transactions, JIM*, 38(5):473–477, 1997.

[115] J. Eckert, N. Mattern, M. Zinkevitch, and M. Seidel. Crystallization Behavior and Phase Formation in Zr-Al-Cu-Ni Metallic Glass Containing Oxygen. *Materials Transactions, JIM*, 39(6):623–632, 1998.

[116] A. Gebert, J. Eckert, and L. Schultz. Effect of oxygen on phase formation and thermal stability of slowly cooled $Zr_{65}Al_{7.5}Cu_{17.5}Ni_{10}$ metallic glass. *Acta Materialia*, 46(15):5475–5482, 1998.

[117] C.T. Liu, M.F. Chisholm, and M.K. Miller. Oxygen impurity and microalloying effect in a Zr-based bulk metallic glass alloy. *Intermetallics*, 10(11-12):1105–1112, 2002.

[118] D.J. Sordelet, X.Y. Yang, E.A. Rozhkova, M.F. Besser, and M.J. Kramer. Oxygen-stabilized glass formation in $Zr_{80}Pt_{20}$ melt-spun ribbons. *Applied Physics Letters*, 83(1):69–71, 2003.

[119] H.X. Li, J.E. Gao, Z.B. Jiao, Y. Wu, and Z.P. Lu. Glass-forming ability enhanced by proper additions of oxygen in a Fe-based bulk metallic glass. *Applied Physics Letters*, 95(161905):1–3, 2009.

[120] W. Yang, Q. Wang, H. Ling, H. Liu, L. Xue, Y. He, Q. Li, and B. Shen. Oxygen-driven impurities scavenging before solidification of Fe-based metallic glasses. *Journal of Alloys and Compounds*, 773:401–412, 2019.

[121] D.A. Porter, K.E. Easterling, and M. Sherif. *Phase Transformations in Metals and Alloys*. CRC Press Taylor & Francis Group, Boca Raton, London, New York, 3th edition, 2009.

[122] H. Hermann, editor. *Treatise on Materials Science and Technology: Ultrarapid Quenching of Liquid Alloys*, volume 20. Academic Press, Inc., New York, 1981.

[123] R. Mehrabian, editor. *Proceedings of the Third Conference on Rapid Solidification Processing: Rapid Solidification Prcocessing Principles and Technologies, III, National Bureau of Standards, Gaithersburg, Maryland*, 1982.

[124] E.J. Lavernia and T.S. Srivatsan. The rapid solidification processing of materials: science, principles, technology, advances and applications. *Journal of Materials Science*, 45(2):287–325, 2010.

[125] H.H. Liebermann, editor. *Rapidly Solidified Alloys: Processes-Structures-Properties-Applications*. CRC Press Taylor & Francis Group, Boca Raton, London, New York, 1993.

[126] A.J. Yule and J. Dunkley. *Atomization of Melts: For Powder Production and Spray Deposition*. Oxford University Press, Oxford, 1994.

[127] H. Liu. *Science and Engineering of Droplets: Fundamentals and Applications*. Noyes Publications, Park Ridge, New Jersey and William Andrew Publishing, LLC, Norwich, New York, 1st edition, 1999.

[128] A. Yanagitani. Production of Metallic Glass Powder by Gas-atomization Process and its Consolidation. *Materials Transactions, JIM*, 60(5):224–227, 2013.

[129] B. Zheng and E.J. Lavernia. *Handbook of Atomization and Sprays*, chapter Melt Atomization, pages 837–848. Springer Science+Business, LLC, Luxembourg, 1st edition, 2011.

[130] C. Czisch. *Effektive Pulvergenerierung aus hochviskosen mineralischen Schmelzen*. PhD thesis, Fachbereich Produktionstechnik, Universität Bremen, 2008.

[131] G.S.E. Antipas. Review of gas atomisation and spray forming phenomenology. *Powder Metallurgy*, 56(4):317–330, 2013.

[132] X.-G. Li and U. Fritsching. *Metal Sprays and Spray Deposition*, chapter Spray Transport Fundamentals, pages 89–176. Springer International Publishing AG, Basel, Switzerland, 2017.

[133] I.E. Anderson and L. Achelis. *Metal Sprays and Spray Deposition*, chapter Two Fluid Atomization Fundamentals, pages 49–88. Springer International Publishing AG, Basel, Switzerland, 2017.

[134] O.D. Neikov. *Handbook of Non-Ferrous Metal Powders: Technologies and Applications*. Elsevier Ltd., 1st edition, 2008.

[135] D. Schwenck, N. Ellendt, J. Fischer-Bühner, P. Hofmann, and V. Uhlenwinkel. A novel convergent-divergent annular nozzle design for close-coupled atomisation. *Powder Metallurgy*, 60(3):198–207, 2017.

[136] M. Jeyakumar, S. Kumar, and G.S. Gupta. The Influence of Processing Parameters on Characteristics of an Aluminium Alloy Spray Deposition. *Materials and Manufacturing Processes*, 24(6):693–699, 2009.

[137] G. Bidone. *Experiencés sur la Forme et sur la Direction des Veines et des Courants d'Eau Lancés par Diverses Ouvertures*. Imprimerie Royale, Turin, 1829.

[138] F. Savart. *Annales de chimie et de physique*, 53:337–386, 1833.

[139] F.R.S. Lord Rayleigh. On the Instability of Jets. *Proceedings of the London Mathematical Society*, 1-10(1):4–13, 1878.

[140] C. Weber. Zum Zerfall eines Flüssigkeitsstrahles. *Zeitschrift für Angewandte Mathematik und Mechanik*, 11(2):136–154, 1931.

[141] A. Haenlein. Über den Zerfall eines Flüssigkeitsstrahles. *Forschung auf dem Gebiet des Ingenieurwesens A*, 2(4):139–149, 1931.

[142] R.P. Grant and S. Middleman. Newtonian jet stability. *AlChE Journal*, 12(4):669–678, 1966.

[143] V. Uhlenwinkel. *Zum Ausbreitungsverhalten der Partikeln bei der Sprühkompaktierung von Metallschmelzen*. PhD thesis, Fachbereich Produktionstechnik, Universität Bremen, 1992.

[144] A.H. Lefebvre and V.G. McDonell. *Atomization and Sprays*. CRC Press Taylor & Francis Group, Boca Raton, London, New York, 2nd edition, 2017.

[145] H. Lubanska. Correlation of Spray Ring Data for Gas Atomization of Liquid Metals. *JOM*, 22(2):45–49, 1970.

[146] N.J. Grant, H. Jones, and E.J. Lavernia. *Elements of Rapid Solidification: Fundamentals and Applications*, chapter Synthesis and Processing, pages 23–47. Springer-Verlag Berlin Heidelberg, 1st edition, 1998.

[147] T. Egami and W.L. Johnson. *Elements of Rapid Solidification: Fundamentals and Applications*, chapter Introduction and Background, pages 1–21. Springer-Verlag Berlin Heidelberg, 1st edition, 1998.

[148] J.H. Perepezko. Role of Nucleation in Rapid Solidification. In P.R. Sahm, H. Jones, and C.M Adam, editors, *Proceedings of the NATO Advanced Reserach Workshop on "Rapid Solidification Technologies: Science and Technology of the Undercooled Melt, Theuern, Germany*, 1985.

[149] R.M. Srivastava, J. Eckert, W. Löser, B.K. Dhindaw, and L. Schultz. Cooling Rate Evaluation for Bulk Amorphous Alloys from Eutectic Microstructures in Casting Processes. *Materials Transactions, JIM*, 43(7):1670–1675, 2002.

[150] X. Liang and E.J. Lavernia. Solidification and microstructure evolution during spray atomization and deposition of Ni_3Al. *Materials Science and Engineering A*, 161(2):221–235, 1993.

[151] H. Jones. *Rapid solidification of metals and alloys*. Institution of Metallurgists (now Institute of Materials, Minerals and Mining - IOM3), London, 1982.

[152] N.J. Grant. A Review of Various Atomization Processes. In R. Mehrabian, B.H. Kear, and M. Cohen, editors, *Proceedings of 1st International Conference on Rapid Solidification Processing: Principles and Technologies, Reston, Virgina*, pages 230–245, 1977.

[153] J.B. Wiskel, K. Naval, H. Henein, and E. Maire. Solidification Study of Aluminum Alloys Using Impulse Atomization: Part ii. Effect of Cooling Rate on Microstructure. *Canadian Metallurgical Quarterly*, 41(2):193–204, 2002.

[154] C.G. Levi and R. Mehrabian. Heat Flow during Rapid Solidification of Undercooled Metal Droplets. *Metallurgical Transactions A*, 13(2):221–234, 1982.

[155] P. Mathur, D. Apelian, and A. Lawley. Analysis of the spray deposition process. *Acta Metallurgica*, 37(2):429–443, 1989.

[156] P.S. Grant, B. Cantor, and L. Katgerman. Modelling of droplet dynamic and thermal histories during spray forming - i. individual droplet behaviour. *Acta Metallurgica et Materialia*, 41(11):3097–3108, 1993.

[157] D. Bergmann and U. Fritsching. Sequential thermal modelling of the spray-forming process. *International Journal of Thermal Sciences*, 43(4):403–415, 2004.

[158] D. Bergmann. *Modellierung des Sprühkompaktierprozesses für Kupfer- und Stahlwerkstoffe*. PhD thesis, Fachbereich Produktionstechnik, Universität Bremen, 2000.

[159] P.C. Mathur. *Analysis of the spray deposition process*. PhD thesis, Department of Materials Engineering, Drexel University, 1988.

[160] P. Mathur, S. Annavarapu, D. Apelian, and A. Lawley. Spray casting: an integral model for process understanding and control. *Materials Science and Engineering A*, 142(2):261–276, 1991.

[161] C.T. Crowe, J.D. Schwarzkopf, M. Sommerfeld, and Y. Tsuji, editors. *Multiphase Flows with Droplets and Particles*. CRC Press, Taylor & Francis Group, Boca Raton London New York, 2nd edition, 2012.

[162] H. Liu, R.H. Rangel, and E.J. Lavernia. Modeling of droplet-gas interactions in spray atomization of Ta-2.5W alloy. *Materials Science and Engineering A*, 191(1-2):171–184, 1995.

[163] D. Bergmann, U. Fritsching, and K. Bauckhage. A mathematical model for cooling and rapid solidification of molten metal droplets. *International Journal of Thermal Sciences*, 39(1):53–62, 2000.

[164] Q. Xu and E.J. Lavernia. Influence of nucleation and growth phenomena on microstructural evolution during droplet-based deposition. *Acta Materialia*, 49(18):3849–3861, 2001.

[165] K.-F. Li, Y.-H. Zhang, C.-J. Song, and Q.-J. Zhai. Numerical study of heat transfer and solidification behavior of gas-atomized Fe-6.5%Si (mass fraction) droplets. *Advances in Manufacturing*, 4(2):150–156, 2016.

[166] G.G. Stokes. On the Effect of the Internal Friction of Fluids on the Motion of Pendulums. *Transactions of the Cambridge Philosophical Society*, 9(part ii):8–106, 1851.

[167] L. Schiller and A. Naumann. A drag coefficient correlation. *Zeitschrift des Vereins Deutscher Ingenieure*, 77:318–320, 1935.

[168] Y. Zhang. *Indoor Air Quality Engineering*. CRC Press Taylor & Francis Group, Boca Raton, London, New York, 1st edition, 2004.

[169] W.E. Ranz and W.R. Marshall. Evaporation from Drops: Part I. *Chemical Engineering Progress*, 48(3):141–146, 1952.

[170] S.I. Moqadam, L. Mädler, and N. Ellendt. Microstructure Adjustment of Spherical Microsamples for High-Throughput Analysis Using a Drop-on-Demand Droplet Generator. *Materials*, 12(3769):1–13, 2019.

[171] S.A. Miller. *Amorphous Metallic Alloys*, chapter Amorphous metal powder: production and consolidation, pages 506–521. Butterworth & Co, 1983.

[172] J. Eitzen. Numerical estimation and prediction of cooling rates during molten metal gas atomization. Technical report, Universität Bremen, UofA Work Term, 2019.

[173] A. Inoue, T. Masumoto, T. Ekimoto, S. Furukawa, Y. Kuroda, and H.S. Chen. Preparation of Fe-, Co-, and Ni-Based Amorphous Alloy Powders by High-Pressure Gas Atomization and Their Structural Relaxation Behavior. *Metallurgical Transactions A*, 19(2):235–242, 1988.

[174] A. Inoue, K. Kita, K. Ohtera, H. Kimura, and T. Masumoto. Al-Y-Ni amorphous powders prepared by high-pressure gas atomization. *Journal of Materials Science Letters*, 7(12):1287–1290, 1988.

[175] I. Endo, I. Otsuka, R. Okuno, A. Shintani, M. Yoshino, and M. Yagi. Fe-Based Amorphous Soft-Magnetic Powder Produced by Spinning Water Atomization Process (SWAP). *IEEE Transactions on Magnetics*, 35(5):3385–3387, 1999.

[176] K.R. Cardoso, A. Garcia Escoríal, M. Lieblich, and W.J. Botta F. Amorphous and nanostructured Al-Fe-Nd powders obtained by gas atomization. *Materials Science and Engineering A*, 315(1-2):89–97, 2001.

[177] Z. Fuqian, X. Ming, L. Jianliang, L. Xianyong, G. Weiming, S. An, and D. Zhongmin. Study of rapidly solidified atomization technique and production of metal alloy powders. *Materials Science and Engineering A*, 304-306:579–582, 2001.

[178] Y. Liu, Z. Liu, S. Guo, Y. Du, B. Baiyun Huang, J. Huang, S. Chen, and F. Liu. Amorphous and nanocrystalline $Al_{82}Ni_{10}Y_8$ alloy powder prepared by gas atomization. *Intermetallics*, 13(3-4):393–398, 2005.

[179] Y. Liu, S. Niu, F. Li, Y. Zhu, and Y. He. Preparation of amorphous Fe-based magnetic powder by water atomization. *Powder Technology*, 213(1-3):36–40, 2011.

[180] S.-Y. Kim, H.R. Oh, H.-A. Kim, A.-Y. Lee, H.-J. Kim, S.-S. Yang, Y.-J. Kim, H.-J. Choi, I.-H. Kim, H.-G. Kim, J. Eckert, J.-R. Kim, and M.-H. Lee. Optimizing the magnetic properties of Fe-based amorphous powder by adjusting atomic structures from vitrification at different temperatures. *Journal of Applied Physics*, 126(165109):1–10, 2019.

[181] S. Pauly, L. Löber, , R. Petters, M. Stoica, S. Scudino, U. Kühn, and J. Eckert. Processing metallic glasses by selective laser melting. *Materials Today*, 16(1-2):37–41, 2013.

[182] Y. Kawamura, H. Kato, A. Inoue, and T. Masumoto. Fabrication of bulk amorphous alloys by powder consolidation. *International Journal of Powder Metallurgy*, 33(2):50–61, 1997.

[183] H.J. Kim, J.K. Lee, T.S. Kim, J.C. Bae, E.S. Park, M.Y. Huh, and D.H. Kim. Mechanical behavior of $Cu_{54}Ni_6Zr_{22}Ti_{18}$ bulk amorphous alloy during multi-pass warm rolling. *Materials Science and Engineering A*, 449-451:929–933, 2007.

[184] T.T. Sasaki, K. Hono, J. Vierke, M. Wollgarten, and J. Banhardt. Bulk nanocrystalline $Al_{85}Ni_{10}La_5$ alloy fabricated by spark plasma sintering of atomized amorphous powders. *Materials Science and Engineering A*, 490(1-2):343–350, 2008.

[185] L. Krämer, Y. Champion, and R. Pippan. From powders to bulk metallic glass composites. *Scientific Reports*, 7(6651):1–9, 2017.

[186] A. List, F. Gärtner, T Schmidt, and T. Klassen. Impact Conditions for Cold Spraying of Hard Metallic Glasses. *Journal of Thermal Spray Technology*, 21(3-4):531–540, 2012.

[187] J.P. Patterson and D.R.H. Jones. Moulding of a metallc glass. *Materials Research Bulletin*, 13(6):583–585, 1978.

[188] J. Schroers. The superplastic forming of bulk metallic glasses. *JOM*, 57(5):35–39, 2005.

[189] M. Stoica, R. Li, A.R. Yavari, G. Vaughan, J. Eckert, N. Van Steenberge, and D.R. Romera. Thermal stability and magnetic properties of FeCoBSiNb bulk metallic glasses. *Journal of Alloys and Compounds*, 504, Supplement 1:123–128, 2010.

[190] R. Ikkene, Z. Koudil, and M. Mouzali. Measurement of the Cooling Power of Polyethylene Glycol Aqueous Solutions Used as Quenching Media. *Journal of ASTM International*, 7(2):1–10, 2010.

[191] P. Sieverding. Entwicklung eines numerischen Modells zur Bestimmung der Abkühlraten amorph erstarrender Metallpulver bei der Gas-Zerstäubung. Master's thesis, Fachbereich Produktionstechnik, Universität Bremen, 2019.

[192] Y.F. Yang and M. Qian. *Titanium Powder Metallurgy: Science, Technology and Applications*, chapter Spark plasma sintering and hot pressing of titanium and titanium alloys, pages 219–235. M. Qian and F. Froes, 1st edition, 2015.

[193] Malvern Instruments Ltd. Mastersizer 2000 User Manual. Technical Report 1.0, 2007.

[194] Malvern Instruments Ltd. Automated Particle Characterization System. Technical report.

[195] *Retrieved from: www.rsc.org/suppdata/c5/ja/c5ja00419e/c5ja00419e1.pdf (2019, April 27)*.

[196] B. Siva Sai Kiran and S. Raja. A Review on Inductively Coupled Plasma Emission Spectrometry (Icp-Oes) with a Special Emphasis on its Applications. *Der Pharmacia Lettre*, 9(10):44–54, 2017.

[197] W. Grimmond, A.J. Moses, and P.C.Y. Ling. Geometrical Factors Affecting Magnetic Properties of Wound Toroidal Cores. *IEEE Transactions on Magnetics*, 25(3):2686–2693, 1989.

[198] N. Yodoshi, R. Yamada, A. Kawasaki, and A. Makino. Evaluation of critical cooling rate of $Fe_{76}Si_9B_{10}P_5$ metallic glass by containerless solidification process. *Journal of Alloys and Compounds*, 643:2–7, 2015.

[199] D.M. Herlach and F. Gillessen. Pd_3Si nucleation in undercooled Pd-Cu-Si melts. *Journal of Physics F: Metal Physics*, 17(8):1635–1644, 1987.

[200] F. Gillessen, D.M. Herlach, and B. Feuerbacher. Transformation Kinetics and Bulk Glass Formation of Pd-Ni-P. *Zeitschrift für Physikalische Chemie*, 156:129–133, 1988.

[201] S. Mukherjee, W.L. Johnson, and W.K. Rhim. Noncontact measurement of high-temperature surface tension and viscosity of bulk metallic glass-forming alloys using the drop oscillation technique. *Applied Physics Letters*, 86(014104):1–3, 2005.

[202] I. Jonas. *Thermophysical and structural properties of the equilibrium and undercooled melt of bulk metallic glasses investigated by electrostatic levitation*. PhD thesis, Naturwissenschaftlich-Technische Fakultät III Chemie, Pharmazie und Werkstoffwissenschaften, Universität des Saarlandes, 2016.

[203] B. Bochtler, M. Stolpe, B. Reiplinger, and R. Busch. Consolidation of amorphous powder by thermoplastic forming and subsequent mechanical testing. *Materials and Design*, 140:188–195, 2018.

[204] I. Jonas, W. Hembree, F. Yang, R. Busch, and A. Meyer. Industrial grade versus scientific pure: Influence on melt properties. *Applied Physics Letters*, 112(171902):1–4, 2018.

[205] W. Hembree, B. Bochtler, and R. Busch. High-temperature rotating cylinder rheometer for studying metallic glass forming liquids. *Review of Scientific Instruments*, 89(113904):1–6, 2018.

[206] G.S. Fulcher. Analysis of Recent Measurements of the Viscosity of Glasses. *Journal of the American Ceramic Society*, 8(6):339–355, 1925.

[207] G. Adam and J.H. Gibbs. On the Temperature Dependence of Cooperative Relaxation Properties in Glass-Forming Liquids. *The Journal of Chemical Physics*, 43:139–146, 1965.

[208] I. Avramov and A. Milchev. Effect of disorder on diffusion and viscosity in condensed systems. *Journal of Non-Crystalline Solids*, 104(2-3):253–260, 1988.

[209] Q. Zheng and J.C. Mauro. Viscosity of glass-forming systems. *Journal of the American Ceramic Society*, 100(1):6–25, 2016.

[210] J.C. Mauro, Y. Yue, A.J. Ellison, P.K. Gupta, and D.C. Allan. Viscosity of glass-forming liquids. *Proceedings of the National Academy of Sciences of the United States of America*, 106(47):19780–19784, 2009.

[211] N. Ciftci, N. Ellendt, L. Mädler, and V. Uhlenwinkel. Impact of Hot Gas Atomization on Glass Forming Alloys. *Hamburg: World PM 2016, European Powder Metallurgy Association*, ISBN: 978-1-899072-48-4, 2016.

[212] J.S. Markus. *Zerstäubung von Metallschmelzen beim Sprühkompaktieren*. PhD thesis, Fachbereich Produktionstechnik, Universität Bremen, 1996.

[213] F. Mostaghimi, J. Fischer-Bühner, L. Heemann, P. Hofmann, A. von Hehl, and V. Uhlenwinkel. Anti-satellite system for the improvement of powder quality in Additive Manufacturing using a Fe-Mn alloy. *Bilbao: Euro PM 2018, European Powder Metallurgy Association*, ISBN: 978-1-899072-50-7, 2018.

[214] S. Hussain, C. Cui, L. He, L. Mädler, and V. Uhlenwinkel. Effect of hot gas atomization on spray forming of steel tubes using a close-coupled atomizer (CCA). *Journal of Materials Processing Technology*, (in review), 2020.

[215] N. Tiedje, P.N. Hansen, and A.S. Pedersen. Modeling of Primary and Secondary Dendrites in a Cu-6 Wt Pct Sn Alloy. *Metallurgical and Materials Transactions A*, 27(12):4085–4093, 1996.

[216] A. von Freyberg, M. Buchholz, V. Uhlenwinkel, and H. Henein. Droplet Solidification and Gas-Droplet Thermal Coupling in the Atomization of a Cu-6Sn Alloy. *Metallurgical and Materials Transactions B*, 34(2):243–253, 2003.

[217] P.R. Sahm, I. Egry, and T. Volkmann. *Schmelze, Erstarrung, Grenzflächen: Eine Einführung in die Physik und Technologie flüssiger und fester Metalle*. Vieweg, Braunschweig, Wiesbaden, 1st edition, 2001.

[218] H. Henein, V. Buchoud, R.-R. Schmidt, C. Watt, D. Malakov, C.-A. Gandin, G. Lesoult, and V. Uhlenwinkel. Droplet Solidification of Impulse Atomized Al-0.61Fe and Al-1.9Fe. *Canadian Metallurgical Quarterly*, 49(3):275–292, 2010.

[219] J.-O. Choi. *Einfluss der Erstarrungsgeschwindigkeit auf Gefüge und Eigenschaften technischer Kupferlegierungen*. PhD thesis, Institut für Metallkunde der Universität und Max-Planck-Institut für Metallforschung Stuttgart, 1987.

[220] J.A. Horwath and L.F. Mondolfo. Dendritic growth. *Acta Metallurgica*, 10(11):1037–1042, 1962.

[221] J.A. Sarreal and G.J. Abbaschian. The Effect of Solidification Rate on Microsegregation. *Metallurgical Transactions A*, 17(11):2063–2073, 1986.

[222] D. Eskin, Q. Du, D. Ruvalcaba, and L. Katgerman. Experimental study of structure formation in binary Al-Cu alloys at different cooling rates. *Materials Science and Engineering A*, 405(1-2):1–10, 2005.

[223] G. Kasperovich, T. Volkmann, L. Ratke, and D. Herlach. Microsegregation during Solidification of an Al-Cu Binary Alloy at Largely Different Cooling Rates (0.01 to 20,000 K/s): Modelling and Experimental Study. *Metallurgical and Materials Transactions A*, 39(5):1183–1191, 2008.

[224] H. Shiwen, L. Yong, and G. Sheng. Cooling Rate Calculation of Non-Equilibrium Aluminium Alloy Powders Prepared by Gas Atomization. *Rare Metal Materials and Engineering*, 38(4):353–356, 2009.

[225] A.M. Mullis, L. Farrell, R.F. Cochrane, and N.J. Adkins. Estimation of Cooling Rates During Close-Coupled Gas Atomization Using Secondary Dendrite Arm Spacing Measurement. *Metallurgical and Materials Transactions B*, 44(4):992–999, 2013.

[226] K. Li, C. Song, Q. Zhai, M. Stoica, and J. Eckert. Microstructure evolution of gas-atomized Fe-6.5 wt% Si droplets. *Journal of Materials Research*, 29(4):527–534, 2014.

[227] C. Si, X. Tang, X. Zhang, J. Wang, and W. Wu. Characteristics of 7055Al powders manufactured by gas-solid two-phase atomization: A comparison with gas atomization process. *Materials and Design*, 118:66–74, 2017.

[228] F. Hitzigrath. *Bestimmung von diffusiblem Wasserstoff in hochfesten Stählen in Bezug auf die Gitterstruktur*. PhD thesis, Fakultät für Chemie, Universität Duisburg-Essen, 2017.

[229] A.J. Maeland. *Hydrogen in disordered and amorphous solids*, chapter Preparation, structure, and properties of glassy metal hydrides, pages 127–138. Springer Science+Business, LLC, Luxembourg, 1986.

[230] Z. Wronski and A. Morrish. Hydrogen in magnetic metallic glasses. *IEEE Transactions on Magnetics*, 19(5):1895–1897, 1983.

[231] R. Kirchheim. Hydrogen solubility and diffusivity in defective and amorphous metals. *Progress in Materials Science*, 32(4):261–325, 1988.

[232] R. Kirchheim. Hydrogen in amorphous and nanocrystalline metals. *Materials Science and Engineering*, 99(1-2):457–462, 1988.

[233] N. Eliaz, D. Fuks, and D. Eliezer. A new model for the diffusion behavior of hydrogen in metallic glasses. *Acta Materialia*, 47(10):2981–2989, 1999.

[234] J. Pei, A.-C. Yang, K. Zhang, H.-H. Li, L.-M. He, Y.-F. Tian, Y.-F. Qin, S.-S. Kang, S.-Q. Xiao, and S.-S. Yan. Hydrogen enhanced magnetization and exchange interaction in amorphous $(FeCo)_{0.70}Ge_{0.30}$-H films. *Journal of Alloys and Compounds*, 658:98–103, 2016.

[235] J. Kováč, L Novák, and J. Kecer. Hydrogenation caused reversible structural changes in FeCrB type metallic glasses monitored by magnetization parameters. *Journal of Alloys and Compounds*, 735:1591–1595, 2018.

[236] S.-I. Yamaura, M. Hasegawa, H. Kimura, and A. Inoue. Effects of Hydrogen on the Properties of $Ti_{50}Ni_{25}Cu_{25}$ Metallic Glass. *Materials Transactions, JIM*, 43(10):2543–2547, 2002.

[237] B. Cantor, W.T. Kim, B.P. Bewlay, and A.G. Gillen. Microstructure - cooling rate correlations in melt-spun alloys. *Journal of Materials Science*, 26(5):1266–1276, 1991.

[238] V.I. Tkatch, A. Limanovskii, S.N. Denisenko, and S.G. Rassolov. The effect of the melt-spinning processing parameters on the rate of cooling. *Materials Science and Engineering A*, 323(1-2):91–96, 2002.

[239] A.A. Gromov, A.P. Il'in, U. Foerter-Barth, and U. Teipel. Effect of the Passivating Coating Type, Particle Size, and Storage Time on Oxidation and Nitridation of Aluminium Powders. *Combustion, Explosion, and Shock Waves*, 42(2):177–184, 2006.

[240] C. Santhaweesuk. *Glass stability and kinetic analysis of iron-metalloid bulk metallic glass*. PhD thesis, University of Wisconsin-Madison, 2013.

[241] B. Huang, Y. Yang, A.D. Wang, Q. Wang, and C.T. Liu. Saturated magnetization and glass forming ability of soft magnetic Fe-based metallic glass. *Intermetallics*, 84:74–81, 2017.

[242] B. Shen, A. Inoue, and C. Chang. Superhigh strength and good soft-magnetic properties of (Fe,Co)-B-Si-Nb bulk glassy alloys with high glass-forming ability. *Applied Physics Letters*, 85(21):4911–4913, 2004.

[243] S. Irukuvarghula, H. Hassanin, C. Cayron, M. Aristizabal, M.M. Attallah, and M. Preuss. Effect of powder characteristics and oxygen content on modifications to the microstructural topology during hot isostatic pressing of an austenitic steel. *Acta Materialia*, 172:6–17, 2019.

[244] J. Luan, P. Sharma, N. Yodoshi, Y. Zhang, and A. Makino. Mechanically strong nanocrystalline Fe-Si-B-P-Cu soft magnetic powder cores utilizing magnetic metallic glass as a binder. *AIP Advances*, 6(055934):1–7, 2016.

[245] Y. Yoshizawa, S. Oguma, and K. Yamauchi. New Fe-based soft magnetic alloys composed of ultrafine grain structure. *Journal of Applied Physics*, 64(10):6044–6046, 1988.

[246] G. Herzer. Grain structure and magnetism of nanocrystalline ferromagnets. *IEEE Transactions on Magnetics*, 25(5):3327–3329, 1989.

[247] K. Suzuki, A. Makino, N. Kataoka, A. Inoue, and T. Masumoto. High Saturation Magnetization and Soft Magnetic Properties of bcc Fe-Zr-B and Fe-Zr-B-M (M= Transition Metal) Alloys with Nanoscale Grain Size. *Materials Transactions, JIM*, 32(1):93–102, 1991.

[248] A. Makino, H. Men, T. Kubota, K. Yubuta, and A. Inoue. FeSiBPCu Nanocrystalline Soft Magnetic Alloys with High B_s of 1.9 Tesla Produced by Crystallizing Hetero-Amorphous Phase. *Materials Transactions, JIM*, 50(1):204–209, 2009.

[249] A. Makino. Nanocrystalline Soft Magnetic Fe-Si-B-P-Cu Alloys with High B of 1.8-1.9 T Contributable to Energy Saving. *IEEE Transactions on Magnetics*, 48(4):1331–1335, 2012.

[250] V.K. Dhir and G.P. Purohit. Subcooled film-boiling heat transfer from spheres. *Nuclear Engineering and Design*, 47(1):49–66, 1978.

[251] O. Gutfleisch, M.A. Willard, E. Brück, C.H. Chen, S.G. Sankar, and J.P. Liu. Magnetic materials and devices for the 21st century: stronger, lighter, and more energy efficient. *Advanced Materials*, 23(7):821–842, 2011.

[252] V. Franco and O. Gutfleisch. Magnetic Materials for Energy Applications. *JOM*, 64(7):750–751, 2012.

[253] H. Lohner. *Zerstäuben von Mineralschmelzen mit Heißgas*. PhD thesis, Fachbereich Produktionstechnik, Universität Bremen, 2002.

[254] B.J. Yang, W.Y. Lu, J.L. Zhang, J.Q. Wang, and E. Ma. Melt fluxing to elevate the forming ability of Al-based bulk metallic glasses. *Scientific Reports*, 7(11053):1–16, 2017.

[255] Q. Li. Formation of ferromagnetic bulk amorphous $Fe_{40}Ni_{40}P_{14}B_6$ alloys. *Materials Letters*, 60(25-26):3113–3117, 2006.

[256] A.Castellero, S. Bossuyt, M. Stoica, S. Deledda, J. Eckert, G.Z. Chen, D.J. Fray, and A.L. Greer. Improvement of the glass-forming ability of $Zr_{55}Cu_{30}Al_{10}Ni_5$ and $Cu_{47}Ti_{34}Zr_{11}Ni_8$ alloys by electro-deoxidation of the melts. *Scripta Materialia*, 55(1):87–90, 2006.

[257] S. Nukiyama. Maximum and minimum values of heat q transmitted from metal to boiling water under atmospheric pressure. *Journal of the Japan Society of Mechanical Engineers*, 37(53-54):367–374, 1934.

[258] L.A. Bromley. Heat transfer in stable film boiling. *Chemical Engineering Progress*, 46:221–227, 1950.

[259] L.A. Bromley, N.R. LeRoy, and J.A. Robbers. Heat Transfer in Forced Convection Film Boiling. *Industrial & Engineering Chemistry*, 45(12):2639–2646, 1953.

[260] R.K. Eckhoff. Water vapour explosions - A brief review. *Journal of Loss Prevention in the Process Industries*, 40:188–198, 2016.

[261] T. Arai and M. Furuya. Effect of Salt Additives to Water on the Severity of Vapor Explosions and on the Collapse of Vapor Film. *Thermal Science & Engineering*, 15(3):91–100, 2007.

[262] C. Schmidt, M. Beck, M. Ahrenberg, C. Schick, O. Keßler, and U. Kragl. Room temperature ionic liquids in a heat treatment process for metals. *RSC Advances*, 4:55077–55081, 2014.

[263] M. Beck, C. Schmidt, M. Ahrenberg, C. Schick, U. Kragl, and O. Keßler. Ionic liquids as new quenching media for aluminium alloys and steel. *Journal of Heat Treatment and Materials*, 70(2):73–80, 2015.

[264] S. Waldeck, M. Castens, N. Riefler, F. Frerichs, T. Lübbens, and U. Fritsching. Mechanisms and process control for quenching with aqueous polymer solutions. *Journal of Heat Treatment and Materials*, 74(4):238–256, 2019.

[265] G.E. Totten, C.E. Bates, and N.A. Clinton, editors. *Handbook of Quenchants and Quenching Technology*. ASM International, Materials Park, United States, 1993.

[266] J. Baumann, P. Hopp, and P. Sieverding. Charakterisierung und thermoplastische Formung von amorphen Metallpulvern. Technical report, Masterprojekt, Fachbereich Produktionstechnik, Universität Bremen, 2018.

[267] J. Valloton, S. Gawor, and H. Henein. Modelling of nucleation in Impulse atomized undercooled droplets. *Computational Materials Science*, 144:176–180, 2018.

[268] S. Takahashi and O. Kuboi. Study on contact angles of Au, Ag, Cu, Sn, Al and Al alloys to SiC. *Journal of Materials Science*, 31(7):1797–1802, 1996.

[269] W.M. Haynes, D.R. Lide, and T.J. Bruno, editors. *CRC Handbook of Chemisty and Physics*. CRC Press Taylor & Francis Group, Boca Raton, London, New York, 97th edition, 2016.

[270] C.F. Beaton. *Heat Exchanger Design Handbook*, chapter Thermal and mechanical properties of heat exchanger construction material. Hemisphere Publishing Corporation, New York, 1st edition, 1985.

List of symbols

Symbol	Description	Unit
Roman Symbols		
a	Constant to calculate the cooling rate through SDAS	-
a_i	Model parameters to calculate the cooling rate	-
A	Constant to calculate the steady-state nucleation rate	-
A_n	Nozzle outlet section / Area of flow (outflow function)	m^2
A_p	Surface area of the droplet	m^2
B	Magnetic induction	T
B_s	Saturation magnetization	T
c	Sound velocity	$m\,s^{-1}$
C_d	Discharge coefficient	-
C_D	Drag coefficient	-
$c_{p,apparent}$	Apparent specific heat capacity of the melt droplet	$J\,kg^{-1}\,K^{-1}$
$c_{p,g}$	Specific heat capacity of the gas	$J\,kg^{-1}\,K^{-1}$
$c_{p,l}$	Specific heat capacity of the liquid	$J\,kg^{-1}\,K^{-1}$
$c_{p,s}$	Specific heat capacity of the solid	$J\,kg^{-1}\,K^{-1}$
D	Nozzle outlet diameter	m
D^*	Fragility parameter	-
$d_{50,3}$	Mass median particle diameter	m
D_{eff}	Effective diffusivity	$m^2\,s^{-1}$
D_l	Liquid stream diameter	m
d_{max}	Maximum attainable amorphous size or critical casting thickness	m
d_n	nth percentile	m
d_p	Droplet diameter	m
f_s	Solid fraction	-
h	Heat transfer coefficient	$W\,m^{-2}\,K^{-1}$
H	Enthalpy of a system at a given temperature	$J\,kg^{-1}$
H	Magnetic field	T
H_c	Coercivity	$A\,m^{-1}$
$h_{f,g}$	Latent heat of vaporization	$J\,kg^{-1}$
H_{SM}	Solid enthalpy at melt temperature	$J\,kg^{-1}$
I_v	Steady-state nucleation rate	$m^{-3}\,s^{-1}$
k	Software threshold value (static particle imaging)	-
K	Constant to calculate the mass median particle diameter (Lubanska equation)	-
k_g	Thermal conductivity of the gas	$W\,m^{-1}\,K^{-1}$
k_l	Thermal conductivity of the liquid or melt droplet	$W\,m^{-1}\,K^{-1}$
k_v	Thermal conductivity of the vapor	$W\,m^{-1}\,K^{-1}$
m	Steepness index to calculate fragility	-

... continued from previous page

Symbol	Description	Unit
$\dot{m}_G$	Gas mass flow rate	$\mathrm{kg\,h^{-1}}$
$\dot{m}_L$	Melt mass flow rate	$\mathrm{kg\,h^{-1}}$
n	Constant to calculate the cooling rate through SDAS	-
n_{arms}	Number of counted arms to calculate SDAS	#
Q	Convective heat transfer	W
q_3	Density distribution (volume-based)	$\mathrm{m^{-1}}$
Q_3	Cumulative mass distribution (volume-based)	-
p	Atomization pressure	Pa
P	Perimeter	m
p_{asp}	Aspiration pressure	Pa
p_u	Relative pressure	Pa
r_a	Radius after spheoridization	m
r_b	Radius before spheoridization	m
R_c	Critical cooling rate required to obtain a fully amorphous sample	$\mathrm{K\,s^{-1}}$
R_s	Specific gas constant	$\mathrm{J\,kg^{-1}\,K^{-1}}$
t^*	Time at maximum transformation rate (see TTT-diagram)	s
t_{sol}	Soldification time	s
t_{sph}	Spheroidization time	s
T	Temperature	K
T_0	Vogel-Fulcher-Tammann temperature	K
T^*	Temperature at maximum transformation rate (see TTT-diagram)	K
T_a	Ambient temperature	K
T_e	Eutectic temperature	K
T_g	Glass transition temperature	K
T_G	Gas temperature	K
$T_{G,0}$	Initial gas temperature	K
T_{liq}	Liquidus temperature	K
T_m	Temperature of the melt droplet at solid fraction = 0.5	K
T_M	Melt temperature	K
T_n	Nucleation temperature	K
T_p	Droplet temperature	K
T_{rg}	Reduced glass transition temperature	-
T_s	Solidus temperature	K
T_{sat}	Saturation temperature	K
T_w	Wall temperature	K
T_x	Crystallization temperature	K
u	Diffusion-controlled crystal growth rate	$\mathrm{m^{-3}\,s^{-1}}$
u_g	Gas velocity	$\mathrm{m\,s^{-1}}$
u_{gl}	Gas velocity at impact with liquid melt stream	$\mathrm{m\,s^{-1}}$

... continued from previous page

Symbol	Description	Unit
u_l	Liquid stream velocity	$\mathrm{m\,s^{-1}}$
u_p	Droplet velocity	$\mathrm{m\,s^{-1}}$
u_{rel}	Relative velocity	$\mathrm{m\,s^{-1}}$
V	Molar volume	$\mathrm{m^3\,mol^{-1}}$
V_d	Volume of the melt droplet	$\mathrm{m^3}$
X_c	Critical crystallized volume fraction	-

Greek Symbols

ε	Emissivity of the liquid melt droplet	-
η	Shear viscosity	Pa s
η_0	Theoretical infinite-temperature limit of viscosity	Pa s
η_l	Liquid dynamic viscosity or melt droplet dynamic viscosity	Pa s
η_g	Dynamic viscosity of the gas	Pa s
η_v	Dynamic viscosity of the vapor	Pa s
λ_n	Dendrite arm spacing	m
λ_T	Constant to calculate a variable gas temperature	-
μ	Permeability	-
ν_g	Kinematic viscosity of the gas	$\mathrm{m^2\,s^{-1}}$
ν_l	Liquid kinematic viscosity or melt droplet kinematic viscosity	$\mathrm{m^2\,s^{-1}}$
κ	Heat capacity ratio	-
ρ_f	Density of the melt droplet at solid fraction = 0.5	$\mathrm{kg\,m^{-3}}$
ρ_g	Gas density	$\mathrm{kg\,m^{-3}}$
ρ_l	Liquid density or melt droplet density	$\mathrm{kg\,m^{-3}}$
ρ_p	Droplet density (corresponding to liquid density ρ_l)	$\mathrm{kg\,m^{-3}}$
ρ_v	Vapor density	$\mathrm{kg\,m^{-3}}$
σ_g	Geometric standard deviation	-
σ_l	Liquid surface tension or melt droplet surface tension	$\mathrm{N\,m^{-1}}$
σ_{sl}	Interfacial energy between liquid and solid	$\mathrm{J\,m^{-2}}$
ΔG	Driving force for crystallization	J
ΔG^*	Activation barrier for nucleation	J
ΔH_M	Latent heat of fusion	$\mathrm{J\,kg^{-1}}$
ΔH_x	Enthalpy of crystallization	$\mathrm{J\,kg^{-1}}$
Δt	Local solidification time	s
ΔT	Temperature difference between melt droplet and surrounding gas	K
ΔT_M	Melt superheat temperature	K
ΔT_x	Supercooled liquid region	K
Θ	Dimensionless temperature	-
Ψ	Material and gas properties	-
Ψ_{max}	Outflow function	-

... continued from previous page

Symbol	Description	Unit
Constants		
g	Acceleration of gravity, $g = 9.81\ \mathrm{m\,s^{-2}}$	
h_p	Planck constant, $h_p = 6.626\,070\,15 \cdot 10^{-34}\ \mathrm{J\,s}$	
k_B	Boltzmann constant, $k_B = 1.380\,649 \cdot 10^{-23}\ \mathrm{J\,K^{-1}}$	
k_{SB}	Stefan-Boltzmann constant, $k_{SB} = 5.670\,374 \cdot 10^{-8}\ \mathrm{W\,m^{-2}\,K^{-4}}$	
N_A	Avogadro constant, $N_A = 6.022\,140\,76 \cdot 10^{23}\ \mathrm{mol^{-1}}$	
Abbreviations		
AF	Amorphous fraction	%
b/l	Aspect ratio (Particle width-to-length ratio)	-
Bi	Biot number	-
BMG	Bulk metallic glass	-
CCA	Close-coupled atomization	-
CP	Commercial purity feedstock	-
CR	Cooling rate	$\mathrm{K\,s^{-1}}$
DSC	Differential Scanning Calorimetry	-
DTA	Differential Thermal Analysis	-
EDX	Energy-Dispersive X-Ray Spectroscopy	-
FFA	Free-fall atomization	-
GFA	Glass-forming ability	-
GMR	Gas-to-melt mass flow ratio	-
HG	Hot gas atomization	-
HP	High purity feedstock	-
ICP-OES	Inductively Coupled Plasma-Optical Emission Spectroscopy	-
MRO	Medium-range order	-
MS	Melt Spinning	-
MYEGA	Mauro-Yue-Ellison-Gupta-Allan	-
NIST	National Institute of Standards and Technology	-
Nu	Nusselt number	-
PEG	Poly(ethylene glycol)	-
Pr	Prandtl number	-
Re	Reynolds number	-
RS	Rapid solidification	-
RT	Atomization at ambient temperature	-
SDAS	Secondary dendrite arm spacing	m
SEM	Secondary Electron Microscopy	-
SPHT	Sphericity	-

... continued from previous page

Symbol	Description	Unit
SPS	Spark Plasma Sintering	-
SRO	Short-range order	-
TTT	Time-temperature-transformation	-
VFT	Vogel-Fulcher-Tammann	-
VSM	Vibrating Sample Magnetometer	-
We_g	Gas Weber number	-
We_l	Liquid Weber number	-
T_{rg}	Reduced glass transition temperature	-
XRD	X-Ray Diffraction	-

Student contribution

During this PhD thesis, the following students have been supervised by the author and some of their results, insights, and discussions have been included in the author's thesis. Note, despite the fact that References [2, 3, 5, 8] have not officially submitted any thesis according to the FB04 Production Engineering, University of Bremen student regulations, their work has been treated according to the Faculty of Engineering's Co-op Program at the University of Alberta, Edmonton, Canada and the Metallurgical Engineering with Emphasis in Materials Science faculty at Federal University of Minas Gerais, Belo Horizonte, Brazil.

[1] P. Hopp. Entwicklung eines konstruktiven Aufbaus zur Ermittlung der Umformbarkeit von metallischen Partikeln. *B.Sc. Thesis*, June 2016.

[2] E. Soares Barreto. Cooling rate determination for gas-atomized CuSn6 powders and phase analysis for glass-forming alloys. *Metallurgical Engineering Diploma With Emphasis on Materials Science*, February 2017.

[3] G. Coulthard. Nature-inspired acid solution sintering of iron-based amorphous powders at room temperature. *University of Alberta Co-op Program*, December 2017.

[4] J. Baumann, P. Hopp, P. Sieverding. Herstellung, Charakterisierung und thermoplastische Formung von amorphen Metallpulvern. *Masterprojekt*, April 2018.

[5] J. Eitzen. Numerical estimation and prediction of cooling rates during molten metal gas atomization. *University of Alberta Co-op Program*, December 2018.

[6] P. Sieverding. Entwicklung eines numerischen Modells zur Bestimmung der Abkühlraten amorph erstarrender Metallpulver bei der Gas-Zerstäubung. *M. Sc. Thesis*, May 2019.

[7] L. Ludwig. Zerstäubung und Charakterisierung von weichmagnetischen amorphen Eisenbasislegierungen. *B.Sc. Thesis*, August 2019.

[8] S. Armstrong. Modelling CCT and TTT curves to predict crystallization. *University of Alberta Co-op Program*, December 2019.